The Photophysics of Small Organic Molecules for Novel Light Emitting Devices

Dissertation zur Erlangung des
naturwissenschaftlichen Doktorgrades
der Julius-Maximilians-Universität Würzburg

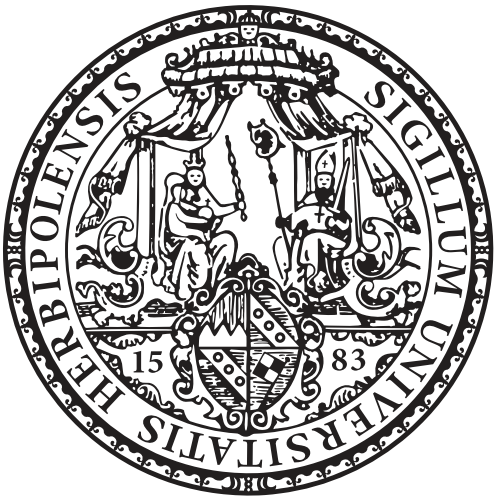

vorgelegt von

Ulrich Genheimer

aus Friedrichshafen

Würzburg, 2022

Eingereicht am: 18.08.2022
bei der Fakultät für Physik und Astronomie

Gutachter der Dissertation:
1. Gutachter: Prof. Dr. Jens Pflaum
2. Gutachter: Prof. Dr. Markus Sauer

Prüfer im Promotionskolloquium:
1. Prüfer: Prof. Dr. Jens Pflaum
2. Prüfer: Prof. Dr. Markus Sauer
3. Prüfer: Prof. Dr. Björn Trauzettel

Tag des Promotionskolloquiums: 24.02.2023

Doktorurkunde ausgehändigt am:

Contents

1 Introduction

Our eyes are *the* broadband connection between our brain and the outside world. The retina in the eye processes about 10 gigabytes per second [1], comparable to a today's fiber optic network connection. Displays are the modern counterpart of this optical connection and represent a possibility to visualize information dynamically. Although it is questionable what percentage of information transmitted by displays represents essential information for our brain, there is no doubt that this connection between displays and our eyes has become increasingly important in recent decades. Our future will be shaped, in particular, by interaction with computer systems. Professional fields such as air traffic controllers, 3D designers and surgeons will be able to use sophisticated displays to capture complex information with increasing ease or to access supporting information during their manual work.

However, the beginnings of color displays were cumbersome. The first color cathode-ray tubes were produced in 1954. Here, small green, red and blue phosphorescent dots on a screen were excited by three separate electron beams. A well-heeled and well-versed customer was thus able to view the first television pictures in color on a rounded display (see Figure 1.1, left) with a dimension of about 160 x 120 pixels, while the entire system consumed about 475 W of electrical power [2]. In contrast, modern organic light-emitting diode (OLED) displays, like the one used in Sony's Xperia 1 (see Figure 1.1, middle) only consume electrical power in the range of 100 mW [3] and could display the pixels of the first color cathode-ray with a resolution of more than 643 pixels per inch on an area of 6 mm × 5 mm. In addition, these OLED displays have become extremely thin. Without substrate, they have a thickness of about 1 µm and thus, allow the production of curved and bendable screens. In the future, ever smaller displays with ever higher resolutions will offer new application possibilities in the field of virtual and augmented reality. For example, contact lenses are conceivable (conception in Figure 1.1, right) which project information directly onto our retina and thus, provide us with auxiliary information or extend our natural visual senses.

However, the resolution of a display is not the only aspect to be optimized on the way to more and more sophisticated displays. Other important aspects include power efficiency,

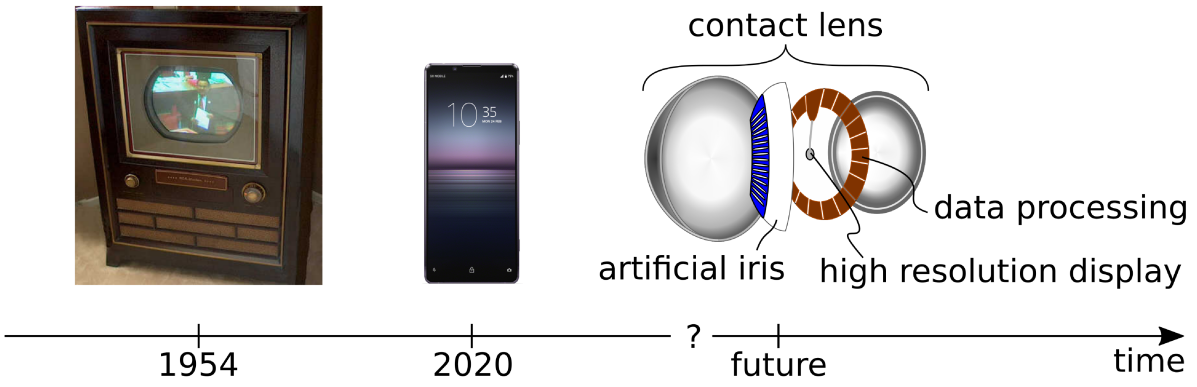

Figure 1.1: Left: First commercial TV screen “Victor CT-100” from 1954 produced by the company RCA with a rounded screen of 160 x 120 pixels. The system is part of a private collection [4] and was restored by Steve Dichter, who kindly granted permissions to use this picture. Middle: Contemporary OLED display used in Sony‘s Xperia 1 [5] utilizing 1644 x 3840 pixels. Right: Conception of a contact lens with integrated high resolution display for future augmented reality applications. In 2020 companies like *Mojo Vision* and *Samsung* demonstrated first prototypes.

color gamut, device lifetime and contrast ratio. As we will see, all these aspects depend on the properties of the luminous small molecules used in the OLEDs. These molecules are at the center of this work, the aim of which is to analyze their photophysics, to demonstrate different modes and mechanisms behind the emission of light and to gain insights that will enable the next generations of light emitting devices. But first, we look at the underlying function of an OLED: The schematic structure is shown in Figure 1.2. The OLED consists of a cathode and an anode connected to a voltage source operating in the range between 1 V to 10 V. Between the electrodes there is a series of thin organic layers that give the OLED its name. Both types of charge carriers enter the emitting layer (EML) via a selective electron transport or hole transport layer (ETL/HTL). In this emitting layer, the luminescent guest molecules are dispersed within a matrix and capture the free charge carriers, so that excitons are formed on the molecular dopants. In an alternative approach, excitons are already formed in the matrix and then transferred to the doping molecules. In either case, the excitons then ideally recombine radiatively at the site of the molecule and one photon per electron-hole pair is emitted.

The optimization of OLEDs is a complex process and the improvement of dopants is not the only challenge. Among others, these challenges include: Finding or modifying materials that are suitable for production steps such as spin coating, inkjet printing or vacuum deposition while maintaining their chemical stability, ensuring that all materials

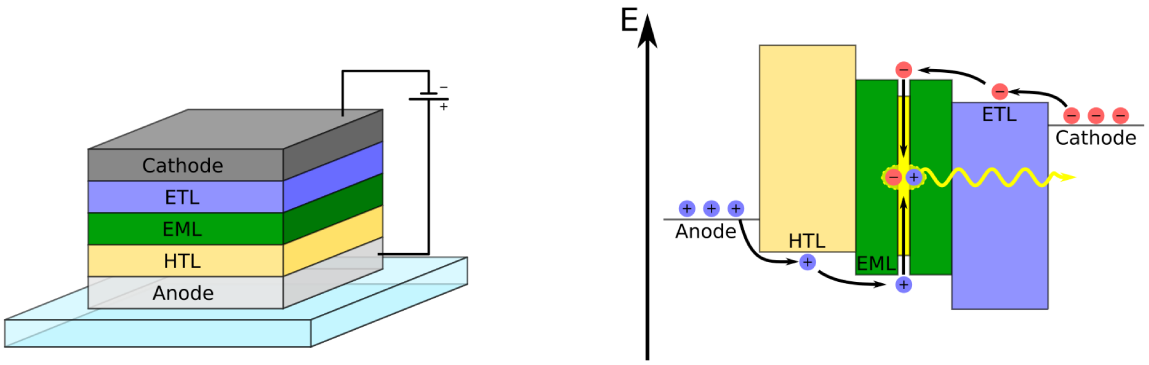

Figure 1.2: Left: Layer structure and principle energy diagram of an OLED: anode/hole transport layer (HTL)/emissive layer (EML)/electron transport layer (ELT)/cathode, Right: Energy levels for electrons and holes in an OLED.

have a sufficiently high glass transition temperature to avoid crystallization of the layer material during device lifetime, minimizing quenching mechanisms by tailoring the respective orbital energies of long living dark states in the host material [6], protecting cathode materials from atmospheric oxidation and designing the cathode-ETL interface with respect to the work function of the cathode, the lowest unoccupied molecular orbital (LUMO) of the ETL, and the resulting electron injection barrier at the metal–organic interface to minimize electric resistance [7], balancing charge carriers in the active device volume to concur with microcavity effects in the OLED and, not least, optimizing light out-coupling of the OLED [8]. Despite these many challenges upon optimizing an OLED, the luminescent molecular dopants have a very direct influence on many properties of the OLED. In the following we will take a closer look at these properties:

Power Efficiency: A high power efficiency is not only desired in order to consume as little electrical power as possible while providing a certain amount of light, but also to keep the waste heat in the components as low as possible. The power efficiency of an OLED is proportional to its external quantum efficiency (EQE) and this quantity is defined as the ratio of emitted photons to injected electron hole pairs. Since there are several largely independent loss mechanisms along the route of an injected electron hole pair to an emitted photon, the EQE (η_{ext}) can be written as the product of different mechanisms [9]:

$$\eta_{ext} = \eta_{ex}\phi_p\eta_{ph} \tag{1.1}$$

Here η_{ex} is the fraction of injected electron hole pairs that form excitons on molecular guests which perform a subsequent radiative transition. This fraction depends on the type of luminescence of the molecule and can be 1 for phosphorescent emitters and as low as 0.25 for fluorescent emitters. Next, ϕ_p is the internal quantum efficiency of the exciton decay, i.e. the probability of observing a radiative decay with non-radiative decay channels as competing processes. Finally, η_{ph} is the fraction of photons that manage to leave the OLED in the direction of the observer. Without special measures like surface structuring [8] or molecular alignment [10], η_{ph} typically lies in the range of 25 % [9] resulting in an overall η_{ext} typically between 10 % and 20 % [6].

Contrast Ratio: The contrast ratio is a measure by which OLEDs stand out from display types based on back lighting such as liquid crystal displays. The contrast ratio describes the brightness ratio between a pixel that is switched on versus its off-state. For marketing reasons, the contrast ratio for OLEDs is often given as infinity, because turned off pixels are completely dark and emit no light at all [3]. However, this neglects ambient light that is scattered on the display. For a high image quality under ambient light, it is therefore desirable to increase the absolute brightness of the individual pixels. However, this cannot be achieved by simply increasing the current density in the OLED device, as at higher exciton densities in the emitting layer, exciton-charge carrier interaction as well as exciton-exciton annihilation processes increase disproportionately and an efficiency roll-off can be observed [11] with dissipated heat causing additional negative effects on other processes in the OLED. Therefore, a primary goal is to keep the radiative recombination rate of excitons on the dopant molecules as high as possible and thus to limit the exciton density in the emissive layer.

Device Lifetime: The lifetime of OLED displays is still a critical issue in the year 2021, especially for electronic goods like TVs, where consumers expect long device lifetimes [3]. Especially, blue emitters are the problem here. The reason for this is the energetically high lying exciton state of blue emitters which are susceptible to irreversible photobleaching [12]. An obvious strategy is therefore again to increase the radiative recombination rate of excitons on the dopant molecules in order to minimize the time a molecule resides in its excited state and is prone to photobleaching.

Color Gamut: In order to develop a display with the most brilliant colors possible, it is necessary to take into account the color perception of the human eye. Our retina has three different types of cone cells, which have different maximum absorption sensitivities in the blue, green and yellow and therefore, are excited to different degrees by light of different colors [13]. If we neglect the absolute brightness of a color, all perceivable colors can be represented in a two-dimensional map established by the *Commission*

internationale de l'éclairage (CIE map), which is illustrated in Figure 1.3. To cover this color space by the emission of a display, the three primary colors red, green and blue are used to form a red-green-blue (RGB) color space. In the early days, when the first color images were generated by cathode-ray tubes, this color space covered only a rather small part of the CIE-map. However, by choosing primary colors located more to the edge of the CIE map the RGB space has been continuously expanded over the past years to cover an ever-increasing proportion of all colors which can in theory be perceived by our eyes. The latest RGB standards take this to the extreme and use individual spectral lines, i.e. monochromatic primary colors, (red: 635 nm, green: 532 nm, blue: 467 nm) as RGB references [14]. However, these colors can currently only be produced by RGB lasers. For OLEDs in application, the goal is therefore, that each of the three colors must be generated by just one type of luminescent molecule. These three colors should be located in the corners of the RGB triangle defined by the corresponding standard and therefore, have to emit at the narrowest possible spectral linewidth. This modification of molecular emission is often achieved by substitution of chemical moieties. As an example, Figure 1.3 illustrates how the substitution of ligands in a copper complex can shift the emission of the species towards the red corner of the RGB color space.

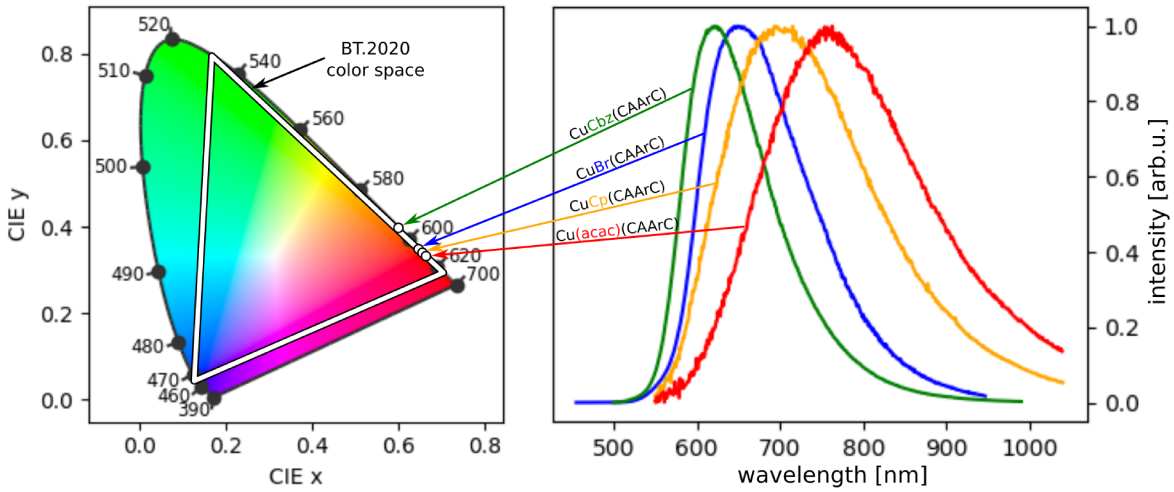

Figure 1.3: Emitters in the CIE map. Left: All perceivable colors can be represented in a two-dimensional CIE map. An RGB standard (BT.2020) covers only the colors within the triangle. Right: The emission of copper complexes can be shifted within this color space by substitution of ligands. Emission data was kindly provided by Markus Gernert from the group of Dr. Andreas Steffen at the Institute of Inorganic Chemistry at the University of Würzburg.

As we have seen, there are several objectives that need to be fulfilled in order to design suited luminescent dopant molecules for OLED applications. Each of these goals is

relatively easy to cope with by its own, while it is very difficult to find molecules which satisfy all relevant aspects. For example, if one only aims to optimize the quantum efficiency of a molecule, it is possible to reach almost 100 % with phosphorescent molecules like $Ir(ppy)_2(acac)$ [15]. But the exciton lifetime of this molecule occurs on a relatively long time scale of µs [16], which leads to problems with device lifetime and limits their maximum brightness. Fortunately, the variety of possible emitters in organic chemistry is almost unlimited. To perform an efficient and targeted search for the best emitters it is necessary to understand the mechanisms to which excitons, and in particular their formation and relaxation, in molecules are subjected. This work aims for the goal to provide valuable insights to this topic by analyzing the photophysics of a number of novel molecules and revealing the underlying mechanisms of emission and non-radiative losses. Many of the findings are based on the direct investigation of single luminescent molecules. In contrast to measurements on molecular ensembles, which average over a large number of identical molecules with different local environments, single-molecule measurements allow to study the interaction of a molecule with its local environment and to separate these effects from its intrinsic properties, thus, disclosing the inherent potential of a given compound. Additionally, the study of photon statistics, i.e. the analysis of the exact temporal distribution of the emitted photons, plays a special role in this work as it allows, among others, to identify single molecule emission.

Part I of this thesis provides the physical background to understand the relevant properties of organic molecules and their interaction with light. Afterwards, a closer look at the photon statistics of single molecules is taken and it is clarified which information about a molecule is contained in the statistics of its emitted photons and how this information can be extracted. Part II describes all materials used in this work. The investigated luminescent organic molecules are classified according to the different mechanisms preceding the emission of a photon and these mechanisms are discussed in detail. Furthermore, all experimental setups and the preparation of the samples are described. Finally, Part III presents the results and discusses the findings that will help to develop the next generations of OLEDs and other novel photon sources. This includes the detailed discussion of the photophysics of several representative small molecules featuring different emission mechanisms, the role of interaction with the local environment on the single molecule level, novel molecules that prove their applicability in OLEDs for the first time and finally, electrically pumped multichromophoric molecules, which are optimized for the emission of single photons and possibly will serve as active entities in future non-classical light sources. These molecules emit so brightly that individual emitting molecules can be observed by eye under the microscope.

2 Physical Background

This chapter provides the physical basis for understanding the behavior of molecules with respect to their emission of light. First, we will look at the structure of organic molecules. Then we will clarify how these molecules interact with light. Finally, we will see what information can be obtained about a molecule from its light emission.

2.1 Molecules, Light and their Interaction

2.1.1 Organic Molecules

Organic molecules are based on carbon compounds and their photophysics is essentially determined by the electronic structure of the constitutive carbon atoms. Here, the most important role is played by sp^2-hybridized carbon which forms three sp^2 hybrid orbitals. These orbitals are oriented in the x-y-plane of the molecule at an angle of 120° with respect to each other. They are singly occupied by electrons and therefore, can form strong sigma bonds to other elements. This type of bond allows for large, predominantly planar, molecules. A representative is benzene (C_6H_6), illustrated in Figure 2.1, in which six carbon atoms bind to form a closed ring.

The single occupied p_z orbitals of each carbon atom in benzene also contribute to the stabilization of the molecule by forming a delocalized π electron system along the ring. The electrons of the p_z orbitals occupy the energetically most favorable π molecular orbitals of binding character. The energy gap between the highest occupied molecular orbital (HOMO) and the lowest unoccupied (anti-bonding $\pi^\star$) molecular orbital (LUMO) essentially determines the photophysical properties of the organic molecules. For most carbon based aromates this energy gap amounts to 1.5 eV to 3 eV, which corresponds to wavelengths between 400 nm and 800 nm and thus, lies in the visible region of the electromagnetic spectrum [10].

By optical or electrical excitation, an organic molecule can be converted into one of the excited configurations shown in Figure 2.2. In this simplified picture of electrons occupying the molecular orbitals, however, the interaction between the electrons is

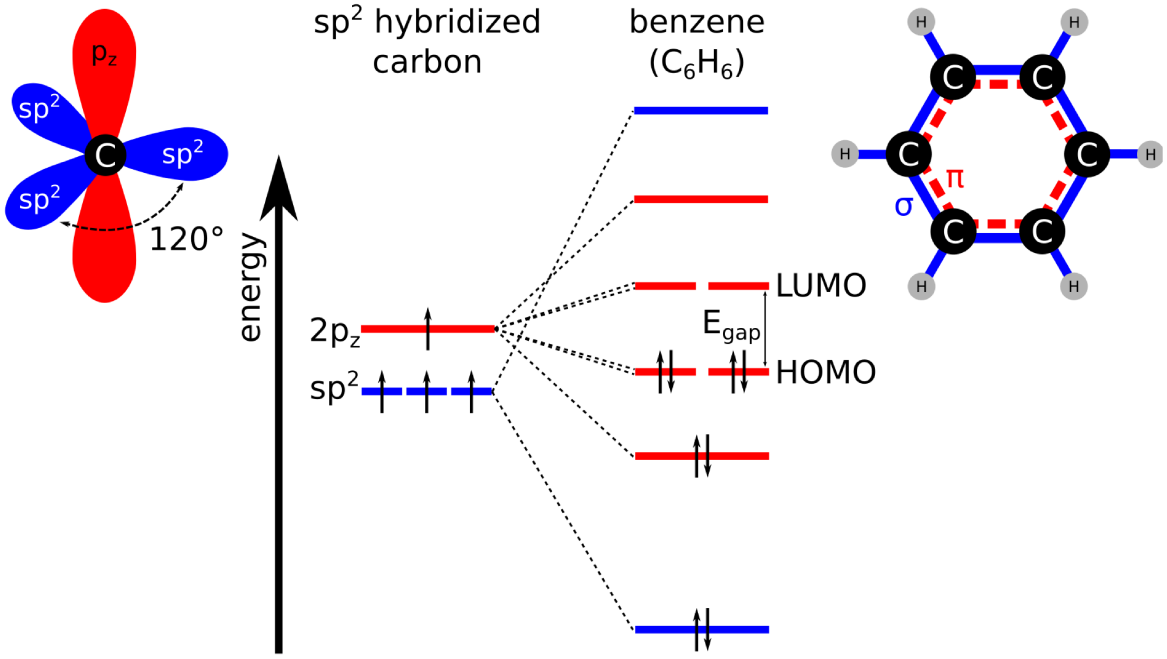

Figure 2.1: Origin of delocalized π-electron systems. Left: sp^2-hybridized carbon has three singly occupied sp^2 orbitals and one singly occupied p_z orbital. Middle: The interaction between several carbon atoms leads to a splitting of the energy levels of the $2p_z$ molecular orbitals. Right: In benzene the p_z orbitals form a delocalized π-electron system delocalized along the ring which determines the optical properties of the molecule.

neglected. Therefore, it is more useful to describe the electronic state of the molecule as a collective state and to indicate its total energy as shown in Figure 2.2 on the right side.

Only then, energetic differences such as those between S_1 and T_1, where only one electron spin is flipped, become apparent. This is extremely important for the photophysics of the molecules. Therefore, in the following the idea of an electron that is excited by a photon from the HOMO to the LUMO is replaced by the view that the whole molecule is excited from its S_0 to its S_1 state.

In order to further refine the picture of processes taking place upon photon absorption and emission in the molecule, vibronic processes of the atomic nuclei are included. In the Born–Oppenheimer approximation, which separates electronic and vibrational wavefunctions, the vibronic processes are described by the Franck-Condon principle [17], shown schematically in Figure 2.3. Here the process of absorption from the S_0 into the S_1 state is indicated by vertical blue arrows and can end in different vibronically excited states. As these transitions exhibit different Franck-Condon factors, i.e. different amount of vibrational wave function overlap, the corresponding absorption bands vary in strength.

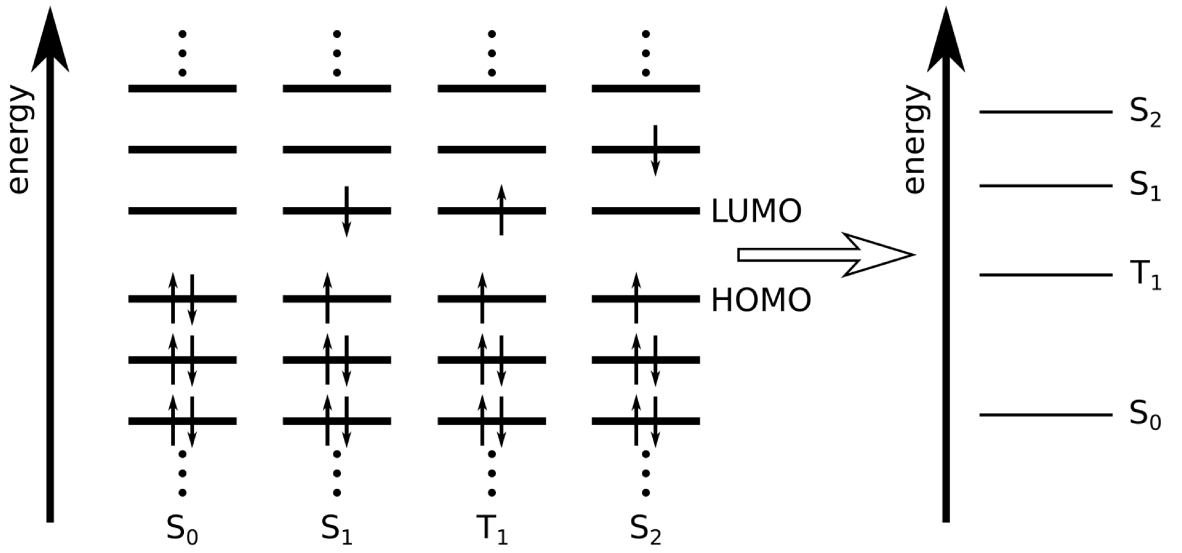

Figure 2.2: From configuration picture to state model. Left: In the configuration picture electrons, indicated by small arrows, occupy the individual molecular orbitals. In this picture, electron-electron interactions are neglected. Right: The states of a molecule are better described by collective states with their corresponding total energies.

The intra-molecular vibrations have frequencies of 10^{12} Hz to 10^{14} Hz [18] and quickly relax to the vibronic ground state of the electronically excited state if there is a possibility to dissipate the excess energy to the environment. This effect also occurs upon light emission, indicated by red arrows in Figure 2.3, which leads to two distinct characteristics of absorption and emission spectra: First, both have a vibronic structure that reflects the vibronic structure of the molecule. Second, the molecule's emission is red-shifted in respect to the absorption.

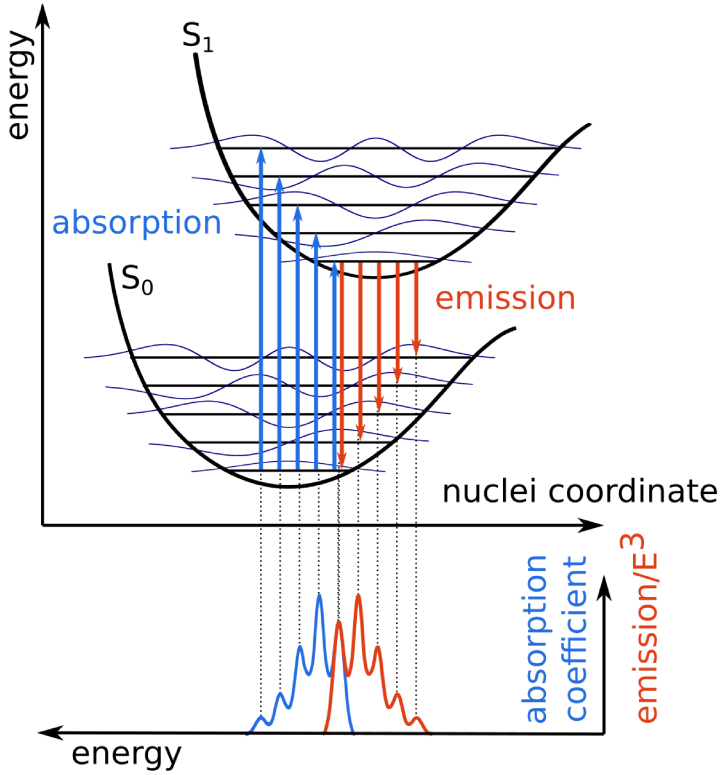

Figure 2.3: Illustration of the Franck-Condon principle. After the absorption (blue arrows) and emission (red arrows) of a photon the molecule can be vibrationally excited. This vibrational energy spectrum becomes apparent in the molecule's absorption and emission spectrum. The process is described in detail in the text.

Besides radiative transitions, non-radiative transitions are another possible relaxation process of the electronically excited state. This includes internal conversion, i.e. non-radiative transitions between states of equal multiplicity, and transitions between singlet and triplet states, known as intersystem crossing. An overview of possible transition processes is shown in the Jablonski diagram in Figure 2.4. The described transitions take place on widely differing time scales: Absorption and fluorescence, i.e. the radiative recombination from S_1 to S_0, have a high oscillator strength and emission runs on the time scale of nanoseconds while the absorption rates depend on the intensity of the excitation light. Transitions between singlet and triplet states are generally spin-forbidden. However, effects such as heavy atoms incorporated in the molecule [19] or processes that mix singlet π,$\pi^\star$ excitations, i.e. excitations between bonding and anti-bonding π-orbitals, and triplet n,$\pi^\star$ excitations, i.e. excitations between non-bonding and anti-bonding π-orbitals, can lift this constraint. Thus, it is also possible to observe phosphorescence, i.e. the radiative transition between T_1 and S_0 state with typical T_1-lifetimes in the range of microseconds.

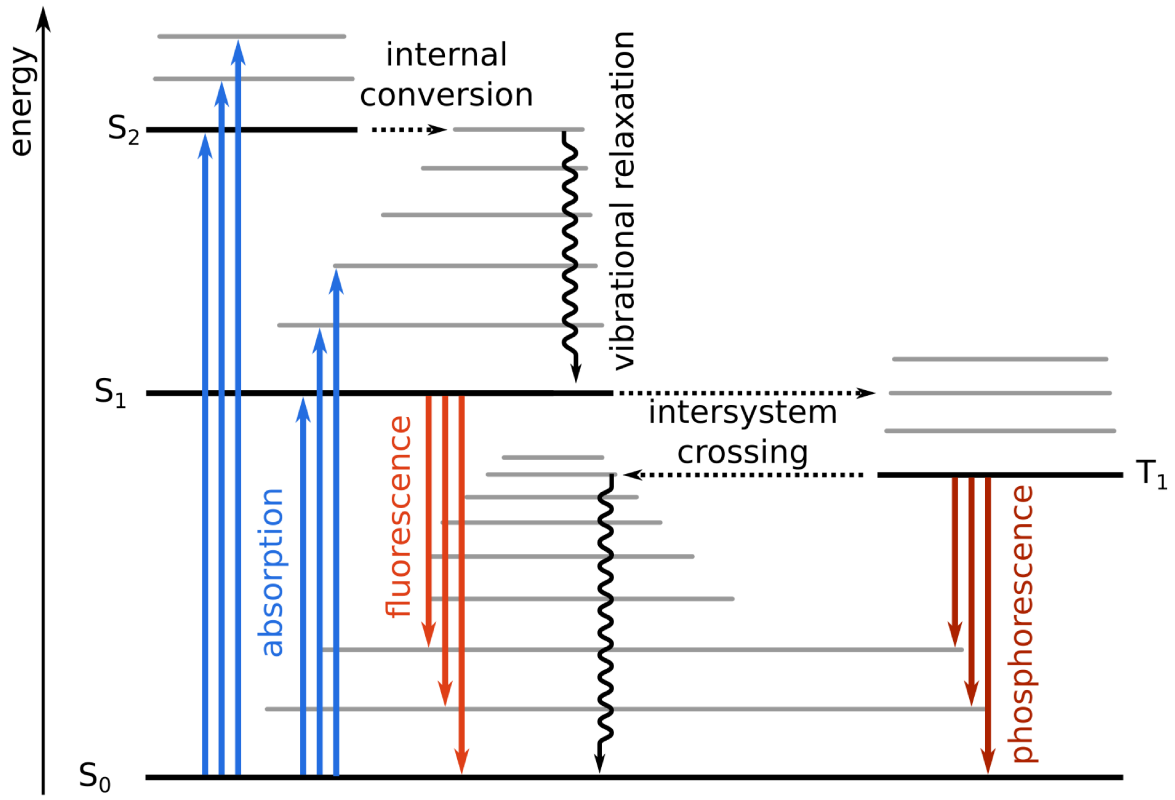

Figure 2.4: Illustration of a molecule's Jablonski diagram. Besides radiative transitions like absorption, fluorescence and phosphorescence there are non-radiative transitions between states of equal multiplicity, i.e. internal conversion, and different multiplicity, known as intersystem crossing, as well as vibronic relaxation channels within different electronic states.

2.1.2 Light

Light can be theoretically described in the basis of planar electromagnetic waves. These waves can be defined by the vector potential

$$\mathbf{A}(\mathbf{r},t) = A_0 \boldsymbol{\varepsilon} \cos(\mathbf{k}\cdot\mathbf{r} - \omega t) \tag{2.1}$$

where each wave is characterized by the normalized vector of polarization $\boldsymbol{\varepsilon}$, the wave vector $\mathbf{k}$ with $\boldsymbol{\varepsilon}\cdot\mathbf{k} = 0$ and the angular frequency of the oscillation $\omega = c\cdot|\mathbf{k}|$. Further, A_0 is the amplitude of the vector potential, $\mathbf{r}$ the position vector and t the time. Starting from this vector potential, the electric and magnetic fields associated with the wave can be obtained by

$$\mathbf{E} = -\frac{\partial_t \mathbf{A}}{c} \qquad \text{and} \tag{2.2}$$

$$\mathbf{B} = \nabla \times \mathbf{A}. \tag{2.3}$$

While planar waves are rather an idealized concept they serve as a mathematical basis to construct waves which are closer to reality by using a superposition of different planar waves with different $\mathbf{k}$ and ω.
An important aspect of these fields is their quantization. While classical theories allow an arbitrary amplitude of the vector potential, the quantization of light predicts single photons with an amplitude of $A_0 = \sqrt{\frac{8\pi\hbar c^2}{\omega V}}$ in the volume V and at energy of

$$E(1\,\text{photon}) = \frac{V}{8\pi}\left(\langle \mathbf{E}^2 \rangle + \langle \mathbf{B}^2 \rangle\right) = \frac{V A_0 \omega^2}{8\pi c^2} = \hbar\omega. \tag{2.4}$$

While Einstein's interpretation of the photoelectric effect indicated that materials absorb radiation in quantized portions [20], the unambiguous experiment which showed the quantization of light was performed by *Clauser* [21] using single photons emitted by a mercury atom and a Hanbury Brown and Twiss photomultiplier configuration [22] for detection. This setup plays a crucial role in this thesis as it allows for the detection and verification of single photons and the characterization of the molecules which emit these photons.

2.1.3 Interaction between Light and Molecules

Absorption and Stimulated Emission

The absorption and emission of light is commonly described by first order perturbation theory. Fermi' golden rule [23] predicts the rate of transition from one discrete state to an other in the case of weak interaction with an electromagnetic field of continuous frequency distribution:

$$\Gamma_{i\to f} = \frac{2\pi}{\hbar}\left|\langle i|\hat{V}_{\pm}|f\rangle\right|^2 \delta(E_i - E_f \pm \hbar\omega) \tag{2.5}$$

where the perturbation operator is given by

$$\hat{V} = \frac{e}{m_e c}\hat{\mathbf{A}}\cdot\hat{\mathbf{p}}. \tag{2.6}$$

Here $\hat{\mathbf{p}}$ denotes the momentum operator, $\hbar$ the Planck constant, ω the angular frequency of the oscillation, e and m_e the charge and mass of the electron and c the speed of light.

This indicates that the processes of absorption and stimulated emission of a two level system have equal probability and are proportional to the intensity of the electromagnetic field interacting with the system. Nevertheless stimulated emission plays a minor role in the experiments of this thesis. The reason for this are the vibrationally excited states which allow the molecule to dissipate part of its energy to the environment. Therefore, after losing part of its energy, the system is no longer susceptible to stimulated emission at the photon energy that causes absorption. As vibrational relaxation happens typically within the femtosecond range [18], its transition rate is several orders of magnitude higher than the transition rate of absorption at moderate excitation intensities. This allows to model the process of absorption with a single rate constant, which describes the transition as an effective one-step process from the ground state to the relaxed electronically excited state with a transition rate proportional to the exciting laser light and without including stimulated emission.

Spontaneous Emission

The vibrational ground state of the first excited singlet state tends to spontaneously decay within several nanoseconds. This process is provoked by the quantization of the electromagnetic field. This leads to a non vanishing amplitude of the vector potential even in the ground state of the electromagnetic field where the amplitude is not zero but its energy is equivalent to half a photon. This in turn results in a finite probability to emit one photon spontaneously. In the dipole approximation the transition rate of spontaneous emission reads

$$P_{i\to f} = \frac{4}{3}\frac{e^2}{\hbar c^3}\left|\langle i|\hat{\mathbf{r}}|f\rangle\right|^2 \omega_{if}^3 \tag{2.7}$$

and thus, provides three important results: First, the transitions between two states might be forbidden, if the transition dipole moment $\langle i|\hat{\mathbf{r}}|f\rangle$ between initial and final state is zero. Whether this is the case is determined by the symmetry of the molecule's HOMO and LUMO wavefunctions. Second, if the transition is dipole-allowed the polarization of the emitted light is determined by the symmetry of the participating molecular orbitals. Third, the rate of spontaneous emission is proportional to ω_{if}^3. This leads to an enhanced spectral weight in blue emission regime of the experiment and has to be considered when evaluating the transition dipole moments of molecular transitions from experimental spectra.

2.2 Design Criteria for Efficient Organic Light Emitting Diode Dopants

As discussed in Chapter 2.1.1, there are several processes by which a molecule can change its electronic state. In particular, the rates of intersystem transitions between singlet and triplet states are crucial for the design of suited OLED dopants with a high quantum efficiency and a strong luminescence. If one had the possibility to tune the transitions rates between the different states of the molecule, what would be the ideal values for this? If we remember the initially defined objectives, one of them was to achieve the shortest possible exciton lifetime. The most obvious approach to achieve this goal would be to utilize a fluorescent transition with a fast radiative decay instead of a phosphorescent transition. However, in the case of electrically pumped OLEDs, it is a challenge to efficiently occupy this state. First of all, due to the electron-electron exchange interaction, the triplet state are energetically lower in energy than the corresponding singlet state and therefore, is preferentially occupied by excitons. Secondly, the triplet state with its total spin 1 is theefold degenerate in its magnetic quantum number $M_s = -1, 0, 1$. This leads to the observation that a fluorescent dopant that is electrically pumped within a matrix is excited only at a probability of 25 % in the singlet state but with a probability of 75 % in its triplet states [6]. Additionally, these triplet states are long living and thus, limit the efficient re-excitation of the fluorophore. Simple fluorescent molecules are therefore of only limited use in OLEDs.

In the present work, two fluorescent monomers, the squaraine *monomer M* and a perylene bisimide monomer, are analyzed. In Chapter 4, these molecules are presented in more detail with respect to their chemical and main physical properties together with other new types of molecules that use multichromophores, thermally activated delayed fluorescence, phosphorescence or open-shell systems to solve the challenge of efficient light generation. Figure 2.5 gives an overview of all guest molecules used in this work for emission studies and classifies them with respect to the underlying mechanism of light generation.

Multichromophores

In comparison to fluorescent molecules with just one chromophore, multichromophores employ the interaction between several identical chromophores. For example, the process of triplet-triplet annihilation allows the generation of a singlet exciton from two triplet excitons. For OLEDs that are operated by electro-fluorescence, a maximum of

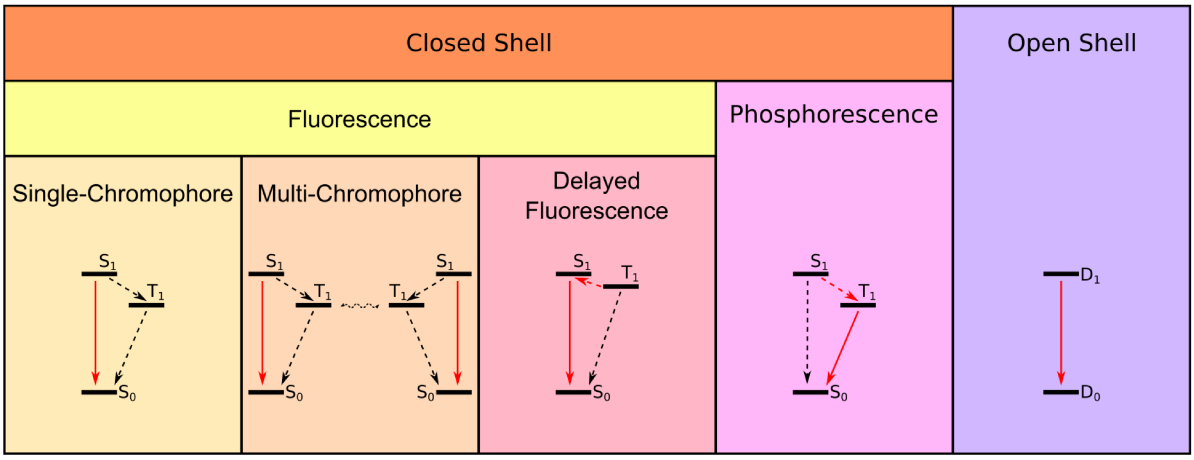

Figure 2.5: Overview of different types of recombination mechanisms. For each category the characteristic path of molecular transitions is shown in red. Radiative transitions are marked by solid lines, non-radiating transitions by dashed lines.

62.5 % (25 % singlet states and $\frac{1}{2}\times$ 75 % triplet states) is theoretically possible [24]. The mechanism of triplet-triplet annihilation allows also for niche applications like OLEDs with an exceptionally small onset voltage of 1 V [25], as the related energy of two generated triplet excitons is sufficient for the generation of a singlet exciton.

In order to control the triplet-triplet interaction precisely, it is possible to covalently link the two involved chromophores and therefore, to keep their distance constant, which is crucial for the strength of the interaction [26]. Moreover, by covalent linking, other properties like chemical stability and solubility can be improved [27]. The crystal structure can be adjusted in a defined way and energy levels can be modified [28]. Finally, the triplet-triplet interaction on one macro-molecule van be used to realize an efficient single photon source [29].

Delayed Fluorescent Molecules

Another possibility to achieve almost 100 % internal quantum efficiency is to transfer the population of the triplet state back to the singlet state and to observe the fluorescence emitted from there [30]. Since S_1 is energetically higher than T_1, this approach requires among other things the smallest possible energy gap between T_1 and S_1 so that the thermal energy of the environment is sufficient to stimulate this transition [31]. This phenomenon was observed in Eosin already in the 1960s [32] and was called *E-type* fluorescence. Nowadays, this process is called thermally activated delayed fluorescence (TADF) and was applied for the first time by SnF_2-porphyrin metal complexes in OLEDs [33], which exhibited still a rather big singlet-triplet energy gap of 390 meV. Today more elaborated

molecules are available, which often involve charge transfer excited states with singlet triplet gaps of only a few meV [34].

Phosphorescent Molecules

Besides fluorescent molecules, one strategy towards efficient OLEDs is to allow for strong occupation of the triplet states and, instead, to focus on the optimization of intersystem crossing and the subsequent phosphorescence. This can be achieved by enhancing spin orbit coupling (SOC) to activate the otherwise spin forbidden $S_0 \leftarrow T_1$ transition [35]. Additionally, an increased spin orbit coupling can enhance the intersystem crossing and, thus, effectively transfer singlet excitons to the triplet states. As a result, nearly 100 % of all generated excitons are converted to photons [15]. In commercial materials, like $Ir(ppy)_3$ [36], the increase of spin orbit coupling is achieved by relativistic effects in the vicinity of heavy atoms incorporated in the molecule [37]. Thus, it is possible to increase the radiative decay rate from the triplet states to the singlet ground states and observe strong phosphorescence. In the case of $Ir(ppy)_3$, the triplet state has a lifetime of 1.57 µs [38], which is short in comparison to other organic molecular species without heavy atoms, typically exhibiting triplet lifetimes in the range of milliseconds [39], but long in comparison to fluorescent lifetimes, which decay within nanoseconds.

Open-Shell Molecules

A completely different approach is based on the use of open-shell molecules instead of closed-shell molecules. In contrast to closed-shell fluorescent or phosphorescent molecules, these radicals have a singly occupied molecular orbital in their ground state. Starting from there, the electron can be excited to the LUMO. Since this excited electron can occupy two degenerated spin states, the excited molecule forms a doublet. Consequently, the emission from this doublet state is not hindered by the Pauli exclusion principle, since the initial molecular orbital is empty. The theoretical upper limit for the internal quantum efficiency is therefore 100 %.

Instead of radicals, biradicals with two singly occupied molecular orbitals can be used. In this case, the doublet states formally become singlet and triplet states again and the Pauli exclusion principle does not prevent emission from an excited state. This results in eight possible radiative transitions, shown in Figure 2.6, which can merely be distinguished spectrally when the coupling between the two electrons is weak. However, by definition, a molecule is a pure biradical only if this interaction is zero which does not occur in real

systems. The stronger the coupling between the two electrons, the more a closed shell character has to be attributed to the molecule.

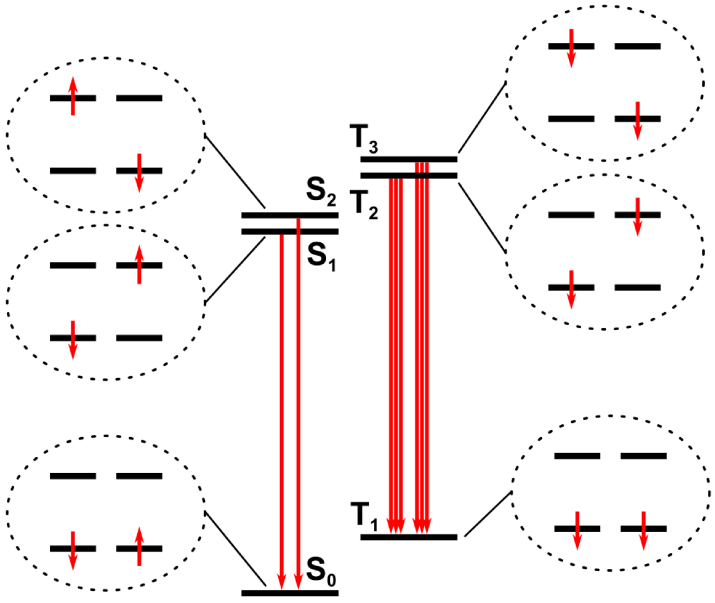

Figure 2.6: Energy diagram of an idealized biradical. In total there are two singlet-singlet and six triplet-triplet radiative transitions, which vary only slightly in energy.

In general, radicals and biradicals have small bandgaps of typically below 1.5 eV [40]. Further, they are highly unstable against chemical variations, since the singly occupied molecular orbitals tend to form new bonds to other molecules to form closed shell configurations. To prevent this formation, one aims to suppress these reactivity by kinetically blocking the site of the singly occupied molecular orbital, using electron-withdrawing groups and/or stabilizing the ground state of the biradicaloids by delocalized π-electron states.

2.3 Quantitative Analysis of Photon Statistics

In the scope of the experiments carried out in this thesis, absorption and spontaneous emission as well as other intramolecular transition processes can be modeled by rate equations. The goal of time correlated single photon counting experiments is to determine the rates within these models. From an experimental point of view, however, only the spontaneous radiative transitions indicated by the emitted photons are perceptible to the photodetector. This happens whenever a photon hits the detector and the timestamp of the event is recorded. This stream of photon events contains all the information which is present in the photon statistic of the emitter. Therefore, we will now take a closer look at possible relations that can be derived from the temporal stream of photon events and discuss the information contained in these functions

A commonly used function to characterize single photon emitters is the intensity correlation function $g^{(2)}(t)$. This function is defined by

$$g^{(2)}(\tau) = \frac{\langle I(t)I(t+\tau)\rangle}{\langle I(t)\rangle^2}$$

with $I(t)$ being the intensity recorded at a specific time t. Vividly, $g^{(2)}(t)$ describes the normalized correlation function to measure the time interval τ between the emission of two photons. In the experiment, the photon detection events are measured on a discrete time basis and the $g^{(2)}(t)$-function is calculated by subtracting the time difference between each pair of photons and sorting these time differences in a histogram.

Suited time correlated single photon counting hardware can calculate this function on the fly avoiding big data files of photon arrival times, which can be as large as gigabits per second for the recorded fluorescence. However, in recent years it has become possible to stream these photon arrival events directly to a computer. Therefore an algorithm for fast calculation of fluorescence correlation data was developed during this thesis and is attached in the Appendix.

In comparison to the full data files of photon arrival times, the $g^2(t)$-function contains to a certain degree the essence of the photon statistic. This raises the question, under what circumstances the $g^2(t)$-function contains *all the information* being present in the photon statistics and when information in neglected. As we will see, all information about the system under investigation is included in the $g^{(2)}(t)$-function in the case of only one radiative transition in the system. This is problematic as the $g^2(t)$-function is often used to prove the presence of a system with only one radiative transition, i.e. a single photon

emitter. When the system contains more radiative transitions the use of the $g^2(t)$-function can neglect important information and can lead to incorrect conclusions.
Therefore, we must consider the *system under investigation* as everything in the experiment that is able to trigger an event in the photon detectors. This includes dark count events of the photo detectors, the respective intensity of the emitter's background or other adjacent, possibly dimmer emitters within the detection volume.

Remarkably, there is no comprehensive discussion on this issue in common literature. Therefore, it is appropriate to present an overview here. First, I want to demonstrate how the moments, i.e. mean, variance etc., of the photon statistics produced by a multi-level system can be calculated from its rate model. Second, we will see how the $g^{(2)}(t)$-function is derived from these moments and what kind of information is neglected in this step. Additionally, in the experimental Section 4.7.1, a reference system will be exemplified that, by the loss of this information, produces a $g^{(2)}(t)$-function, which may lead to erroneous conclusions on a material. Additionally, two possible strategies to solve this problem of lack of information will be presented in Section 4.7.2 and 4.7.3: The first approach utilizes the direct measurement of the third order correlation function and the second approach is based on a change of the mode of photoexcitation from a continuous to a step-like function and demonstrates how this allows an undisturbed and precise determination of transition rates between different states of a molecule.

In order to calculate the stream of photons emitted by a multi-level system an approach is used to derive a generating function similar to that of *Barkai et al.* [41]. However, here this approach is further expanded and is generalized by making no assumptions on the state of the system after emission of a photon.

We start with an n-level system with radiative and non-radiative transition rates between these levels. The population of these levels is described by a master equation based on the transition matrix $\hat{\mathbf{T}}$:

$$\frac{\mathrm{d}}{\mathrm{d}t}\begin{pmatrix} P_1(t) \\ P_2(t) \\ \vdots \end{pmatrix} = \underbrace{\begin{pmatrix} -\sum_{i\neq 1} k_{1\mathrm{i}} & k_{21} & \cdots \\ k_{12} & -\sum_{i\neq 2} k_{2\mathrm{i}} & \\ \vdots & & \ddots \end{pmatrix}}_{\hat{\mathbf{T}}} \underbrace{\begin{pmatrix} P_1(t) \\ P_2(t) \\ \vdots \end{pmatrix}}_{\mathbf{P}} \tag{2.8}$$

Here t is the time since the beginning of the time correlated single photon counting measurement. Now, this scheme is expanded by a parameter n so that $P_{i,n}(t)$ describes

the probability of finding the system in the state i after emitting n photons. In the next step, by introducing an auxiliary parameter s, one can define a generating function $G(s,t)$:

$$\mathbf{G}_i(s,t) = \sum_{n=0}^{\infty} \hat{\mathbf{P}}_{i,n}(t) s^n \tag{2.9}$$

and

$$G(s,t) = \sum_i \mathbf{G}_i(s,t) \tag{2.10}$$

Here, the notation follows the convention that scalar quantities are printed in regular font, vectors printed in bold font and matrices are printed in bold font with hat. From equations 2.8, 2.9 and 2.10 one obtains the differential equation in time which defines the evolution of the system

$$\frac{\mathrm{d}}{\mathrm{d}t}\mathbf{G}(s,t) = \hat{\mathbf{M}}(s)\mathbf{G}(s,t) \tag{2.11}$$

where $\hat{\mathbf{M}}(s)$ is equal to the matrix $\hat{\mathbf{T}}$ but with a factor s multiplied to every radiative transition rate (i.e. $\hat{\mathbf{M}}(s=1) = \hat{\mathbf{T}}$).
The solution for this differential equation is

$$\mathbf{G}(s,t) = e^{\hat{\mathbf{M}}(s)\,t}\mathbf{P}(t \to \infty). \tag{2.12}$$

The initial condition are assumed to be equal to the stationary case as every fluorescence experiment starts some time after the excitation laser has been turned on and the system has reached its steady state equilibrium. The generating function is constructed in a way that now it can be used to calculate the factorial moments of the system's photon statistics:

$$\langle n \rangle = \left.\frac{\mathrm{d}}{\mathrm{d}s}\right|_{s=1} G(s,t) \tag{2.13a}$$

$$\langle n(n-1) \rangle = \left.\frac{\mathrm{d}^2}{\mathrm{d}s^2}\right|_{s=1} G(s,t) \tag{2.13b}$$

$$\vdots$$

$$\langle n(n-1)\ldots(n-m+1) \rangle = \left.\frac{\mathrm{d}^m}{\mathrm{d}s^m}\right|_{s=1} G(s,t) \quad . \tag{2.13c}$$

As n is the total number of photons emitted since the beginning of the measurement, $\frac{\mathrm{d}}{\mathrm{d}t}\langle n\rangle$ is the current photon intensity which is emitted by the system and the first moment of the photon statistics. By the emitted intensity itself, one is not able to distinguish between a classical and non-classical light source. The nature of non-classical light manifests itself in the second moment of the photon statistics: For uncorrelated light, which follows a Poisson-distribution, the generating function reads $\mathrm{e}^{-\lambda t(1-s)}$ and the variance of emitted photons is equal to λt, where λ is the only parameter characterizing the photon statistics. For non-classical emitters, e.g. a single fluorescent molecule, however, this variance can increase slower, leading to a more uniform photon emission. In Figure 2.7 the two systems are compared regarding their stream of photons and their variance of photon emission. Despite this, the $g^{(2)}(t)$-function is another measure to prove the non-classical properties of single photon emitter. Among different advantages, the $g^{(2)}(t)$-function is neither affected by the uncorrelated loss of photons, e.g. by a photon detection efficiency of less than 100 %, nor by the dead time of the photodetectors if it is measured in a Hanbury Brown and Twiss configuration with two independent photodetectors. The $g^{(2)}(t)$-function expressed in terms of factorial moments reads [42]

$$g^{(2)}(t) = \frac{t^2}{2\langle n\rangle^2}\frac{\mathrm{d}^2}{\mathrm{d}t^2}\left(\langle n(n-1)\rangle + \langle n\rangle\right). \tag{2.14}$$

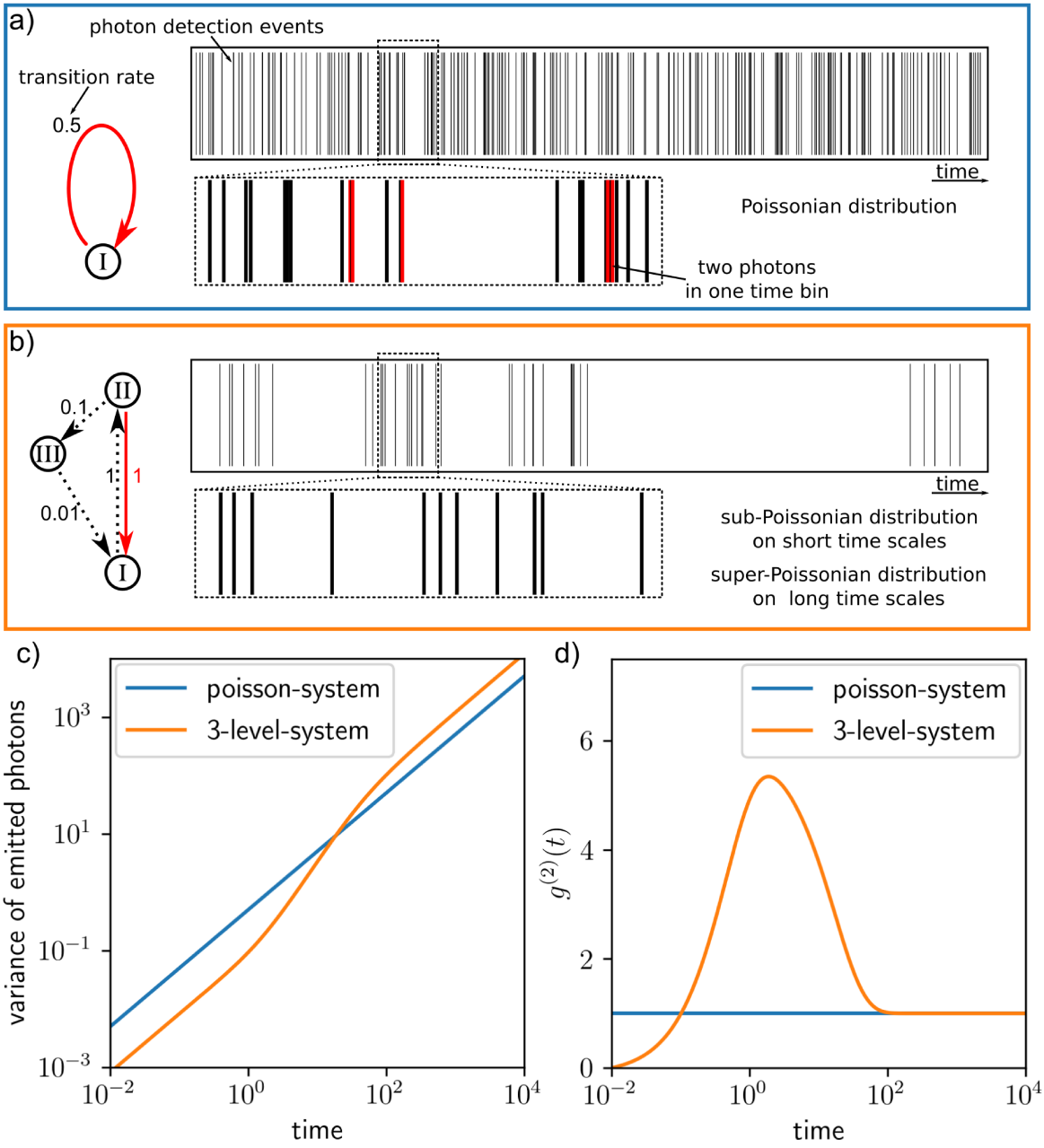

Figure 2.7: Comparison between a system obeying Poissonian photon statistic (blue) and a three level system with one radiative transition (orange). In a) and b) the models are illustrated together with the respective transition rates. Their simulated stream of photon events on the right side shows uncorrelated photon events for the Poissonian system including several time bins with multiple photon detection events, indicated in red. In the three level system, photon antibunching, i.e a sub-Poissonian distribution, on short timescales and bunching, i.e a super-Poissonian distribution, on long time scales is observed. In c) and d) these properties are clarified by the variance of detected photons in a certain time interval and the corresponding $g^{(2)}(t)$-functions.

In Figure 2.7 the $g^{(2)}(t)$-function is compared for a system governed by Poissonian photon statistics (in blue) and a three level systems (in orange). For $t = 0$ the $g^{(2)}(t)$-function of the three level system approaches $g^{(2)}(t) = 0$, which proves the system to be a single photon emitter while the one level system is not a single photon emitter, although, it also has just one radiative transition. The $g^{(2)}(t)$-function can be calculated by the first two moments of the photon statistics, which means that moments of higher order are not included in the $g^{(2)}(t)$-function. This bears the question, unter what circumstances the information of higher order moments can be neglected. This question can be answered by considering the third order correlation function, which can be expressed solely by third order factorial moments [41]. Simultaneously, a closer look at the $g^{(3)}(t)$-function reveals that its mathematical structure refers to the tensor product of two $g^{(2)}(t)$-functions if and only if the system is in the same state after emission of a photon. This is the only case in which the third order factorial moment of the photon statistics does not contain more information than the second order factorial moment or the $g^{(2)}(t)$-function.

To summarize: *A generating function contains the complete information on the photon statistics of a given system, including the information about the infinite set of factorial moments of the statistics. The intensity correlation function $g^{(2)}(t)$ contains information regarding the first two of these moments. Moments of higher order, $n > 3$, can be neglected if and only if the system under investigation is in the same state after the emission of a photon. The quantitative evaluation of the $g^{(2)}(t)$-function can lead to erroneous conclusions on the system if this later assumption is not fulfilled.*

Now that the tools are on hand to compare measured photon statistics with a theoretical model, we want to take a look at the different characterization methods that were used to detect single photon arrival times and other spectral properties of organic molecules within this thesis.

3 Characterization Methods

As described in the previous chapter, for this thesis most of the information about the molecular host-guest systems is obtained by the stream of photon emission events of the respective molecules. In addition other properties of the emitted light besides its emission statistics can also be obtained: These include the spectral distribution, spatial information, temperature-, polarization- and angle-dependent emission characteristics. This chapter presents an overview of the experimental setups used to analyze these properties.

3.1 Confocal Microscopy Setup

A confocal microscopy setup was used in this work to detect the photoluminescence of molecular dopants down to the single molecule level. Thus, the setup design aims for a high spatial resolution while simultaneously maximizing its detection efficiency. Figure 3.1 provides an overview of the main components of the setup employed for these studies. For photoexcitation, several continuous wave and pulsed lasers were available. As an example, a 532 nm excitation laser is shown in the overview. A spatial mode filter was utilized to shape the beam profile and thus, to achieve a resolution close to the diffraction limit, a low background noise and a sufficiently high photon flux at the position of a single molecule. The spatial mode filter consists of a lens with small focal length, a pinhole that suppresses higher transverse laser modes and a second lens that collimates the transmitted light to a Gaussian beam profile of a diameter equal to the 5 mm aperture of the objective.

In the following, the light was deflected by a beam splitter into the main optical axis, i.e. the vertical axis between avalanche photo diodes and the sample in Figure 3.1. The laser power guided to the sample could be measured by a Si-photodiode based power meter and could be controlled by a combination of attenuators in the optical path. An immersion oil objective (Olympus UAPON 100XOTIRF) with a numerical aperture of 1.49 was used in an inverted epi-fluorescence microscope geometry to focus the laser beam to a diffraction-limited spot and to collect the photoluminescence from the sample over a solid angle of $0.41 \times 4\pi$ or $\pm 79°$ with respect to the surface normal. For detection of the red shifted fluorescence, the reflected laser was suppressed by appropriate longpass filters. In

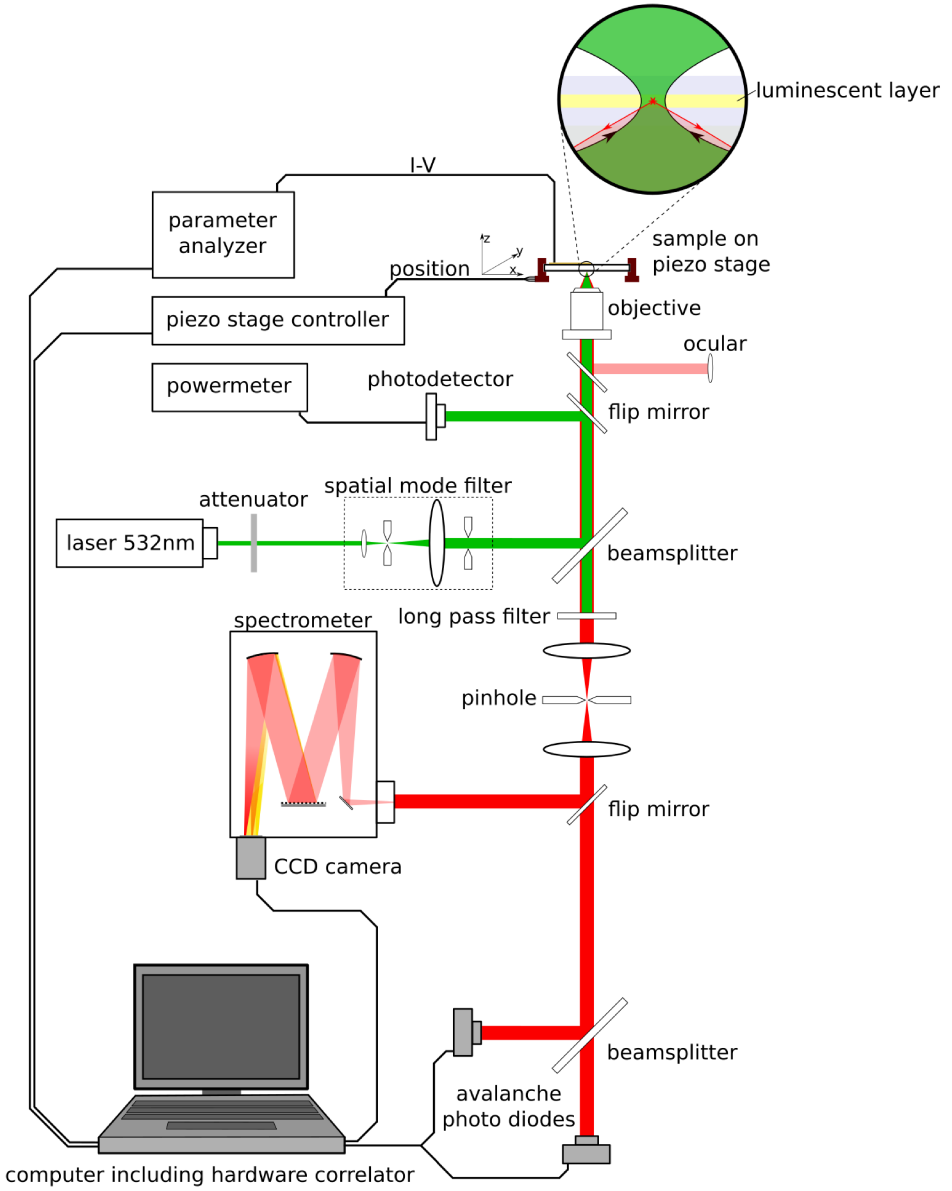

Figure 3.1: Schematic diagram of the main components constituting the confocal microscopy setup. Every optical component is either mounted on a three-axis translation stage or a pair of adjustable mirrors is placed in front of the component to align the position and direction of the optical path.

conventional confocal microscopy setups, which aim merely on high resolution, a lens in the detection path creates a virtual image of the sample and a pinhole positioned in the coresponding focal plane is used to improve the resolution of the microscope at the cost of a reduced detection intensity. We also utilized this concept, but choose a pinhole that is big enough so that hardly any fluorescence intensity was lost. For typical measurements of single molecule photoluminescence a pinhole with a diameter of 75 µm turned out

to be the proper choice. Nevertheless, this pinhole reduced the amount of diffusivly scattered light from above and below the focal plane of the objectives, which otherwise would be detected by the photodetectors. Further, two possibilities exist to analyze the fluorescent light: Either, light could be deflected to a spectrometer (Acton SP2300) where it was spectrally resolved and detected by a thermoelectrically cooled CCD camera (Pixis 400B). Alternatively, the light could be detected by two avalanche photo diodes (APD) (Excelitas SPCM-AQRH-14) in a Hanbury Brown-Twiss configuration [22]. Time tagging was performed by a *Becker&Hickl* correlator card (DPC-230) which recorded the single photon arrival times and processes the $g^{(2)}$-data. An overview of the data processing underlying $g^{(2)}$-measurements is provided in Figure 3.4. During the measurement, the sample was mounted on a piezo stage (NPoint) with a lateral (vertical) traveling distance of 200 µm (25 µm). By scanning the sample through the laser spatial fixed spot and simultaneously recording the photoluminescence intensity per pixel, it was possible to generate photoluminescence maps of the sample surface and thereby, to locate the single molecules. Finally, to analyze single molecules in OLEDs under electrical excitation, a parameter analyzer (Agilent Technologies, 4155C) was used to provide and record the applied voltage and current during operation.

3.2 Temperature Dependent Micro-Photoluminescence Setup

Temperature dependent measurements of different materials such as Cu(carbazolate)(2-(2,6-diisopropylphenyl)-1,1-diphenyl-isoindol-2-ium-3-ide) CuCbzCaarC, tetracene and 2,2'-ditetracene were carried out by a micro-photoluminescence setup in combination with a helium cooled contact cryostat schematically illustrated in Figure 3.2. In this work, this setup was used for two types of experiments: On the one hand, temperature dependent spectrally resolved photoluminescence was recorded during continuous wave laser excitation. On the other hand, photoluminescence lifetime measurements were performed under pulsed laser excitation by means of spectrally resolved time-correlated single photon counting. For both types of experiment the samples were mounted on a brass base in the helium cryostat (CryoVac) which allows for cooling the sample down to 4 K. The temperature can be controlled precisely by resistive heating the sample stage in the temperature range up to 475 K. The entire cryostat is mounted on a piezo stage (NPoint) which was especially designed to carry the weight of the cryostat and to move the sample in three dimensions over a distance of 300 µm each. An objective (Olympus,

SLMPLN 50X) with a numerical aperture of $NA = 0.35$ and a long working distance of 18 mm is used to focus the excitation light onto the sample surface and to collect the resulting photoluminescence light. Precise positioning of the incident laser beam on the sample surface was achieved by an additional ocular lens together with a flip mirror. As in the confocal microscopy setup, the excitation power is measured by a Si-photodiode based power sensor and can be adjusted by a combination of different neutral density filters.

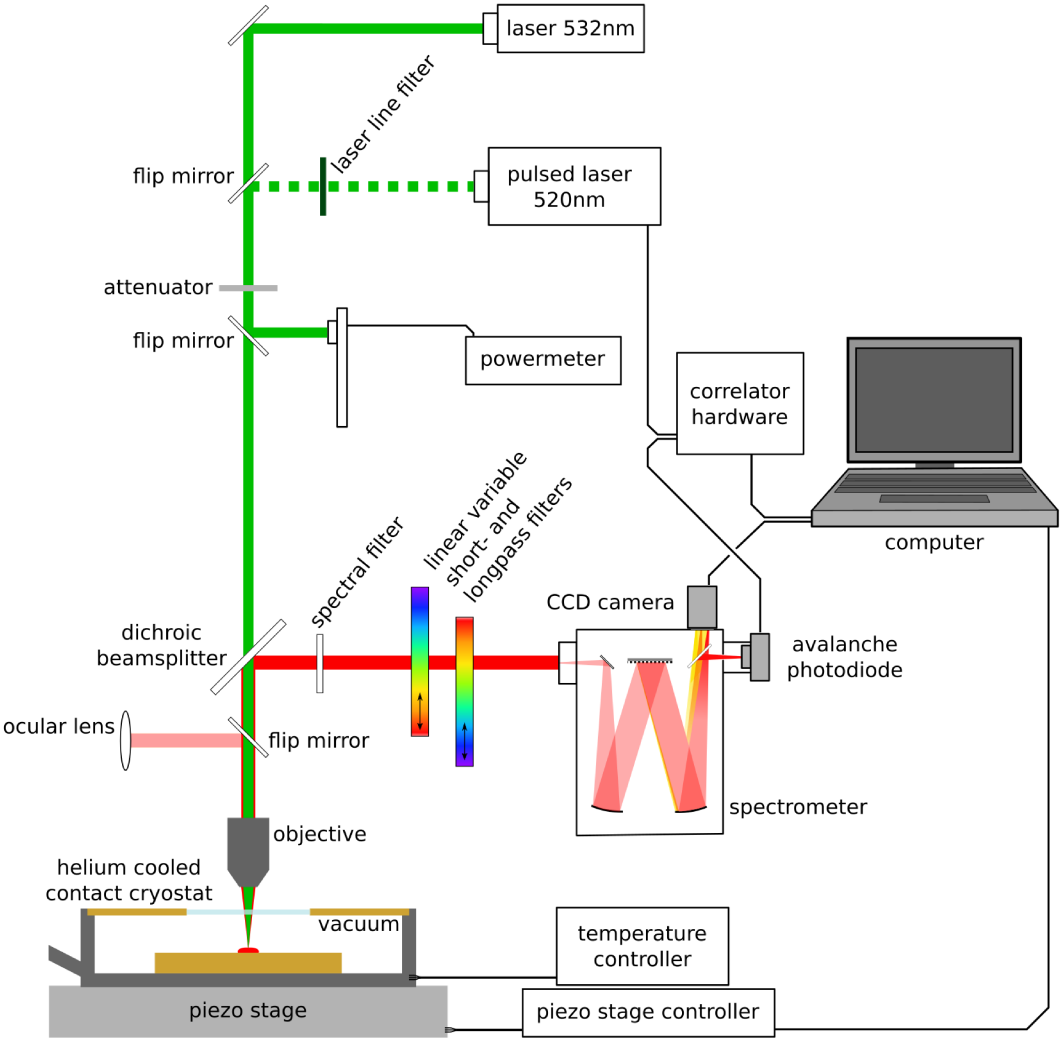

Figure 3.2: Main components of the µ-PL setup which is used for temperature dependent measurements.

Photoluminescence measurements under continuous wave laser excitation are performed in a similar way as with the confocal microscopy setup. The only difference is that the light is detected by the APD (Laser Components, Count-100C) after passing the spectrometer (Princeton Instruments, Acton SP-2558). This allows for either collecting the whole spectral range when the grating of the spectrometer is aligned at its zeroth-order or selecting only

a small spectral region when the grating is aligned to the respective central wavelength. For spectroscopic analysis three different gratings with 300, 1200 and 1500 lines per mm are available, all of which can be used in combination with the CCD camera (Princeton Instruments, Pixis eXcelon). Especially, for photoluminescence lifetime measurements it is desirable to detect only certain parts of the emitted spectra that comprise emission bands of different decay constants. Therefore, two variable short- and longpass filters, shown in Figure 3.3 (Delta Optical Thin Film A/S, 3G LVSWP and 3G LVLWP) are used in combination and are located in front of the photodetector to define a lower and an upper cut-off for the wavelength range of interest.

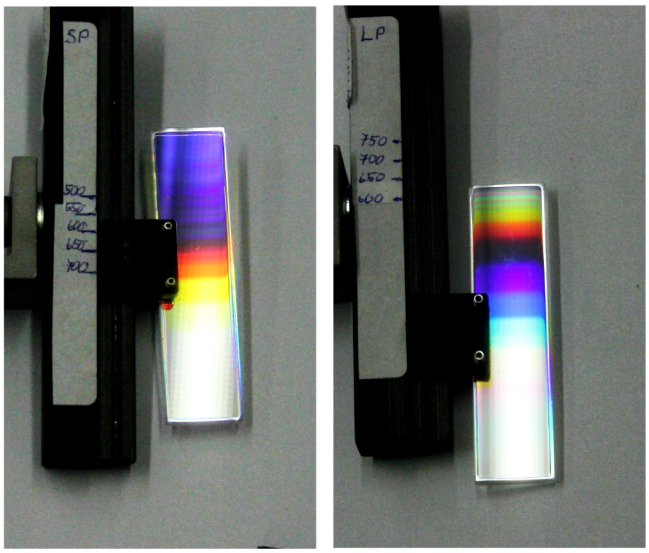

Figure 3.3: For the photoluminescence lifetime measurements, two variable short- (SP) and longpass (LP) filters were used in combination for spectral filtering the emergent photoluminescence light in the optical detection path.

The lifetime measurement is performed with a pulsed laser diode (kindly provided by the 3rd Physics Institute of the University of Stuttgart) of 520 nm wavelength. In its continuous mode, this laser diode provides an excitation power of up to 40 mW. Under pulsed operation, which is realized by triggering with a pulse generator (iC-Haus, iC149) the diode is rapidly turned on and off at a frequency between 1 kHz and 2 MHz. The width of the electric trigger pulses can be tuned over a wide range leading to shortest laser pulses of about 700 ps for an electrical pulse width of 4.25 ns. The difference between electrical and optical pulse length is a result of the electronic processes within the semiconductor laser diode and of the time needed to generate population inversion before reaching the laser threshold. An overview of the data processing underlying fluorescence lifetime measurements is provided in Figure 3.4.

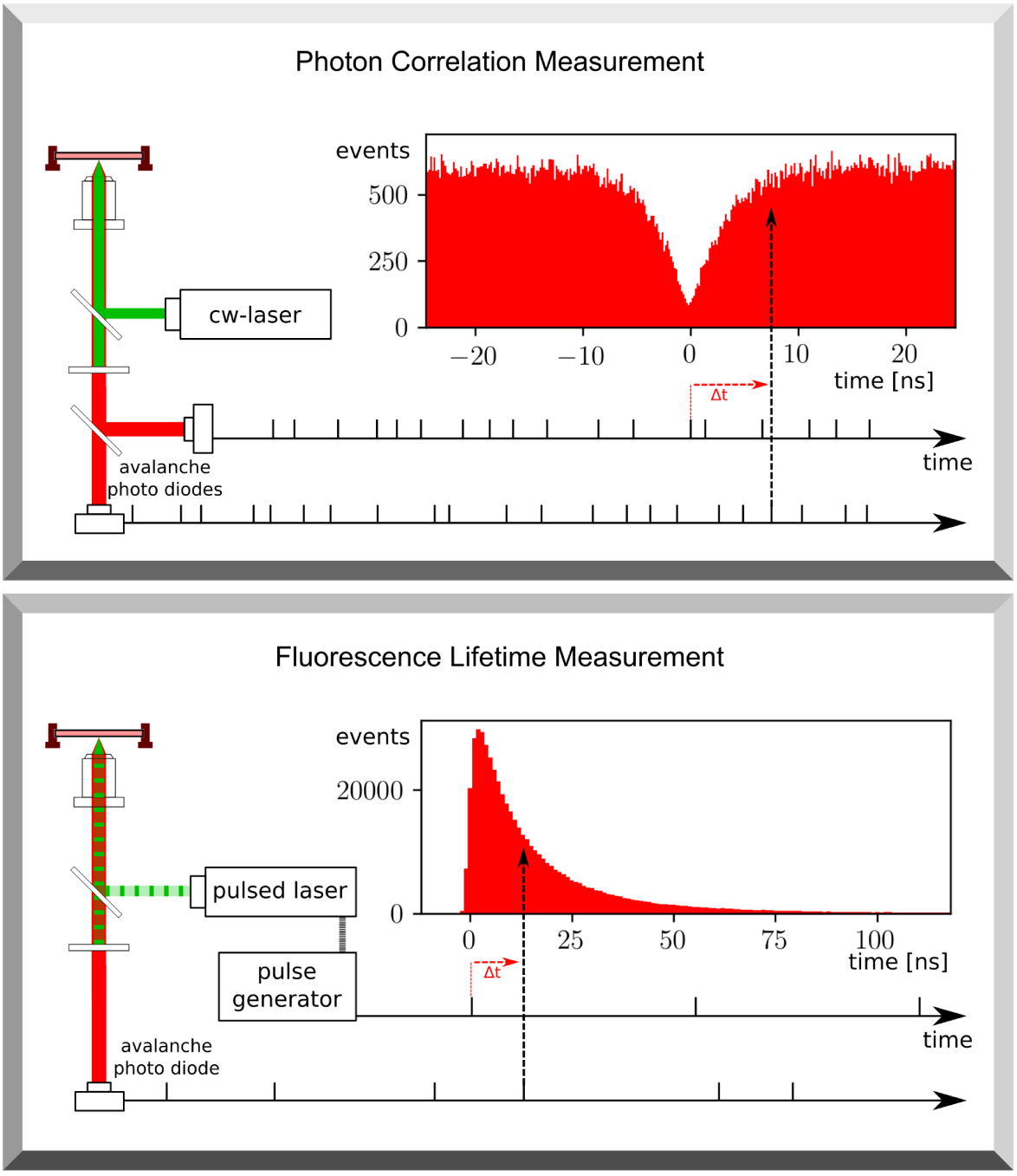

Figure 3.4: Overview of the data processing carried-out for photon correlation (top) and fluorescence lifetime measurements (bottom). For the calculation of $g^{(2)}$-events the time difference between each pair of photons detected by the separated detectors is calculated and plotted in a histogram. The fluorescence decay function can be obtained by measuring the time difference between the trigger pulses of the laser and the related photoluminescence detection events.

The optimization of the pulsed laser setup with respect to the instrument response function was part of the master thesis [43] of Maximilian Frank in our group. Taking into account the time resolution of the correlator hardware (Picoquant, PicoHarp 300) this setup enables a time resolution of 1.1 ns under standard operation. Applying special measures, e.g. by adding an objective in front of the APD, a time resolution of even 0.8 ns could be obtained.

3.3 Photoluminescence Measurements with Periodic Excitation Modulation

The photoluminescence intensity of perylene bisimide based emitters was analyzed in dependence of the excitation intensity. At high (mW) excitation powers the rapid photobleaching of the molecules within seconds imposed a constraint on the experiments. Therefore, a modified setup was developed including a continuously variable neutral density filter as optical key element which, under rotation, alters the excitation intensity over two orders of magnitude. The corresponding experimental configuration is illustrated in Figure 3.5.

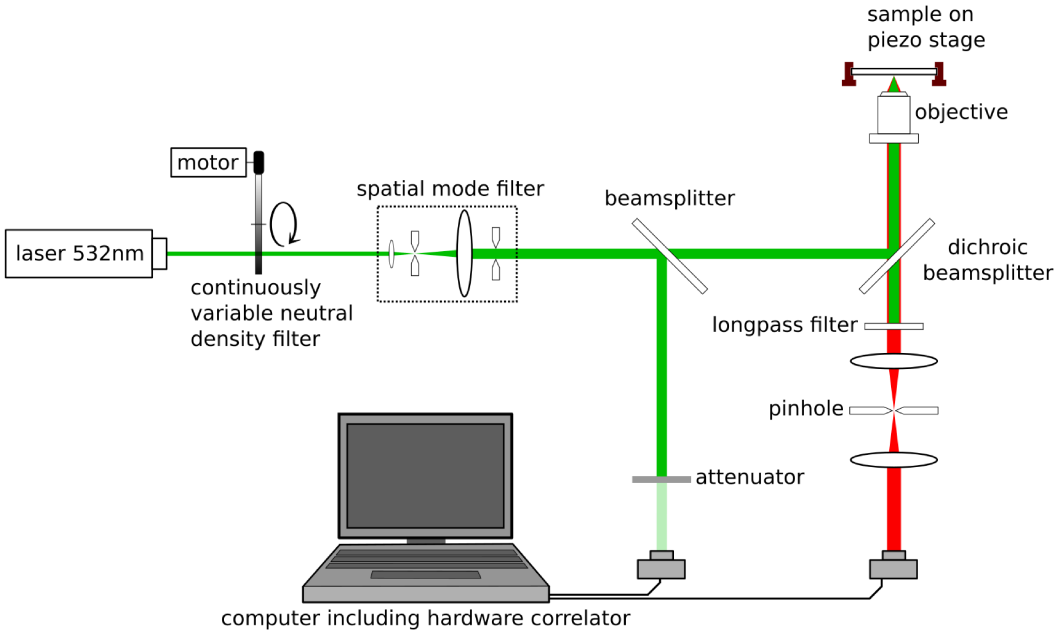

Figure 3.5: Main components of the modulated excitation setup for repeatedly measuring the photoluminescence intensity of single molecules in dependence of the excitation intensity over a time interval of 250 ms.

Two APDs were used to detect the photoluminescence signal as well as the excitation intensity, while the arrival time of each photon was recorded for both APDs and stored for later analysis. This setup makes it possible to measure the response of single molecules at different excitation intensities over a total time period of 250 ms. The measurement could be repeated many times until photobleaching of the respective molecule occurred, which overall improves the statistics of the data analysis.

3.4 Angular Dependent Photoluminescence Measurements

Dipole emitters near dielectric interfaces exhibit a rich emission characteristic [44]. For example, a dipole emitter that is located below and oriented perpendicular to a dielectric interface will generate an emission profile similar to a radially polarized doughnut mode [45]. In order to analyze the angular dependence of the emitted intensity of a molecule, the setup illustrated in Figure 3.6 was used. In this setup, the photoluminescence is collimated so that each spatial emission direction of the emitter corresponds to a lateral position perpendicular to the optical path. An electric motor moves a pinhole of 30 µm diameter slowly, within one hour, across the entire cross section of the photoluminescence profile to select small parts of the emission profile while simultaneously the respective spectrum is analyzed by the spectrometer.

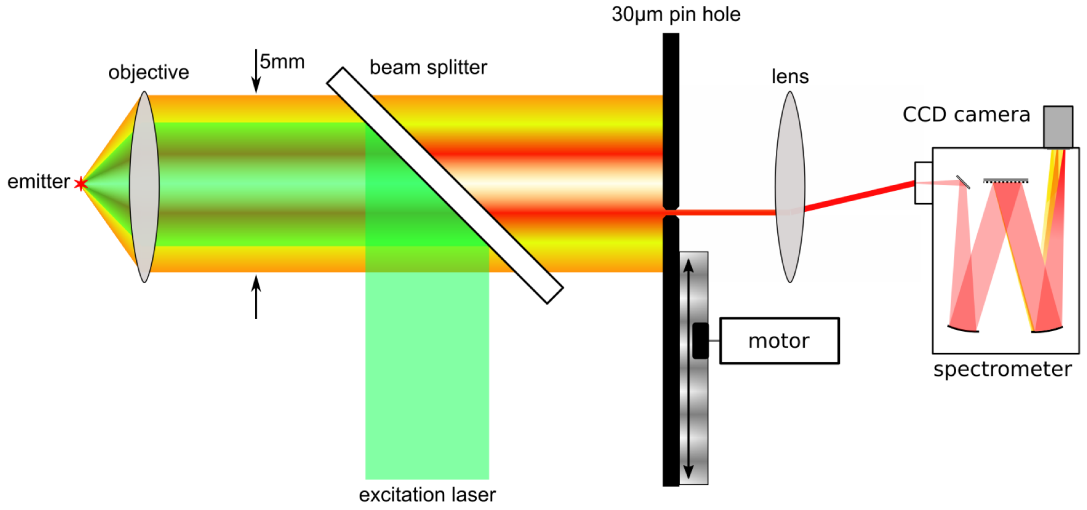

Figure 3.6: Main components of a setup which is used to measure the angle dependent photoluminescence of a sample.

4 Results and Discussion

As we have seen in the previous methods chapter, all experiments performed on the confocal microscopy setup are suitable for single molecule spectroscopy, which is an excellent tool to study organic semiconductors in their role as dopants. The most unique feature, which predestines this method as a key tool in this work, is that the molecules can be measured one by one and, therefore, prevent information loss by averaging over an ensemble. The first two sections of this chapter focus on the effects of molecular blinking, photobleaching and the local environment on the photophysics of single molecules.

4.1 Photostability: Blinking and Photobleaching

If, for example, an ensemble of molecules is excited continuously with by laser over several seconds, one can observe that the fluorescence intensity decreases exponentially over time. This mechanism is known as photobleaching. A premature conclusion from this ensemble observation could be that each molecule behaves identically and that each molecule becomes inoperable with a certain probability rate during photoexcitation. In reality, however, the situation is more complex and had been revealed only when the first measurements on single molecules at room temperature became possible [46]. At the single molecule level, it can be observed that individual molecules suddenly stop emitting, but emit brightly again a few seconds later [47]. This mechanism is called photoblinking and can be observed for a variety of quantum emitters like nitrogen-vacancy centres in diamond [48], organic molecules [49, 50, 51] or semiconductor quantum dots [52]. In some cases, the fluorescence intensity of a single emitter disappears completely for a short period of time, in other cases only to a certain percentage. Further observations at the single molecule level include varying exciton dynamics, like shorter or longer exciton lifetimes, or fluctuations of the spectral positions of absorption and emission lines [53]. This shows that by sequential investigation of individual molecules, it is possible to determine whether these effects are intrinsic to the molecular species or an effect of the interaction with the environment.

In the host-guest samples prepared in this work, blinking of molecules could also be detected. The initial aim was, therefore, to identify the underlying mechanisms of this blinking and evaluate whether it has a positive or negative effect on the performance of the emitter in an OLED.

For this purpose, squaraine-based fluorescent emitters were analyzed. This molecule with the full name 4-((5-bromo-1-(3,7-dimethyloctyl)-3,3-dimethyl-3H-indol-1-ium-2-yl)-methylene)-2-((5-bromo-1-(3,7-dimethyloctyl)-3,3-dimethylindolin-2-ylidene)methyl)-3--(dicyanomethylene)cyclobut-1-en-1-olate and its common name *Monomer M* is depicted in Figure 4.1. The molecule was synthesized and characterized by Sebastian F. Völker in the group of Prof. Dr. Christoph Lambert at the Institute of Organic Chemistry at the University of Würzburg in 2012 [54] and its optoelectronic properties have been studied thoroughly by Stender et al. [55]. Monomer M was chosen for this experiments as it exhibits an outstanding photo-stability which made it an ideal reference emitter for demonstrating fundamental shortcomings of other fluorescent monomeric emitters and for analyzing its interaction with the local environment.

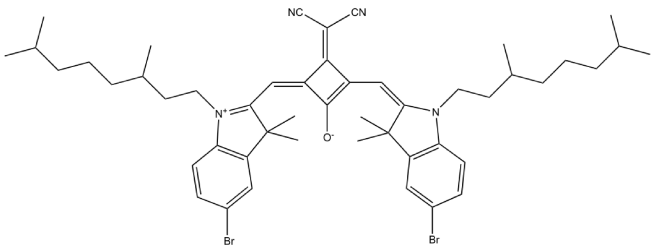

Figure 4.1: Chemical structure of the squaraine 4-((5-bromo-1-(3,7 -dimethyloctyl)-3,3-dimethyl-3H-indol-1-ium-2-yl)methylene)-2-((5-bromo-1-(3,7-dimethyloctyl)-3,3-dimethylindolin-2-ylidene)methyl)-3-(dicyanomethylene)cyclobut-1-en-1-olate molecule.

As amorphous and transparent matrix for the Monomer M emitters polymethyl methacrylate (PMMA) was used. The bandgap of PMMA is approximately 4.2 eV with an indirect optical transition [56]. Although the density of states, like for other disordered matrices, is not narrrow and has tails extending into the energy gap [57] the band gap sufficiently wide so that PMMA, like anthracene, is transparent at 532 nm wavelength and can be considered optically inactive in the photoluminescence experiments. However, the polarity of the matrix can influence the energy levels of the dopant and can narrow its energy gap. The chemical structure of PMMA is depicted in Figure 4.2.

Doped PMMA thin film samples were prepared at a molecular concentration of Monomer M being small enough to allow for the spectroscopy of single molecules within

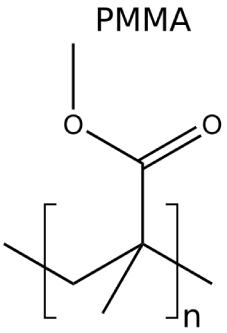

Figure 4.2: Chemical structure of polymethyl methacrylate (PMMA).

the matrix. For the preparation of these films, the raw material was first dissolved in chlorobenzene. In the next step, a serial dilution was prepared down to concentrations of 10^{-12} mg ml^{-1}. Then PMMA was added at a concentration of 5 mg ml^{-1} and, finally, the resulting mixture was spin-coated on a thin glass substrate at 1500 rpm for 30 s. The glass substrate had been previously cleaned in an ultrasonic bath by distilled water, acetone, isopropanol and in a plasma-etching chamber for 10 min. The goal of the applied purification procedure was to get rid of all luminescent species on the substrate, rather than of all carbon compounds per se. In a last step, the spin-coated thin film sample was encapsulated by a cover slide which was glued to the substrate by a low vapor pressure epoxy (supplier: Kurt J. Lesker, *Torr Seal*). The entire process was carried out in a glovebox under nitrogen atmosphere to minimize the amount of residual oxygen in the encapsulated volume. For other single molecule experiments similar samples were prepared and Figure 4.3 shows such a doped PMMA thin film sample.

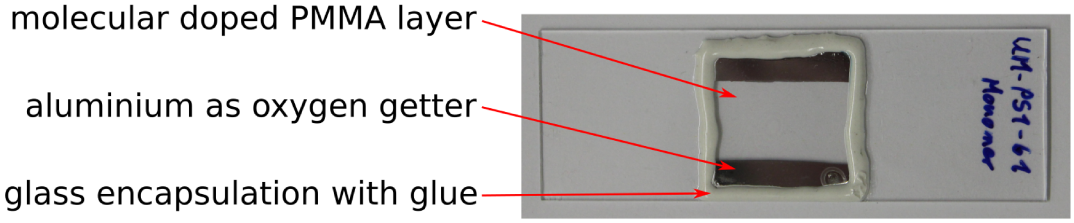

Figure 4.3: A typical sample for single molecule spectroscopy: Between two glass slides, the dopant molecules are embedded in a 100 nm thick layer of PMMA. Two stripes of aluminum serve as oxygen getters. The sample is prepared under nitrogen atmosphere and encapsulated by using a low vapor pressure epoxy.

During the experiment, the fluorescence intensity time trace of a single monomer M molecule excited by a linear polarized continuous wave laser at 532 nm wavelength was

recorded over several minutes. The presence of a single molecule was indicated by its characteristic brightness and corroborated by an observed blinking of the emission intensity. Figure 4.4 shows a small representative section of this time trace over which the intensity was measured as the number of photons detected by the APDs in a certain time interval. When selecting such a time interval, it must be ensured that it is neither too short nor too long. If it is chosen too short, noise will be too large to distinguish different states of the molecule. If the interval is chosen too long, the intensity is averaged over this time period and mechanisms on shorter time scales may not be resolved. To meet both requirements, a time interval of 1 ms has proven appropriate for these measurements. Additionally, the measured intensity was plotted as a histogram in the right graph of Figure 4.4 over the total duration of the measurement between 0 s and 510 s, until irreversible photobleaching occurred. In this histogram, an 'on' and an 'off' state of the molecule occurred. The 'on' state is characterized by about 160 photons per millisecond while in the 'off' state only about 50 photons per millisecond were recorded. Moreover, e.g. at time 316 s in the trace, a slightly brighter dark state could be observed emitting about 80 photons per millisecond as detected the APDs.

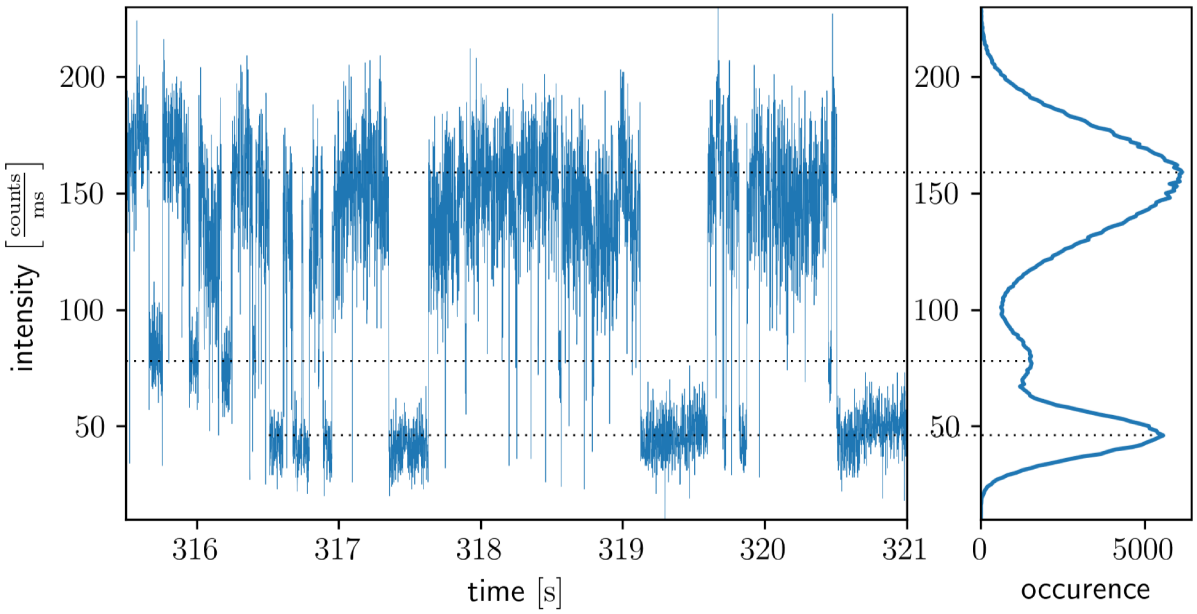

Figure 4.4: Photoblinking of a monomer M molecule. Left: Intensity time trace of a single monomer M molecule reveals photoblinking on different time scales. Right: The histogram of the occurrence of different intensities indicate 'on' and 'off' states of the molecule.

Different mechanisms may be responsible for the observed blinking: The first process can be a temporally altered absorption of the molecule. This might be caused by a partial

rotation of the entire molecule and, therefore, of the molecular transition dipole relative to the polarization of the exciting laser [52]. However, a similar on-off fluorescence intensity ratio is confirmed for different molecules, which would require all molecules to perform similar rotations relative to the incident laser light. Further, a controlled switching between just two well defined states in the disordered PMMA matrix is rather unlikely. An alternative possibility to consider is a spectral diffusion of the absorption profile of the molecule [58]. While considered a probable mechanism at low temperature, at room temperature the absorption lines of a single molecule are broadened to such an extend that the spectral shift would have to be in the range of 50 meV to be detected, which is too large for being a likely mechanism. A third mechanism is the presence of radical-ion dark states [59]. This would require that an electron is separated from the molecule and returns back to it after a few seconds. This mechanism can be ruled out, however, as the matrix for the single molecule sample is PMMA, which is an insulator and, thus, does not allow free movement of electrons in the material. Two more mechanisms are possible: First, an intrinsic molecular dark state within a quantum jump model, that can be occupied upon excitation of the molecule with a certain probability [60] and second, the interaction of the molecule with diffusing oxygen in the matrix [61]. To determine whether one of these two mechanisms is relevant in our case, it was evaluated how long the single monomer M molecule is in its 'on'/'off' state and how likely it is to observe such a time interval. Figure 4.5 shows the correlation between the molecule being in its 'on'/'off' state for a certain duration and the probability density to observe one of these cases.

First, let us examine the 'on', i.e. bright, periods of the molecule. The plot of the data on a logarithmic scale reveals an exponential decline. This means that it is exponentially unlikely to observe longer bright periods of the molecule with time or, in other words, that there is a constant rate for the molecule to switch from the bright state to the dark state. One can see that the functional relationship is not perfect. This is due to the fact that a certain cutoff intensity must be selected to separate the "on"/"off" states. But since the intensity distributions of these states overlap in the experiment, there is an overestimation of the probability of small time intervals. When plotting the 'off', i.e dark state periods in a similar way, one recognizes that the probability distribution does not follow such an exponential low. However, when the data are plotted on a log-log scale, as in the right graph of Figure 4.5, we observe a linear dependence. This indicates that the probability of observing a certain dark state cycle follows a power-law distribution according to $P(\tau) = \tau^{-1}$.

These results help to assess both of the proposed mechanisms, the quantum jump and the diffusion model. The model of an internal dark state, which has to be described by

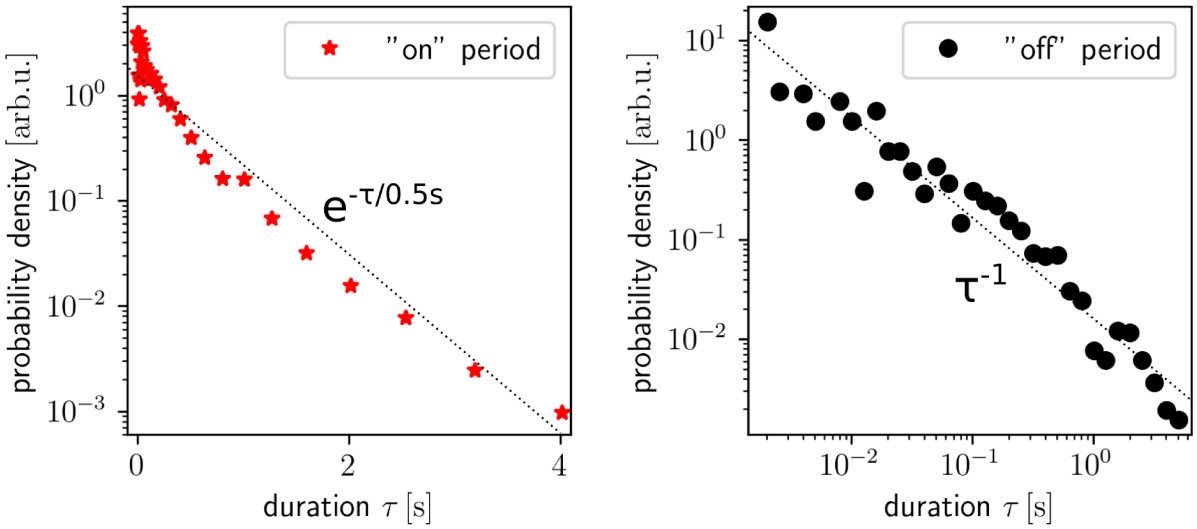

Figure 4.5: Correlation between a monomer M molecule being in its 'on'/'off' state (left/right) for a certain duration and the probability density to observe the respective case. In the left graph, where the data is plotted on a log-lin scale, one can observe an exponential decline. On the right graph the data is plotted on a log-log scale which reveals an underlying power-law distribution.

a quantum jump model, predicts an exponential distribution of finding the molecule in either of its molecule's states, i.e. bright or dark state, for a given time. By observing a power-law distribution for the duration of the "off" cycle, this model can be ruled out. In contrast to this, a power-law statistics is strongly connected to diffusion processes [62]. For example the first passage time, i.e. the time it takes for a diffusing object to return to its starting position, follows a $\tau^{-D/2}$ distribution, where D is the number of dimensions of the system. In our case, we have to assume that our sample is effectively two dimensional, as the PMMA layer is only about 50 nm think but several cm wide. With D = 2, this predicts a first passage time obeying a τ^{-1} distribution, which is consistent with the experimental result.

But how exactly does diffusing oxygen alter the molecule's brightness? The proposed mechanism here is the interaction between an oxygen molecule and the triplet state of the emitter (see Figure 4.6 right). In an isolated environment the excited triplet state of the molecule represents a long living dark state, as the transition to the singlet ground state is spin forbidden. Molecular oxygen also has a singlet and triplet state Δ and Σ, which can quench the triplet exciton of the excited molecule by allowing the emitter to change its spin quantum number while simultaneously switching from triplet to singlet oxygen. This mechanism is known to reduce the triplet lifetime of an emitter by several orders of magnitude [61, 63, 64]. Thus, this mechanism leads to a reduction of the time the emitter

stays in the dark triplet state, while its quantum efficiency remains unchanged. With a certain probability, which is caused e.g. by a kinetic potential barrier, the oxygen can move away from the location of the molecule and diffuse through the PMMA layer. During this period the molecule is in its 'off'-state. After a certain time, which is described by the power-law statistics, an oxygen molecule returns to the location of the emitter and the molecule becomes bright again.

To corroborate that this mechanism is responsible for a significant increase in photoluminescence of monomer M, the population dynamics of the molecule was simulated. The basis for the simulation is a 3-level-system with transition rates of $k_{21} = 3.25 \times 10^8\,\mathrm{s}^{-1}$, $k_{23} = 1.2 \times 10^5\,\mathrm{s}^{-1}$ and $k_{31} = 5 \times 10^4\,\mathrm{s}^{-1}$, which were determined by Benedikt Stender in the context of his doctoral thesis [65]. It was also assumed that the triplet lifetime is reduced by about three orders of magnitude in the presence of molecular oxygen. The exact value is not critical here, as the simulation also shows that a reduction of this quantity by a factor of 100 is sufficient to observe no further difference in photoluminescence, since the k_{23}-rate represents the limiting rate for the non-radiative decay via the triplet state. The left graph of Figure 4.6 shows the fluorescence intensity for a system with and without triplet quenching as function of time (this behavior is identical to the intensity correlation function $g^{(2)}(t)$) since the excitation laser was switched on. After 0.01 s (right end of the time scale) the monomer M molecule without triplet quenching has reached its steady state and as can be observed by comparison the same molecule with triplet quenching shows an fluorescence intensity, increased by a factor of three during continues wave excitation. This corresponds in good agreement to the detected increase in fluorescence from 50 counts/ms to 160 counts/ms. In order to assess the result of this simulation, it should be mentioned that the transition rates used here were determined experimentally with a considerable statistical error (partly over 30 % relative error). Furthermore, the transition rates can vary significantly depending on the molecule under investigation since the local environment of the molecule has a crucial influence on its photophysics. Nevertheless, simulated and experimentally observed fluorescence increase agree very well, which confirms diffusing oxygen as the main mechanism for the blinking of monomer M.

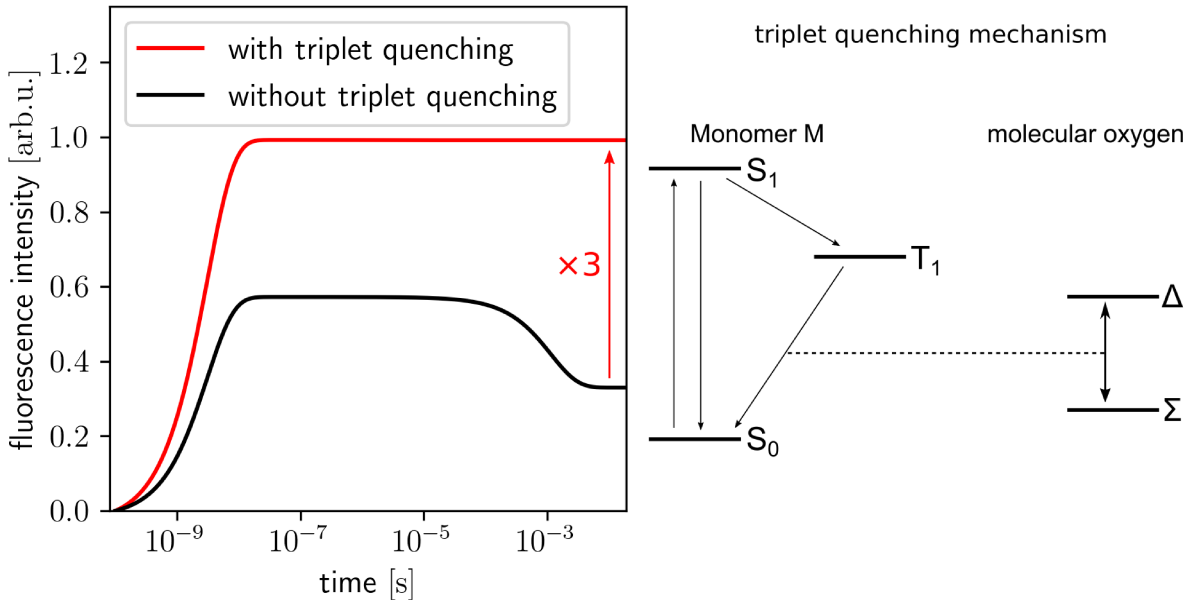

Figure 4.6: Photostatistics of Monomer M with and without interaction with oxygen. Left: Simulated fluorescence intensity with the excitation laser being turned on. Without triplet quenching (black) the molecule reaches a steady state within 1×10^7 ns which is 3 times darker in intensity as the corresponding state with increased triplet quenching (red). Right: Schematic illustration of the interaction triplet quenching by interaction with molecular oxygen.

Finally, we will discuss whether the result of this experiment and the concomitant simulation can be utilize molecular emitters in a more efficient way. As the intentional interaction with oxygen does not increase the quantum efficiency of a molecular emitter, the purposeful interaction with oxygen it is not a suitable approach to improve the emission of a molecular based OLED device. However, for single photon emitters it might be advantageous to actively quench the triplet state population by oxygen to increase the rate of single photon emission or to intentionally control the single photon emission rate. In contrast, the presence of oxygen within the sample generally has a detrimental effect on the overall lifetime of an emitter as well as of the entire device. Therefore, a long operational lifetime is generally ensured by preparing the sample in an inert, oxygen-free and water free atmosphere. But often, even in such samples prepared in nitrogen atmosphere an increase in photoluminescence can be observed shortly before irreversible photobleaching of an emitter, as it is shown in Figure 4.7.

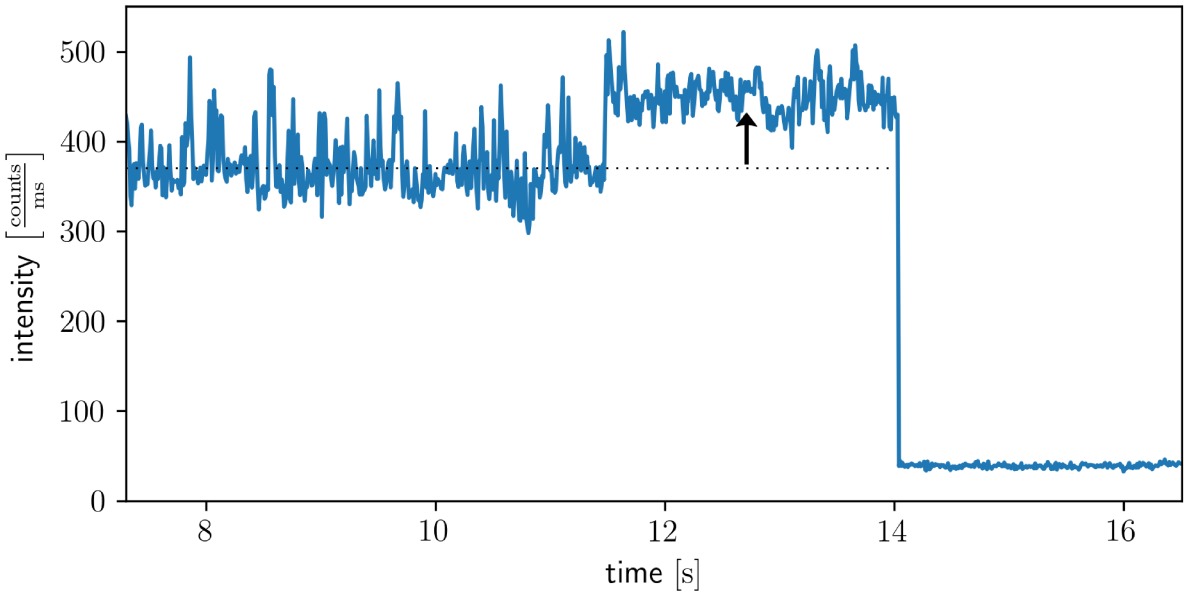

Figure 4.7: Photobleaching of a perylene bisimide monomer. The emitter was doped into a layer of PMMA under nitrogen atmosphere. The photoluminescence of the molecule is increased at 11.5 s prior to photobleaching at 14 s, which is a frequently observed behavior for fluorescent emitters and as described in the text can be related to the presence of oxygen.

4.2 Influence of the Local Molecular Environment

In this sub-chapter, the influence of the local environment on the photophysics of an emitter is explored more deeply. Single molecule spectroscopy, again, turns out to be the tool of choice as it allows by examining identical molecules at different locations in the sample to separate internal properties of a molecule from influences by its environment. Particularly, in disordered matrices individual molecules can exhibit surprisingly different behavior, which can be attributed to the varying degrees of interaction with the local environment. Thus it is of great importance to study these interactions and their effect on the photophysical properties of an emitter and to draw conclusions are drawn to assist in the design of more efficient emitters for applications in ensemble or single photon based opto-electric devices.

We will proceed in the following way. First, we look at the different photophysical properties that can be quantified for a given individual molecule and that can be compared among identical molecules at a different locations in the sample. Then, we will analyze what correlations might occur between these parameters. For example, we will see how the fluorescence lifetime correlates with the spectral emission of a molecule. Finally, we will clarify how the variations in the measured photophysical quantities can be attributed to different degrees of interaction with the local environment of the molecule and of what nature the underlying mechanisms are.

As model system, fluorescent perylene bisimides (PBIs) were chosen as they exhibit extraordinary photostability, which is of vital importance for this experiment. The spectroscopic characteristics of these chromophores will be introduced in Chapter 4.6.2 were the compound is analyzed in more detail and will be compared to their macrocyclic derivatives. To conduct a series of different measurements on these PBI molecules, it is necessary to prevent photobleaching during measurements. After identification of residual oxygen in the sample (see previous section 4.1) an additional strategy was applied to minimize the amount of free oxygen: Two stripes of aluminum were added to serve as oxygen getter material (see Figure 4.3) in the encapsulated sample volume. This preparational add-on reduced the probability of photobleaching for a single molecule during the 20 minutes measurement cycle below 10 %. In all other respects, the same sample preparation procedure was applied as described in the previous Chapter 4.1.

Let us start by looking at six different photophysical properties of interest. Four of these quantities are derived from the emission spectrum of the single molecule. A representative emission spectrum is shown in Figure 4.8. Here, at least three emission maxima can be identified and can be attributed to the vibronic structure of the molecule.

In reality, however, the molecule has not only three but more than 200 normal modes of nuclear motion, which, when coupling to the electronic transition, contribute to the emission spectrum by different weights. Additionally, each of these emission lines is inhomogeneously broadened by the fluctuation of the local emitter environment of the molecule at room temperature. Therefore, we are faced with a very complex situation from which inherent material parameters must be reliably derived. The first of these characteristics is the transition energy of the zero phonon line (m). This quantity represents the energetic position of the 0-0-electronic transition, i.e. the energy difference between the excited singlet state and the neat singlet ground state with no excited phonons. Due to the broadening of the emission lines by static and dynamic effects as well as by the close vicinity of other emission lines, the 0-0-emission line cannot be resolved directly. However, since the 0-0-transition in the single molecule spectrum makes the largest contribution to the highest energy emission maximum, its position is employed as an approximation for the transition energy m.

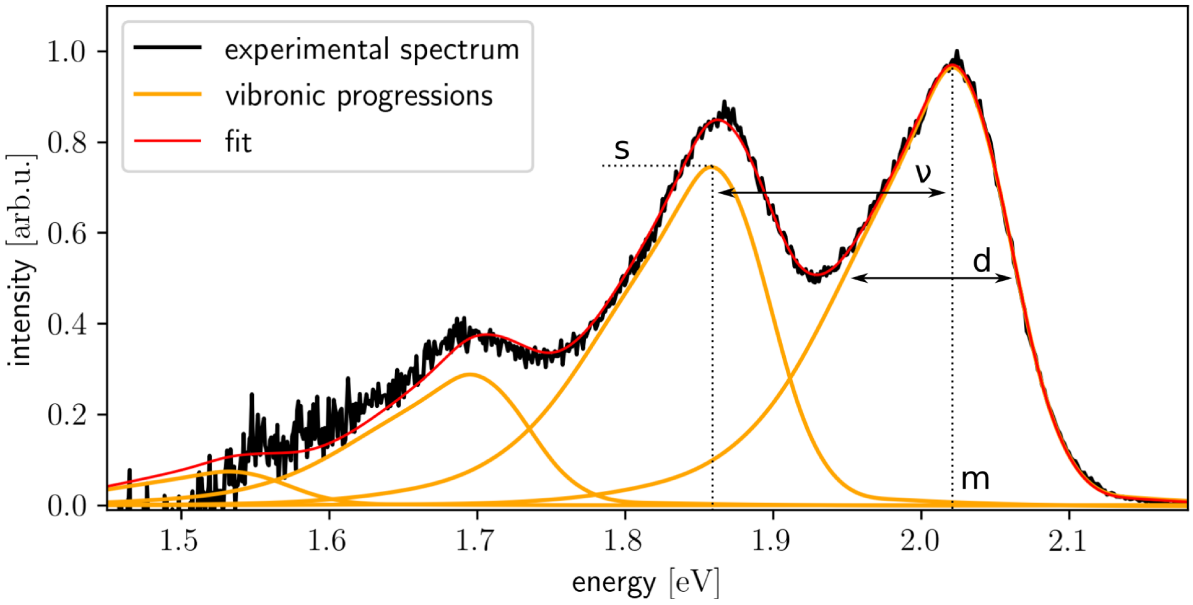

Figure 4.8: Emission spectrum of a perylene bisimide monomer decomposed into several peaks of the vibronic progression at an equidistant energy spacing ν and broadening d. The parameter m characterizes the position of the 0-0-transition while s quantifies the Huang-Rhys parameter.

The other maxima in the emission spectrum are, not by coincidence, located lower energy positions equally spaced by about 165 meV. The emissions of photons with a lower energy go along with the excitation of vibrations of the molecule. The observed value of 165 meV is typical of PBIs [66] and other polyaromatic hydrocarbons [67]. These emission

lines correspond to a variety of C-C and C=C vibrations of the carbon atom scaffold which constitutes the basis of the conjugated π-electron system. In PBIs, these oscillations couple very efficiently to the electronic transition, since the electronic wave function loses a total of three nodal planes during the transition from LUMO to HOMO [66]. Therefore, after the electronic transition, particularly many pairs of adjacent carbon atoms are far from their new equilibrium position and the equilibrium distance along the molecular carbon backbone lengthens and shortens, alternately. In the fluorescence spectrum, this strong coupling becomes apparent as emission maxima recurring at spacing of about 165 meV. However, again the situation is more complex and these emission peaks consists of a multitude of individual single vibronic transitions. As a possibility to quantify this distance, a progression of identical, locally confined functions was fitted to the spectrum. To include corresponding vibronic transitions into one local function, they form slightly asymmetric peaks which are calculated with a certain vibronic spacing v and an amplitude distribution of $s^n e^{-s}/n!$ according to the Franck–Condon overlap integrals with the Huang-Rhys parameter s for the n^{th} vibronic peak. Hence, the vibronic splitting v is approximately identical to the energy difference of the first and second emission maximum but takes into account other superimposed vibrational contribution. The fourth quantity obtained from the molecular spectrum is the width d (FWHM) of the emission peaks, which are broadened by both, contributions by different vibronic transitions to a peak and by inhomogeneous broadening effects.

Before continuing, we have to make some general remarks on how the recorded spectral data were processed. At first, the emission intensity of single molecules is quite weak. Therefore, background intensity is significant and had to be measured at a location without molecules under study and subtracted from the actual molecular emission. Next, the spectrum was corrected for the wavelength dependent detection efficiency of the setup. Further, the emission spectrum was recorded by a spectrometer with a grating monochromator working in the wavelength domain as an spectral density integrator, i.e. summing up the intensity in a certain wavelength interval. To transform the resulting spectral density function to the energy scale proper Jacobian transformation [68], here by multiplying λ^2, had to be applied. Also, when evaluating parameters like the Huang-Rhys factor, one has to take into account the photon mode density in the matrix material hosting the individual emitter. This can be altered by dispersion and cavity effects in the sample but nonetheless shows an E^2-dependence as in the vacuum. Finally, the square of the transition matrix element and thus, the probability of a transition is proportional its transition energy [69]. Correcting for all these effects, the spectral density function of the emission increases in the lower energy part in comparison to the higher energy part

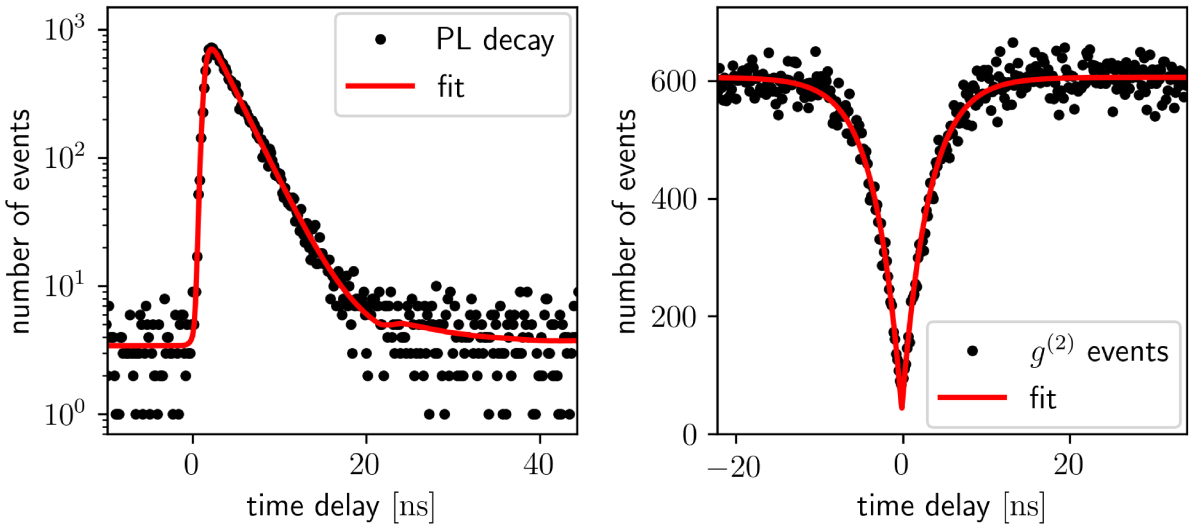

Figure 4.9: Time correlated measurements on single perylene bisimide molecules. Left: Photoluminescence (PL) decay of a perylene bisimide monomer after pulsed photoexcitation. Right: $g^{(2)}$-function recorded during continuous laser excitation.

of the spectrum, which is why the processed spectrum displayed in Figure 4.8 shows a particularly poor low signal to noise ratio at its low energy side.

After the emission spectrum of a single molecule has been analyzed, two further quantities can be deduced from the photon statistics of molecular emission. If the molecule is excited by a pulsed laser, the fluorescence decay allows to determine the lifetime t of the excited state. Such a decay in fluorescence is shown in the left graph of Figure 4.9 with a typical lifetime of a few nanoseconds. Further, if a single molecule is photoexcited continuously, an antibunching behavior with a characteristic temporal width $\Delta\tau$ can be observed as $g^{(2)}$-function of the emitted photons. This is shown in the right graph of Figure 4.9.

The brightness of a molecule's fluorescence is also influenced by its local environment but depends much more sensitively on its orientation relative to the excitation and detection axis. Nevertheless, the brightness of each molecule was recorded at the beginning and the end of each measurement cycle in order to determine whether the molecule has experienced reorientation in the matrix during the measurement. In case of the latter (for 8 of the 32 examined molecules) this molecule was excluded from further analysis. Additionally, three molecules were excluded because of their photobleaching during the experiment. This leaves 21 complete data sets for evaluation which is a high enough number to find fundamental correlations between the quantities but far below the number necessary to analyze functional relations. As a first representative overview, Figure 4.10 shows the $g^{(2)}$-functions, lifetime measurements and emission spectra of molecule #8

and #9. The other molecules show the same correlations of their properties. For example, molecules showing a broader antibunching dip usually exhibit a longer lifetime and a red-shifted emission.

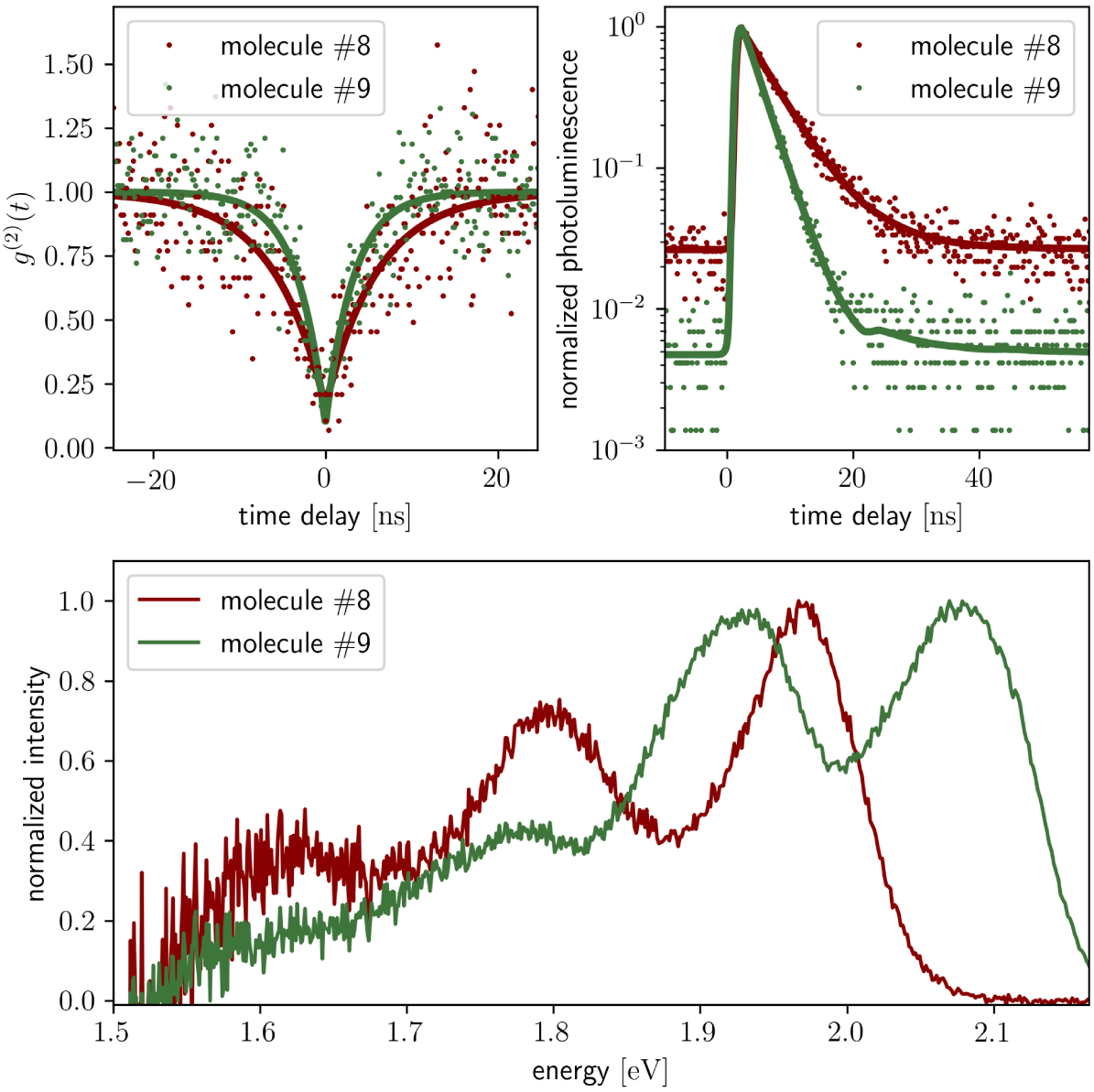

Figure 4.10: Representative data sets of the photophysical properties of molecules #8 and #9. Top left: $g^{(2)}$-function at continuous laser excitation. Top right: Fluorescence decay after pulsed photoexcitation. Bottom: Emission spectra. Other molecules show the same correlation between the width of the antibunching dip, the fluorescence lifetime as well as redshift in emission.

Now we want to find possible correlations between all of the six examined parameters. For this purpose, the probability (p-value) of the Null hypothesis, i.e. the probability that the measurement results for different quantities are uncorrelated and random, is calculated for each pair of two of the quantities. Figure 4.11 illustrates these correlations for the case of four of these parameters while Table 4.1 lists all the relevant p-values, where the red coloring indicates the degree of significance.

Table 4.1: *p*-values of the linear regression

t	1.86e-03				
Δτ	1.55e-03	6.85e-10			
s	0.0264	0.0138	0.0649		
m	0.358	0.192	0.224	1.45e-03	
d	0.764	0.192	0.358	0.883	0.117
	ν	t	Δτ	s	m

An overview over all analyzed parameters and their correlations are given in Figure 4.12. For a coherent picture without logical contradictions, it is necessary that either all parameters pairwise correlate positively or that the quantities can be divided into two groups, with only positive correlations within one group and only negative correlations (i.e. anticorrelation or inverse correlation) when picking one variable from each groups. This second case is clearly visible in the data. The first group consists of the variables ν, t and $\Delta\tau$, while the second group contains of the variables d, m and s.

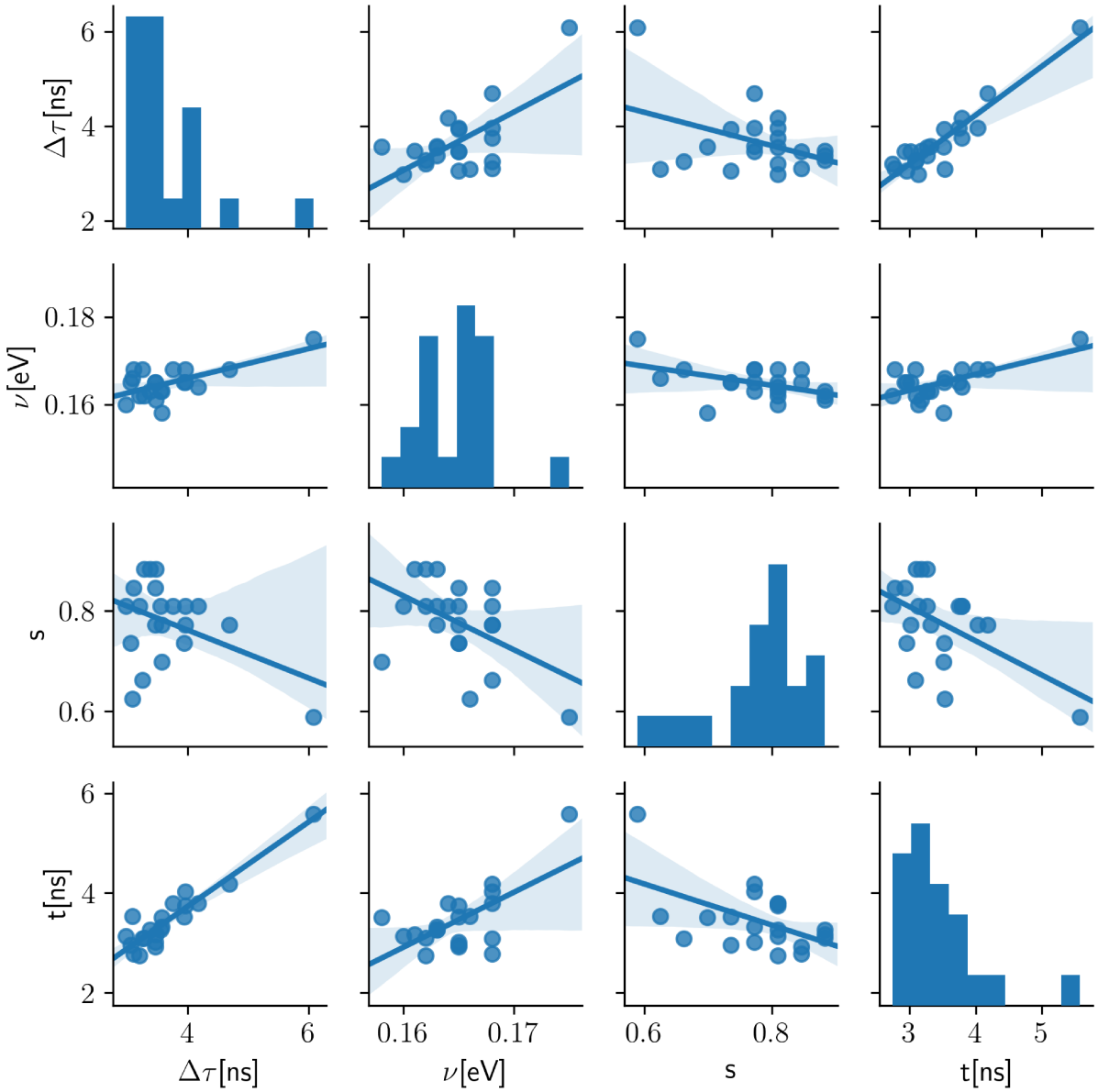

Figure 4.11: Correlation between the width of the $g^{(2)}$-antibunching dip $\Delta\tau$, the Huang-Rhys parameter s, the fluorescence lifetime t and the vibronic splitting ν. Areas highlighted in blue around regression functions indicate the confidence interval of the respective linear regression, where some of the parameters pairs show a distinct pair wise correlation (e.g. $\Delta\tau$ and t) while others do not (e.g. s and $\Delta\tau$).

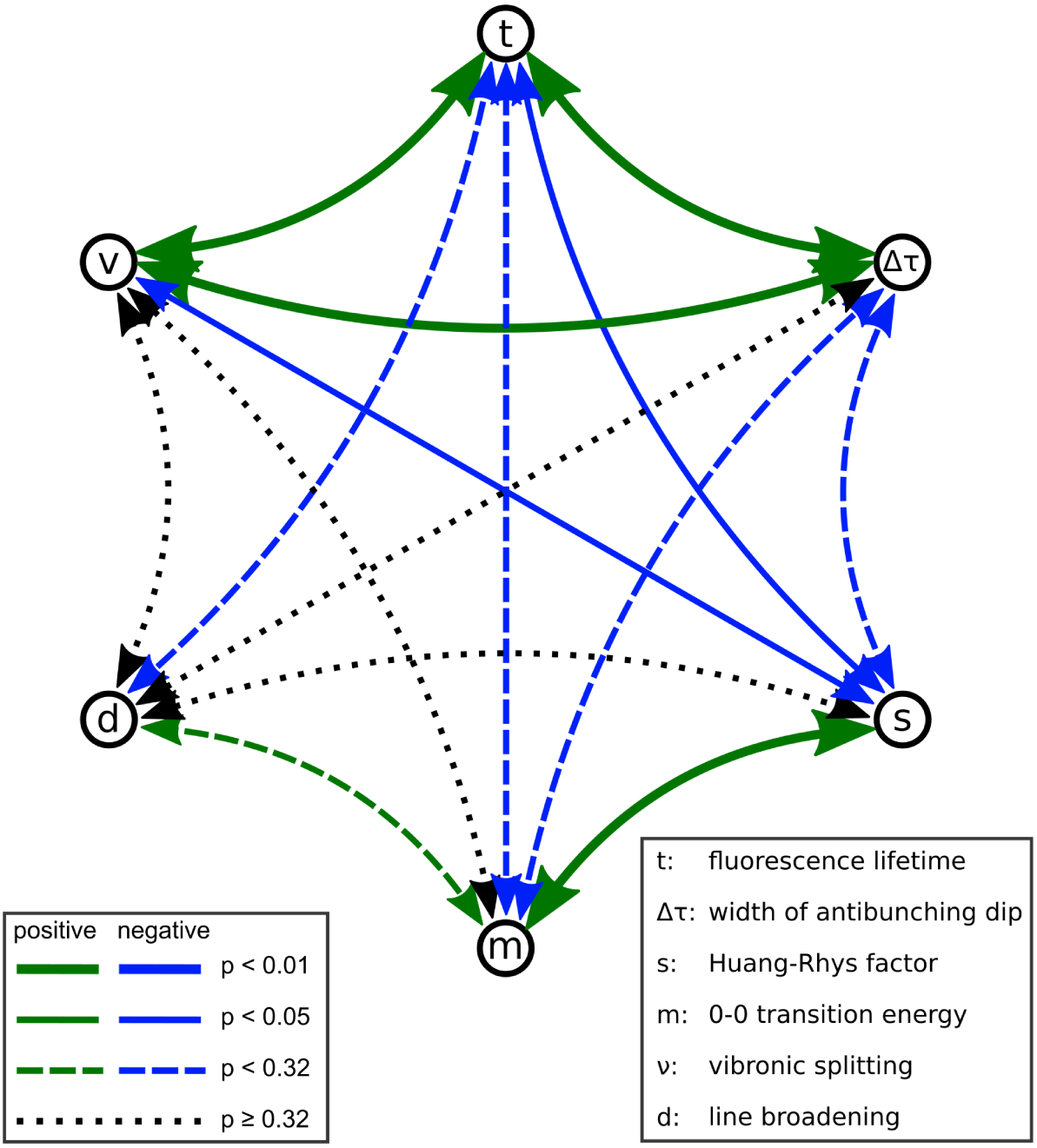

Figure 4.12: Overview of the photophysical parameters and their interrelations measured on a set of single molecules. Green lines indicate a positive correlation, blue lines a anticorrelation and dotted lines refer to correlations with the significance below one standard deviation.

Although for some pairs of measured parameters the statistical power is too small to prove a direct correlation, a reliable statement can be made via the indirect correlation by their group members. For example, the variables m and v only show a week direct negative correlation below one standard deviation, but m and v have either a negative correlation followed by a positive or a positive correlation followed by a negative amongst the variables t, $\Delta\tau$ and s. This makes the interrelation between every two parameters significant.

When observing correlations between variables in real systems, it is often difficult to distinguish cause and effect. In our case, this turns out to be simple. Since all molecules are identical in their photophysical properties the origin of the observed effects must be imposed externally. Therefore, we can attribute the measured changes in the photophysical properties to the interaction with the environment of the molecules. But how does this interaction look like exactly and how does it influence the measured properties?

First, let us consider the differences between molecules in solution and in a solid state matrix. In the first case, molecules interact with the dynamically changing environment of the solvent, which can be described as a time average by just three solubility parameters [70]. Among these parameters, the polarity of the solvent is the most decisive one for the photophysics of the molecule [71]. On the other hand, a spin coated PMMA thin film is a highly non-equilibrium thermodynamical state, i.e the state does not reach its most energetically favorable state during processing. This includes significant amount of structural heterogeneities [72]. Therefore, the local environment of a single molecule will be very complex and varies substantially across the PMMA film. Looking at the scattering of data in Figure 4.11, it becomes obvious that, although there are correlations between the analyzed quantities, these are by no means based on a simple scalar relation that describes the interaction with the environment by a number. If this would be the case, all measured photophysical quantities would correlate maximally with each other, except for small deviations due to noise in the measurements. Rather, the interaction with the environment has to be described as a multidimensional process in which influencing factors such as the local dielectric constant, the local polarity and the local electrostatic potential must be taken into account. These factors can vary over a wide range in disordered PMMA matrices as demonstrated by Yadigarli et. al. [73] using single molecules as probes for the effective local dielectric constant, which varied between 5.9 and 8.3.

The effective local polarity of the matrix, most likely, has the biggest influence on the photophysics of the guest molecules and the resulting changes in their photophysical quantities can be understood in the following way. Comparing the energetic positions of the S_0 and S_1 states in vacuum and in a polar environment, we find that the polarity

of the environment lowers both the excited and the ground state energy of the molecule. However, since in perylene bisimides the S_1 state has a stronger dipole moment, it is lowered to a larger extend, which reduces the energetic distance between the two levels and thus, shifts the emission wavelength of the emitter towards the red. A systematic increase in emission wavelength can also be observed for solvents of increasing polarity [73], but even weak Van der Waals interactions in a noble gas atmosphere of low pressure can be sufficient to yiel a red shift in emission [74].

Next, we notice that the red-shifted emission goes along with a prolonged radiative lifetime of the excited state. This was also observed for other emitters in solution and PMMA matrices [72] and is attributed to the local polarity of the matrix as well. The mechanism behind this observation was proposed by Kapusta et al. in 2003 [75]: The lowering of the S_1 state in a polar environment reduces non-radiative decay processes which include the intersystem crossing from S_1 to T_N states. These non-radiative decay process via triplet states are also responsible for a large part of the non-radiative recombination in PBIs [76, 77]. Additionally, the smaller density of photonic states at longer wavelengths reduces the radiative transition rate of the excited state. But the latter effect alone is not sufficient to explain the observed variation in the lifetime of the excited state.

Naturally, there is strong correlation between the width of the antibunching dip $\Delta\tau$ and the lifetime of the excited state t. For a two level system $1/\Delta\tau = k_{12} + 1/t$ holds, where k_{12} is the rate of absorption. This is the reason why we observe the most significant correlations for these variables in Figure 4.11 and Table 4.1. Additionally, plotting $1/\Delta\tau$ over $1/t$ one observes a smaller k_{12} in molecules with red-shifted emission. This is consistent with the PBI absorption spectra, shown in Figure 4.50, as the excitation wavelength of 532 nm is located on the high energy side of the absorption spectrum and the absorption is reduced when the absorption spectrum is shifted to longer wavelengths.

The local polarity of the matrix also affects the shape of the emission spectrum, which is decisive for the color gamut of the corresponding OLED devices. Ideally, one would prefer narrow emission lines, which in theory could be induced by an additional external electrostatic potential which would increase the frequencies of vibronic oscillations in the emitter or could suppress them completely. The former leads to a bigger splitting of the vibronic bands in the experiment. Additionally, the Huang-Rhys parameter is reduced and the intensity of the 0-0 transition line is increased relative to the other emission lines. This interrelation is also evident in the correlated parameters.

In summary, the observed correlations are described qualitatively well by the effect of the local polarity. This effect shift the emission of PBI emitters by more than 100 meV,

narrows its emission lines and minimizes the non-radiative decay channels of the excited states, which is visible in a prolonged exciton lifetime. Nevertheless, the influence of local polarity is not the only mechanism which affects the photophysics of an emitter. Assuming full control over the local environment, one could optimize the properties of an emitter individually by many independent parameters, for example, by modifying the structure of the matrix into which the emitter is embedded. This approach is presented in Section 4.6.1. An other approach is the design of macrocycles molecules with the respective chromophore being just a small part of the entire molecule. In this case, the local environment of the chromophore is well-defined by the polarity and the interaction with other parts of the molecule. In the group of Prof. Dr. Frank Würthner at the at the Institute of Organic Chemistry at the University of Würzburg, this approach was utilized to suppress vibronic modes in a BPI based emitter by an additional linker between chemical moieties. As a result, the Herzberg-Teller vibronically induced spin orbit coupling s minimized and thus, the intersystem crossing rate is reduced by an order of magnitude [78]. In addition, this group produced macrocycles [79], which will be characterized in this thesis in more detail in Chapter 4.6.2.

4.3 Phosphorescent Molecules in Organic Light Emitting Diodes

In the last two chapters, some general properties of single organic molecules in matrices were analyzed. Now, in the following chapters, we want to examine the performance of several dopants, which cover all kinds of recombination mechanisms which were presented in Chapter 2.2, i.e. open-shell molecules, phosphorescent molecules, multichromophoric molecules and molecules exhibiting delayed fluorescence. Here we start with a phosphorescent emitter.

In commercially utilized phosphorescent emitters, like Ir(ppy)3 [36], a strong spin orbit coupling (SOC) achieved by relativistic effects in the vicinity of heavy atoms [37] is used to enable an efficient radiative transition between excited triplet and singlet ground state allowing for almost 100 % internal quantum efficiency. Instead of heavy atoms such as iridium(III), up-tp-date emitters utilize cheaper and more easily available materials [80]. Indeed, iridium is one of the rarest materials in the earth's crust [81]. In comparison, copper is a much more abundant metal, which has, however, a significant smaller atomic number ($Z_{\mathrm{Cu}} = 29$ versus $Z_{\mathrm{Ir}} = 77$) and thus, a smaller SOC ($\xi_{\mathrm{Cu}} = 857\,\mathrm{cm}^{-1}$ versus $\xi_{\mathrm{Ir}} = 3909\,\mathrm{cm}^{-1}$) [82]. Besides better availability, which itself is not crucial, copper has some decisive beneficial properties when used in metal complexes: Firstly, a flexible coordination geometry allows tetrahedral and trigonal as well as linear complexes [82], the later promise the least amount of excited state distortions [83]. Secondly, the d-orbitals of copper are completely occupied so that there is no possibility for the occurrence and thus occupation of metal-centered d-d* states, which tend to lie low in energy and recombine non-radiatively [84]. Thus, linear Cu^{I} complexes, like the complexes studied in this work, are promising candidates for high quantum efficiencies.

Finding suited ligands for efficient phosphorescent and fluorescent complexes defines an additional important task. Here, the choice usually falls on strongly π-accepting ligands like carbenes [85] in order to create a strong metal-ligand charge transfer (MLCT) character of the excited state. To demonstrate phosphorescence and thermally activated delayed fluorescence based on linear copper complexes, two new types of molecules, both presented in Figure 4.13, had been synthesized and pre-characterized by Markus Gernert in the group of Dr. Andreas Steffen at the Institute of Inorganic Chemistry at the University of Würzburg.

As phosphorescent material CuCl-1-(2,6-diisopropylphenyl)-3,3,5,5-tetramethyl-2--pyrrolidine-ylidene, in short CuCl($\mathrm{CAAC}^{\mathrm{Me}}$) where Me denotes the methyl moieteis, was

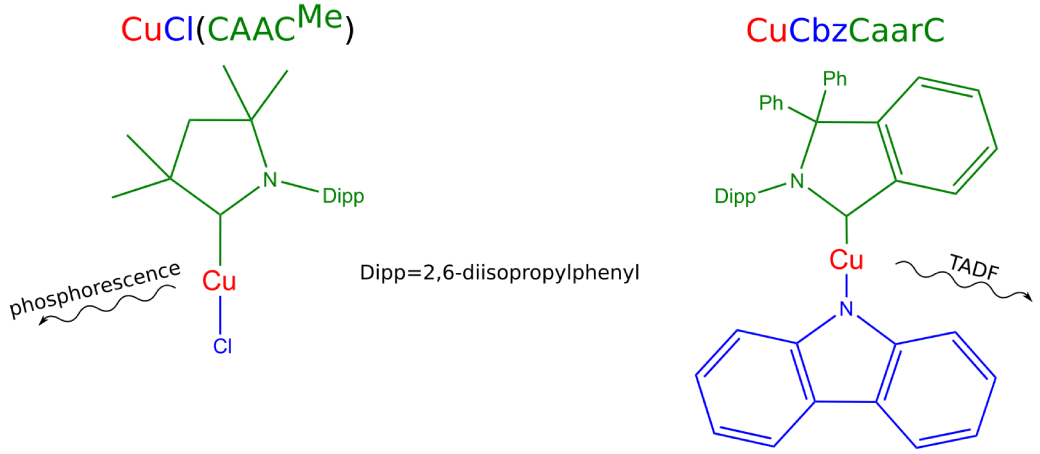

Figure 4.13: Chemical structure of CuCl-1-(2,6-diisopropylphenyl)-3,3,5,5-tetramethyl-2-pyrrolidine-ylidene (CuCl(CAAC^{Me})) and Cu(carbazolate)(2-(2,6-diisopropyl)-phenyl-1,1-diphenyl-isoindol-2-ium-3-ide) (CuCbzCAArC).

synthesized [83]. The left side of Figure 4.13 shows this complex with the copper atom linearly coordinated to a CAAC ligand and a chlorine ligand.

According to pre-characterization of the solid state aggregate, the resulting complex shows an emission maximum located at 511 nm (full emission spectrum provided in Figure 4.20), the rate of the radiative transition from the triplet state to the singlet ground state is $2.3 \times 10^4\,s^{-1}$ and the quantum efficiency amounts to 60 %. Further, a strong MLCT-character of 45 % was calculated and direct absorption from the ground state to the triplet state ($S_0 \rightarrow T_1$) was observed which indicates a strong SOC. Finally, temperature-dependent lifetime measurements have shown that the complex exhibits no TADF. Although the properties of the complex may change to a certain extent depending on the matrix material employed, these findings indicate the suitability of CuCl(CAAC^{Me}) as a phosphorescent material for OLED applications. Besides, the compound containing the chlorine ligand complexes with halides such as bromine and iodine, as well as a second CAAC ligand were synthesized, but showed an inferior quantum efficiency together with an emission wavelength shorter than 400 nm [83], which lies outside the visible spectral range.

Before discussing the properties of CuCl(CAAC^{Me}) as active emitter in OLED applications, the sample preparation methods and the materials used will be described.

Devices which need to be electrically contacted and simultaneously optically characterized require a conductive and transparent electrode at the interface to the glass support. This is realized by Indium-Tin-Oxide (ITO), which consists of the wide band gap semiconductor indium oxide, which is heavily doped with tin, resulting in quasi-free charge carriers at a density of about $10^{19}\,cm^{-3}$ to $10^{21}\,cm^{-3}$ in the conduction band of the material [86].

ITO substrates were purchased from SPI Supplies Brand and have a thickness of 150 µm and a sheet resistance of 30 $\Omega\square^{-1}$ to 60 $\Omega\square^{-1}$ while the work function of the material is located at values between 4.2 eV and 5.2 eV depending on the oxygen concentration at the surface and thus, the sample preparation technique [87].

At first, the ITO substrates were cleaned in a three-step process with water, acetone and isopropanol in an ultrasonic bath to prepare the substrates for etching of lateral structured contacts. Etching of these contacts is necessary to obtain OLEDs with a small active area defined by the lateral overlap of anode and cathode structure. For optical measurements one aims at small active regions as this reduced the probability of short circuits for a given OLED and increases the number of independent testable OLEDs per batch.

For structuring the desired T-shape of the ITO anode the shape was printed on a transparent foil. Then, the ITO substrates were spin-coated at 2500 rpm for 60 sec with a thin layer of the positive photoresist (AZ1518), dried on a heat plate at 100 °C for 50 sec and exposed to UV light with the printed foil as a photomask. The photoresist was then developed in a three-step process with help of the of water-diluted developer AZ351B (developer concentration for the three steps: 25 %, 20 %, and 0 %). Afterwards, the samples were dried on a heat plate at 120 °C for 60 sec and, consequently, the ITO was etched at the exposed areas by aqua regia (H_2O:HCl(37 %):HNO_3(65 %) at a ratio of 12:12:1) to obtain the desired final structure, which is illustrated in Figure 4.14.

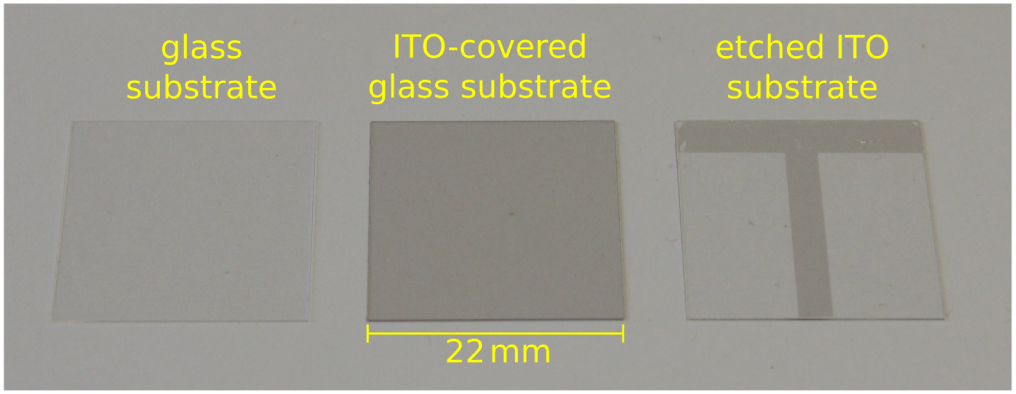

Figure 4.14: Lateral structuring of ITO substrates. ITO-covered glass substrates (middle) are processed with a method described in the text to obtain a conducting T-shape (right) confining the active region of the OLEDs. For comparison a pristine glass substrate is shown on the left, which is used for samples that are not driven electrically.

Once again, the samples were cleaned (water, acetone and isopropanol in an ultrasonic bath) and treated in a plasma-etching chamber with oxygen plasma for 10 minutes to

oxidize and remove residual organic material from the surface which could pose defects for the subsequent film growth or a source of unwanted luminescence during the experiments.

Prior to the deposition of the active OLED compounds, a thin layer of poly-3,4-ethylendioxythiophen:polystyrene sulfonate (PEDOT:PSS, supplier: CLEVIOS P VP AI 4083), with a thickness of approximately 40 nm was spin-coated from aqueous solution onto the ITO substrates. This composite consists of the two polymers PEDOT and PSS depicted in Figure 4.15, where PSS is used for hole doping of PEDOT and to increase the solubility, thus enabling processing from solution [88]. This has several advantages: At first, the roughness of the underlying ITO surface is reduced, yielding a minimization of local high electric field strengths at discontinuities of the ITO surface. These may lead to local short circuits of the OLED or the formation of filament-like current during operation. Secondly, the diffusion of oxygen-containing species from the ITO surface into the OLED is prevented, which has a positive effect on the lifetime of the active molecular materials [89]. Thirdly, the injection of holes into the OLED is improved as the contact between ITO and PEDOT:PSS is ohmic [90]. These advantages lead to lower operating voltage and longer durability in comparison to OLEDs without PEDOT:PSS [91, 92].

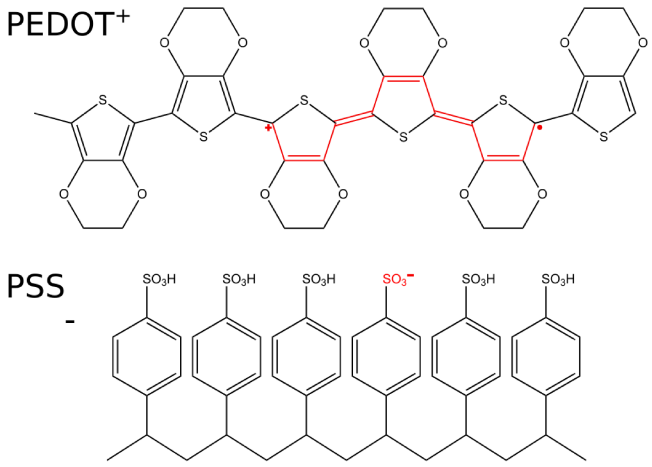

Figure 4.15: Chemical structure of poly-3,4-ethylendioxythiophen (top) and polystyrene sulfonate (bottom). The red marks indicate the location of the charge transfer between the two polymers.

The PEDOT:PSS starting material was filtered by a nylon membrane filter (pore size: 0.2 µm) and spin-coated at 4800 rpm for 30 sec on the pre-structured sample to receive a PEDOT:PSS cover layer of 40 nm thickness. Afterwards, the sample was dried on the heating plate at 135 °C for 30 min to remove residual water and finally, the sample was transferred to a glovebox with nitrogen atmosphere for further processing.

For the active emitting layer, the polyspirobifluorene-based copolymer SPB-02T was chosen as a matrix material. This polyspirobifluorene-based copolymer SPB-02T, illustrated in Figure 4.16, is a sky-blue emitting copolymer with the HOMO (LUMO) level located at −5.5 eV (−2.0 eV) below the vacuum level [93]. The raw material was purchased from *Merck KGaA* under the trademark *livilux A.80827* and used without further purification. OLEDs comprising an ITO/PEDOT:PSS anode and a neat SPB-02T layer as active material exhibit an emission maximum at 490 nm. Hole mobility values between 6×10^{-8} cm^2/Vs and 2×10^{-7} cm^2/Vs have been reported [94, 95] and the material has proven suited for the electrical excitation of dopant molecules and polymers [96].

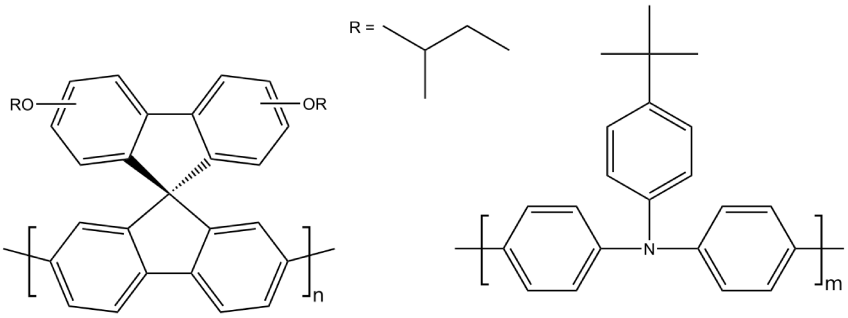

Figure 4.16: Chemical structure of the polyspirobifluorene-based copolymer SPB-02T. The two segments occur statistically along the polymer chain.

For the processing of the active layer CuCl(CAAC^{Me}) was added in a concentration of 20 wt% to SPB-02T and solved at a concentration of 5 mg ml^{-1} in spectroscopy grade dichloromethane. Subsequently, the solution was spin-coated on top of the PEDOT:PSS layer at 1500 rpm for 30 sec.

Without exposure to oxygen, the samples were transferred to an evaporation chamber where cathode contacts were deposited. To create efficient cathodes for electron injection one aims at low work function materials [7]. However, these materials are usually prone to oxidization, which limits the lifetime of devices. As a trade-off between these requirements, a 20 nm thick layer of calcium (deposited at a rate of 1 Å s^{-1}) with a work function of −2.9 eV covered by a 120 nm thick layer of aluminum (deposited a a rate of 8 Å s^{-1}) to prevent oxidization was used. Although there exists more efficient cathode designs, the combination of calcium/aluminum provides robust contacts [97], stable enough for the measurements carried out, and can be produced with reliable reproducibility. During this process, the samples were covered by a shadow mask illustrated in Figure 4.17 to define the shape of the cathode contacts and thus to confine the active area of the OLEDs.

Figure 4.17: A shadow mask (left) is used for lateral structuring of the cathode materials calcium and aluminum (middle). Subsequently, the OLED is encapsulated and wires are contacted to the eight cathodes of different active regions and the ITO anode.

In a final step, all OLEDs were encapsulated under inert conditions within the glovebox by a glass substrate (bisected microscope slide) glued to the processed OLED by a low vapor pressure epoxy (Kurt J. Lesker, Torr Seal) and dried for 12 hour under nitrogen atmosphere. In order to facilitate the external electrical contacting, wires were clued on the contact areas by silver conductive paste and mechanically fixed by a two component adhesive. The structure and energy landscape, disregarding interface dipoles, of the final OLED is shown in Figure 4.18.

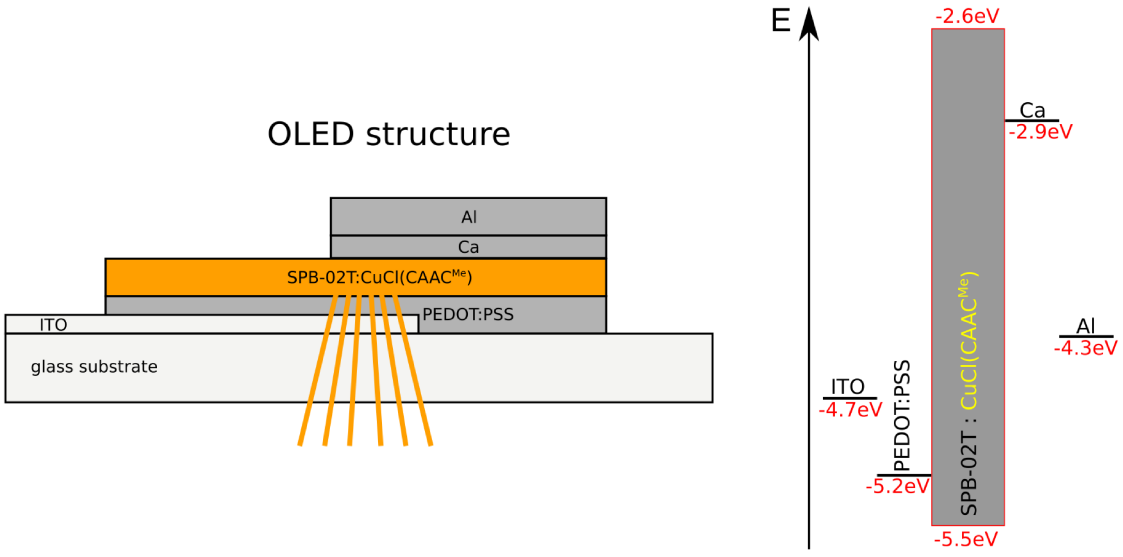

Figure 4.18: CuCl(CAAC^{Me}) based OLED architecture. Left: Layer structure of the SPB-02T-based OLED doped with CuCl(CAAC^{Me}). Right: Energy landscape for electrons and holes in the OLED.

Let us now look at this OLED under operation: Above 5 V driving voltage white emission with a blueish tint could be observed. Figure 4.19 provides a visual impression of the emission while Figure 4.20 shows the measured emission spectrum. We see that the measured electroluminescence spectrum exhibits light emission over almost the entire visible range, which explains the white color impression of the emitted light.

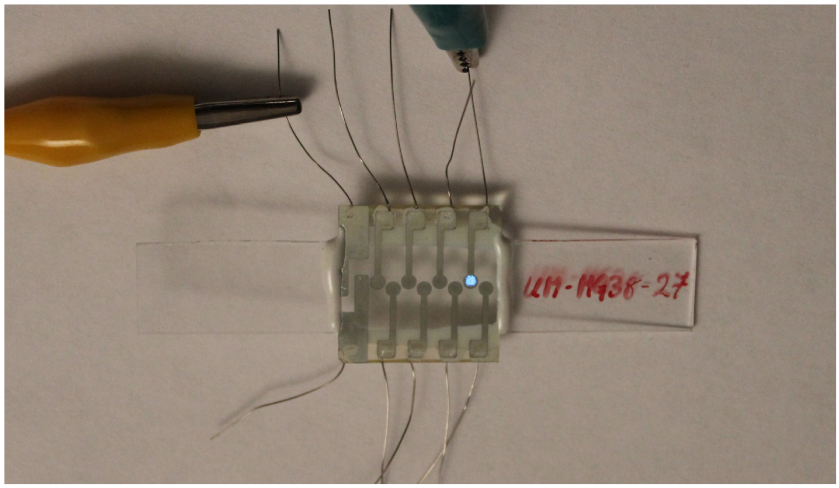

Figure 4.19: CuCl(CAAC^{Me})-OLED under operation at 7 V.

The spectral features around 500 nm coincide with the emission of an undoped SPB-02T OLED, which allows to deconvolute dopant emission from matrix contributions. This is indicated by the orange and blue spectra in Figure 4.20. While having a similar spectral shape, the electro-phosphorescence of CuCl(CAAC^{Me}) is red-shifted by about 1880 cm^{-1} (233 meV) in comparison to its solid state emission. This shift is induced by the polymeric host either by affecting the specific packing and agglomeration of the dopants or by a variation of the contributing Frank–Condon factors. Additionally, the electroluminescence tends to be red-shifted in comparison to the photoluminescence as the emission in electrically pumped devices happens predominantly from the energetically lowest states in a disordered environment. With increasing driving voltage, the emissions from SPB-02T and CuCl(CAAC^{Me}) increase monotonously but the relative fraction of the CuCl(CAAC^{Me}) emission decreases which is shown in the right side of Figure 4.20.

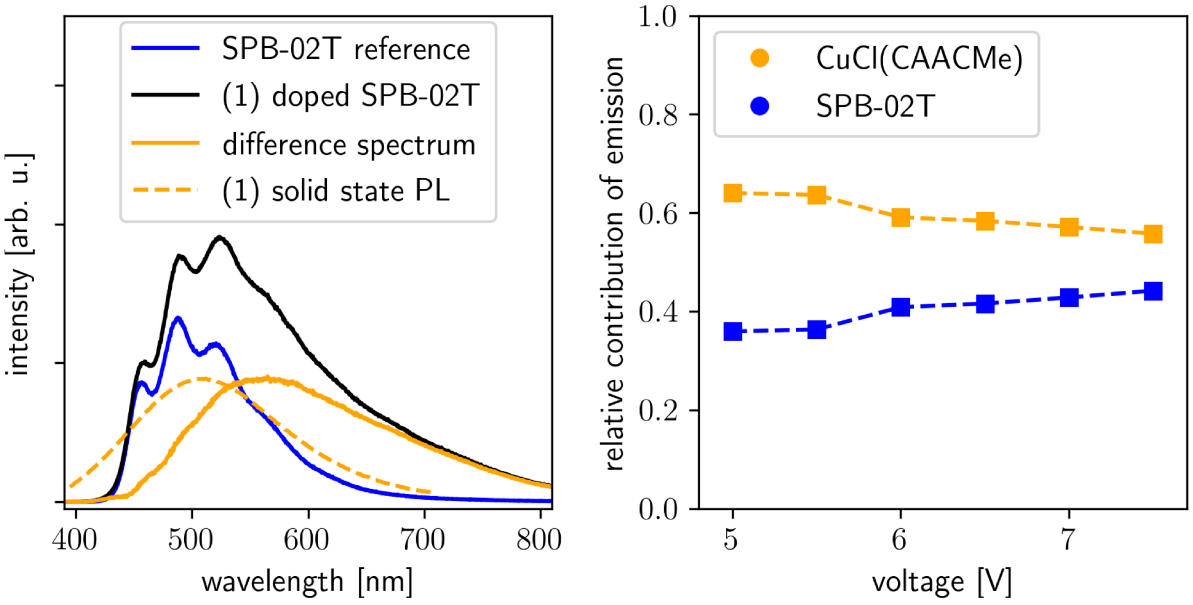

Figure 4.20: Emission from CuCl(CAAC^{Me}) doped OLEDs. Left: Electroluminescence spectrum of a CuCl(CAAC^{Me}) doped OLED in black. The emission is decomposed in the contribution from the SPB-02T matrix (blue line) and that from the phosphorescence of CuCl(CAAC^{Me}) (orange, solid line), the latter is red-shifted by about 1880 cm^{-1} in comparison to the solid state photoluminescence. Right: Increasing percentage of SPB-02T emission with higher driving voltage and thus, higher current density.

This finding indicates that to a certain degree the phosphorescence of CuCl(CAAC^{Me}) is saturated at higher driving voltages which is either caused by non-radiative channels, like exciton-exciton or exciton-charge annihilation, or by the saturation of the underlying energy-transfer mechanism. The external quantum efficiency of the device was estimated to be 0.03 %, which is well below the quantum efficiency of 60 % of the raw dopant material. However, the OLED architecture and the combination of OLED and dopant molecules were not optimized for a high quantum efficiency. Nevertheless, this device demonstrated for the first time the application of CAAC-Cu(I)–based phosphorescent emitters in OLEDs.

4.4 Molecules with Thermally Activated Delayed Fluorescence in Organic Light Emitting Diodes

Linear copper complexes, which possess the advantages mentioned before, can also utilize the process of thermally activated delayed fluorescence (TADF) to harvest both singlet and triplet excited states. To investigate the photodynamics of CuCbzCaarC, single-molecule photon-correlation experiments at room temperature as well as temperature dependent fluorescence lifetime measurements were conducted. Samples for the single molecule studies were prepared in the similar way as described before in Chapter 4.1, i.e. mixing a highly diluted solution of CuCbzCaarC in dichloromethane with PMMA and spin-coating this mixture onto a thin glass substrate.

The samples were then analyzed by means of the confocal microscopy setup under illumination by a laser with a wavelength of 532 nm. Figure 4.21 illustrates the distribution of photoluminescence intensity across different lateral positions of the thin film sample. Above a low noise background, bright spots indicate the positions of single CuCbzCaarC molecules. Peaks of different intensities – up to a maximum of 78 000 counts per second – can be observed, as the transition dipole moments of the molecules are oriented in a random fashion within the sample.

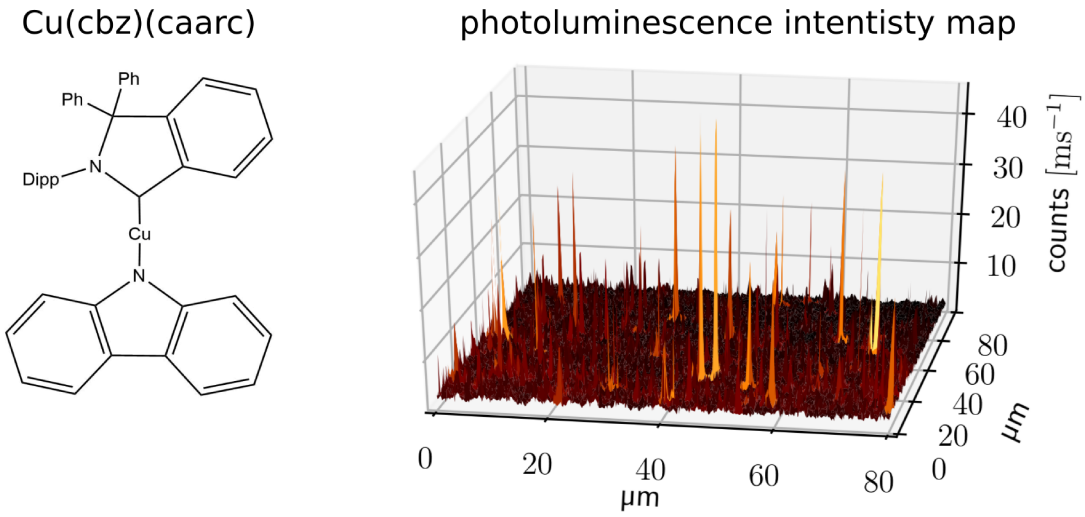

Figure 4.21: CuCbzCaarC as a single photon emitter. Left: Molecular structure of CuCbzCaarC, Right: Photoluminescence intensity map of the thin film sample photoexcited at 532 nm wavelength and a power of 195 µW.

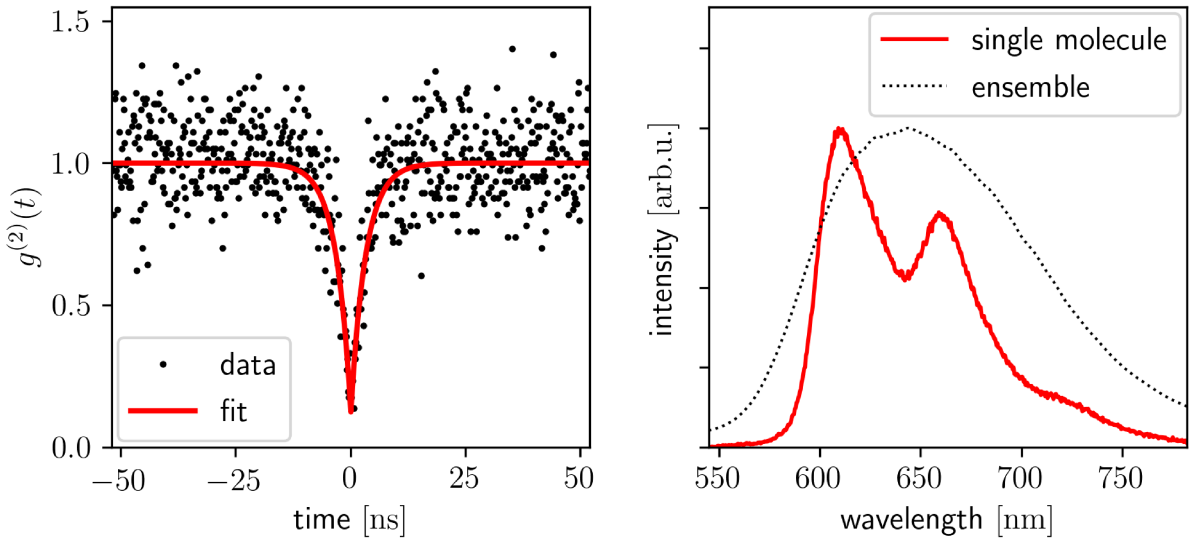

Figure 4.22: Single molecule experiment on CuCbzCaarC. Left: The $g^{(2)}(t)$ function of the photoluminescence from the highest spot in Figure 4.21 shows antibunching at zero time delay indicating light emission from a single CuCbzCaarC molecule. Right: The photoluminescence spectrum of a single molecule shows distinct emission lines with vibronic progressions rather than the broad emission spectrum present in the photoluminescence of an ensemble of molecules.

When calculating the second order correlation function $g^{(2)}(t)$ of the detected photons (see Figure 4.22) a distinct antibunching at zero time delay can be observed, which indicates emission from individual CuCbzCaarC molecules. During the experiment, the single molecules are pumped strongly enough to reach photoluminescence saturation. Nevertheless, the molecules are stable enough to emit several millions of photons prior to irreversible photobleaching.

The $g^{(2)}$-function yields two important information about the system: Firstly, one can calculate the width of the antibunching, which yields information about the sum of absorption rate, radiative emission rate and non-radiative decay rates from the excited state. Secondly, the absence of photon bunching at time differences greater than 25 ns (not shown in the graph) proves the efficient transition from singlet to triplet excitons and vice versa. Especially, the transition between the two states is considerably faster than the singlet lifetime. We can calculate a lower limit (details below) for the singlet-triplet transfer rate by including the results from temperature dependent fluorescence lifetime measurements.

For these measurements a polished copper substrate manufactured by the mechanical workshop of the physics faculty was used as a substrate and CuCbzCaarC dissolved in dichloromethane was dropcasted onto the substrate. Subsequently, the substrate was

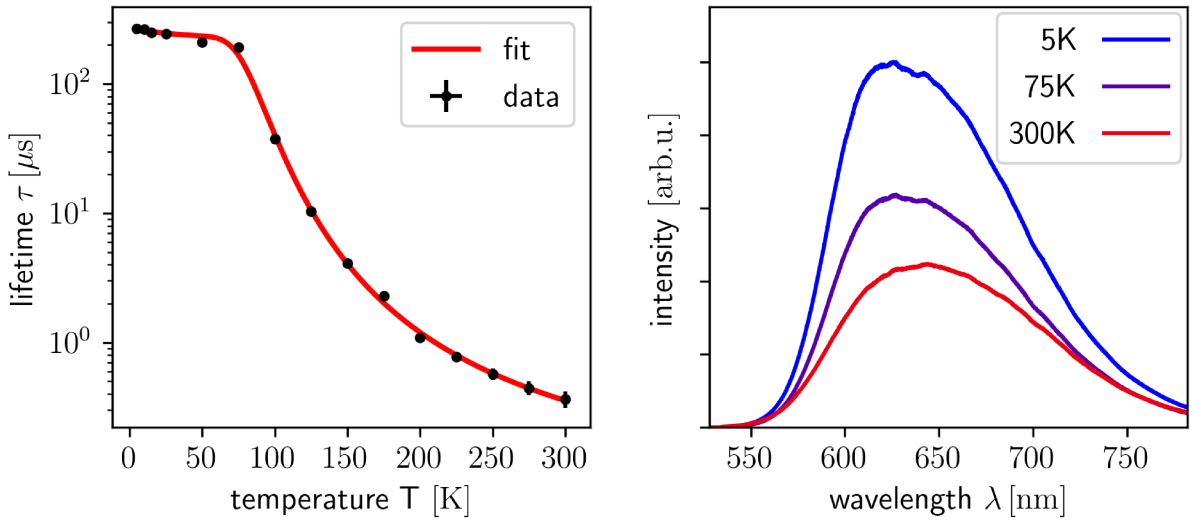

Figure 4.23: Temperature dependent measurements on CuCbzCaarC. Left: Lifetime of the delayed fluorescence as a function of temperature. Right: Temperature dependent photoluminescence spectra.

glued to the cooling finger of the cryostat with commercially available silver conducting paste.

When a pulsed laser with a pulse duration of 1 ns and a wavelength of 520 nm excites the molecules to their S_1 excited state, one can observe prompt fluorescence on a sub-nanosecond time scale. To extract the time constant of the delayed fluorescence, however, a single exponential function was fitted to the long tail of the decay function. This time constant increases significantly upon cooling of the sample as can be seen in the left graph of Figure 4.23.

As derived from the single molecule experiments, the transfer rate between singlet and triplet excited state is much faster (see calculated values below) than the S_1 decay rate. This allows to model the excited states of the system as a common reservoir of singlet and triplet excitons, which are populated according to a Boltzmann distribution. By lowering the temperature from 300 K to 75 K fewer excitons populate the S_1 state in comparison to the T_1 state, which leads to a slower depopulation of the common reservoir of S_1 and T_1 excitons and, therefore, to an effectively increasing delayed fluorescence lifetime. Further, the slight but significant increase of the lifetime from 75 K to 5 K can be explained by a minor zero field energy splitting of the triplet sublevels. A common approach to take this into account is to allow one of the triplet sublevels (T_X) to differ in energy by a positive or negative amount D from the other two triplet states (T_Y and T_Z). By assuming a Boltzmann distributed occupation of the excited singlet and triplet states the temperature dependent lifetime reads

$$\tau(T) = \frac{2 + e^{\frac{D}{k_B T}} + e^{\frac{E_{ST}}{k_B T}}}{\frac{2}{\tau_{T_y,T_z}} + \frac{e^{\frac{D}{k_B T}}}{\tau_{T_x}} + \frac{e^{\frac{E_{ST}}{k_B T}}}{\tau_{S_1}}}. \tag{4.1}$$

In this equation k_B is the Boltzmann constant, E_{ST} denotes the energy splitting between singlet and triplet states and τ_{S_1,T_x,T_y,T_z} the lifetimes of the respective states, which are defined by their inverse decay rate to the ground state. The entire model is illustrated in Figure 4.24.

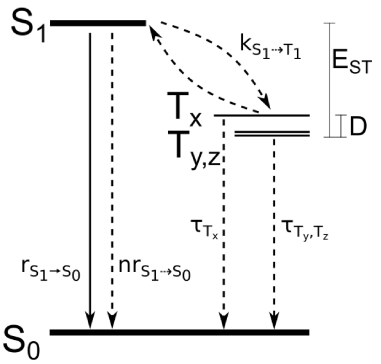

Figure 4.24: Model of the ground and excited states of the CuCbzCaarC molecule.

The fit to determine the free parameter of the model were calculated via maximum likelihood estimation and Markov chain Monte Carlo [98] and the results are listed in Table 4.2:

Table 4.2: Energy spacing and lifetimes of the excited states of CuCbzCaarC.

	most likely	16 % - 84 % percentile
D	3.0 meV	0.72 meV – 6.5 meV
E_{ST}	64.9 meV	63.7 meV - 66.1 meV
τ_{S_1}	9.8 ns	9.1 ns - 10.5 ns
τ_{T_x}	172 µs	135 µs - 234 µs
τ_{T_y,T_z}	260 µs	247 µs - 283 µs

In the definition of the model above, the radiative and the non-radiative transition rates ($r_{S_1 \rightarrow S_0}$, $nr_{S_1 \rightarrow S_0}$) of the S_1-state to the ground state contribute to the value of τ_{S_1}. From the

observed photoluminescence intensity of a single molecule and the detection efficiency of the setup (5 %), we can estimate the contribution of both transitions (see Table 4.3) assuming that the molecule is in one of the excited states for most of the time during the single molecule experiment with continuous laser excitation. Indeed, the width of the antibunching of 6.5 ns indicates that the molecule can be found in one of the excited states with a probability of 98.8 % during continuous wave photoexcitation at a wavelength of 532 nm and an excitation power of 195 µW. By simulation of a single molecule's rate model, with the time constants derived above, one can show that bunching appears in the $g^{(2)}$-function of the emitted light if the singlet-triplet transition rate is slower than $7 \times 10^9\ s^{-1}$. Hence, from the absence of bunching in the experiment, we can conclude that the intersystem crossing rate must be faster.

Table 4.3: Estimation of transition rates for CuCbzCaarC at room temperature.

$r_{S_1 \rightarrow S_0}$	$6 \times 10^7\ s^{-1}$
$nr_{S_1 \rightarrow S_0}$	$4 \times 10^7\ s^{-1}$
$k_{S_1 \rightarrow T_1}$	$> 7 \times 10^9\ s^{-1}$

Additionally, the fluorescence spectra of CuCbzCaarC under continuous wave excitation was recorded and a behavior in accordance to our previous findings was found: When lowering the temperature of the dropcasted CuCbzCaarC, the non-radiative transition rate from S_1 to S_0 slows down, increasing the quantum efficiency of prompt and delayed fluorescence and brightening the overall photoluminescence (see Figure 4.23). Additionally, in this graph one can observe an increased portion of prompt fluorescence at lower temperatures, which is slightly blue-shifted (maximum at 626 nm) in comparison to the delayed fluorescence. The later is red-shifted (maximum at 644 nm) as the triplet to singlet transition can favor energetically lower S_1 states in disordered environments and, therefore, the delayed fluorescence emission is shifted to longer wavelengths.

In summary, the copper(I) complex CuCbzCaarC was analyzed in the solid state as well as on the single molecule level. The incorporation of the two ligands carbazolate and (2,6-diisopropylphenyl)-1,1-diphenyl-isoindol-2-ium-3-ide seems to produce a small singlet-triplet energy gap of only 65 meV. In combination with a fast singlet decay time of τ_{S_1} = 9.8 ns this leads to an efficient thermally activated delayed fluorescence process, which was demonstrated for the first time for the new class of the copper(I) complexes.

4.5 Biradicals in Organic Light Emitting Diodes

As outlined in Chapter 2.2, biradicals have the potential for 100 % internal quantum efficiency. However, they tend to be chemically unstable, which can lead to problems, especially during processing into a light emitting device. This chapter focuses on two different types of biradical compounds which were tested as dopants in OLEDs. An isoindigo based biradical synthesized by Rausch in the group of Prof. Dr. Frank Würthner at the Institute of Organic Chemistry at the University of Würzburg in 2018 [99] and a polychlorinated pyridyldiphenylmethyl radical synthesized by Hattori et al. in the group of Prof. Dr. Christoph Lambert at the Institute of Organic Chemistry at the University of Würzburg in 2019 [100]. These biradical species were synthesized and characterized in the framework of the DFG research training school GRK 2112 on *Molecular biradicals: structure, properties and reactivity*.

Both emitters provide a stable emission on the long wavelength range of the visible spectrum. Also, both emitters exhibit absorption bands which overlap with the emission

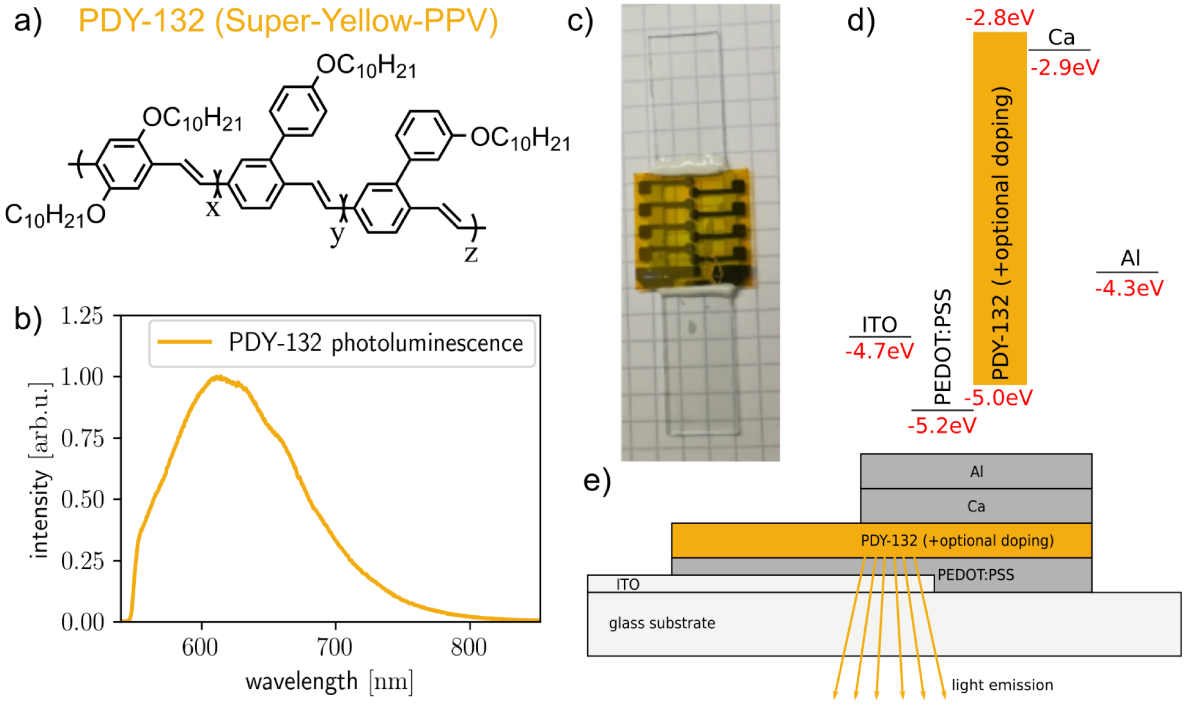

Figure 4.25: PDY-132 based OLEDs. a) Molecular structure of PDY-132. The three different segments x, y and z of the copolymer occur statistically along the polymer chain. b) Photoluminescence spectrum of a spin-coated film at 532 nm excitation. c) Photograph of a PDY-132 reference OLED. d) Energy landscape of the OLEDs raw materials with respect to the vacuum level. e) Layer structure of the OLED.

of the poly(p-phenylene vinylene) copolymer *PDY-132*, whose molecular structure is illustrated in Figure 4.25a. This renders PDY-132 a suited matrix for the excitation of these molecules that emit further in the red. PDY-132 is commercially available from the company *Sigma Aldrich* under the trade mark *Super Yellow*. The HOMO(LUMO) level is located at 5.2 eV(2.9 eV) below the vacuum level [101] and the polymer exhibits a hole mobility of $0.5 \times 10^{-6}\,\mathrm{cm}^2/\mathrm{Vs}$ while the mobility of electrons is mainly hindered by trap states [102]. Holes can be efficiently injected from an ITO/PEDOT:PSS anode [103] into PDY-132 for an electrical excitation of guest molecules within an OLED stack [55]. PDY-132 based OLEDs were produced as reference without doping and with different concentrations of doping (ITO/PEDOT:PSS/PDY-132:biradicals/Ca/Al). The photoluminescence of PDY-132 and the OLED architecture are illustrated in Figure 4.25. In addition to the electroluminescence measurements, the photoluminescence of these samples was analyzed at lateral positions without ITO or metal contacts.

4.5.1 Isoindigo Based Biradicals

6,6'-bis(3,5-di-tert-butyl-4-phenoxyl)-1,1'-bis(2-ethylhexyl)-[3,3'-biindolinylidene]-2,2'--dione, depicted in Figure 4.26, is a biradical based on the dye isoindigo and is abbreviated by IIn$^{\bullet\bullet}$, where the two dots indicate the two unpaired electrons of the compound. These unpaired electrons are located at the oxygen atom of the 2,6-di-tert-butyl-phenoxyl substituents. Several measures protect these sensitive sites against chemical reactions, in particular, photo-induced reduction: First of all, the two tert-butyl moieties on both sites of the oxygen atom kinetically block chemical reactions. Secondly, the electron-withdrawing core of isoindigo shifts the electron density back into the center of the chromophore. Lastly, the four aromatic rings stabilize the biradical character of the molecule in comparison to the closed shell resonance structure with double bonds at the oxygen atoms but non-aromatic rings. The value of the biradical parameter is $y = 0.79$ where 0 corresponds to a closed-shell and 1 to a completely open-shell configuration, i.e. neat radical molecule.

Photo- and electroluminescence of In$^{\bullet\bullet}$ doped DPY-132 OLEDs were measured and the resulting spectra are presented in Figure 4.26. The photoluminescence of the DPY-132 matrix is almost entirely quenched upon 5 wt% doping with In$^{\bullet\bullet}$. The remaining photoluminescence spectrum is particularly suppressed in the spectral range between 600 nm and 700 nm, where the strong absorption band of In$^{\bullet\bullet}$ is located. Simultaneously a weak emission can be detected at 770 nm, which coincides with the photoluminescence of the neat In$^{\bullet\bullet}$ material in solution or matrices like para-terphenyl or PMMA. This indicates an efficient Förster resonance energy transfer from the matrix to the guest material but,

in addition, also a small quantum efficiency of the $In^{\bullet\bullet}$ emission in DPY-132. Looking at the electroluminescence at 1 wt% doping, the emission from the DPY-132 matrix is distinctly quenched, again especially between 600 nm and 700 nm, but a shoulder in the emission spectrum can be observed at 770 nm which can be ascribed to the $In^{\bullet\bullet}$ electroluminescence.

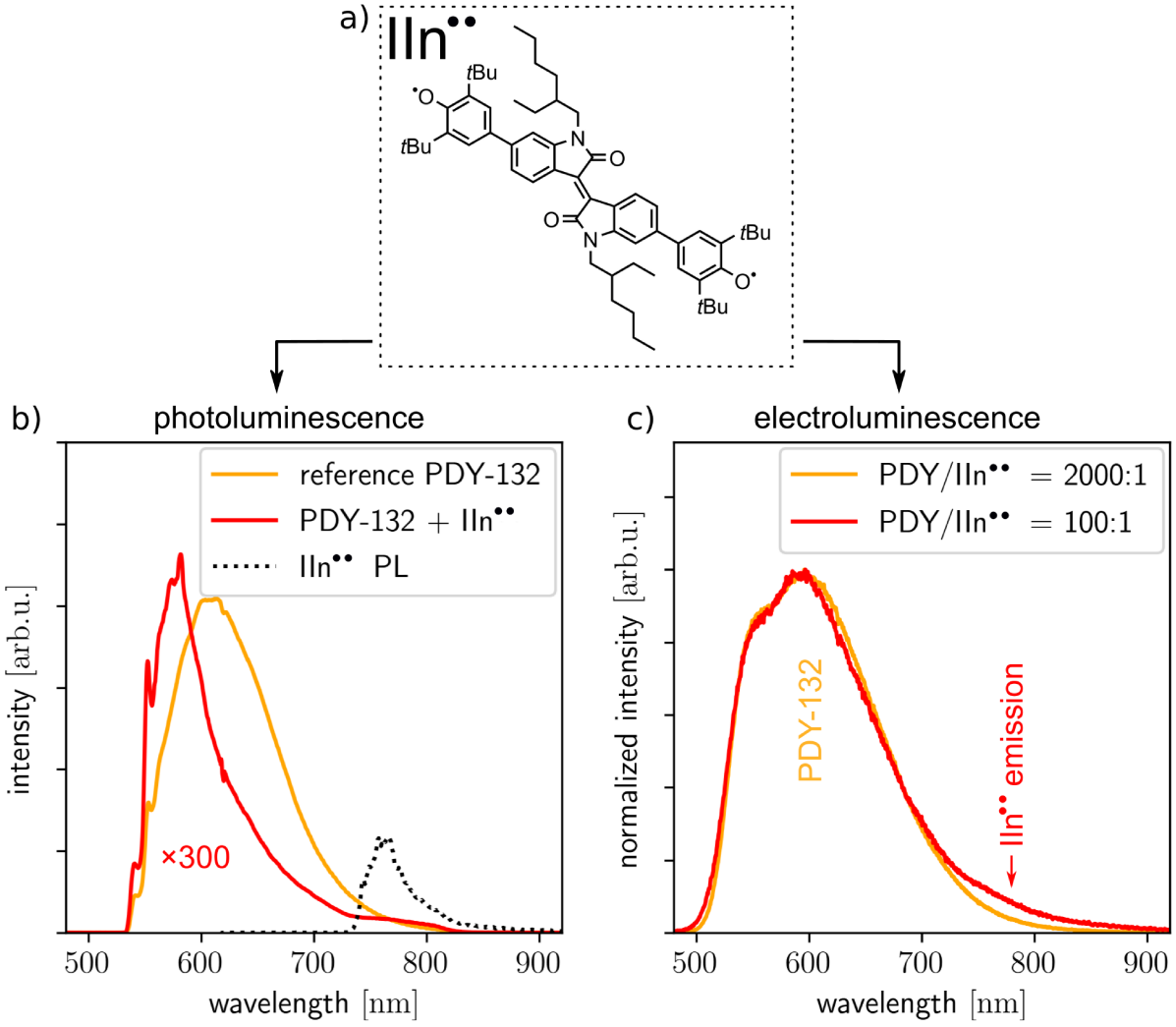

Figure 4.26: a) Chemical structure of 6,6'-bis(3,5-di-tert-butyl-4-oxidaneyl-phenyl-1,1'-bis(2-ethylhexyl)-[3,3'-biindolinylidene]-2,2'-dione) ($IIn^{\bullet\bullet}$). b) Photoluminescence at 532 nm excitation. The emission from $In^{\bullet\bullet}$ doped PDY-132 (5 wt%) is enhanced by a factor 300 for better visibility. c) Normalized electroluminescence of two OLEDs with different doping concentration. With increasing doping a stronger quenching of the PDY-132 matrix and a stronger emission from $In^{\bullet\bullet}$ can be observed.

Despite the small efficiency the overall performance of In$^{\bullet\bullet}$ is week, the operation of the molecules in the devices shows two important things. Firstly, it demonstrates that biradicals, which are usually known to be quite unstable, can be designed stable enough for continuous operation in OLEDs. Secondly, the observation of the biradical electroluminescence enables further measurements in the future like optically detected electron spin resonance [104], which can provide information about the electronic states of the emitter during OLED operation.

4.5.2 Diphenylmethylpyridine Based Biradicals

4-(5-(bis(2,4,6-trichlorophenyl)methyl)-4,6-dichloropyridin-2-yl)-N-(4-(5-(bis(2,4,6-trichlorophenyl)methyl)-4,6-dichloropyridin-2-yl)phenyl)-N-(4-methoxyphenyl) aniline, abbreviated by TPA(OMe)(PyBTM")$_2$ and depicted in Figure 4.27a, is a biradical belonging to the class of polychlorinated pyridyldiphenylmethyl radicals. The biradical was synthesized by bridging two of these radicals by triphenylamine, which comprises an electron donating methoxy group. This moiety can be used to shift the fluorescence intensity maximum of the biradical from 730 nm close to 800 nm, i.e. to the near infrared spectral range. The biradical is chemically stable in solution under ambient conditions because bulky chlorinated diphenylmethyl groups protect both unpaired electrons. Like In$^{\bullet\bullet}$, TPA(OMe)(PyBTM")$_2$ also turned out to be stable enough to be used as an emitter in OLEDs. In the photoluminescence experiment (Figure 4.27b) the almost complete loss of the matrix emission was observed, while between 750 nm and 1000 nm the emission of TPA(OMe)(PyBTM")$_2$ emerges. The efficiency of Förster resonance energy transfer is therefore close to 100 % even at doping concentrations of only 5 wt%. During electrical operation (Figure 4.27c) at a doping concentration of 20 wt%, almost exclusive emission from the biradicals was detected. In comparison to the photoluminescence spectrum, a slight redshift was observed in the electroluminescence which originates predominantly from the biradicals with the energetically lowest states in the disordered matrix material.

If the operating voltage is increased up to 20 V, the total electroluminescence increases steadily, but the fraction of the biradical emission is saturated in places of high current density. There the emission of the matrix material dominates. Figure 4.28a shows the current density-voltage characteristics of this OLED test device. It can be regarded as a near infrared emitter whose emission is invisible to the human eye. However, the camera that recorded the photograph in Figure 4.28b is sensitive even to wavelengths beyond 800 nm, which makes it possible to take a photograph of the OLED during operation. The yellow emission of the matrix material is located in the center of the electrically pumped area while it is still completely quenched in the outer part of the matrix.

In summary, under electrical operation this OLED utilizes the Förster resonance energy transfer mechanism to populate the excitons of the biradicals. Beyond that, one would expect an advantageous spin statistic even when the biradicals directly capture free charge carriers [105] in comparison to closed shell molecules, which in this case would form dark triplet states.

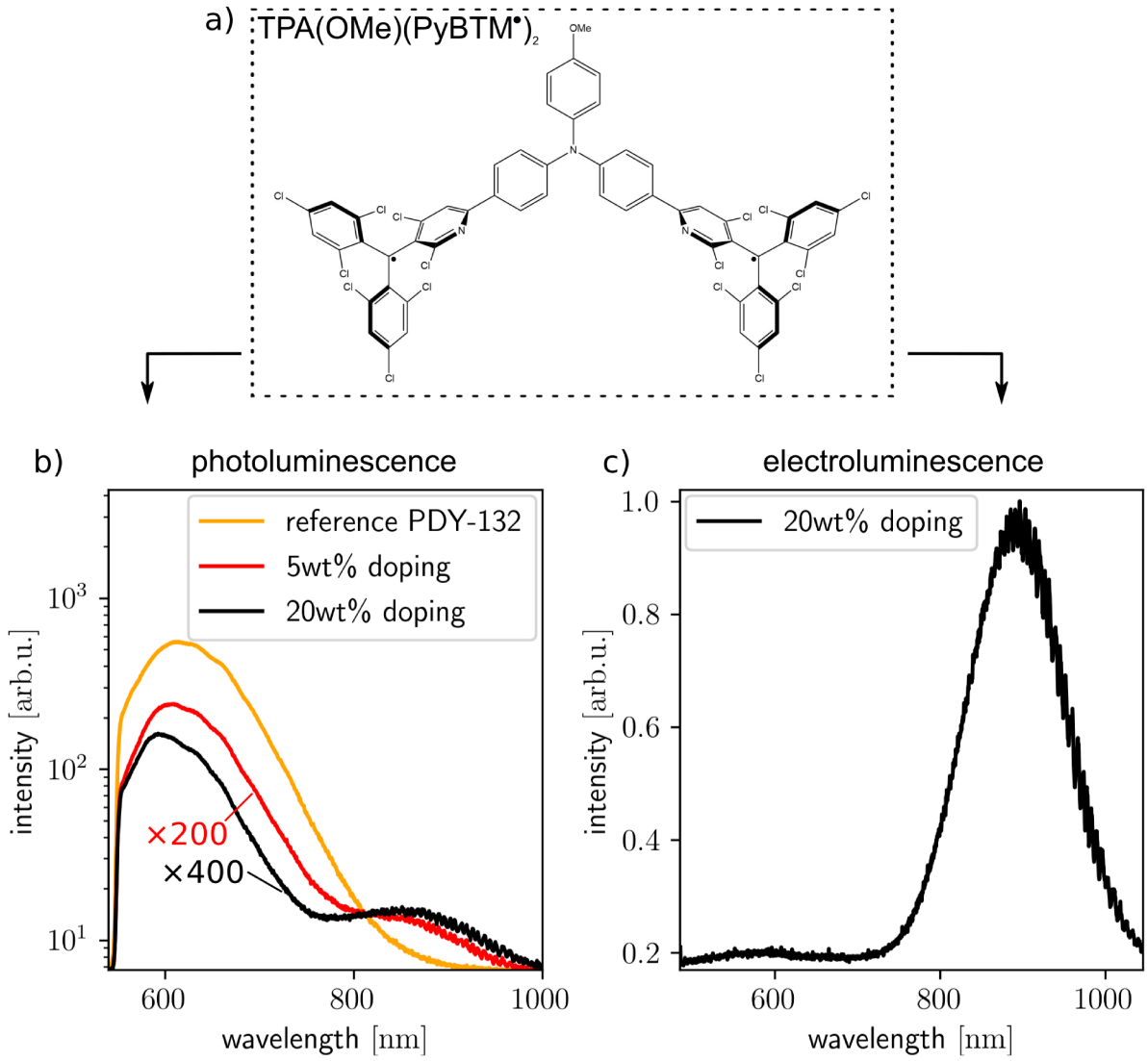

Figure 4.27: a) Chemical structure of the 4-(5-(bis(2,4,6-trichlorophenyl)methyl)-4,6-dichloropyridin-2-yl)-N-(4-(5-(bis(2,4,6-trichlorophenyl)methyl)-4,6-dichloropyridin-2-yl)phenyl)-N-(4-methoxyphenyl)aniline biradical TPA(OMe)(PyBTM")$_2$. b) Photoluminescence at 532 nm excitation of DPY-132 layers with different doping concentrations. Already at 5 wt% doping, the photoluminescence of the matrix is nearly completely quenched. The red/black emission spectrum is increased by a factor of 200/400, respectively, for better visibility. In doped samples a photoluminescence at 880 nm can be observed, which can be assigned to the biradical emission. c) Under electrical operation at 14 V and 10^{-2} A/cm^2 almost complete emission from the biradical, with a maximum at 890 nm, is observed.

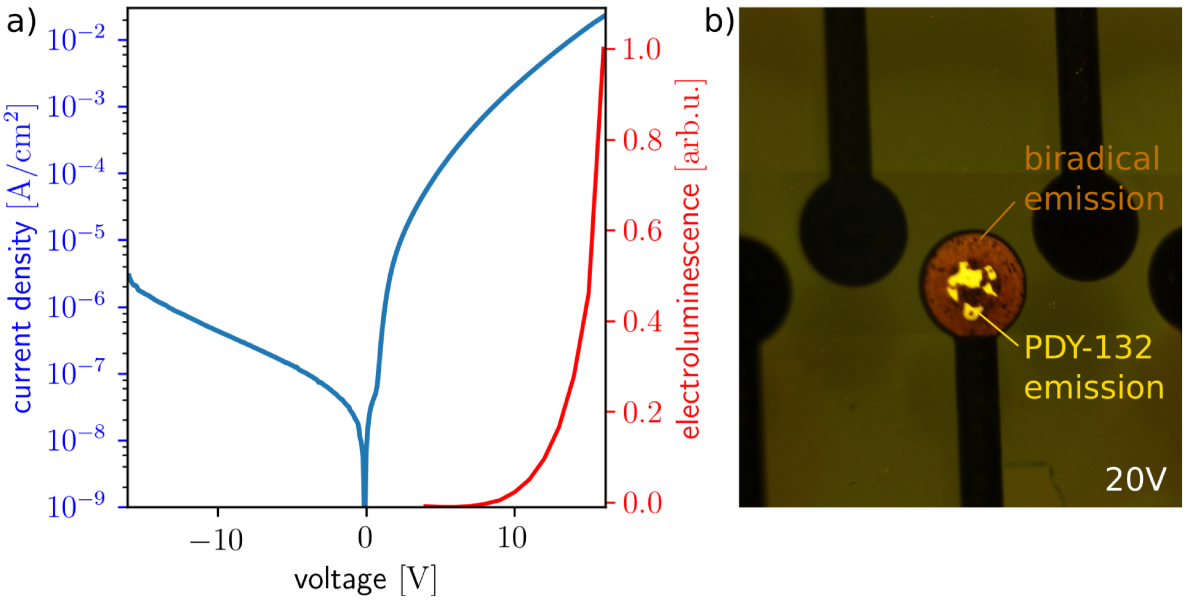

Figure 4.28: TPA(OMe)(PyBTM")$_2$ based OLEDs. a) Current density-voltage characteristics and normalized electroluminescence of the TPA(OMe)(PyBTM")$_2$ based OLED. b) Photograph of the OLED at 20 V driving voltage. In addition to the emission of the dopant in the outer part of the contact pad, the emission of the matrix in yellow is observed in the middle region where the current density is strongest.

4.6 Multichromophores

In Chapter 4.2 we have seen how sensitive the photophysics of a single chromophore is to its local environment. The idea behind designing multichromophoric systems is to tailor the interaction between adjacent chromophores while conserving the optical properties of the individual chromophores. Ideally, this interaction with other chromophores improves the photophysics of the individual emitter as it is the case for the two multichromophoric systems analyzed in this work. In the first system, 2,2'-ditetracene, the interaction between the two tetracene chromophores is quite strong as they are separated only by a single C-C covalent bond. The following chapter analyzes whether the properties of the tetracene chromophores are altered and whether the photophysics of the entire system is improved. The second system consists of para-xylylene bridged perylene bisimide chromophores. The interaction between these chromophores is much weaker, so that excitons presumably can hop from one chromophore to another. Chapter 4.6.2 demonstrates how this interaction makes this multichromophoric system an exceptionally potent single photon emitter.

4.6.1 2,2'-Ditetracene

Parts of the results of the following chapter have been published in [106]. Tetracene is a well-studied polycyclic aromatic hydrocarbon consisting of four linearly annulated benzene rings, shown in Figure 4.29a. Its electronic transition between the S_0 and the S_1 state exhibits a strong dipole moment parallel to the short axis of the molecular plane [107], which makes it possible for a 100 nm thick layer of crystalline tetracene to absorb over 95 % of the incident light at 520 nm wavelength [108]. In principle, this makes tetracene a promising candidate for OLED applications. While various acene derivatives like anthracene [109], tetracene [110] and pentacene derivatives [111] were implemented successfully in OLEDs, the application of neat tetracene is, however, challenging [112] due to its high Diels-Alder reactivity [110].

In its crystalline form, the tetracene molecules are protected to a certain degree from chemical reactions but here the process of thermally activated singlet fission, i.e. the non-radiative decay of an excited singlet exciton into two triplet excitons, quenches singlet excitons with almost 100 % efficiency at room temperature [113, 114]. Studies of time resolved absorption and emission found the singlet exciton lifetime to be in the range of 40 ps to 80 ps [115, 116], which renders the material unsuitable for the use in OLED applications. Further, the photophysical properties of crystalline tetracene are affected by

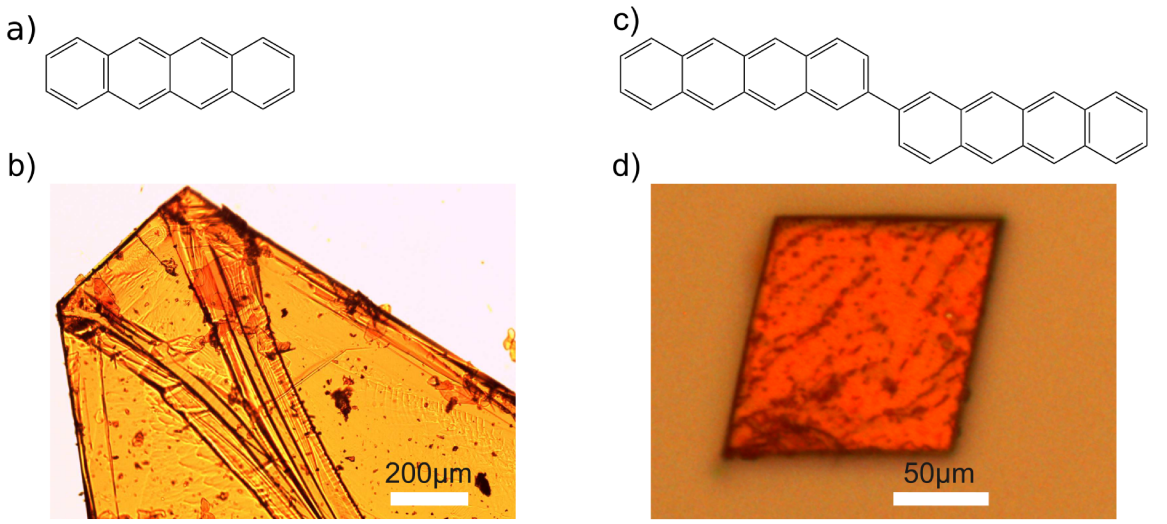

Figure 4.29: Comparison between tetracene and 2-2'-ditetracene a) Chemical structure of tetracene. b) Photograph of a tetracene single crystal. c) Chemical structure of 2-2'-ditetracene. d) Photograph of a 2-2'-ditetracene single crystal.

a pressure and temperature dependent structural phase transition, which is influenced by subtle differences in sample history and preparation [117] such as substrate temperature during growth and crystal size [118].

In the past, one approach to maintain the beneficial optial properties of tetracene while simultaneously improving its quantum efficiency and chemical stability was the synthesis of tetracene dimers that are connected at their 5-position [119, 120]. In this work, a similar approach was tested with 2,2'-ditetracene, which consists of two covalently linked tetracene chromophores depicted in Figure 4.29c. 2,2'-ditetracene was first synthesized by the group of Michael Roth at the Technische Universität Darmstadt and implemented in organic thin film transistors [28]. Later, an improved synthesis route was established by Lena Ross in the group of Prof. Dr. Anke Krüger at the Institute of Organic Chemistry at the University of Würzburg [106]. This provided the neat material for the comparative studies of 2,2'-ditetracene as single guest molecules and bulk crystals to the corresponding properties of tetracene, with the pristine tetracene being purchased from Sigma Aldrich.

This chapter compares the properties of 2,2'-ditetracene (DTc) and tetracene (Tc) to demonstrate the effects in the photophysics for DTc by its interlinked chromophores and to identify the origins of these modifications. We initiate this section by having a look on the photophysics of these two chromophores at the single molecule level.

In collaboration with Marcel Krumrein who carried-out his bachelor thesis in our group anthracene crystals were grown in a vertical gradient sublimation oven (according to the

setup of Lipsett [121]). By co-evaporation, anthracene was doped with the two materials, Tc and DTc, respectively.

Anthracene is a small linear conjugated hydrocarbon based on three aromatic rings whose molecular structure is depicted in Figure 4.30. It is a suitable material to prepare both, amorphous [122] or crystalline host matrices allowing for doping by various guest molecules such as terrylene [123], dibenzoterrylene [124] or tetracene [125]. In principle, anthracene can be electrically pumped [125] but in this work it is used for photoluminescence experiments with tetracene or 2,2'-ditetracene as dopant. These molecules are incorporated into the crystal lattice of anthracene, whose crystal structure is monoclinic and corresponds to a $P2_1$ space group symmetry with two anthracene molecules per unit cell.

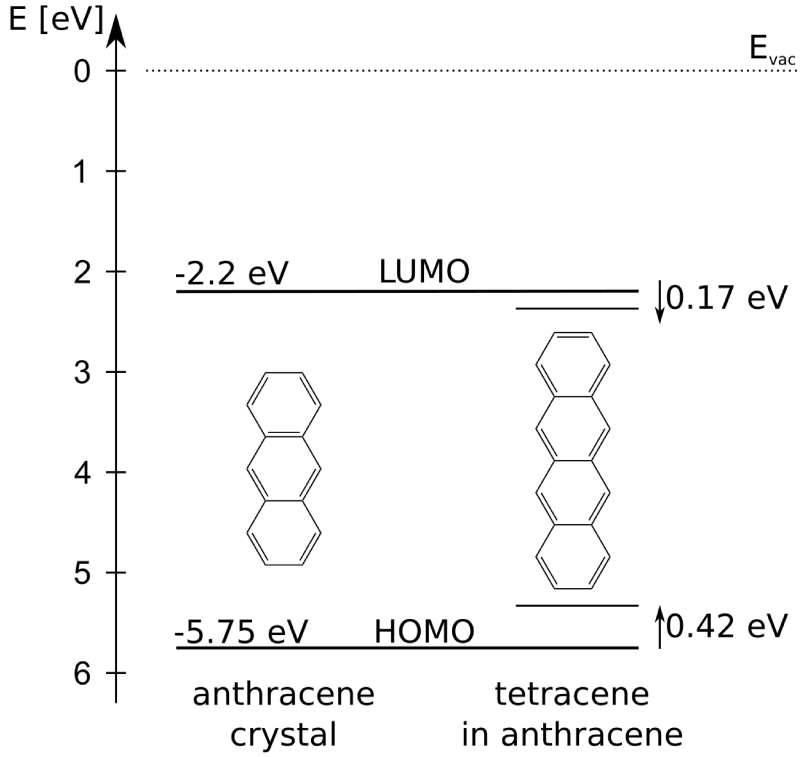

Figure 4.30: Energy levels of crystalline anthracene and tetracene single molecules embedded in a crystalline anthracene host [126, 127].

The HOMO/LUMO energy levels of crystalline anthracene together with the HOMO/LUMO energy levels of tetracene single molecules embedded in a crystalline anthracene host are illustrated in Figure 4.30. Due to its large band gap of 3.5 eV, anthracene is transparent at 532 nm laser excitation used for the optical studies on tetracene and its derivatives. As the energy levels of tetracene are located completely within the band gap

of anthracene [127], the later provides an ideal matrix for photoluminescence experiments on the two dopant materials of interest.

Representative crystals obtained by the vertical vapor phase growth process are shown in Figure 4.31. Due to its high sublimation temperature, the concentration of DTc in the crystals shown in Figure 4.31c is already sufficiently small to obtain dispersed DTc molecules without agglomerations and allows for the detection of independent DTc molecules. Although the doping concentration was much higher in the Tc doped samples (Figure 4.31b), it was still possible to find small crystals that contain Tc without agglomerations.

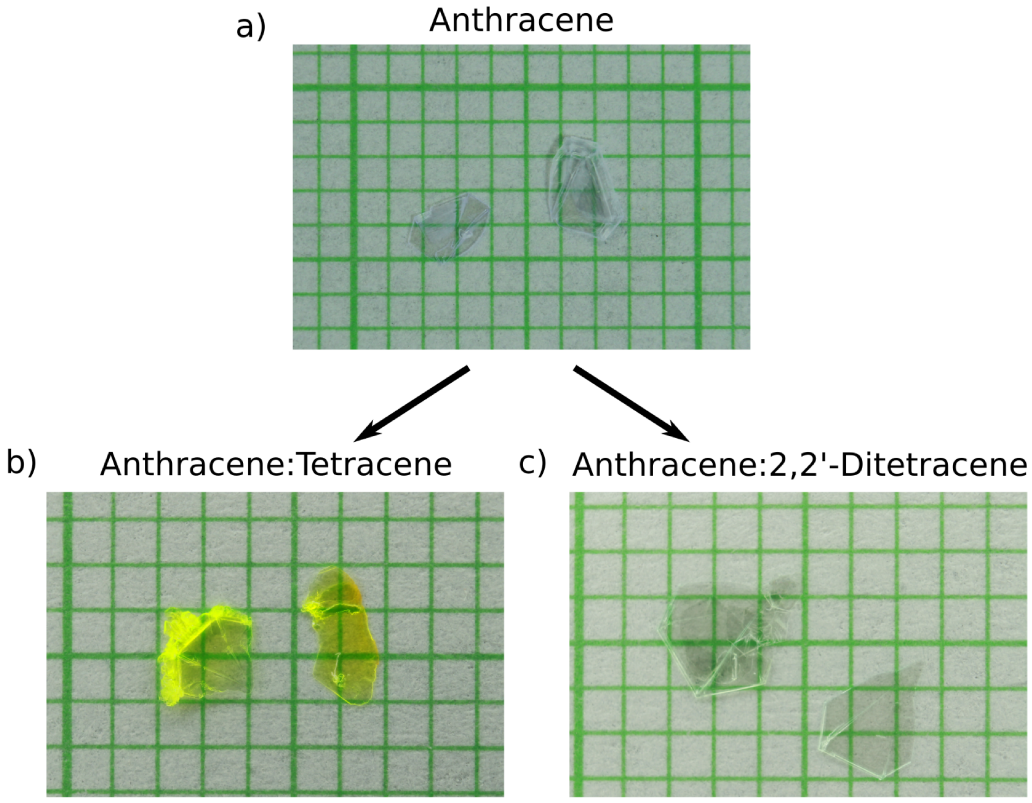

Figure 4.31: Doped anthracene crystals. a) Neat transparent antracene crystal serving as matrix. b) Tetracene doped anthracene crystals with high doping concentrations. c) 2,2'-ditetracene doped anthracene crystals.

By means of the confocal microscopy setup the two types of crystals were analyzed. In Figure 4.32a the normalized photoluminescence spectrum is plotted for the two species upon photoexcitation with a 405 nm continuous wave laser. The emission of both compounds exhibits a series of peaks with a typical linewidth of about 75 meV and a spacing of 170 meV. This small line broadening indicates that both compounds emit in a highly ordered environment and that the anthracene crystal structure is only slightly

disturbed by the incorporated doping materials that may occupy several of the anthracene lattice sites. Differences in the nuclear relaxation potential result in different Franck-Condon factors for both materials. Nevertheless, the peak positions of both materials coincide nearly perfectly, which indicates that the optical properties of the tetracene chromophores in DTc molecule is preserved.

Prof. Dr. Bernd Engels and his Ph.D student Marian Deutsch performed complementary computations for energy levels of DTc and Tc based on vibrationally resolved time-dependent density-functional theory in the gas phase. In case of the emission spectra, the analysis of HOMO/LUMO energy levels and the vibronic modes revealed nearly identical emission spectra for DTc and Tc and that differences in the Franck-Condon factors are not inherent to the molecular species but must result from the influence of the anthracene matrix. This expands the perspective of earlier results by Roth and coworkers [28] who interpreted the redshift in DTc thin films as the effect of an enlarged π-system in the DTc molecule.

All peaks, which are present in the Tc emission spectrum, can be ascribed to different vibronic components of its $S_1 \rightarrow S_0$ transition. Therefore, all of TC's emission peaks, see 4.32a), should exhibit the same fluorescence decay time constant. The same is true for DTc, however, a different fluorescence decay time constant is expected. This is confirmed by a monoexponential fluorescence decay after pulsed photoexcitation of both materials. In Figure 4.32a a decay constant of 14 ns (5 ns) was found for the emission of Tc (DTc). The reason for the decrease in lifetime of excitons in DTc lies in the enhanced density of vibrational modes due to the much larger degrees of motional freedom of the molecule, which promotes radiative and non-radiative decay channels.

The interpretation of these findings was supported by the theoretical calculation that showed that the vibronic modes of DTc are superpositions of the vibrational modes in Tc [106]. Correspondingly, the HOMO and LUMO of DTc are linear combinations of the molecular orbitals in Tc. This demonstrates how the optical properties of the two tetracene chromophores are preserved by the covalent linking in DTc despite the molecular orbitals being delocalized over the entire molecule.

Additionally, single molecule experiments were conducted, which support this finding. For these experiments, single molecule samples were prepared with DTc embedded in a layer of PMMA in a concentration of 10^{-10} wt% using acetonitrile as a solvent. The inset of Figure 4.33 shows the intensity scan of this sample. Here, individual spots represent single DTc molecules. By analyzing the photon statistic of these spots at continuous laser excitation, a distinct antibunching can be observed. Without correcting for background signals the $g^{(2)}$ value at zero time delay is below 0.5 for most of the spots and the photon

statistics is well modeled by a two level system at weak laser excitation indicated by the fit function in Figure 4.33. If DTc would consist of two completely independent and identical chromophores, one would expect antibunching with $g^{(2)}(t = 0) \geq 0.5$. Therefore, we can conclude that on a single molecule level DTc consists of two chromophores but emits only one photon at a time, indicating two strongly coupled chromophores.

The width of the antibunching in Figure 4.33 is 6 ns. Considering the weak laser excitation of 10 µW, which is about two orders of magnitude below the saturation intensity of the molecule, this result is in line with the 5 ns we found for the lifetime measurements on the DTc ensemble in anthracene.

In molecules like pentacene dimers [128] and other oligoacene heterodimers [129] singlet fission on molecules in solution was observed while for other types of tetracene dimers [119] no singlet fission was observed. For 2,2'-ditetracene, the observed antibunching in combination with the absence of photon bunching and the overall brightness of the single molecules indicates that singlet fission does not take place on a single DTc molecule.

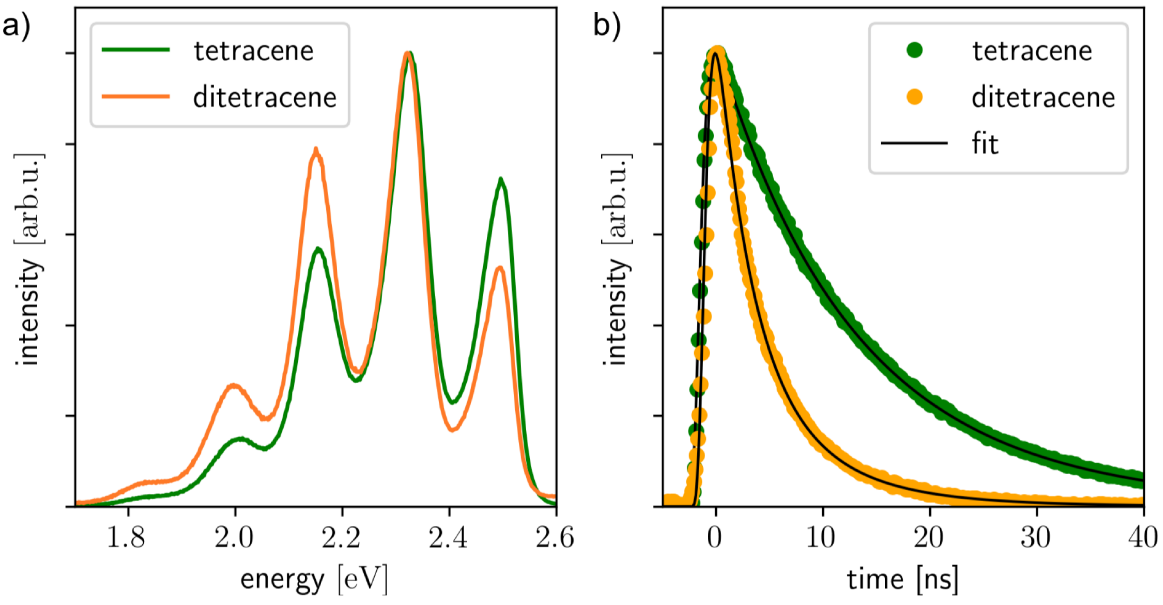

Figure 4.32: Photoluminescence of tetracene and 2,2'-ditetracene on a single molecule level. a) Fluorescence spectra of tetracene and 2,2'-ditetracene as dopants in anthracene matrices upon photoexcitation with a 405 nm laser. b) Fluorescence decay after pulsed laser excitation of both materials, exhibiting a lifetime of 14 ns for tetracene and 5 ns for 2,2'-ditetracene.

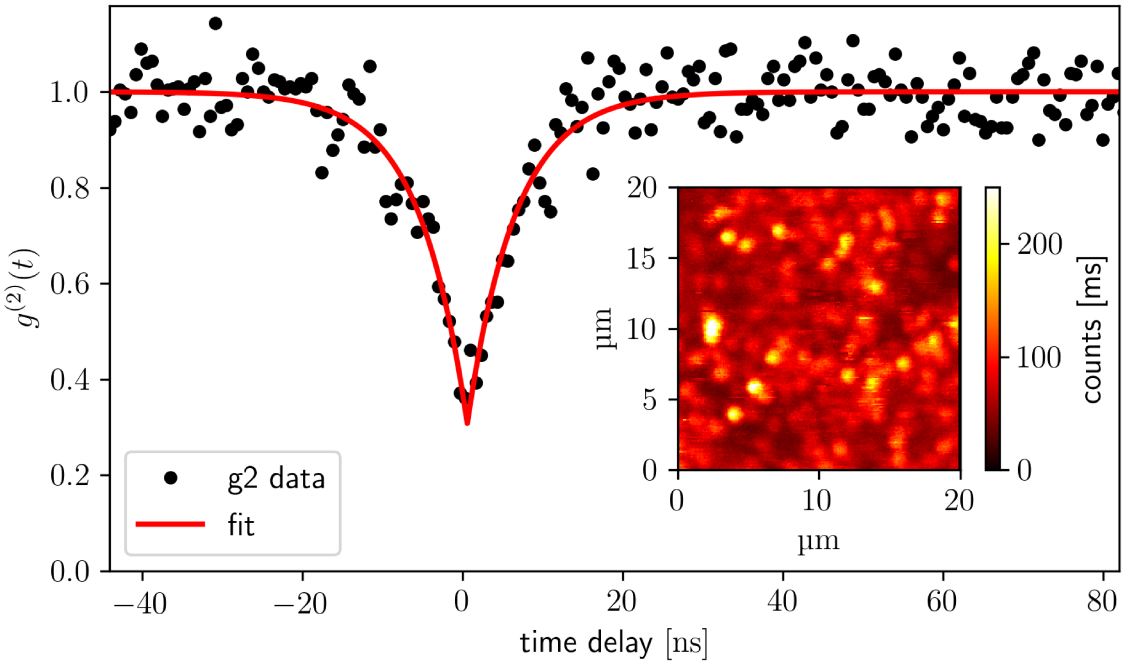

Figure 4.33: $g^{(2)}$-function of the photon statistic of 2,2'-ditetracene. Inset: Photoluminescence-scan of a sample of 2,2'-ditetracene doped PMMA at a concentration of 10^{-10} wt% at photoexcitation of 40 mW at 532 µm.

After having studied the behavior of single DTc molecules, we will shed light on the photophysical bahavior of aggregated Tc and DTc. Purification and growth of 2,2'-ditetracene single crystals were conducted in collaboration with Sebastian Hammer of our group. Both processes utilized a gradient sublimation oven in which the raw material was placed at one side of a heated glass tube. The material sublimates at 420 °C and from its starting position is carried by a steam of inert nitrogen (N6) gas to the colder end of the glass tube. In case of purification the material condenses along a gentle temperature gradient of about 2.5 $\mathrm{K\,cm^{-1}}$ in which unwanted residual chemical species are spatially separated from the pure material. Details of this process are described elsewhere [130]. For the growth of single 2,2'-ditetracene crystals, the same process was applied, however, with a steeper temperature gradient of 4 $\mathrm{K\,cm^{-1}}$ to achieve crystal growth in a defined region of the glass tube where plate-like crystals with linear dimensions of up to 2 mm could be obtained.

Subsequently, the single-crystal structure of 2,2'-ditetracene was determined by Alexandra Friedrich in the group of Prof. Dr. Todd Marder at the Institute for Sustainable Chemistry & Catalysis with Boron at the University of Würzburg with a BRUKER D8 QUEST 4-circle diffractometer. This diffractometer utilizes $\mathrm{Mo_{K\alpha}}$ radiation of 0.710 73 Å and a CMOS area detector. For the measurements, the crystal was cooled to 77 K. Methods of

image processing and structure solving are described in the Supporting Information of the respective publication [106]. The complete structural data on the 2,2'-ditetracene crystal structure is published as supplementary publication no. CCDC-1885507 at the *Cambridge Crystallographic Data Centre*.

The crystal structure of DTc (monoclinic space group $P2_1/n$, a = 5.9583 Å, b = 7.4184 Å, c = 48.227 Å, β = 91.057°) was determined and is shown in Figure 4.34 together with the molecular structure and a picture of a single crystal. In comparison to the structure of Tc (triclinic space group $P\bar{1}$, a = 6.0565 Å, b = 7.8376 Å, c = 13.0104 Å, α = 77.127°, β = 72.118°, γ = 85.792°)[131], which is shown in Figure 4.35, DTc consist of a similar herringbone arrangement of molecules in the (ab)-plane. Along the c-direction, the unit cell comprises two layers of DTc molecules resulting in a total of four molecules per unit cell instead of two for Tc. Roth and coworkers [28] also determined the lattice constant of DTc thin films by X-ray diffraction in the [001]-direction. They found a lattice constant of 24.24 Å, which corresponds to about half of the lattice constant observed for our single crystals. The reason for this is either that a Roth et al. measured a different phase due to the interaction with the substrate or that the diffraction peak with the smallest angle was misinterpreted as the [001]-peak, while in fact the [001]-peak is forbidden for our crystals and the [002]-peak corresponds to the peak with the smallest diffraction angle.

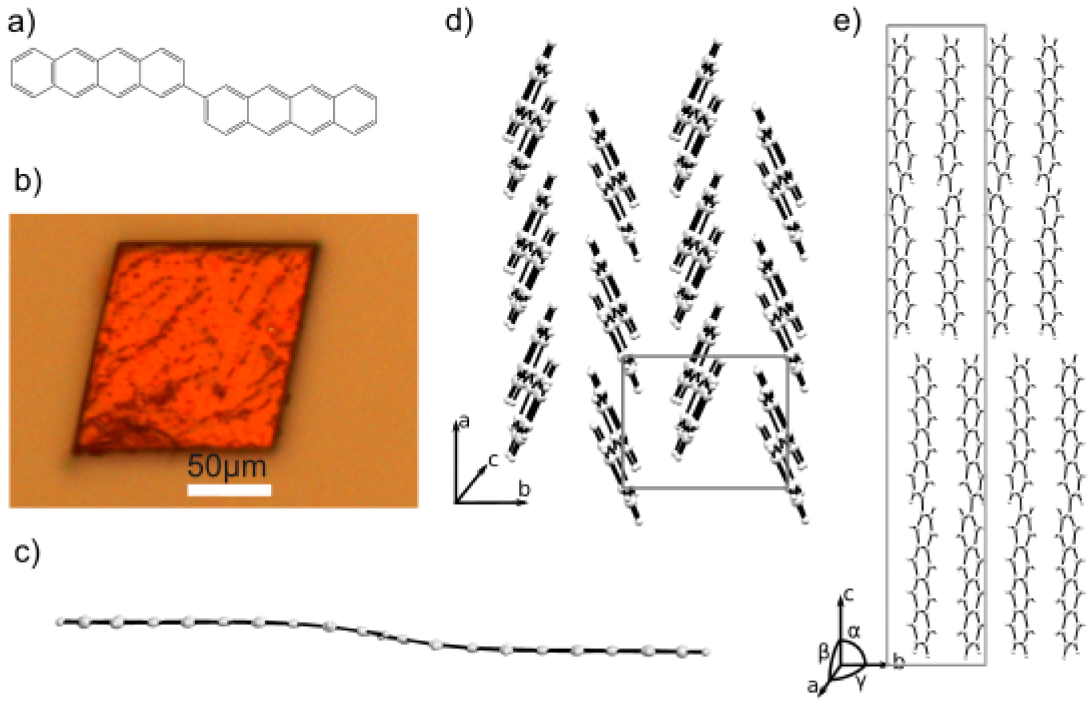

Figure 4.34: a) Chemical structure and crystal structure of 2,2'-ditetracene. b) Image of a 2,2'-ditetracene crystal. c) Bended shape of a single 2,2'-ditetracene molecule within the crystal structure. d) View on the crystal structure along the longest molecular axis. e) Crystal structure of 2,2'-ditetracene in the (bc)-plane.

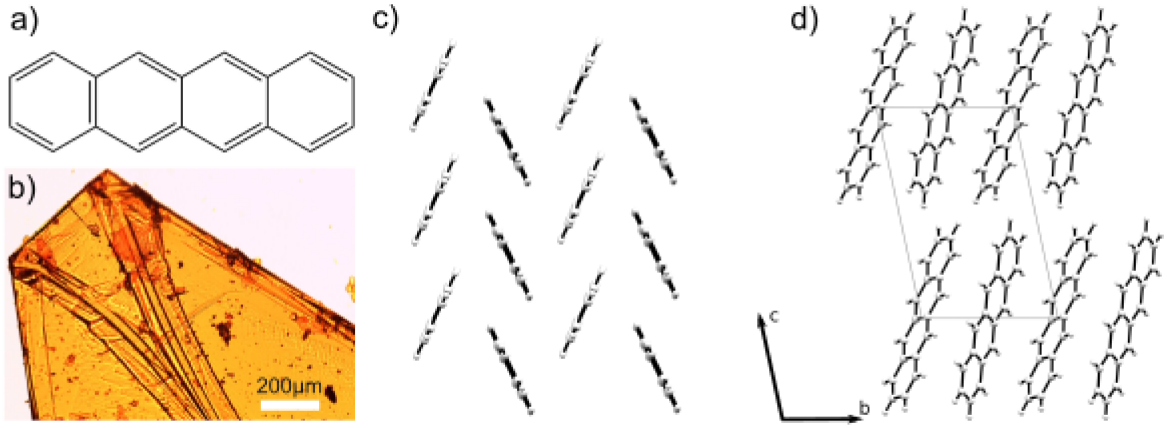

Figure 4.35: a) Chemical structure and crystal structure of tetracene. b) Image of a tetracene crystal. c) View on the crystal structure along the longest molecular axis. d) Crystal structure according to Holmes et al. [131] along the a-viewing direction.

DTc as well as Tc exhibit an excellent photo stability in the crystalline phase. As shown in Figure 4.36b, after one hour of continuous excitation with 10 µW at 532 nm no indication of a decline in emission intensity could be observed. Figure 4.36a shows the angular emission profile, i.e. the total emission intensity in dependence of the emission angle with respect to the surface of the DTc crystal measured with the setup described in Chapter 3. Most of the emission light is emitted at an angle of 66°, which is typical for emitting dipoles located at a dielectric interface [45]. As the refractive index of the crystal depends on the frequency of the emitted light one would expect different wavelengths to be preferably emitted in slightly different directions. Additionally, different orientations of the material's transition dipoles may emit light in different direction. Indeed, identical emission peaks with a different relative intensity could be observed when measuring the photoluminescence spectrum in the µ-PL setup, which collects the emission from a smaller part of the solid angle (see dark gray region in Figure 4.36a.

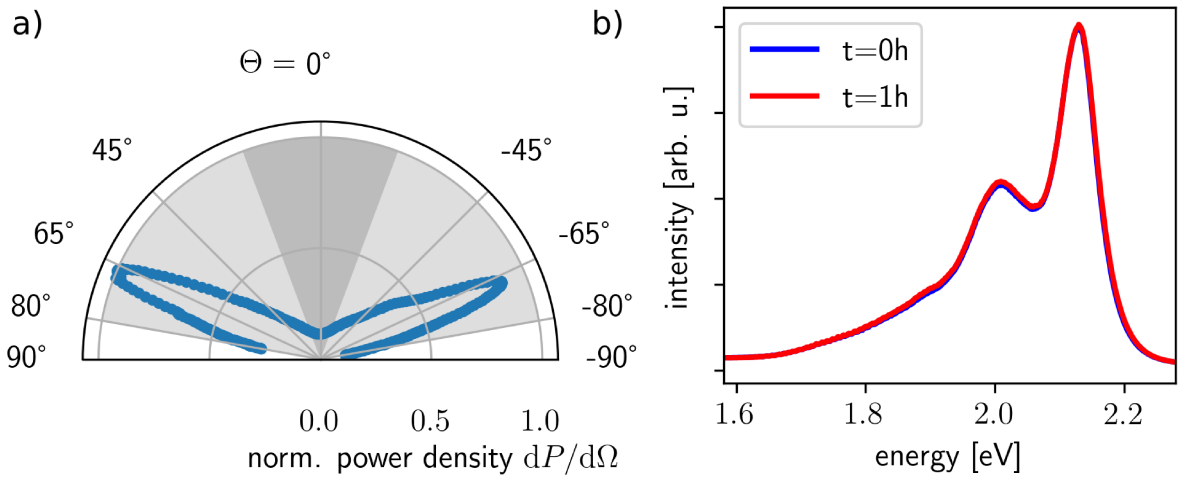

Figure 4.36: Emission characteristics of 2,2'-ditetracene. a) Total emission intensity of 2,2'-ditetracene per solid angle in dependence of the emission direction. Most intensity is emitted at an angle of 66° to the crystal surface normal. The light/dark gray area indicates the collection angle of the confocal/µ-PL microscopy setup. b) Photoluminescence of 2,2'-ditetracene before and after continuous laser excitation at 532 nm and 10 µW for about one hour.

Next, we will have a detailed look at the absorption and emission spectra of Tc and DTc crystals. 2,2'-ditetracene is hardly soluble in various solvents which hinders the measurement of spectral absorption in solution. But it is possible to measure the spectral absorption of crystalline 2,2'-ditetracene. For this, it is necessary to prepare crystals with thicknesses that are small enough to transmit a sufficient fraction of incident light in the relevant spectral region so that it can be detected above the noise level of the setup. A 2,2'-

ditetracene crystal of sufficient lateral dimentions was therefore exfoliated by a transparent adhesive tape, a method established for the exfoliation of 2D materials like graphene [132]. However, there are no covalent bonds between the molecules in the (ab)-plane of the crystal, which could ensure a sufficient stabilization of the extended sheets like for other 2D materials. Therefore, it is important to exfoliate the 2,2'-ditetracene with a minimum of lateral stress. The largest fragments of the exfoliated crystal, like those at the bottom part of Figure 4.37 which have a size of about 10 µm × 10 µm, were used for absorption measurements.

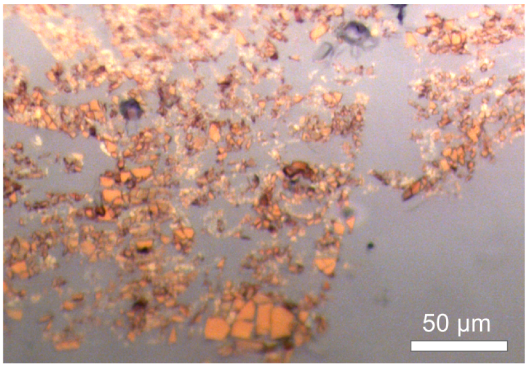

Figure 4.37: Microscope image of exfoliated crystalline 2,2'-ditetracene fragments.

These measurements were conducted with a UV/Vis Spectrometer (Jasco V-650) under ambient conditions. To determine the absorption spectrum of 2,2'-ditetracene, transmission (T) and reflection (R) were measured and the absorption (A) was calculated according to the formula $A = 1 - T - R$ in a wavelength range between 300 nm and 900 nm. Complementary, emission spectra were recorded at the confocal microscopy setup, which is able to collect emission from the crystal within a wide angle (±80°, see Figure 4.36a).

The respective absorption and emission spectra are shown in Figure 4.38. The two spectra resemble one another but are spectrally shifted with respect to each other. In comparison to the single molecule emission, the emission of Tc single crystals is shifted by 200 meV while the emission of DTc bulk crystals is shifted by 350 meV. This difference is an indication of a different coupling strength of the dipoles within the unit cells of Tc and DTc. Furthermore, a Stokes shift, i.e the energy difference between the lowest-lying absorption peak and the highest-lying emission peak, of 29 meV (234 cm^{-1}) is determined for DTc crystals. This is slightly larger than the Stokes shift of 25 meV (202 cm^{-1}) determined for crystalline Tc and indicates a slightly higher reorganization energy for the individual chromophores in crystalline DTc. Additionally, both emission spectra were analyzed in dependence of the polarization to disclose effects of a Davydov splitting on the observed

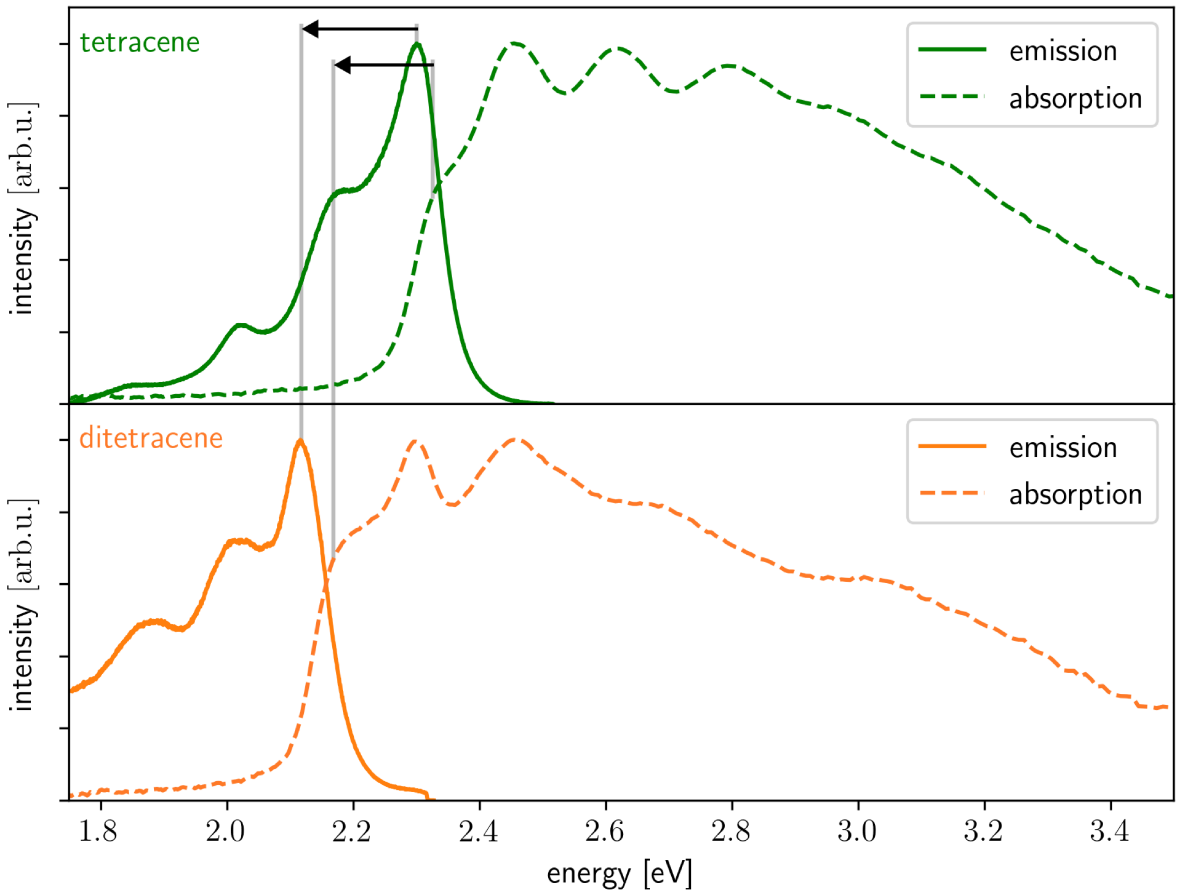

Figure 4.38: Absorption and emission spectra of tetracene and 2,2'-ditetracene in the crystalline phase. The two spectra resemble one another but are spectrally shifted by 150 meV.

peaks. However, in agreement with previous reports [108], no indication of such transitions could be found. Looking at the absorption spectra of both materials in more detail, we find that, taking into account the red shift of DTc, the first shoulder and the following two absorption peaks coincide. However, above 2.8 eV, the absorption lines of the two compounds begin to deviate.

Cluster calculations of Marian Deutsch, which take into account the intermolecular interaction of a dimer pair and its next-neighboring molecules, are able to explain all observed features of DTc and Tc single crystals. First, the observed red shift in TDc is a result of the stronger dipolar coupling between the DTc molecules caused by its modified crystal structure in comparison to the Tc crystal structure. Next, analysis of the HOMOs and LUMOs, as well as the vibrational modes of both materials, revealed that the emission and absorption line spectra of both materials can be associated with each other, since the states in DTc represent positive and negative linear combinations of the states in the

two tetracene units. Finally, detailed analysis of the relaxation of excited states disclosed slightly different potential energy landscapes for the two compounds. Therefore, the absorption spectra of both materials deviate when higher vibronic modes are excited.

Let us continue by taking a detailed look at the emission spectra of both materials. Here, a smaller distance between consecutive peaks in the emission of DTc and Tc solid states, in comparison to the single molecules occurs and indicates a more complex exciton dynamics except for neat vibronic progressions. To disclose the origin of the different peak positions and spacing, temperature-dependent photoluminescence studies were conducted on neat single crystals of DTc and Tc. As shown in Figure 4.39, the DTc photoluminescence spectra exhibit a much more complex behavior with temperature. While the increase in photoluminescence of Tc can be solely explained by the decreasing influence of non-radiative decay channels upon cooling, DTc emission discloses different groups of emission peaks, which react particularly sensitive to a temperature reduction in different temperature regimes. For example, the peak at 2.09 eV increases substantially between 120 K and 60 K while the peak at 2.14 eV increases predominantly between 40 K and 10 K. This indicates that each of the observed emission peaks located at 2.14 eV, 2.09 eV, 2.03 eV and 1.88 eV can be attributed to a different kind of excited state in DTc, which will be discussed in detail below. Comparing Figure 4.38 and 4.39, a significant difference can be noticed between the emission spectra of DTc recorded by the confocal microscopy setup and by the μ-PL setup. Especially, the intensity ratio between the peaks at 2.14 eV and 2.03 eV is considerably different in both measurements. This is an indication of different transition dipoles of both associated excited states, which results in different radiation characteristics for each decay channel.

At this point, a remark on possible temperature induced phase transitions has to be given. For Tc, a temperature or pressure induced phase transition is known in literature [117], which shows significant deviations of the transition temperature among different crystals and sensitively depend on the sample preparation and storage. This phase transition causes new emission lines and a change in relative peak heights below a certain temperature [133]. Based on our observed emission spectra of Tc no such phase transition could be confirmed. For DTc, a structural phase transition cannot be completely ruled out, but observation of the X-ray diffraction pattern during cooling to 77 K gave no indication of such a transition.

The dynamics and, hence, the origin behind the observed emission peaks were determined by temperature and wavelength dependent fluorescence decay measurements. For both materials identical measurements procedures were applied on three different crystals, each to check for consistency of the observed data. At each temperature step, distinct spectral regions were carefully selected by short- and longpass filters and analyzed in terms of their fluorescence decay signal. The final goal was to obtain the individual decay time constants that come along with each of the emission peaks. Figure 4.40 shows two examples of this evaluation where in each case the long wavelength part of the spectrum was analyzed, one for DTc (left column) and one for Tc single crystals (right column). In the first row, a) and d), the red part of the emission spectrum is selected by the filter com-

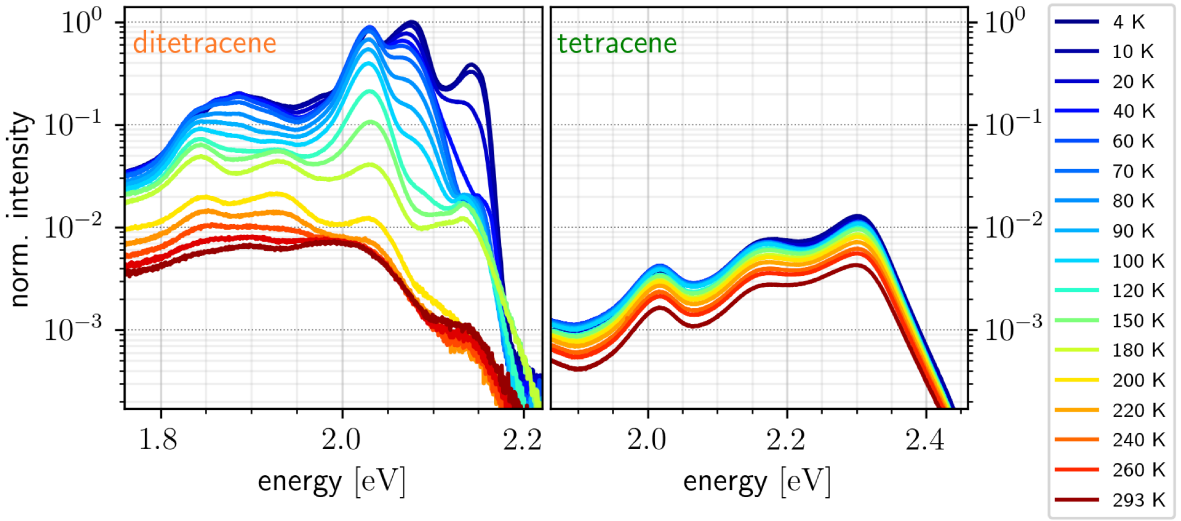

Figure 4.39: Photoluminescence of DTc and Tc single crystals recorded at different temperatures between 293 K and 4 K. Unlike Tetracene, DTc brightens up by two orders of magnitude. Its emission peaks at room temperature show a complex dependence on the temperature, resulting in e.g. a new peak 2.14 eV emerges below 120 K.

bination shown in Figure 3.3. In the second row, b) and e), a lifetime density analysis is performed according to Landl et al. [134], which utilizes an inverse Laplace-transform and different regularization methods. This results in a pseudo-continuous distribution of decay constants, which are plotted in the lower row, Figure 4.40c and f). Coinciding results for the three examined Tc crystals and good agreement for the three DTc crystals validate the applied lifetime density analysis.

The lifetime density distribution of Tc shows a broad asymmetric distribution of decay time constants in the range between 100 ns and 1 s. This is a signature of triplet diffusion and triplet-triplet annihilation processes that follow the splitting of singlet excitons into two triplet excitons in Tc. As the amount of delayed fluorescence from triplet-triplet annihilation depends on the square of the triplet populations, a fluorescence decay can be observed which is not monoexponential and, therefore, exhibits a broad distribution of decay times. In the decay constants obtained for DTc single crystals, extended time constants could not be observed, which indicates that this decay channel is absent in DTc in contrast to Tc.

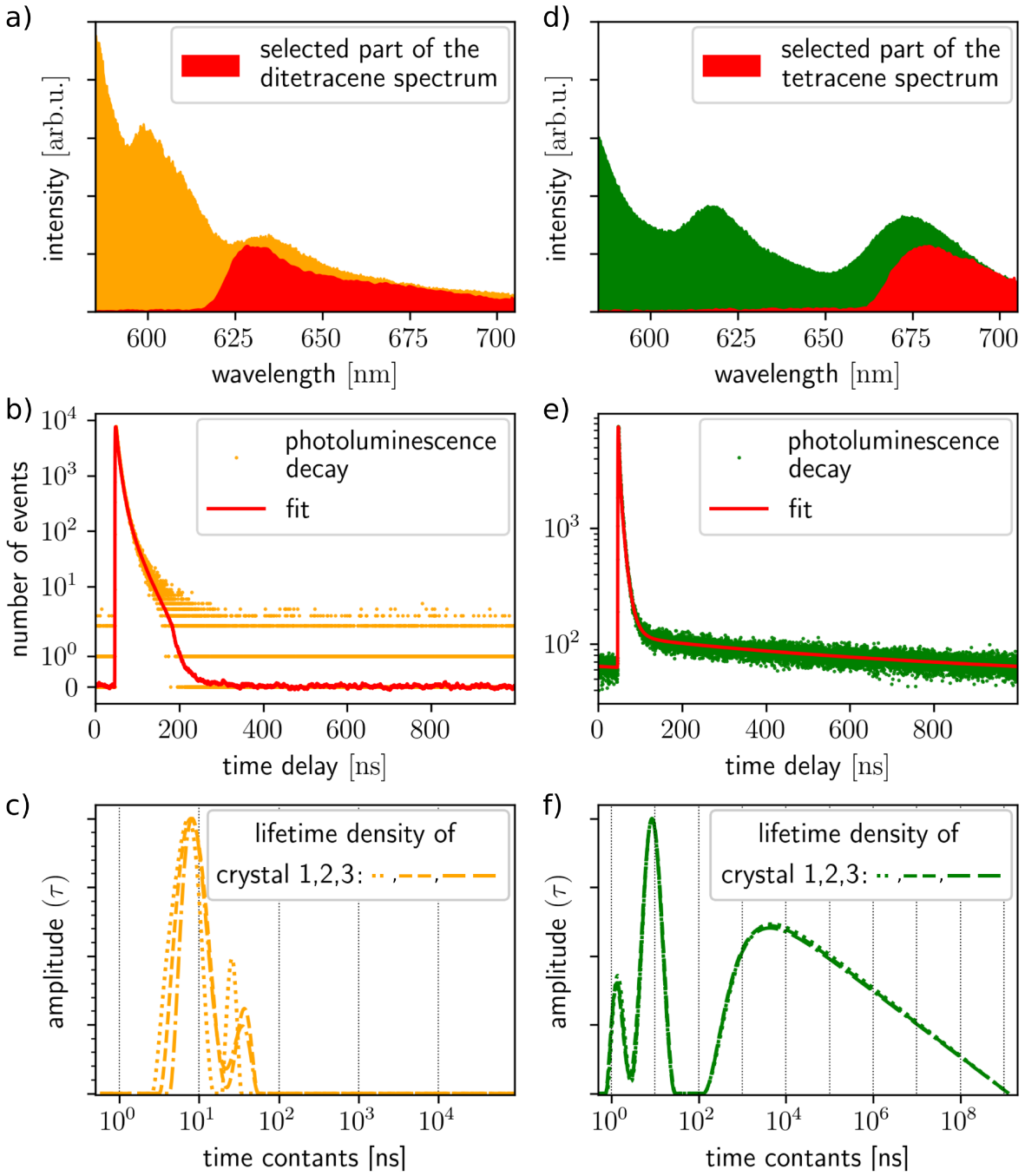

Figure 4.40: Examples of the lifetime density analysis of the photoluminescence spectra of 2,2'-ditetracene (left) and tetracene (right). Part of the photoluminescence spectrum is selected, a) and d), and its photoluminescence decay signal is fitted, b) and e), with a pseudo-continuous distribution of decay times, c) and f).

Besides concluding on the absence of singlet fission in DTc, which is also corroborated by the photoluminescence decay studies of Figure 4.47 later in this chapter, the analysis of decay time constants can be used to take a closer look at the photophysical processes in DTc. In general, the obtained decay time constants within a narrow spectral region can arise either from the targeted peak or other peaks with spectral overlap. This can be separated by analyzing the fluorescence decay at adjacent spectral positions. Further, the decay of a emission peak can be composed of different decay time constants, which can be related to the direct radiative or non-radiative decay of the associated excited state or arise from more complex dynamic processes determining its population or depopulation after pulsed photoexcitation. These effects can be identified by observing one emission peak at different temperatures. To demonstrate each case, two slices (fixed temperature of 77 K at different emission energies and fixed emission energy of 2.14 eV at different temperatures) are presented in the following from a total data set of 248 fluorescence lifetime measurements conducted at different temperatures, different spectral positions and different crystals, before an interpretation of the overall mechanism will be provided.

First, we analyze the decay time constants of DTc single crystals at 77 K. Here, Figure 4.41 gives an overview and a first impression of the observed fluorescence decay signals which we will analyze in detail below. In top graph, Figure 4.41a, the photoluminescence decay is plotted for eleven spectrally selected parts of the emission spectrum. In this representation it is hard to distinguish different processes influencing the data. The only characteristic, which can be identified directly here, is a rather fast (< 1 ns) decay of the highest energy emission peak at 2.14 eV, while a slower fluorescence decay can be observed for the emission peak with the highest emission intensity at 2.03 eV. In the bottom graph, Figure 4.41b, the photoluminescence decay is decomposed into its various decay time constants. The purpose of this 3D-plot is to give an overview over different time constants present in the signals and demonstrate that smooth transitions between adjacent spectral positions can be observed. In fact, three different time constants contribute to the overall decay of the photoluminescence signal, which are differently weighted at different spectral positions, one at 25 ns, at 9 ns and below 1 ns. The applied method of lifetime density analysis calculates optimal values for decay time constants even below the the instrumental time resolution of 1 ns. However, these values should only be interpreted as *the respective time constant is shorter than* 1 ns.

In Figure 4.42, three of the lifetime density distributions from graph 4.41 are plotted to demonstrate the assignment of time constants to the different emission features of the photoluminescence spectrum. Starting with the longest time constant of 25 ns, this decay is present at all spectral positions due to the spectral overlap of its corresponding

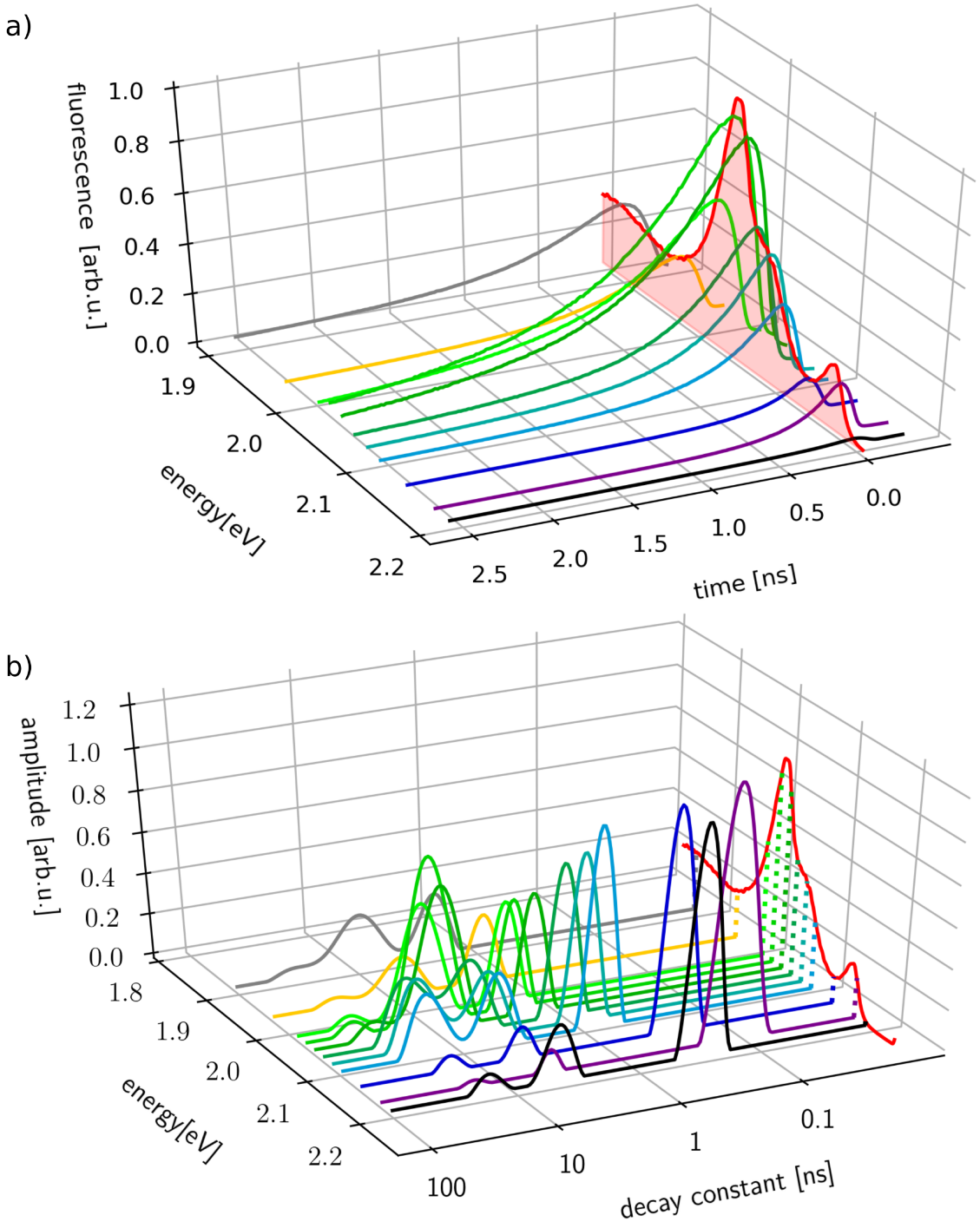

Figure 4.41: a) Spectrally resolved photoluminescence decay of 2,2'-ditetracene single crystal at 77 K. b) Photoluminescence decay decomposed into its various decay time constants at this temperature. In both graphs the red curve on the back plane is showing the complete photoluminescence spectrum.

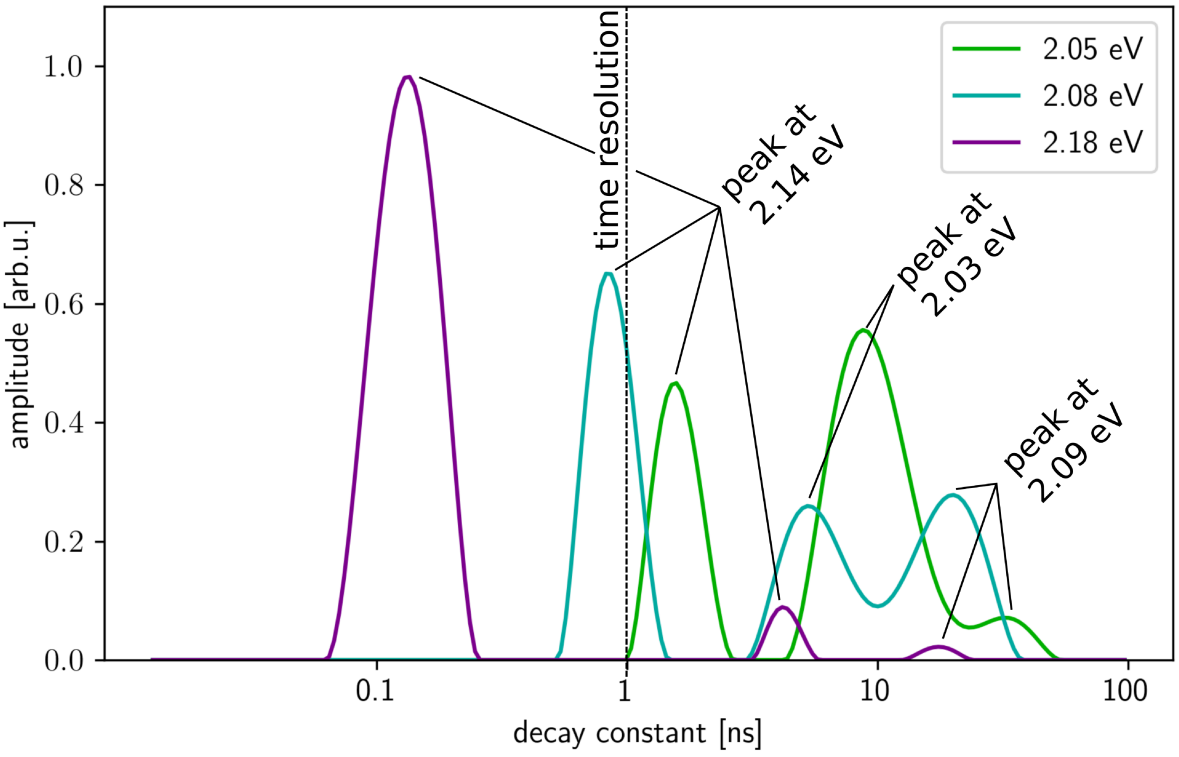

Figure 4.42: Three selected lifetime density distributions from graph 4.41 for photons emitted at 2.05 eV, 2.08 eV and 2.18 eV and the assignment of the observed decay constants to the peak in the overall spectrum. Calculated time constants below 1 ns, i.e. the instrumental time resolution, have to be interpreted as *shorter than* 1 ns

state whose contribution is most pronounced at 2.08 eV. Therefore, the emission shoulder at 2.08 eV can be ascribed to this time constant of 25 ns. Further, the time constant of 9 ns is predominantly present at the spectral position of 2.03 eV and, therefore, coincides with the photoluminescence peak at 2.05 eV. Finally, the peak at 2.14 eV mainly relates to photons that are emitted with a time constant faster than 1 ns. Additionally, a contribution by a time constant of 9 ns can be found again, which, however, is too strong to stem solely from a spectral overlap with the peak at 2.05 eV. Rather, this is a property of the photoluminescence decay at this spectral position which we will discuss in the following. All together, this behavior hints at more complex mechanisms which are responsible for the photoluminescence dynamic of the emission at 2.14 eV.

Temperature dependent measurements allow to disclose the underlying mechanisms by analyzing how the respective fraction of the two contributing time constants changes as function of temperature. This photoluminescence decay and the relative contribution of the two time constants are shown in Figure 4.43. Starting at room temperature, the fraction of photons emitted at a time constant below 1 ns increases upon cooling until the fastest

fluorescence decay can be observed at 75 K. From there, further cooling results again in a slower fluorescence decay.

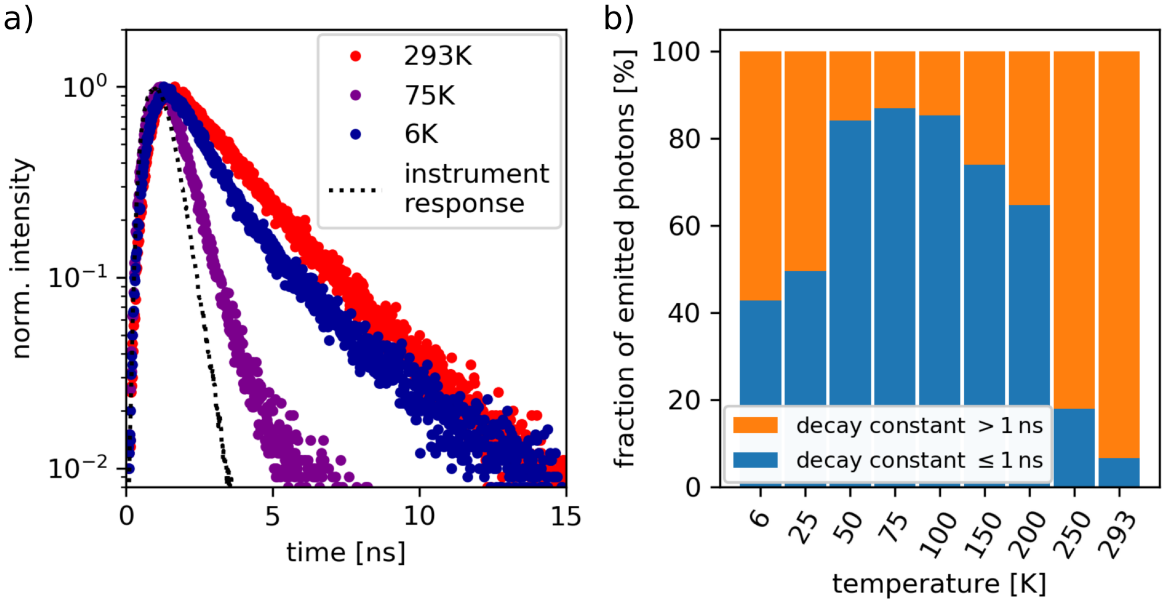

Figure 4.43: a) Fluorescence decay of the S_1 state of 2,2'-ditetracene referring to the emission at 2.14 eV for different temperatures. b) Two time constants, one below 1 ns and one above, contribute to the decay while the fraction of these contributions alter with different temperatures. The fastest fluorescence decay is obtained at 75 K.

Taking all these observations into account, we are now able to suggest a first model that is able to explain the findings. The peak of highest emission energy at 2.14 eV is attributed to the $S_1 \rightarrow S_0$ transition. Radiative and non-radiative decay channels contribute to this transition with a total rate of $3 \times 10^8\,s^{-1}$ at 6 K. The emission peak at 2.03 eV is attributed to an excited dimer state. Following the nomenclature of Zimmerman et al. [135], who simulated a similar state in tetracene and which has been experimentally observed [116], this state is referred as *D state*. The origin of this state is a multi-exciton electronic state, which is located at energies above S_1 when the state is in the vibrational ground state configuration of the S_1 state. However, by reduction of the distance between two adjacent molecules this state can lower its energy below that of the S_1 state while a shallow asymmetric barrier allows for excitons to pass from one state to the other. From the temperature dependent intensity and lifetime data, an asymmetric barrier height of approximately 1 meV (6 meV) for the $S_1 \rightarrow D$ ($D \rightarrow S_1$) transition can be deduced for DTc. In comparison, Tayebjee and coworkers report for tetracene that the transition to the *D state* is frozen out at about 4 K [116]. The emission from the D state exhibits a radiative transition rate of $1 \times 10^8\,s^{-1}$ to the ground state at 6 K. Although the difference in excited

state energy between the S_1 and D state is only 5 meV, the red shift of the D state emission in comparison to the S_1 state amounts to 140 meV because the radiative decay of the D state ends in a vibronically highly excited electronic ground state. This mechanism is illustrated in Figure 4.44. The detailed population dynamics between S_1 and D state and the resulting lifetimes of the states are determined by the temperature of the system. At room temperature, the shallow barrier between S_1 and D state is too small to prevent back-transitions. Therefore, S_1 and D state represent a common reservoir of excitons, which exhibit a common fluorescence lifetime of 3 ns, i.e. essentially the reciprocal transition rate from the S_1 to the S_0 state. By cooling the system to 75 K, excitons cannot return from the D to the S_1 state any more. This results in a distinct brightening of the D state emission, while its fluorescence decay constant increases. Simultaneously, the fluorescence lifetime of the S_1 state becomes exceptionally shortened as the S_1 state can still undergo a transition to the D state. The thermal energy required for this transition becomes scarce only at 6 K where a brightening of the S_1 state emission in combination with a return of the 3 ns time constant can be observed. An additional peak at 2.09 eV is observed which increases in brightness continuously on cooling of the crystal. At 6 K this peak is the most intense one with a lifetime of about 25 ns. The origin of this emission peak has not been clarified finally but it is most likely caused by localized, energetically defined interface states, which occur either at the crystal surface or at domain boundaries. Especially, in mechanically stressed samples this emission peak is dominant. Finally, the broad emission peak at 1.88 eV is attributed to vibronic progressions of the different emission peaks discussed before.

From the population model described above one would expect that only a small fraction of all excitons occupy the S_1 state in the crystal at 75 K where back-transfer from the D to the S_1 state is no longer possible. To verify this prediction, photoluminescence spectra were recorded at 75 K for different excitation intensities. The resulting emission spectra are normalized to the respective excitation intensities as shown in Figure 4.45. Indeed, in contrast to all other states, no indication of a saturating behavior was found for the S_1 state emission. This corroborates the low occupation probability of the S_1 state while simultaneously underlining its high dipole strength in comparison to the other transitions.

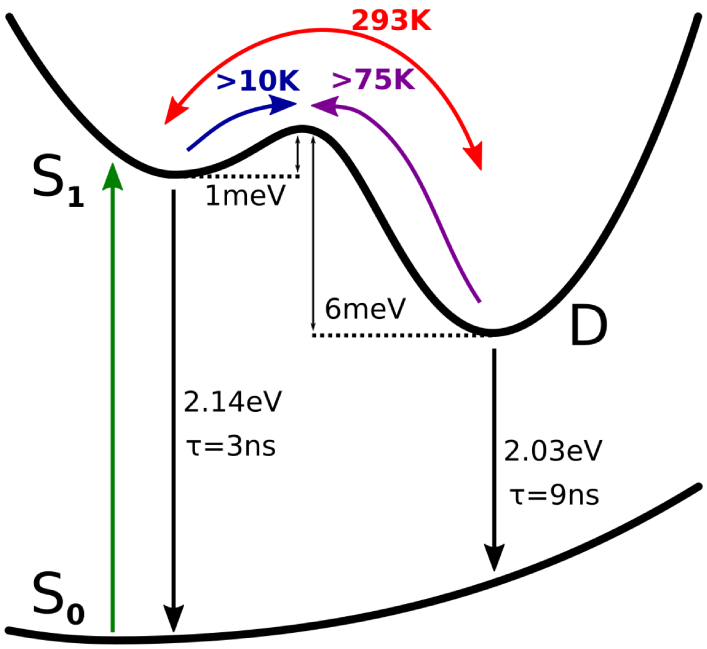

Figure 4.44: Energy landscape of S_0, S_1 and the D state in 2-2'-ditetracene single crystals. The curved S_0 ground state level below the dimer state illustrates the intermolecular relaxation after the decay of the dimer state.

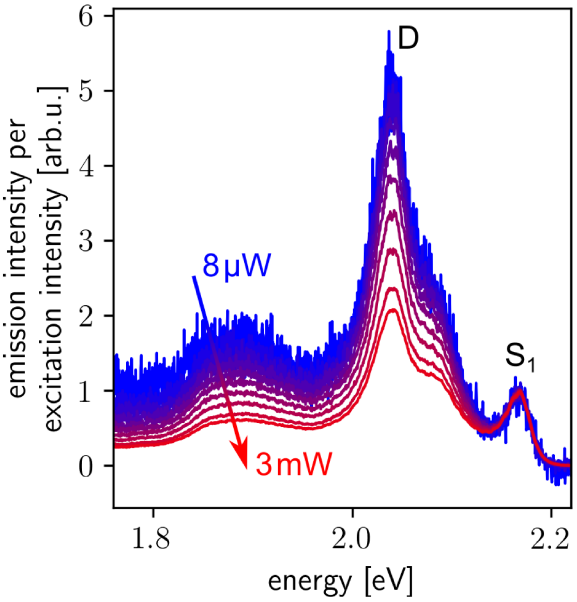

Figure 4.45: Emission of 2-2'-ditetracene at 75 K normalized to the excitation intensity. No saturating behavior can be observed for the S_1 state emission at 2.14 eV.

The characteristics of the excimer D state are determined by the interaction between adjacent molecules within the (ab)-plane of the crystal. However, we have not yet taken a closer look at the interaction along the c-direction of the crystal. To address this aspect, photoluminescence spectra of exfoliated layers of DTc were analyzed on 159 different positions on these flakes. Figure 4.46a shows the photoluminescence intensity map of this sample. These measurements provide emission spectra of crystals of different thickness. Besides the total emission intensity, which for thin and thus relatively transparent crystals is a measure of the thickness of the respective crystal, variations in the position of the S_1 emission line and the D state emission intensity could be observed. In Figure 4.46c, the S_1 peak position and the ratio between the S_1 and D state emission intensity are provided as a scatter plot in dependence of the total emission intensity. Four spectra along the red trend line are shown in Figure 4.46b.

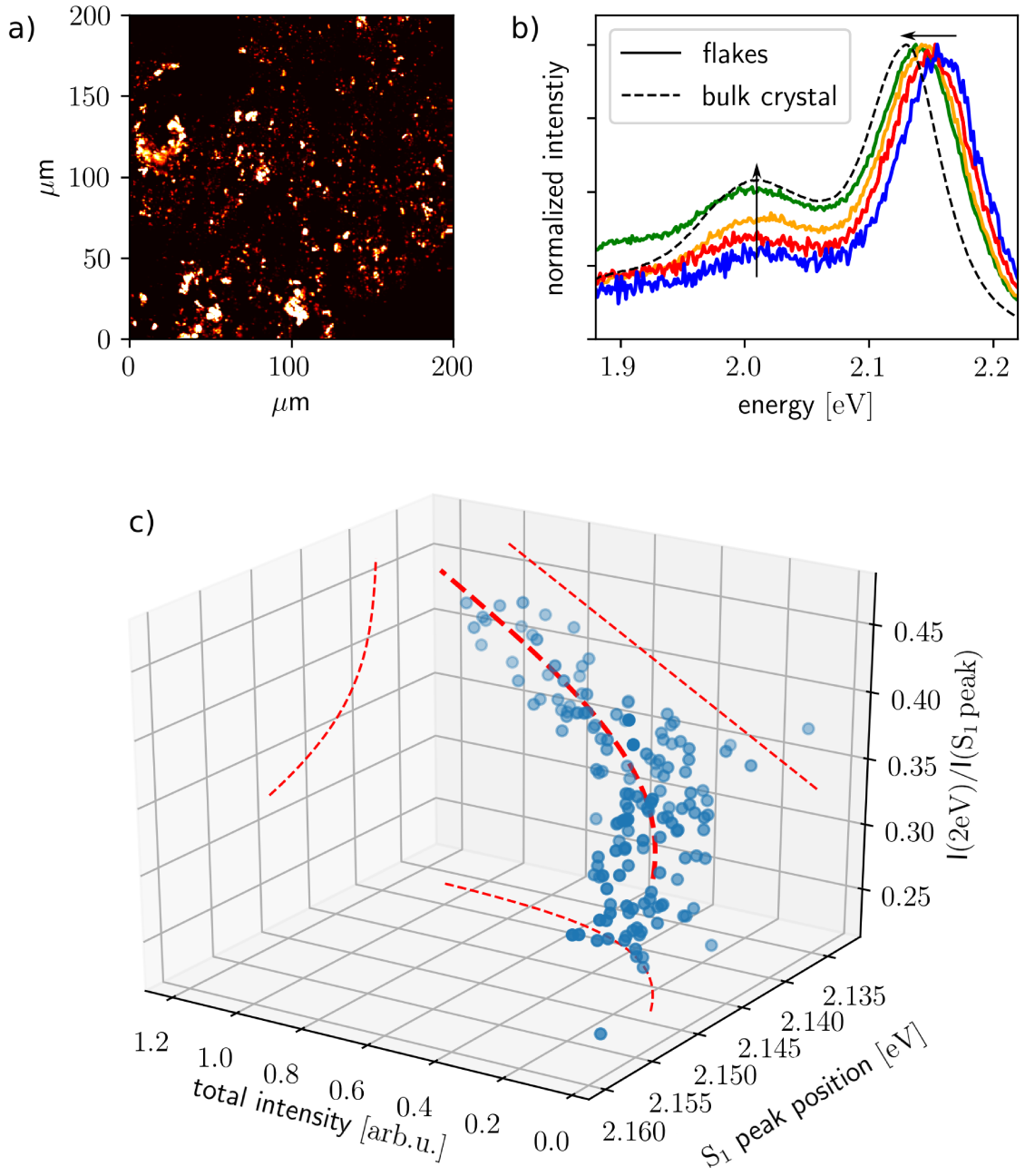

Figure 4.46: Photoluminescence of thin 2,2'-ditetracene flakes at room temperature. a) Photoluminescence intensity map of a sample of exfoliated DTc flakes. By analyzing many different positions on the sample, a correlation can be observed between peak positions and the respective heights. In b), four representative spectra along the thick red trend-line in c) are shown.

As expected, for higher emission intensities, i.e. thicker crystal flakes, these spectra approach the emission profile of the bulk crystal. On the other extreme, the emission spectra approach precisely the spectrum measured by Roth et al. [28] in thin films. Also their X-ray diffraction determined lattice constant of DTc thin films in c-direction coincides with the lattice constant of the bulk crystal. This suggests that differences in the emission spectra in thin TDc flakes are due to electronic coupling between different layers of molecules rather than a change in crystal structure. Considering the distribution of the measured emission intensities, in particular the lack of clustering of measurement points at high intensities, it can be concluded that the thicknesses of the flakes are in a range where the Beer-Lambert law can be approximated by a linear function, i.e significantly below 50 nm. Therefore, it can be assumed that the layer thicknesses of the thinnest flakes consist of only a few molecular layers. Between thin film and bulk emission spectra two trends can be observed. Firstly, a redshift of the S_1 state emission and, secondly, a relative increase in the D state emission 2.0 eV. The redshift between thin flakes and the bulk S_1 state emission amounts to only 30 meV and depends only significantly on the layer thickness if the crystal flakes are very thin. This indicates that the S_1 state at room temperature is delocalized only over a small number of molecules in the c-direction of the crystal. The relative increase of D state emission is most likely caused by an increased light outcoupling efficiency for transition dipoles at larger distances from the crystal surface along with an increased amount of self-absorption of short wavelength light.

So far, we looked at the photophysical behavior of DTc. To determine the differences to Tc, we analyzed this material with the same temperature and wavelength dependent fluorescence decay measurement as described above. The results coincide with the results from literature [116]. In detail, we found a short lifetime of the S_1 state emission, well below the time resolution of our setup of 1 ns. This is due to the process of singlet fission, which is slightly endothermic in Tc but efficiently driven by entropic gain and higher temperature ranges [136]. Additionally, as shown in 4.40, we found a delayed fluorescence characteristic for triplet-triplet annihilation. Finally, at 6 K we observed a relatively weak emission component at 2.25 eV with a fluorescence lifetime of about 10 ns. This is in line with an observation made by Tayebjee and coworkers in tetracene thin films [116], who ascribed it to an excimer state with a similar dynamic as was found for DTc in our experiments. The most important difference between DTc and Tc is the absence of singlet fission in DTc. A direct comparison between the photoluminescence of both compounds is shown in Figure 4.47. Here, no delay fluorescence can be observed for DTc. In contrast, Tc shows a pronounced delayed fluorescence, only a small part of which has decayed within the repetition period of the pulsed laser excitation of 900 ns.

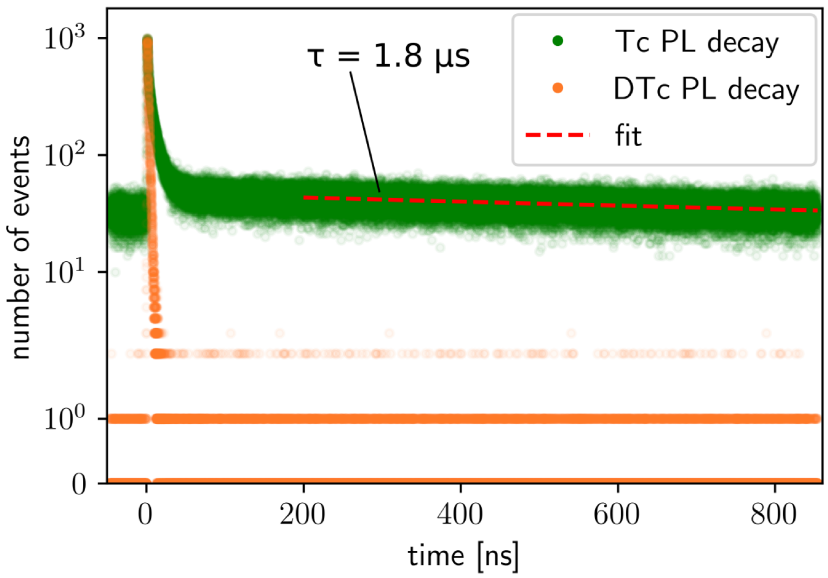

Figure 4.47: Fluorescence decay of tetracene and 2-2'-ditetracene measured at room temperature. In the case of tetracene the decay exhibits a pronounced delayed fluorescence with a time constant of $\tau = 1.8\,\mu s$ assuming a monoexponential decay, which is missing in the case of 2-2'-ditetracene.

To theoretically substantiate these observations, Marian Deutsch performed detailed ground- and excited state optimizations and energy calculations for singlet and triplet states in Tc and DTc. Their results provide a conclusive picture of the processes in both materials: The decisive difference between the two materials is the extent of the energetic relaxation that follows an optical excitation. Potential energy curves for DTc and Tc are shown in Figure 4.48, where the potential energy curve of the S_1 state shows a significantly steeper slope for DTc after adiabatic excitation than for Tc. Among other coordinates, this relaxation happens by a tilting of the molecules in the crystal lattice and results in a 200 meV lower energy of the relaxed S_1 state for DTc compared to Tc. At the same time, the potential energy curves for the corresponding triplet states changes to a much lesser degree. In the experiment, these differences manifest themselves in a red-shifted emission of the S_1 state of DTc compared to Tc, as it was shown in Figure 4.38. At the same time, the condition $E(S_1) \geq 2 \times E(T_1)$ is no longer fulfilled and the process of singlet fission is therefore energetically unfavorable and suppressed in DTc in contrast to Tc. Technical details of these calculations can be found in the corresponding publication [106].

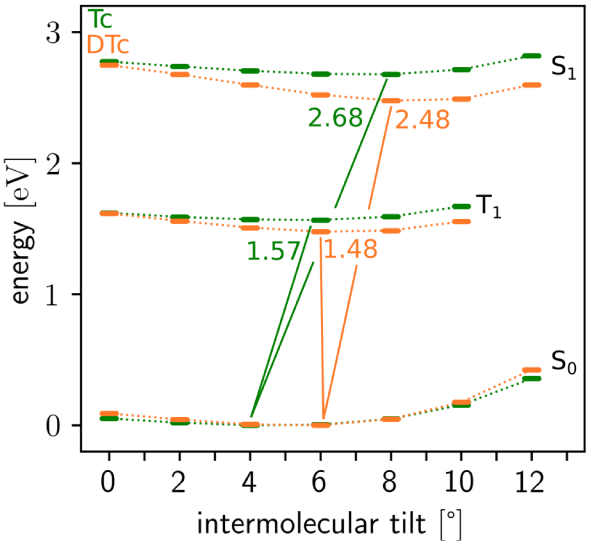

Figure 4.48: Potential energy curves of tetracene and 2,2'-ditetracene of the ground as well as the excited singlet and triplet states. After excitation, the S_1 state can relax significantly more energy in DTc than in Tc, which renders singlet fission less favorable. Relaxation corrections found for the single molecules are not included in the energy values given in this graph.

The suppression of singlet fission in DTc leads to a significant improvement in the photophysics of the material, in particular an increasing quantum yield of the photoluminescence. In Figure 4.49 the total photoluminescence is plotted in the temperature range between 6 K and room temperature. At room temperature, DTc yields by a factor of two more photoluminescence than Tc under same excitation power. This difference in performance increases at lower temperatures up to a factor of 46 at 6 K.

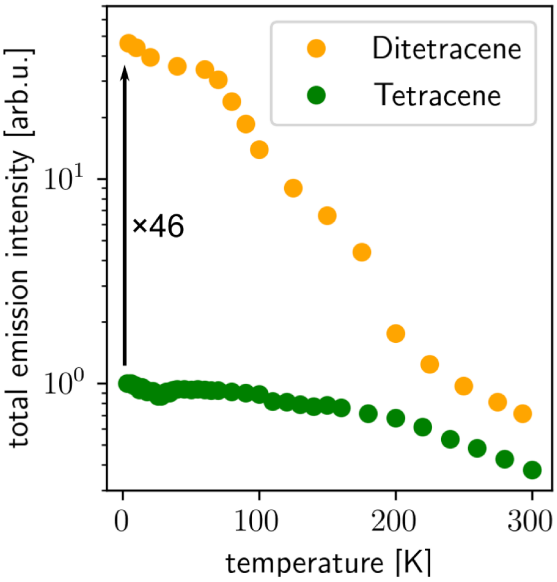

Figure 4.49: Total photoluminescence intensity of 2-2'-ditetracene and tetracene in dependence of the temperatures. While 2-2'-ditetracene is already brighter at room temperature, the luminescence of 2-2'-ditetracene at 6 K is 46 times brighter than the luminescence of tetracene.

In summary, the covalent linker between the two tetracene chromophores in DTc creates a multichromophoric system, which conserves the optical properties of the single chromophores. Simultaneously, in its crystal form the linker affects the crystal structure, which leads to decisive changes in the energetics of the excited states. Therefore, the process of singlet fission is effectively suppressed in DTc and the photoluminescence yield is substantially increased. This could render DTc useful for applications as an emitting material in OLEDs or lasers.

4.6.2 Perylene Bisimides

Parts of the results of the following chapter have been published in [137]. Para-xylylene bridged perylene bisimide (PBIs) macrocycles are multichromophoric macromolecules synthesized by Peter Spenst in the group of Prof. Dr. Frank Würthner at the Institute of Organic Chemistry at the University of Würzburg [79]. PBIs are based on the polycyclic aromatic hydrocarbon perylene, shown in Figure 4.50a. In the configuration of a tetracarboxylic acid bisimide the absorption maximum of the perylene bisimide chromophore is shifted from the blue end of the visible spectrum to the green [138]. Due to its thermal and chemical stability as well as its photo-stability, the dye is used in industry as a red pigment [139]. Here, the chemical variability of the substituents of the chromophores plays an important role. To produce different shades of red pigments the R_1 moiety is substituted. By substitution of the bay-area moieties, i.e. the R_2-site of the molecule, a wider shift between 511 nm and 686 nm can be realized. Simultaneously, this substitution affects the solubility and agglomeration of the dye, which are important parameters for industrial processing as well. Finally, when using the proper moiety, the chromophore becomes almost independent of the influences of the local environment and can reach quantum yields close to 100 % [138].

In this work PBIs are analyzed both as monomers as well as para-xylylene bridged trimers and tetramers, see Figure 4.50b. The later promise a weak but yet defined interaction between the individual chromophores. In other perylene bisimide-based macrocycles incoherent hopping in the picosecond time range and exciton-exciton annihilation was found [140]. The shape of the PBIs' absorption spectra does not differ between the monomer, trimer or tetramer configuration, see Figure 4.50c, while the absorption coefficient is proportional to the number of chromophores in the macrocycle. This indicates that the chromophores, in fact, interact weakly. Upon weak laser excitation, i.e. far below the saturation of photoexcitation, the emission is also proportional to the absorption, indicating that the quantum efficiency is unchanged upon covalent linking. The dimer species, not included in the work of this thesis, was also synthesized and extensively studied by Peter Spenst and colleagues [79]. It shows a coplanar arrangement with enhanced interaction of the two chromophores, which was undesirable for the experiments in this work.

In comparison to the two chromophores in 2,2'-ditetracene, which are coupled strongly and form delocalized electronic states, the chromophores of perylene bisimide multichromophores are linked by para-xylylene bridges and excitons can be considered more localized [79]. Nevertheless, one can expect a pronounced interaction between

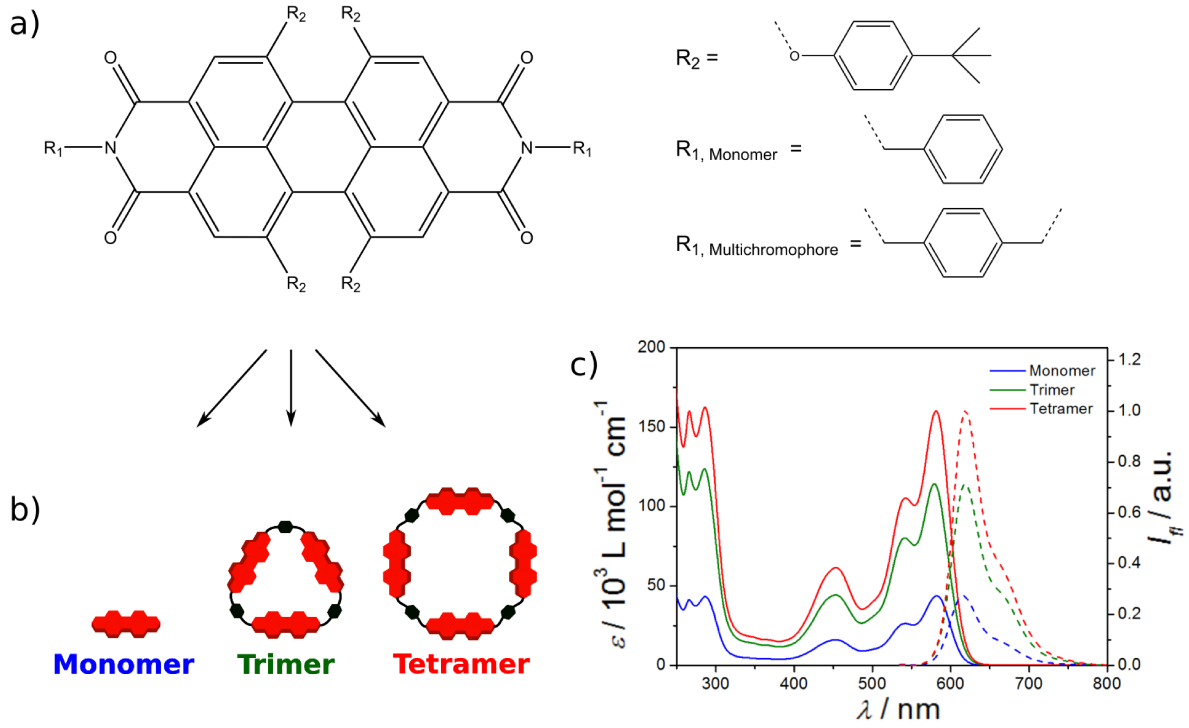

Figure 4.50: Perylene bisimide (PBI) based multichromophores. a) Depicts the chemical structure of the perylene bisimide chromophore and its respective substituents. b) Monomers are connected to multichromophores via para-xylylene linkers. c) Absorption and emission spectra of the monomers, trimers and tetramers are shown.

excitons on different chromophores as it was shown for perylene bisimide with different linkers [140]. This chapter will demonstrate how this interaction can be utilized to improve the ability of the multichromophores to serve as single photon emitters.

We start by analyzing at the photoluminescence of the PBI monomer, trimer and tetramer as single molecules in a PMMA matrix. The samples for these single molecule studies were prepared in the similar way as described before in Chapter 4.1, i.e. mixing a highly diluted solution of the respective PBI multichromophore in dichloromethane with PMMA and spin-coating it onto a 170 µm thick glass substrate. The top row of Figure 4.51 shows the photoluminescence intensity maps of these samples where bright emission spots indicate the presence of one or several single molecules. Analyzing the photon statistics of the emitted light reveals that all species exhibit distinct antibunching and can serve as single photon emitters upon optical excitation. The reason for this is the possibility of exciton-exciton annihilation in the multichromophores, which is expected for weakly [141] and strongly [142] coupled molecules. This non-radiative annihilation

process quickly terminates the presence of multiple excitations on one multichromophore before radiative emission occurs.

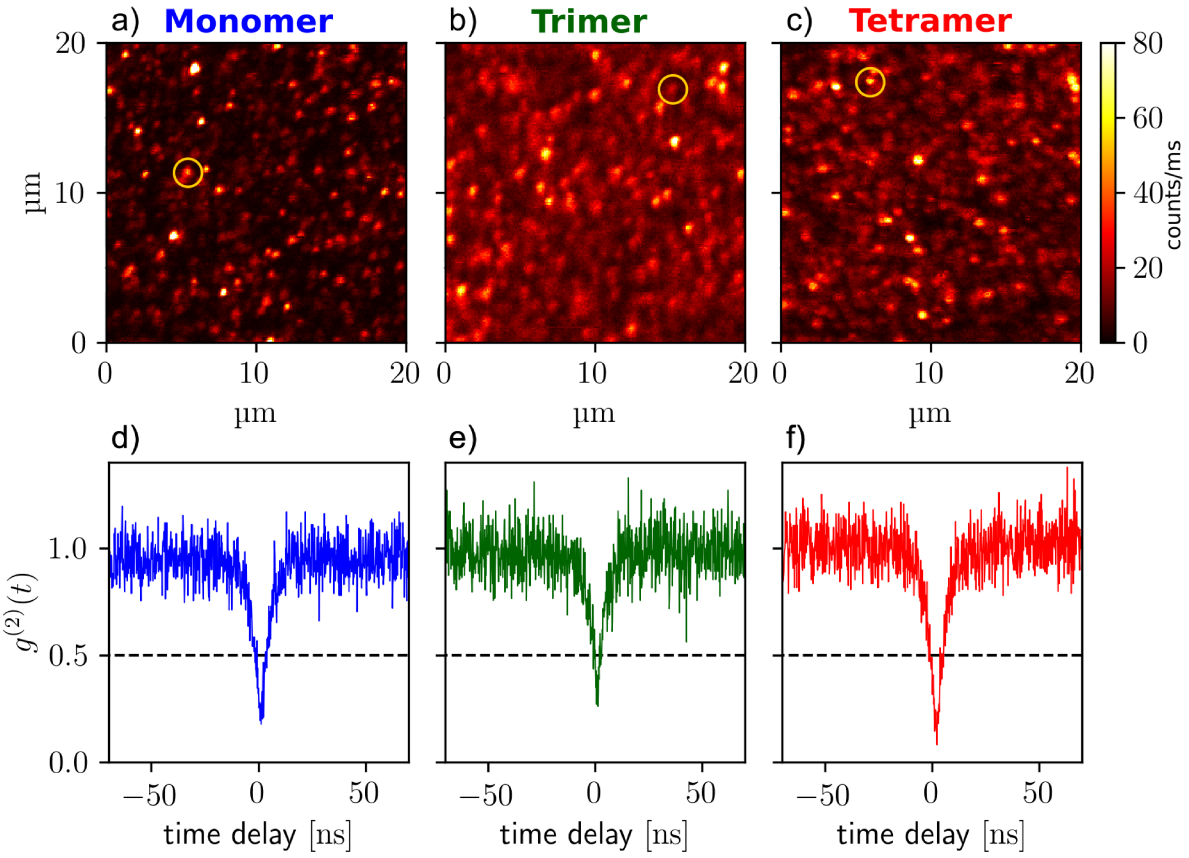

Figure 4.51: PBI Multichromophores at the single molecule level. a)/b)/c): Photoluminescence intensity maps from samples of diluted PBI Monomer/Trimer/Tetramer in PMMA. d)/e)/f) corresponding $g^{(2)}$-functions recorded at the yellow-circled region of the respective sample. All species show distinct single photon emission. Photoexcitation was performed by a 532 nm laser at 1 µW power.

In order to provide evidence for a double excited state in the multichromophores the $g^{(2)}$-functions of the molecules' emission were recorded at different excitation intensities. In general, a 3-level-system comprising a ground state, a singlet excited state and a dark triplet excited state is a good approximation to the behavior of a PBI monomer. The probability of an intersystem crossing from the excited singlet to the triplet state is responsible for a photon bunching typically on the µs timescale (compare the simulation in Section 2.7). The amplitude of this bunching (defined in Figure 4.52) is connected to the probability of intersystem crossing and the photoexcitation rate during the experiment. In Figure 4.52b the bunching amplitude for a tetramer and a monomer is plotted in

dependence of the excitation power. For a 3-level-system the bunching amplitude is expected to show a saturation behavior modeled by the blue line. In contrast, for the tetramer a bunching height is observed, which has a quadratic dependence of the excitation power. This cannot be reproduced by a 3-level-system and indicates the presence of a double photoexcited molecular state. Figure 4.52c shows the corresponding $g^{(2)}$-function on a logarithmic timescale. These functions have been modeled by a 4-level-system, i.e. a 3-level-system with an additional double excited S_1+S_1 state, where the transition rates between the states are free parameters of the system. This theoretical $g^{(2)}$-functions of this model is shown in Figure 4.52d.

The transition rates of this theoretical model show two decisive properties. Firstly, the double excited S_1+S_1 state exhibits an exceptionally short lifetime mainly due to non-radiative decay to the S_1 state. Secondly, the intersystem crossing from the double excited S_1+S_1 state is two orders of magnitude faster in the S_1+S_1 state than of the S_1 state. This makes it the predominant channel of intersystem crossing at higher excitation intensities.

In general, fluorescent molecules have a decisive disadvantage compared to phosphorescent molecules when using them as electrically driven single photon emitters. For fluorescent emitters the energetically favorable triplet state is a dark state, which, according to the theoretical modeling of $g^{(2)}$-functions, has a lifetime of about 25 µs. This leads to a high occupation probability of the triplet state during continuous wave photoexcitation. At an excitation power of 100 µW the probability to find the tetramer, examined in Figure 4.51, in its dark state is about 96 %, while typical values for the PBI monomer are around 80 %. In the case of electrically driven fluorescent molecules the situation turns out to be even worse as the triplet states can be directly populated by capturing charge carriers from the matrix. Therefore, until now only phosphorescent emitters have been utilized as electrically driven molecular single photon sources [143].

The decisive innovation here is to use multichromophores as emitters. To demonstrate how these systems can make the emission of single photons more efficient, we initially examine the photoluminescence of the three PBI species at laser excitation intensities well above the saturation intensity, i.e. above the excitation power where the absorption rate is equal to the S_1 decay rate. With the setup illustrated in Figure 3.5, the excitation power is swept between 0 mW and 4 mW at a frequency of 4 Hz while the corresponding photoluminescence signal from the different types of host-guest-systems is detected. Figure 4.53 shows this photoluminescence intensity on identical y-scales, while the data points of each sweep is connected by a solid line.

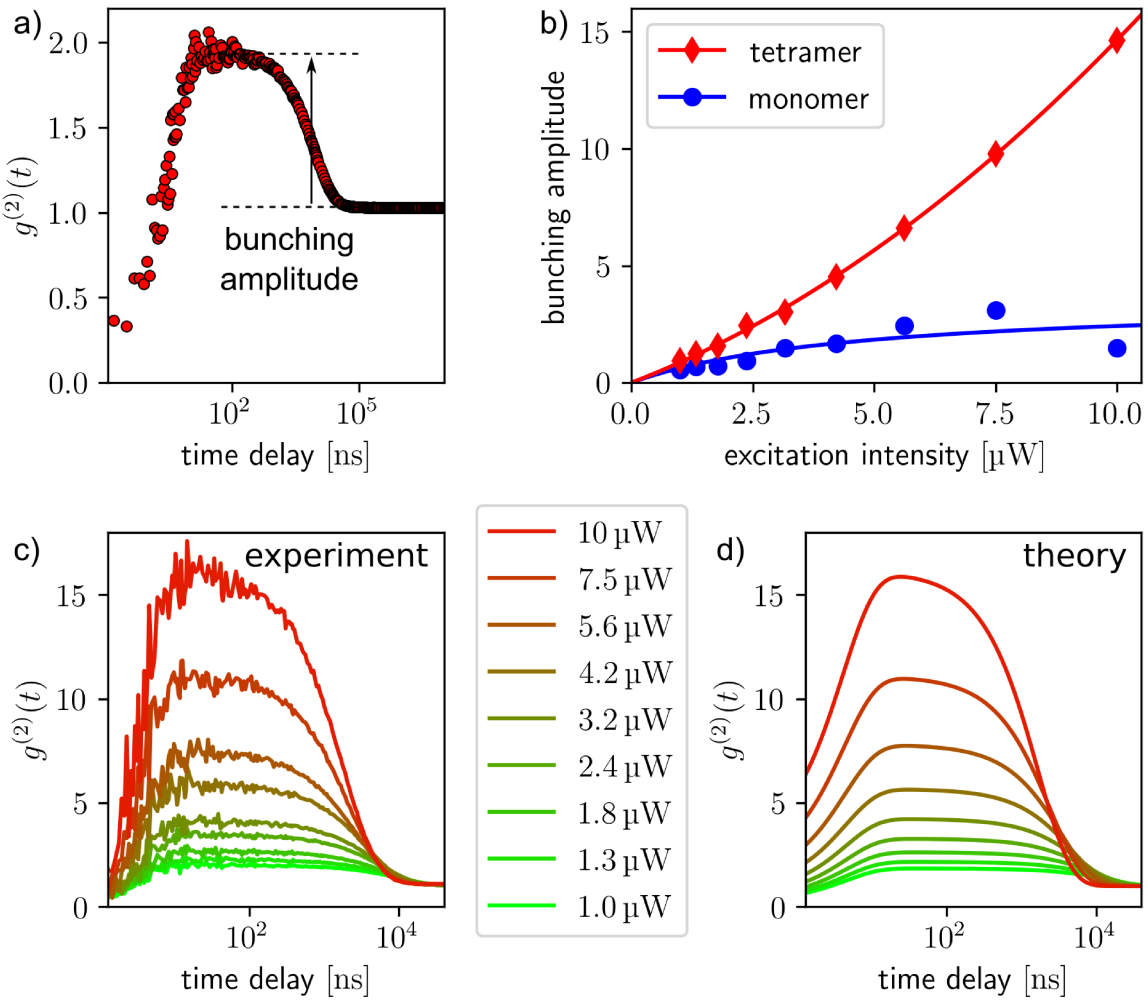

Figure 4.52: Photon bunching from perylene bisimide multichromophores. a) Definition of the bunching amplitude, which is plotted in b) for a perylene bisimide monomer and a tetramer in dependence of the excitation power. A quadratic dependence can be observed for the $g^{(2)}$-functions of the tetramer, which are shown in c) and theoretically modeled by a 4-level-system in d).

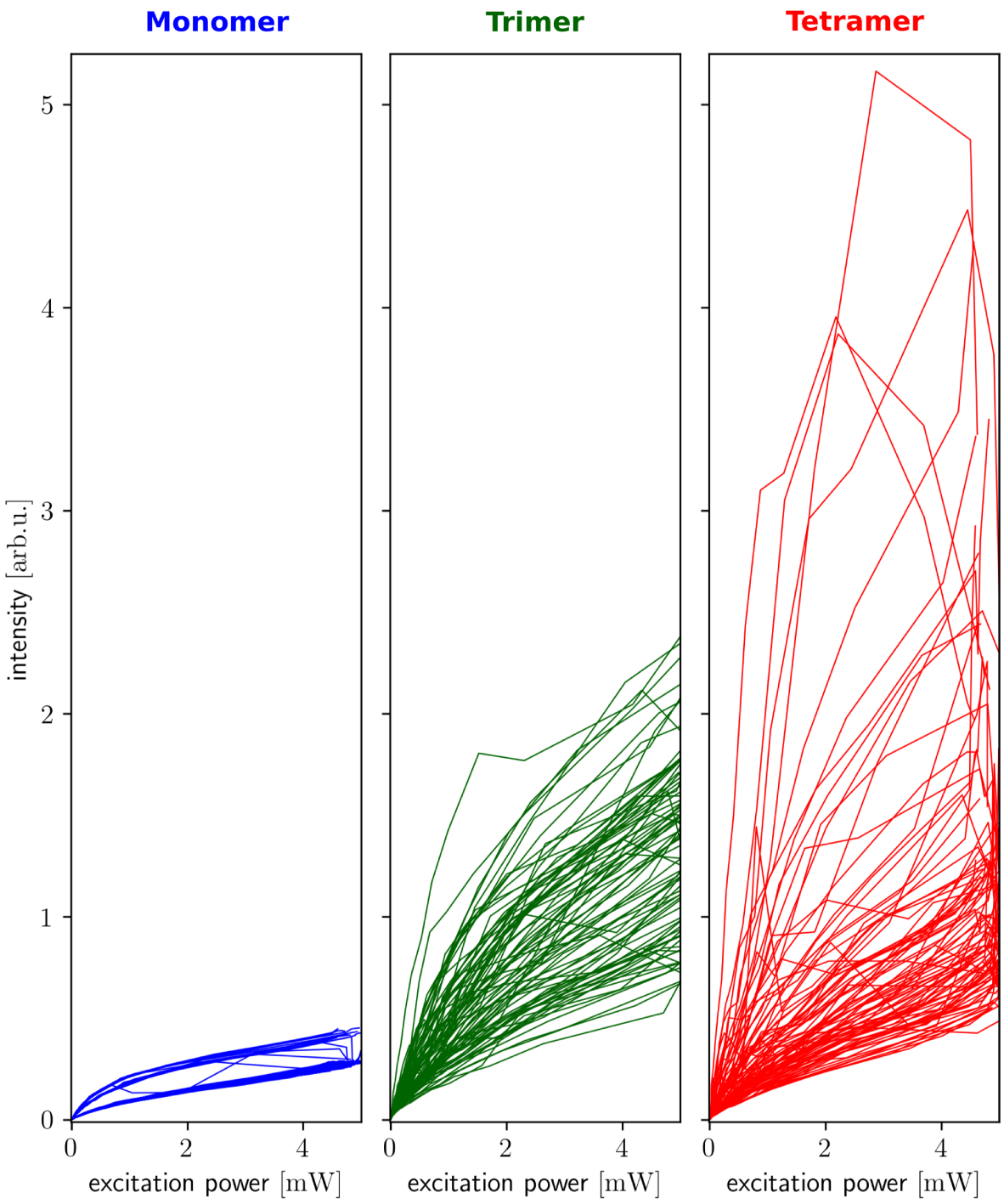

Figure 4.53: Photoluminescence of PBI monomer, trimer and tetramer at high excitation powers. The lower branch in the monomer signal represents the background intensity from the fluorescent sample. No saturation can be observed in the emission of trimers and tetramers.

For the monomer we observe two intensity branches. The lower branch represents the molecule in its dark state and the photons recorded stem from background fluorescence of the sample, which tends to be proportional to the excitation power. In contrast, the upper branch represents the molecule in its bright state. After subtraction of the background signal, it becomes clear that the photoluminescence intensity of the monomer does not depend on the excitation power above 1 mW. The reason for this is the saturation of the excited state, i.e. when light emission is limited by the radiative decay rate of the excited state. For a two-level system, the measured photoluminescence intensity follows $I \propto r_{21} k_{12}/(k_{21} + r_{21} + k_{12})$, with r_{nm} denoting the radiative and k_{nm} denoting the non-radiative transition rates from level n to m. If $k_{12} \ll k_{21} + r_{21}$, i.e. in the case of small excitation powers, the measured photoluminescence is proportional to k_{12} and therefore proportional to the excitation power. However, the intensity shows saturation for $k_{12} \gg k_{21} + r_{21}$, i.e. in the case of high excitation powers. The issue looks different for the trimer and tetramer, however. Firstly, the photoluminescence intensity traces do not show a lower branch. This indicates that, during continuous laser excitation of these molecules, there is no molecular state which is completely dark. Secondly, although the photoluminescence is very unstable at high excitation intensities, it does not saturate like the photoluminescence of the monomer.

Based on the previous findings at weak laser excitation, we would expect only a marginal increase in brightness for trimers and tetramers as the effect of singlet-singlet annihilation prevents an efficient simultaneous emission of identical chromophores in one multichromophore. However, we observe that the emission of trimer and tetramer is significantly enhanced in comparison to the monomer. Note that this enhancement is even greater than one would expect for three or four individual monomer chromophores.

The explanation of this finding is the process of triplet-triplet annihilation between adjacent chromophores. This process ensures that there are always chromophores within the multichromophore in their electronic ground state. These chromophores can be excited by the laser at any time and can emit additional photons. Therefore, the multichromophore has neither a complete dark state nor a state in which the fluorescence from the molecule is saturated. It is likely that singlet-triplet annihilation processes and interactions of excitons with free charge carriers are also present in these systems but are not crucial for the theoretical description of the molecular system.

As we have seen, trimers and tetramers can be exceptionally bright single photon emitters at strong photoexcitation intensities. This advantage is expected to persist in

electrically driven devices, where triplet excitons can be generated directly by electrons and holes. To demonstrate this, an OLED containing single PBI trimers was fabricated.

As a matrix material for this OLED a blend of poly(vinylcarbazole) (PVK) with HOMO(LUMO) level at −5.5 eV(−2.0 eV) and 2-tert-butylphenyl-5-biphenyl-1,3,4-oxadiazol (PBD) with HOMO(LUMO) level at −6.1 eV(−2.5 eV), depicted in Figure 4.54, was used. The two materials were purchased from *Sigma Aldrich*. The blend is known to exhibit a number of excited states like PVK:PBD exciplexes, electroplexes, PVK electromers and PBD electromers [144]. These states have proven to transfer energy efficiently to guest molecules like $Ir(DPPF)_3$ [145] or quantum dots [146], with the process of Dexter transfer identified as the dominant energy transfer mechanism.

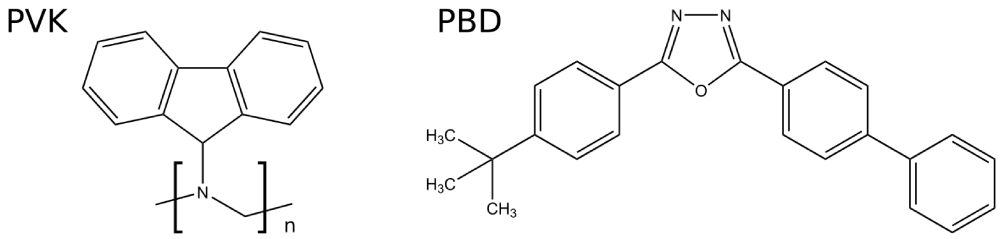

Figure 4.54: Chemical structure of polyvinylcarbazole (PVK) and 2-tert-butylphenyl-5-biphenyl-1,3,4-oxadiazol (PBD).

The OLED was manufactured in the same way as described in Chapter 4.3 but an additional layer of Tris-[3-(3-pyridyl)mesityl]borane (3TPYMB) with a thickness of 100 nm was used as an electron transport layer between the PVK:PBD matrix and the Ca/Al cathode. 3TPYMB, purchased from *Merck KGaA*, exhibits an electron mobility of 10^{-5} cm^2/Vs and was first synthesized by Tanaka et al. in 2006 [147]. The compound shows two specific properties: Firstly, the empty p-orbitals of the boron atom and the electron-withdrawing pyridine units provide a high electron affinity, which facilitates the injection of electrons from the metal cathode. Secondly, the twisted molecular structure of 3TPYMB reduces the singlet-triplet energy gap resulting in a high energy of the triplet state of 2.95 eV relative to the singlet excited state at 3.32 eV [148]. This renders the material especially useful as a host for applications in which the guest compound exhibits a high energy triplet state, like TADF materials or short wavelength phosphorescent emitters. HOMO and LUMO energies were determined to be 6.8 eV and 3.3 eV below the vacuum level [147].

The final (ITO/PEDOT:PSS/PVK:PBD+trimers/3TPYMB/Ca/Al) OLED was spectroscopically analyzed and the results are shown in Figure 4.56. The graph a) shows the photoluminescence intensity map during photoexcitation with a wavelength of 532 nm. Here, single bright spots can be identified, whose emission spectra, shown in b), can

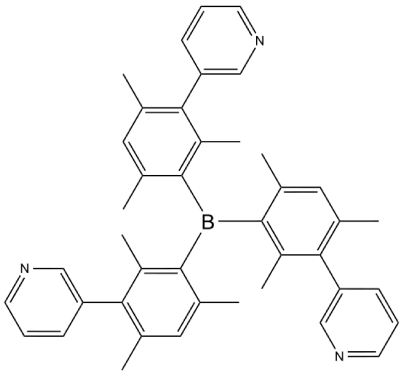

Figure 4.55: Chemical structure of Tris(2,4,6-trimethyl-3-(pyridin-3-yl)phenyl)borane.

be clearly assigned to the emission of PBI chromophores. The photon statistics of the emission in c) shows distinct antibunching on the timescale that is expected for PBI chromophores. During electrical operation, bright emission spots can be identified in d), which coincide with the spots in a). Dotted lines in the plots a) and d) facilitate the identification of corresponding emission spots. These spots are bright enough, that they can be seen by eye under the microscope. While the emission from the PVK:PBD host matrix is blue, the emission from the PBI trimer appears as broadband/whitish emission spots. Figure 4.56 e) shows a photograph of the OLED emission under the microscope at another position of the sample. Here, the red channel of the picture was globally enhanced to highlight the emission spots. The observation of photon antibunching in f) is complicated by significant background emission of the OLED. Nevertheless, without correcting for background signals, the best fit for $g^{(2)}(\tau = 0)$ reveals a value of 0.96. The probability value of the antibunching ($p = 2.3\sigma$) is limited by the Poisson distribution of the detection events, while the total measurement time is limited not by the photobleaching of the multichromophores but by the increasing amount of background radiation of the OLED during electrical operation. The electroluminescence intensity for the spot analyzed in f) is 107 counts per ms.

Until now, at room temperature only phosphorescent emitters such as $Ir(piq)_3$ have been utilized as single electrically driven molecules [143]. As expected, in comparison to $Ir(piq)_3$ molecules, which rely on phosphorescent emission with a lifetime of about 1 µs, the fluorescent PBI trimers exhibit a single photon emission intensity, which is enhanced by a factor of 25. Apart from possible effects of the background signal, the identification of a significant photon antibunching on the nanosecond timescale requires the collection of 10^6 times as many photons as are necessary for the equivalent observation on the microsecond timescale. Nevertheless, the brighter emission and the excellent photostability of PBI chromophores made this measurement possible.

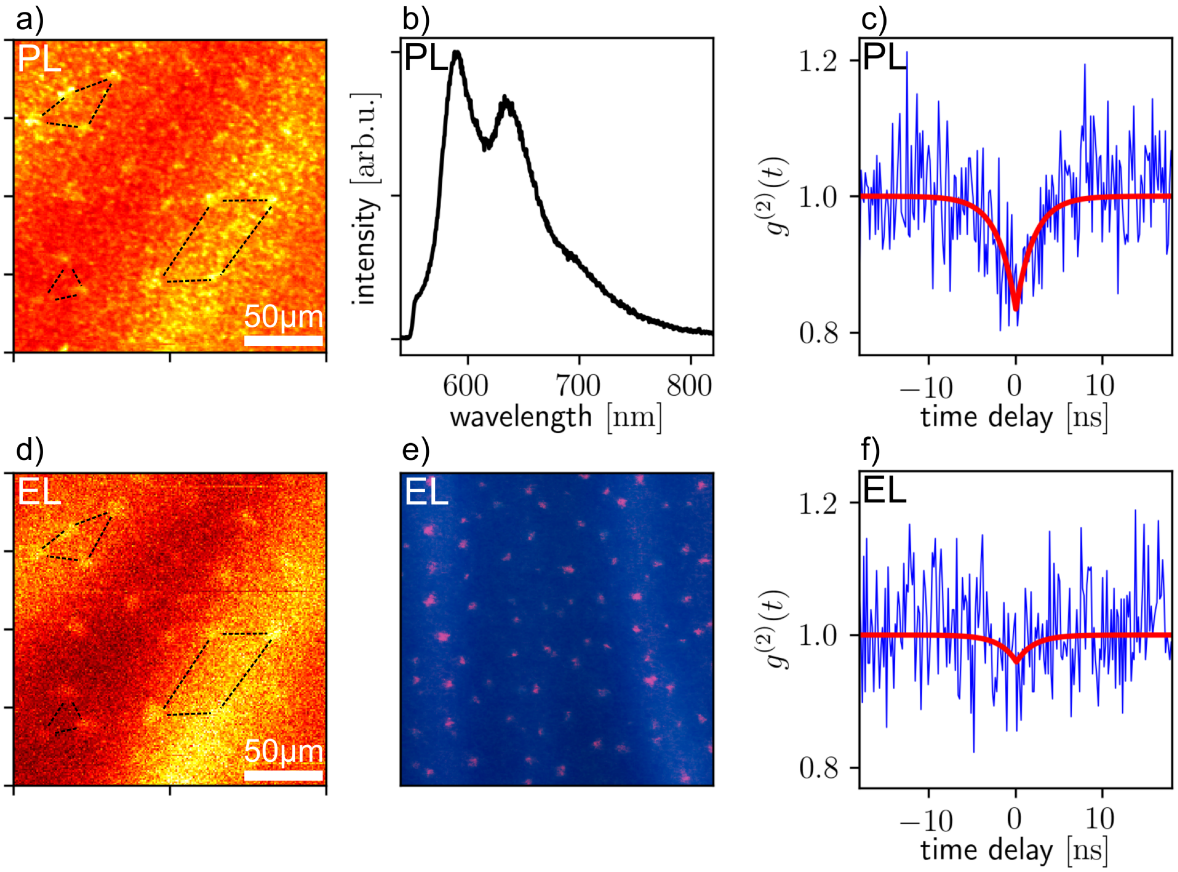

Figure 4.56: Perylene bisimide trimer (PBI) doped OLEDs. a) Photoluminescence (PL) of an OLED doped by perylene bisimide trimers on the single molecule level. b) Photoluminescence spectrum of a bright spot in a) exhibits the spectral signature of a perylene bisimide emitter. The $g^{(2)}$-function of this spot in c) shows distinct antibunching, which indicates that the emission stems from a single molecule. The electroluminescence (EL) intensity map in d) offers an identical emission pattern as the photoluminescence intensity map in a). Dotted lines in the plots a) and d) facilitate the identification of corresponding emission spots. e) shows a micrograph of the sample during electrical excitation. f) The $g^{(2)}$-function of the electrically pumped perylene bisimide trimer molecules exhibit antibunching.

In summary, PBI chromophores are bright and photostable. Using para-xylylene bridges as covalent linkers between several of these chromophores yields multichromophoric systems that exhibit exceptionally bright single photon emission at strong photoexcitation. While effective singlet-singlet-annihilation hinders the simultaneous emission of multiple photons and guarantees single photon emission, effective triplet-triplet-annihilation prevents the formation of a complete, long-living dark state of the multichromophore and, thus, enhance the overall emission rate. This characteristic can be exploited to create an OLEDs with electrically pumped fluorescent single photon emission at room temperature.

4.7 Quantitative Experiments Evaluating the Photon Statistics

As we have seen in Section 2.3, a single photon emitter, for instance a single molecule, generates a stream of photons with a photon statistics, which differs from a Poisson statistics on different time scales. This information is used to derive details about the transition rates between different states of the emitter. In this chapter different methods to analyze the photon statistics and their respective advantages and disadvantages will be discussed, especially in regard to their handling of background contributions. As conclusion, a new measurement scheme is presented which circumvents problems commonly encountered during the measurement of $g^{(2)}$-functions by a Hanbury Brown and Twiss setup.

4.7.1 $g^{(2)}$-functions

For molecules which can be described by a simple, e.g. 3-level-model, an analytical solution for the $g^{(2)}$-function exists [149], which reads

$$g^{(2)}(\tau) = 1 - (1 + \frac{A_2}{A_3})e^{s_1\tau} + \frac{A_2}{A_3}e^{s_2\tau}. \tag{4.2}$$

Here the parameters A_2, A_3, s_1 and s_2 are unwieldy functions of the molecular transition rates, which are not easy to break down. These parameters are in general complex numbers, but can be approximated by real numbers assuming $k_{21} \geq k_{12} \gg k_{23} \geq k_{31}$ [149], where the state *1* is the ground state of the 3-level-system depicted in Figure 4.57. Remembering Section 2.3, we considered a more direct method in which the generating function of a system was calculated with the radiative and non-radiative transition rates of the molecule as free parameters. From this generating function the $g^{(2)}$-function can be derived and compared to the experimental data. No matter if one uses an analytical solution or the generating function approach, moments of order $n \geq 3$ are neglected in the evaluation of the $g^{(2)}$-function. This chapter demonstrates how this can lead to erroneous conclusions about the system and proposes how these problems can be circumvented to reliably determine the transition rates of fluorescent emitters.

Each measurement of a $g^{(2)}$-function contains photon detection events that do not originate from the molecule being analyzed. Among the unwanted detection events are: Photons emitted by other emitters located in the detection volume, scattered light and

dark counts of the avalanche photo diodes (APDs). While all sources generate events that are uncorrelated to the photon statistics of the emitters, effects like scattered light and the dark counts of the APDs generate a Poisson contribution to the $g^{(2)}$-function. These influences on the measured $g^{(2)}$-function can be corrected by suited reference measurements according to

$$g^{(2)}_{corrected}(\tau) = \frac{g^{(2)}_{uncorrected}(\tau) - (1-\rho^2)}{\rho^2}, \tag{4.3}$$

where $\rho = S/(S+B)$ is the signal-to-background ratio [150]. When performing this correction for the $g^{(2)}$-function of a single emitter, we would expect $g^{(2)}(\tau = 0) = 0$. However, according to literature [151, 143] and my own observations, often $g^{(2)}(\tau = 0)$ is well above 0 even after correcting for background noise. The reason for this can be another emitter with likewise non-Poisson photon statistics present in close vicinity to the investigated emitter. The extent to which this superimposed emission can affect the resulting $g^{(2)}$ measurement and whether this effect can be corrected or not will be discussed now.

For the discussion of the problem we assume two emitters as model system. Emitter A is to be analyzed and can be described by a 2-level system for simplicity. As a coexisting emitter, we also assume an emitter B, which can be described by a 3-level system. While emitter A shows only antibunching, the transition rates of emitter B are such that emitter B shows bunching on a similar time scale as the antibunching of emitter A, but is much dimmer than emitter A in the time average. In addition, when emitter B is not in its dark state, it is brighter than emitter A. This is reflected by higher absorption and emission rates in the model for emitter B. It must be remembered that the transition rates in these models describe not only the emitter, but also the experimental setup. Therefore, large differences in the absorption rate may be the result of, for example, the absorption cross section of the molecule at the excitation wavelength, the orientation of the dipole moment with respect to the excitation lasers' polarization, or the intensity of the laser at the position of the emitter. Overall, the transition rates of these two systems, shown in Figure 4.57a), are arbitrary and do not aim to describe a physical system as realistically as possible, but serve as an example to illustrate the core of the problem as simply as possible.

Based on these assumptions, we now can calculate the $g^{(2)}$-function of the superimposed system that is a tensor product mixture the two individual molecular entities. Figure 4.57b) shows the resulting $g^{(2)}$-function on a logarithmic time scale, which allows the comparison to experimental data later in this chapter. The $g^{(2)}$-functions are calculated

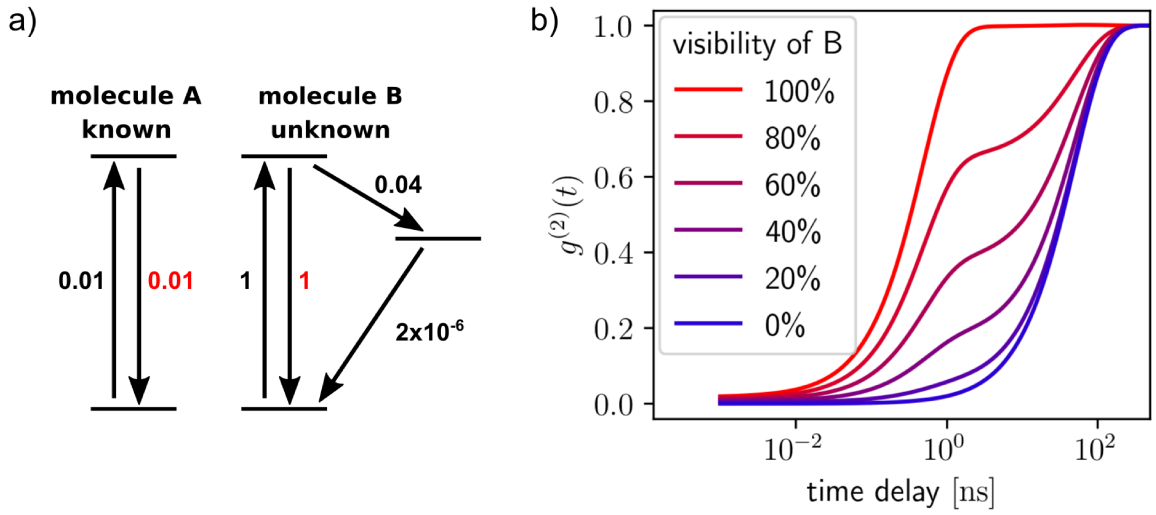

Figure 4.57: Simulation of the $g^{(2)}$-functions for a mixed system comprising an intended emitter A and a coexisting emitter B. The level schemes for both emitters as illustrated in a) where the transition rates are given in units per nanosecond. In b) the $g^{(2)}$-functions for the combined emission of both emitters are plotted for different visibilities of emitter B. At 0 % visibility, only the $g^{(2)}$-function of emitter A is observed with a distinct antibunching. At 100 % visibility of emitter B, both emitters are detected equally efficient, which results in a $g^{(2)}$-function with a narrower antibunching.

for different degrees of visibility of emitter B, ranging from not visible (0 %) to the same visibility as emitter A (100 %). Here, a low visibility is caused either by a situation where the unknown emitter is not located perfectly in the center of the detection volume or by a misaligned transition dipole of the emitter with respect to the optical axis of the objective. At 0 % visibility, it is possible to determine the transition rates k_{12} and k_{21} of molecule A from the width of the antibunching. At 100 % visibility of emitter B, we observe again an antibunching in the $g^{(2)}$-function, which is however much narrower. Without knowing that emitter B is present, one would derive incorrect transition rates for molecule A. Thus, the question arises: Is there a way to detect the presence of emitter B? For this purpose, let us have a look at the $g^{(2)}(\tau = 0)$ value, which is asymptotically approximated in 4.57b. As we notice, the $g^{(2)}(\tau = 0)$ value is influenced only very little by the presence of emitter B. In fact, the difference to the neat single molecule configuration can be arbitrary small and, therefore, can be hidden in the noise of the experiment if emitter B exhibits unfavorable transition rates. The reason for this is the different fraction of fluorescence intensity provided by the two emitters A and B in the experiment. If their fluorescence intensity would

be equal, one would observe a $g^{(2)}(\tau = 0)$ value of 0.5. Therefore analyzing the $g^{(2)}(\tau = 0)$ value is not a secure method to identify a disturbing emitter.

Other approaches to identify a possible, yet unknown emitter would be the analysis of the emission spectrum or the polarization dependence of the fluorescence. However, these methods are also linearly sensitive to the intensity of the superimposed emitter, which can be arbitrarily weak. In contrast, by its nature the number of events of the $g^{(2)}$-function are sensitive to the square of the emitted intensity in a certain time interval, which can be significant when the unknown emitter exhibit photoluminescence blinking. To summarize the problem:

> *An unknown emitter with non-Poisson photon statistics that is emitting weakly enough not to be detected by its emission intensity, can alter the shape of the $g^{(2)}$-function, e.g. detected by a Hanbury Brown and Twiss setup, to any extent and lead to erroneous conclusion about the system. Simultaneously, the $g^{(2)}(\tau = 0)$ value for the superimposed system of known and unknown emitter can persist arbitrary close to 0.*

What are possible solutions to this problem? One method to identify unwanted emitters is the measurement of higher orders of the photon statistics, which will be discussed in the next section.

4.7.2 $g^{(3)}$-functions

In general, three APDs are required to measure the third order correlation function on time scales shorter than the dead time of the APDs. Such an experimental setup is illustrated in Figure 4.58. Here, two beamsplitters distribute the emitted light and the $g^{(3)}$-correlation are calculated by the time differences between the photon events detected by the three individual APDs.

To test the usability of this approach, an experiment was conducted with the experimental data recorded at discrete time intervals of 165 ps. For the histogram of 3-photon-events, logarithmic time intervals between $165\,\text{ps}\times 2^{n}$ and $165\,\text{ps}\times 2^{(n+1)}$ were used, while theoretical simulations were calculated on an identical scale of time.

Let us start by analyzing the theoretical differences between the $g^{(3)}$-function and the $g^{(2)}$-function for a system comprising emitters A and B, the visibility of the later was chosen to be 25 % as an example. In Figure 4.59a the outer product between two $g^{(2)}$-functions

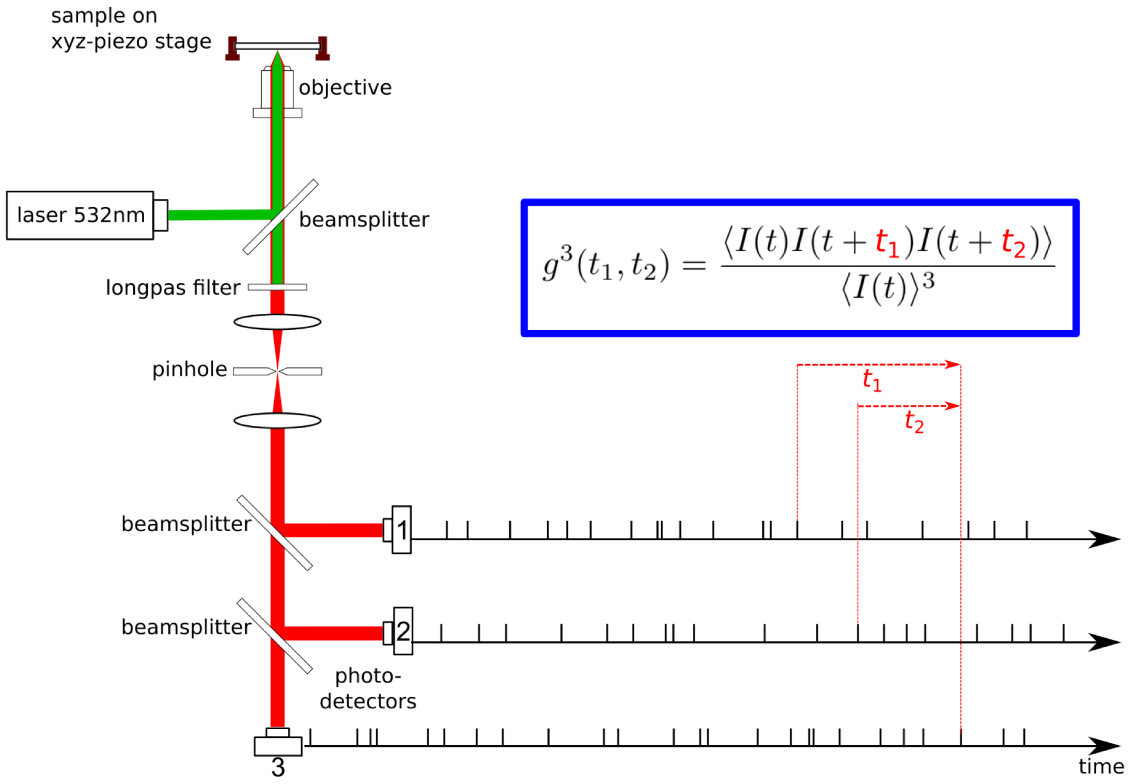

Figure 4.58: Experimental setup to determine the $g^{(3)}$-function of the photon statistics of an emitting host-guest-system.

is plotted for the mixed system. These data contain the same information as the 2D-graph in Figure 4.57b. In comparison, the $g^{(3)}$-function is plotted in Figure 4.58b. Here the influence of the disturbing emitter B is clearly visible as a peak at $\approx 4 = \log_2(t/165\,\text{ps})$, i.e. $t \approx 2\,\text{ns}$, which corresponds to the duration of an excitation-emission-cycle of molecule B. Simultaneously, the plateau and the decay of the $g^{(3)}$-function at $\approx 10 = \log_2(t/165\,\text{ps})$, i.e. $t \approx 200\,\text{ns}$, correspond to the duration of the excitation-emission-cycle of molecule A.

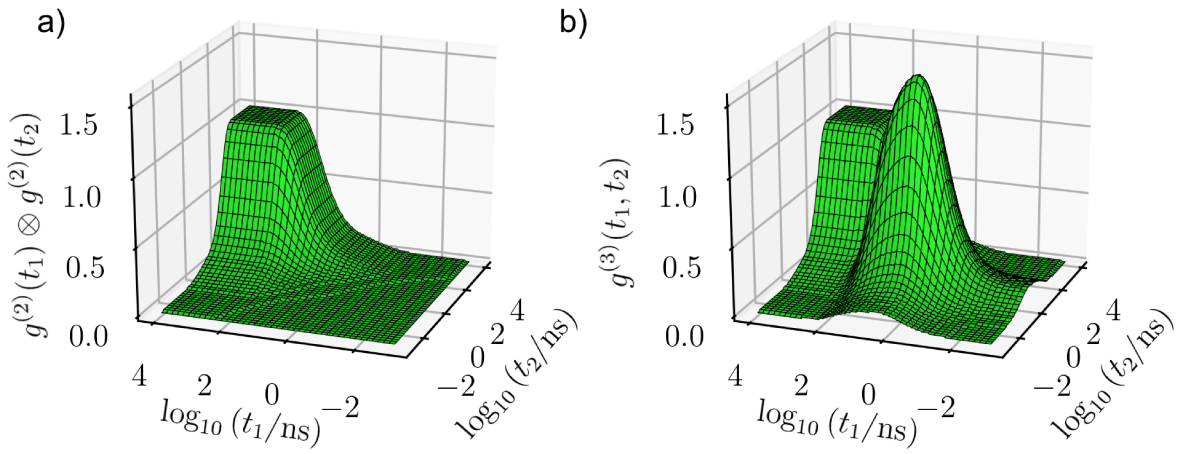

Figure 4.59: For a system comprising emitter A and B, described in the text, the outer product of $g^{(2)}$ and $g^{(2)}$ is plotted in a) while the $g^{(3)}$-function is plotted in b). While the influence of the superimposed emitter B can be identified as peak in the $g^{(3)}$-function, hardly any change can be observed in the $g^{(2)} \otimes g^{(2)}$-function.

Motivated by the differences between graphs 4.59a and b) and the fact that the $g^{(3)}$-function is equal to the outer product of the $g^{(2)}$-function if and only if the system under investigation is in the same state after the emission of a photon, a detailed analysis of the difference between these functions

$$\Delta(t_1, t_2) = g^{(3)}(t_1, t_2) - g^{(2)}(t_1) \otimes g^{(2)}(t_2) \tag{4.4}$$

will be presented. The function $\Delta(t_1, t_2)$ can be used to detect the presence and quantify the influence of a coexisting emitter. Figure 4.60a and b illustrates this difference for the neat molecules A and B. For both cases the $g^{(3)}$-function does not contain more information than the $g^{(2)}$-function does as the molecule is always in the same ground state after the emission of a photon. This leads to $\Delta(t_1, t_2) = 0$. The situation changes if the emitters A and B are mixed as shown in Figure 4.60c. Here, the influence of the additional emitter B remains visible as a peak at 2 ns. This illustrates how the $\Delta(t_1, t_2)$-function is able to identify the coexistence of several emitters in case of suited transition rates.

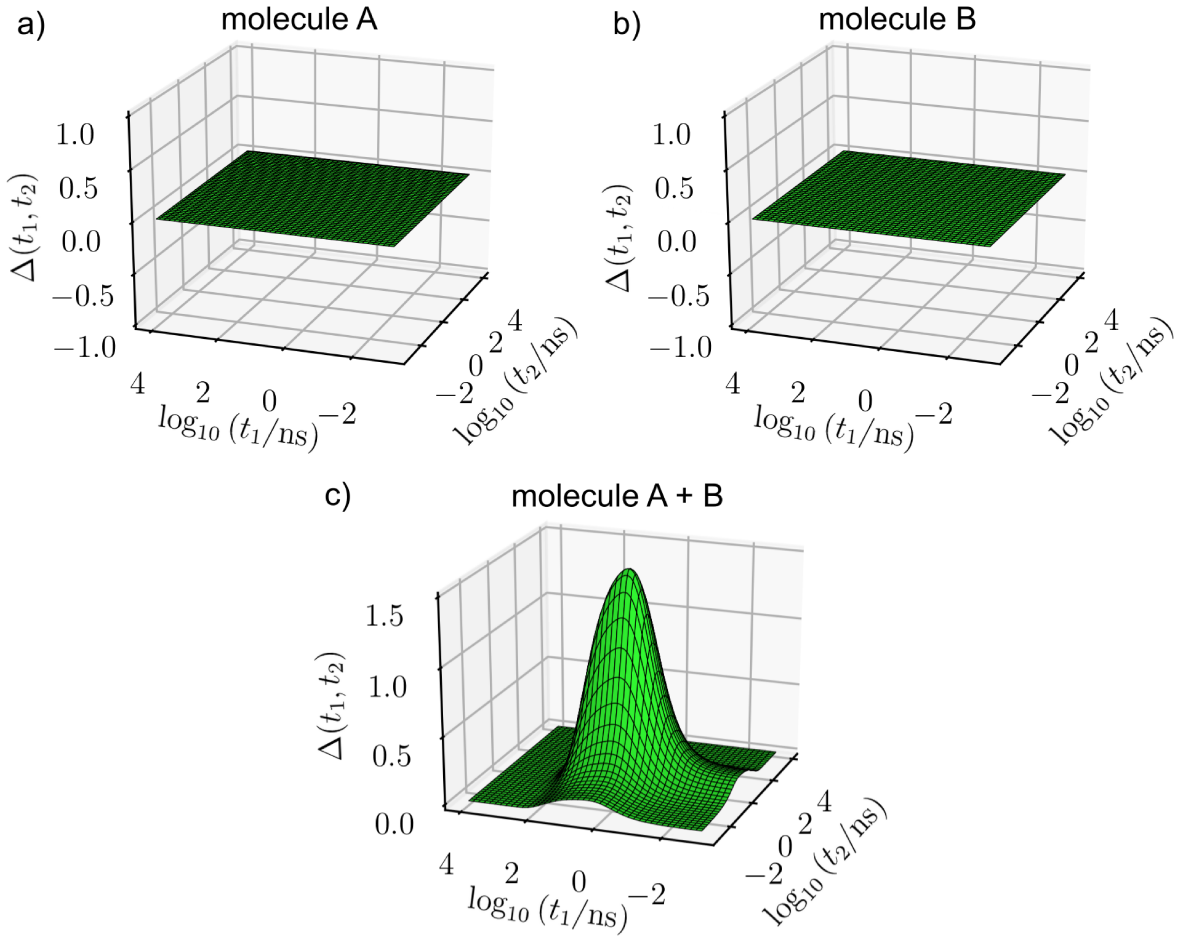

Figure 4.60: The function $\Delta(t_1, t_2) = g^{(3)}(t_1, t_2) - g^{(2)}(t_1) \otimes g^{(2)}(t_2)$ is plotted for an A, B and A+B model system to analyze the influence of additional emitters. a) and b) show this quantity for the pure single molecule A and B. For each configuration, there is only one ground state adopted by the molecule after the emission of a photon, which results in $\Delta(t_1, t_2) = 0$. For mixed systems, the influence of the superimposed emitter becomes apparent in the correlation function. In c), the correlation function for a mixed A and B emitter system (discussed in the text) exhibits a peak, which indicates the influence of the coexisting emitter B.

How does the $\Delta(t_1, t_2)$-function look like if the emission from the molecule A is superimposed by an identical molecule A', which is located slightly outside the optical axis? For the respective simulation, the visibility of emitter A' was set to 25 % and the correlation functions are shown in Figure 4.61. While in graphs a) and b) the $g^{(2)}(t_1) \otimes g^{(2)}(t_2)$ and $g^{(3)}(t_1, t_2)$ functions appear to be identical, the $\Delta(t_1, t_2)$ function reveals a difference below the characteristic lifetime of $1/k_{12} + 1/k_{21} = 200\,\text{ns}$ of the two emitters.

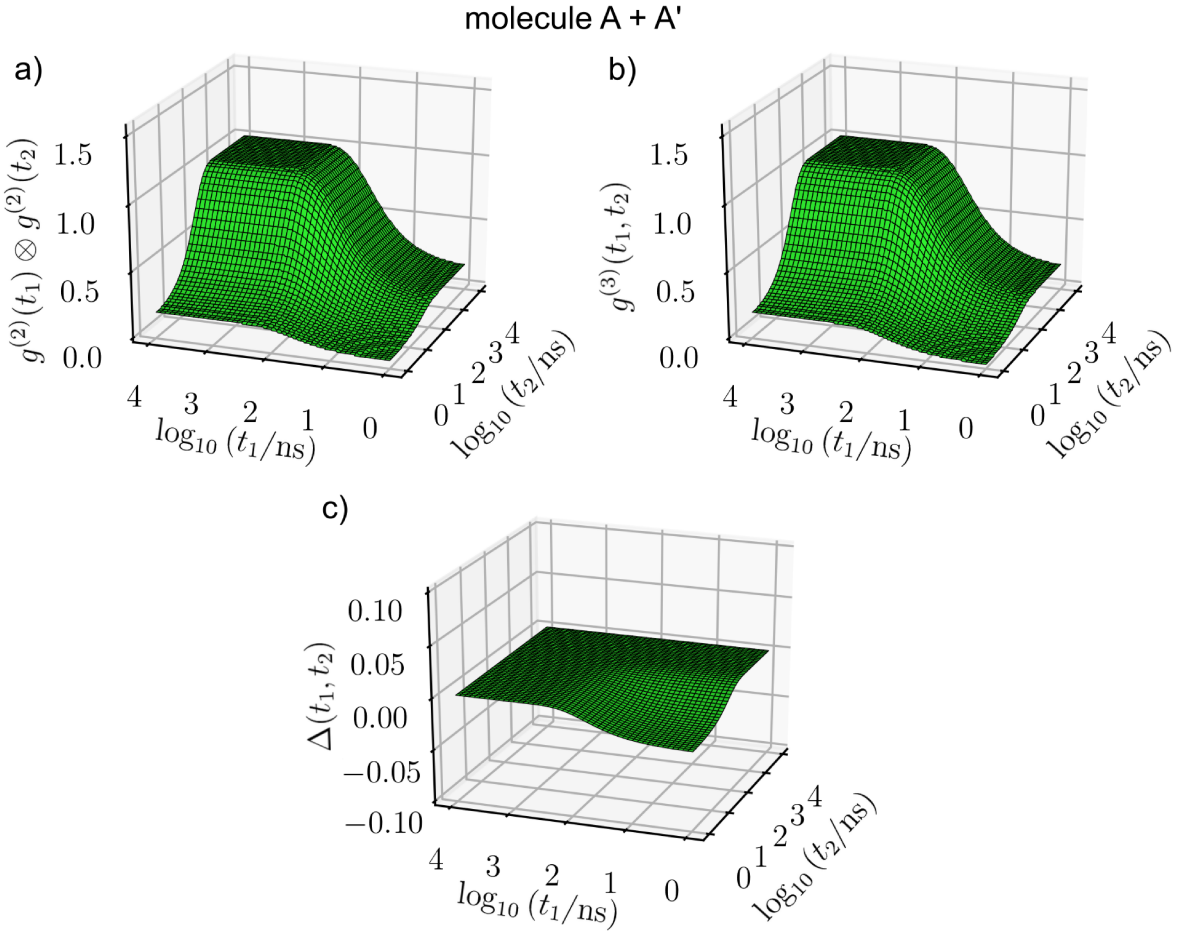

Figure 4.61: Simulations of the correlation functions for a mixed system of an emitter A with transition rates $k_{12} = k_{21} = 0.01\,\text{ns}^{-1}$ and an identical emitter A' with visibility 25 %. The $\Delta(t_1, t_2)$ function in graph c) represents the difference between the correlation functions $g^{(2)}(t_1) \otimes g^{(2)}(t_2)$ and $g^{(3)}(t_1, t_2)$ in a) and b), which differ below $1/k_{12} + 1/k_{21} = 200\,\text{ns}$.

After these theoretical considerations, we will have a look at the $g^{(3)}$-experimental data obtained on PBI monomers. The individual measurement last for 2 s at an excitation power of 0.5 mW and 532 nm excitation wavelength. In Figure 4.62 the recorded $g^{(3)}$-function is plotted, with each 3-photon-event illustrated as thin red dot. White trenches with a lower number of detection events can be identified at $t_1 = 0$, $t_2 = 0$ and $t_1 = t_2$. The reason for this is the low probability to detect two photons simultaneously, as it is also the case for an antibunching in the $g^{(2)}$-function. Projecting all events onto the t_1 axis, we find a $g^{(2)}(t = 0)$ value of 0.25.

The experimental data, presented in Figure 4.62, were transformed by folding and binning to a logarithmic time scale, which allows for comparison with the simulations before. In Figure 4.63 the data are presented on logarithmic timescales. In a) and b) the $g^{(2)}(t_1) \otimes g^{(2)}(t_2)$ and $g^{(3)}(t_1, t_2)$-functions are plotted. Please notice that in the experiment the number of $g^{(3)}$-events is significantly lower than the number of $g^{(2)}$-events, which results in a higher noise level in the normalized $g^{(3)}$-function. Finally, in Figure 4.63c the difference between the two functions is presented. While this difference is zero on long timescales above 10 ns, a significant lower amount of events was recorded for times below 5 ns, which is characteristic for the excitation-emission-cycle of a PBI monomer. In agreement to the theoretical simulation presented in Figure 4.60d, this finding suggests that indeed, at least, a second monomer M molecule contributes to the detection events of the experiment.

In summary, measuring the $g^{(3)}$-function can provide a useful tool to detect unintended emitters in photon statistics experiments on single quantum emitters. Further, additional information can be obtained for emitters with more than one radiative transition in different molecular states. This can be relevant for multichromophoric molecules with weak coupling between the chromophores or quantum dots with biexcitonic states. Like other photon correlation experiments, the measurement of the $g^{(3)}$-function is especially limited by the small rate of $g^{(3)}$-correlation events whose detection probability is proportional to the emitted intensity to the third power and, therefore, requires for strong emission of the emitter.

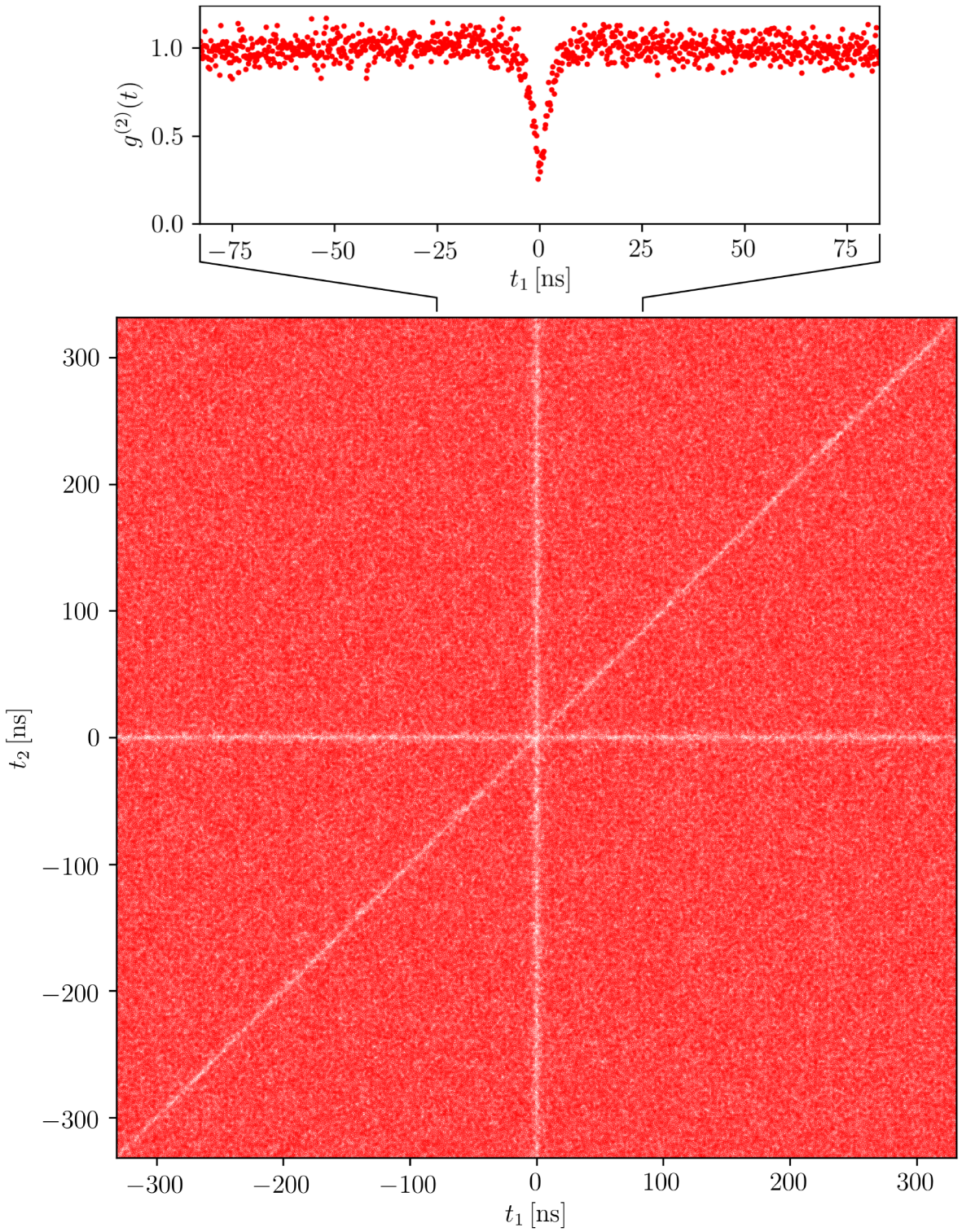

Figure 4.62: $g^{(3)}$-events of the emission of a perylene bisimide monomer. Each 3-photon-event is marked by a thin red dot. In the vicinity of $t_1 = 0$, $t_2 = 0$ and $t_1 = t_2$ a lower than average density of detection events can be observed. Projection on the t_1 axis yields the second order correlation function with $g^{(2)}(t = 0) = 0.25$.

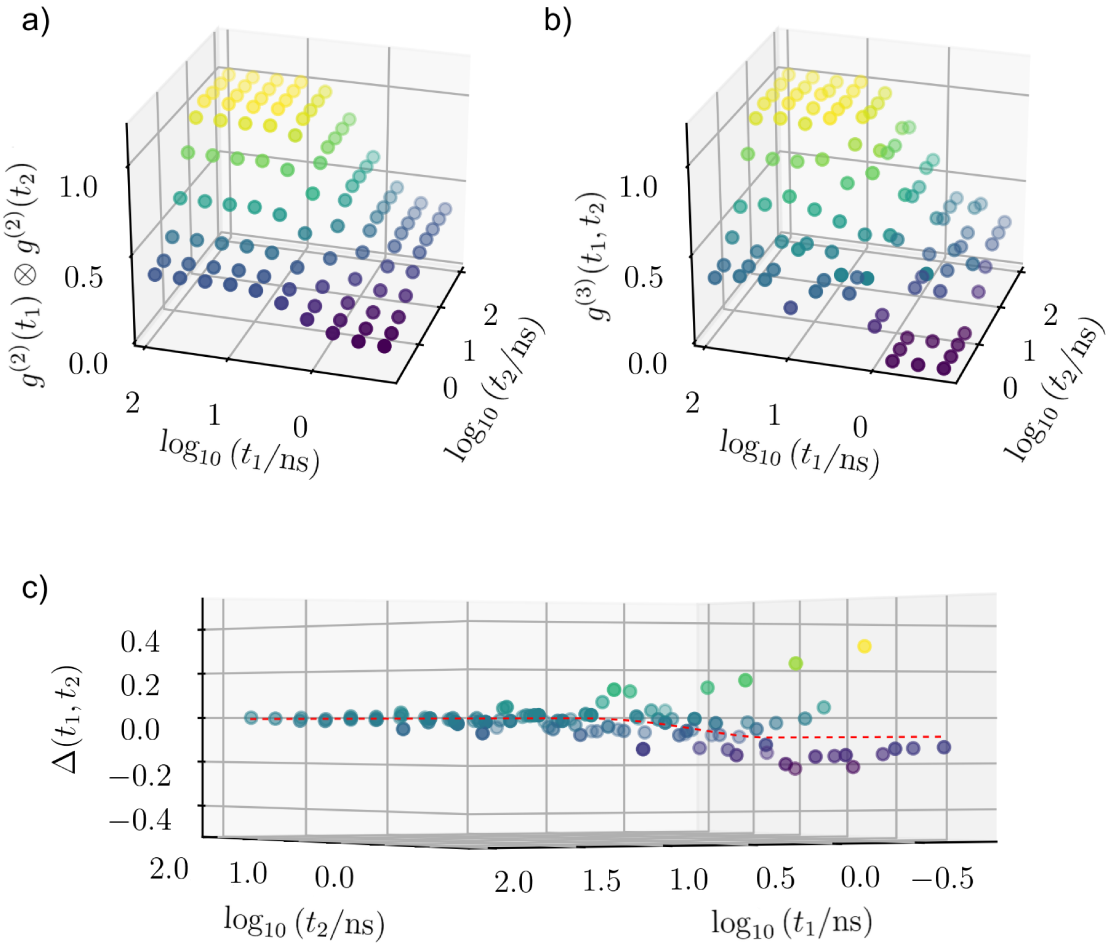

Figure 4.63: Experimental results of a $g^{(3)}$-measurement on a perylene bisimide monomer. In a) the outer product of two $g^{(2)}$-functions and in b) the $g^{(3)}$-function is plotted. In c) the difference between a) and b) is calculated. This function, $g^{(3)}(t_1, t_2) - g^{(2)}(t_1) \otimes g^{(2)}(t_2)$, shows negative values at short time intervals below 5 ns. The dashed red line represents a guide to the eye.

4.7.3 Stepfunction Photoexcitation

A totally different way to interpret the $g^{(2)}(t)$-function is to relate it to the photoluminescence transient of an emitter which is in its ground state at $t = 0$. One of the two avalanche photo diodes in a classical Hanbury Brown and Twiss setup is used to herald the emitter being in the ground state by detecting an emitted photon. Consequently, the second photo diode records the photoluminescence transient of the emitter after re-excitation.

The corresponding photoluminescence transient function can be obtained in a two step process: In the first step, the emitter is initialized in its ground state by waiting for a sufficient time interval without photoexcitation. In the second step, the continuous wave photoexcitation is turned on and the photoluminescence transient is observed for a desired time interval. After this second step the excitation laser can be turned off again and the measurement can be repeated at a kHz to MHz repetition rate to increase the signal to noise ratio.

This measurement technique provides some decisive advantages over the $g^{(2)}(t)$-function measurement by a Hanbury Brown and Twiss setup: Firstly, superimposed emitters only contribute linearly to the detection signal. Therefore, they can be identified by analyzing the polarization or spectral resolved photoluminescence. Secondly, the measurement time is significantly reduced, especially, for weak emitters or detection schemes with low photon collection efficiency, because the observation of the photoluminescence transient function requires only one photon detection event instead of two. Lastly, the measurement does not require just a single quantum emitters to observe the associated $g^{(2)}(t)$-function but measurements on an ensemble of individual emitters are possible. Therefore, the signal-to-noise ratio is inherently better. This technique has been applied in the past to examine conjugated polymers [152] with measurements accessing the microsecond time range of the photoluminescence transient. Today, with the development of fast optical modulators, similar experiments can be performed on the nanosecond timescale, i.e. on fluorescent emitters.

To demonstrate this approach, a sample of the TADF emitter *TXO-TPA* (2-[4-(diphenylamino)phenyl]-10,10-dioxide-9H-thioxanthen-9-one) mixed in a concentration of 10^{-4} wt% with a mCP (1,3-Bis(N-carbazolyl)benzene) matrix was dropcasted on a glass substrate. The compounds are illustrated in their chemical structure in Figure 4.64.

In collaboration with Jonas Gehrig, a master student in our group, a setup was designed and installed to allow for step function photoexcitation with a rise time of about 1 ns. In addition to the confocal microscopy setup, that was described in Chapter 3, a fast electro-optical modulator (Qubig PCA2B-532) was utilized to turn the light of the laser on

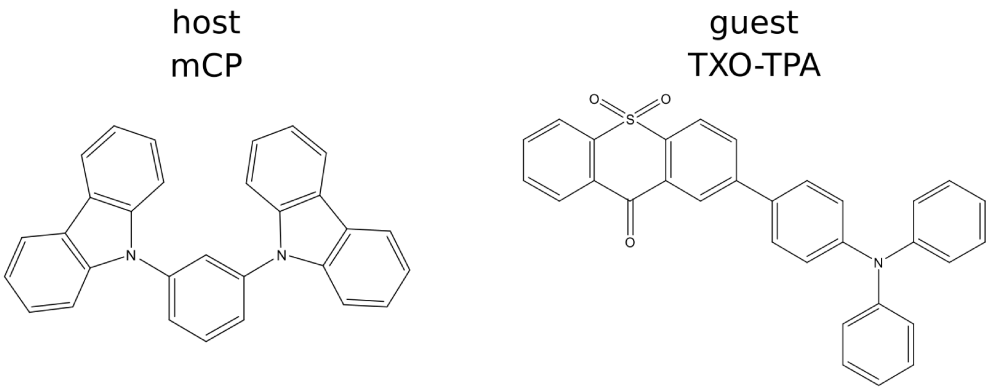

Figure 4.64: Chemical structures of 1,3-Bis(N-carbazolyl)benzene (mCP), used as host for the guest molecule 2-[4-(diphenylamino)phenyl]-10,10-dioxide-9H-thioxanthen-9-one (TXO-TPA).

and off. By means of this setup, the sample was illuminated by a 532 nm laser and the photoluminescence transient was recorded by a silicon avalanche photodetector with a time resolution of 700 ps.

The measurement procedure described above was repeated for different excitation intensities with the goal to record a series of characteristic photoluminescence transients that can be compared to simulations to derive the molecular transition rates. For this reason, it is desirable to perform the measurements with a range of excitation powers that span several orders of magnitude, while the exact values are not crucial. The respective transients of the *TXO-TPA* emitters are shown in Figure 4.65.

Apart from the effect of averaging over many emitters, the measured transients indeed behave exactly like $g^{(2)}$-functions measured on single emitters, both in their shape and in their dependence on excitation power. In Figure 4.66a, the power dependent transients are plotted on a logarithmic time axis. Here, two distinct time periods can be identified before steady state photoluminescence. Within the first 100 ns of each respective transient an increase in fluorescence intensity can be observed for all excitation intensities. Within this period, the *TXO-TPA* emitters reach an equilibrium in the occupation probability between the singlet excited state and the ground state. In the case of the lowest excitation power of 8 µW, this state is slightly darker than the steady state. For all other excitation intensities above 8 µW this state shows up as a peak in the photoluminescence transient. Finally, on the time scale of µs, the *TXO-TPA* emitters reach an equilibrium between singlet, triplet and ground state and thus steady-state fluorescence intensity.

All observed time constants, as well as the height of the fluorescence peak depend on the transition rates between the molecular states. To derive these transition rates for this

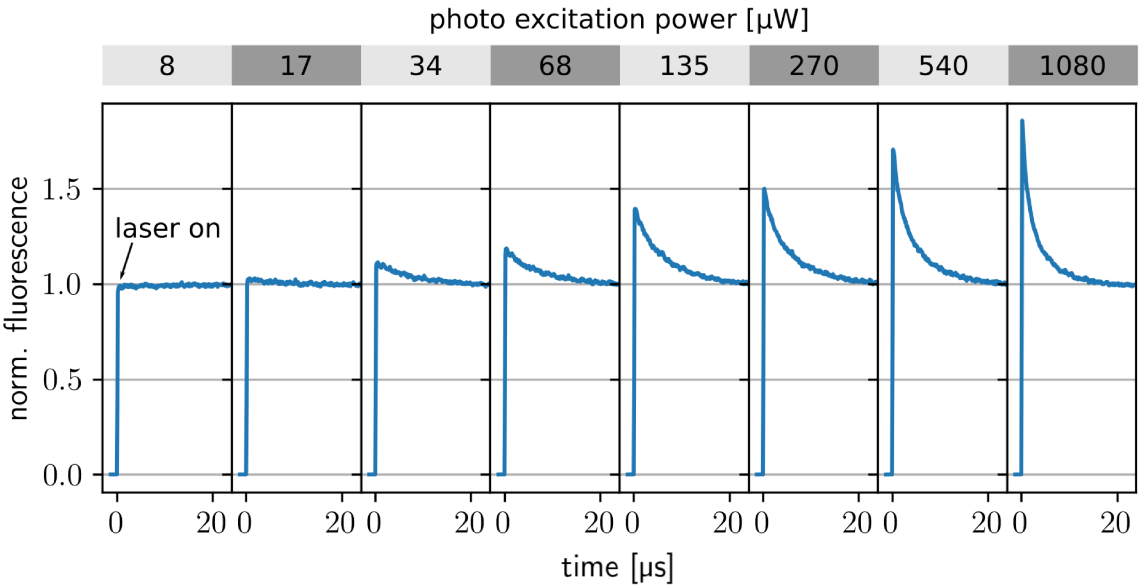

Figure 4.65: A series of normalized photoluminescence transients of TXO-TPA doped in mCP recorded at different photo excitation powers after the laser is turned on at $t = 0$.

material combination, a TADF model system has been utilized, which has three levels and is depicted in Figure 4.66c. In this model, the rate k_{12} at which the molecules are excited from the ground state to the first excited state is proportional to the excitation power. By its nature, this model is a simplification of the emitters in the sample, where each molecule interacts with its local environment, which affects its transition rate. However, a global fit, i.e. fitting one model simultaneously to all photoluminescence transients, can yield mean values for these transition rates. The obtained time constants for each transition are shown in Figure 4.66d with the associated simulated excitation power dependent transients shown in Figure 4.66b. Error estimations of the obtained transition rates are ±5 % for k_{23} and k_{32} and ±25 % for r_{21}.

The aim of this chapter is to present the approach of using a step function photoexcitation in combination with luminescent transient recording applied to the nanosecond range as an alternative measurement method to common methods, rather than giving a in-depth insight about the analyzed material system, which was used as an example. Usually, the information about the transition rates obtained from this experiment is gained by more elaborate measurement techniques. Either by measurements on single molecules, where sample preparation often presents a challenge, or by temperature-dependent fluorescence lifetime measurements, for which a cryostat is required, which in turn places constraints on the samples to be studied. Here it was shown, how the use

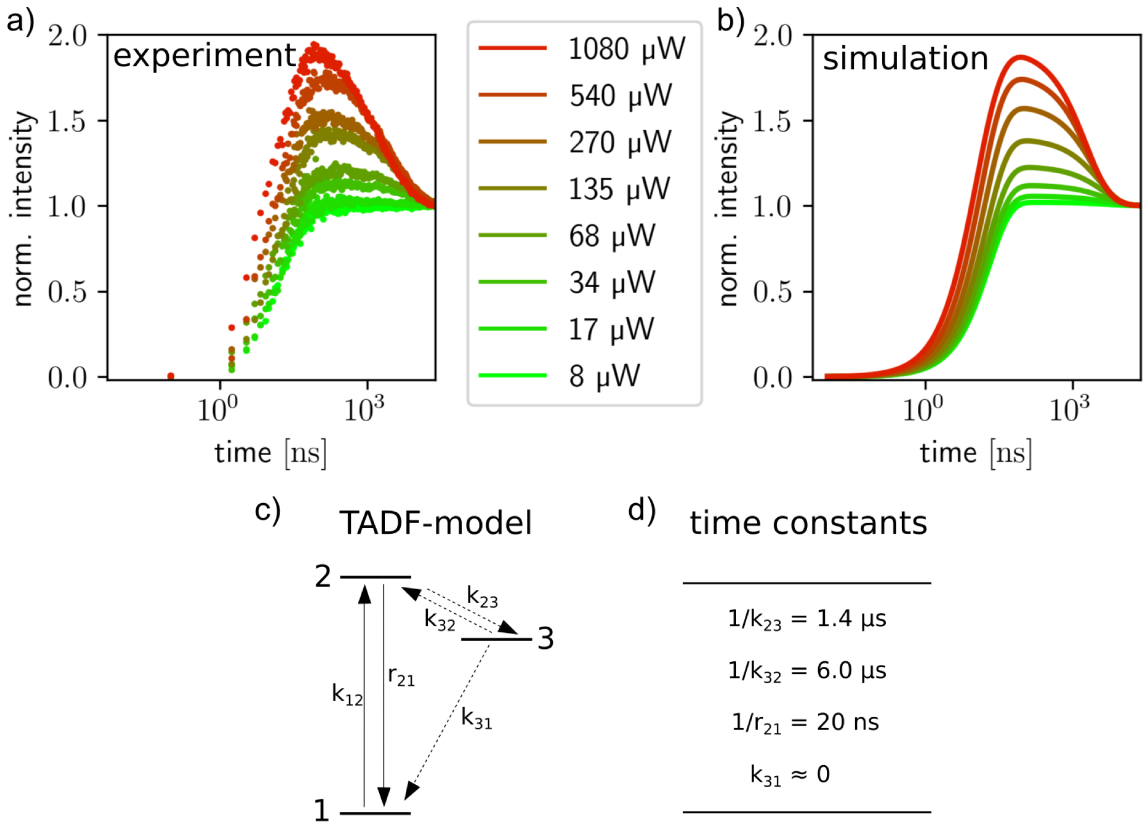

Figure 4.66: a) A series of measured photoluminescence transients of TXO-TPA doped in mCP at different photo excitation powers on a logarithmic timescale. The transition rates within the TADF-model depicted in c) are fitted to the experimental data, which yields the simulated transients shown in b) and the respective transition rates shown in d).

of a step function photoexcitation in combination with luminescent transient recording generates a rich photoluminescence response function that contains information about the intramolecular transition rates of an emitter. For closed-shell fluorescent and TADF emitters, these photoluminescence response functions depend particularly sensitively on the singlet-triplet transition rates of the respective molecule. In the future, this approach could also be a simplified method to study external factors influencing molecular transition rates.

5 Conclusion

In the introduction of this work, it was pointed out that the variety of possible emitters within organic chemistry is almost unlimited. To perform an efficient and targeted search for the best emitters it is necessary to understand the mechanisms to which excitons in molecules are subjected. Especially, when new emission concepts are applied, it is necessary to disclose the underlying mechanisms of emission and non-radiative losses. This work analyzed a variety of molecular emitters and used a wide range of methods to reveal the underlying pathways to light emission.

It has been shown how various approaches on the molecular design can be used to improve different aspects of molecular emitters. For example, for linearly coordinated copper compounds it was shown how the employment of carbazolate donor ligands combined with electrophilic carbenes can be utilized to create a small singlet-triplet energy splitting. This switches light emission from phosphorescence to temperature activated delayed fluorescence and thus, significantly increases the radiative transition rates of the compound. In another example, it was shown how perylene bisimide chromophores can be interconnected to macrocycles, which utilize exciton-exciton-annihilation to quenches dark states as well as prevent the simultaneous emission of multiple photons from just one macrocycle which makes them exceptionally bright single photon sources at room temperature. These are selected examples of the results of this work, which contribute to a fundamental understanding and an efficient search for new molecular emitters in future.

One challenge, other than the design of the molecular emitters themselves, is to control the influence of the surrounding matrix. It has been demonstrated that this interaction between emitter and matrix can substantially enhance the light emission. However, the most suitable matrix used in the scientific experiment may be different from the preferred matrix for an optoelectronic device. A possible solution in future could be to sysnthetize emitters together with their local environment as macromolecules, so that not only the processes in the chromophore but also the interaction with the environment can be fully controlled.

6 Summary

This PhD thesis addresses the photophysics of selected small organic molecules with the purpose of using them for efficient and even novel light sources. In particular, the studies presented focused on revealing the underlying exciton dynamics and determining the transition rates between different molecular states. It was shown how the specific properties and mechanisms of light emission in fluorescent molecules, molecules with phosphorescence or thermally activated delayed fluorescence (TADF), biradicals, and multichromophores can be utilized to build novel light-emitting devices. The main tool employed here was the analysis of the emitters' photon statistics, i.e. the analysis of the temporal distribution of emitted photons, during electrical or optical excitation.

In the introduction of this work, the working principle of an organic light-emitting diode (OLED) was introduced, while Chapter 2 provided the physical background of the relevant properties of organic molecules and their interaction with light. In particular, the occurrence of discrete energy levels in organic semiconductors and the process of spontaneous light emission were discussed. Furthermore, in this chapter a mathematical formalism was elaborated with the goal to find out what kind of information about the studied molecule can be obtained by analyzing its photon statistics. It was deduced that the intensity correlation function $g^{(2)}(t)$ contains information about the first two factorial moments of the photon statistics and that higher order factorial moments do not contain any additional information about the system under study if the system is always in the same state after the emission of a photon. To conclude the introductory part, Chapter 3 introduced the utilized characterization methods including confocal microscopy of single molecules, time correlated single photon counting and temperature dependent photoluminescence measurements.

To provide the background necessary for an understanding of for the following result chapters, in Section 4.1 a closer look was taken at the phenomenon of blinking and photobleaching of individual molecules. For a squaraine-based fluorescent emitter rapid switching between a bright and dark state was observed during photoexcitation. Using literature transition rates between the molecular states, a consistent model was developed that is able to explain the distribution of the residence times of the molecule in the bright

and dark states. In particular, an exponential and a power-law probability distribution was measured for the time the molecule resides in tis bright and dark state, respectively. This behavior as well as the change in photoluminescence intensity between the two states was conclusively explained by diffusion of residual oxygen within the sample, which had been prepared in a nitrogen-filled glovebox. For subsequent samples of this work, thin strips of atomic aluminum were deposited on the matrices to serve as oxygen getter material. This not only suppressed the efficiency of photobleaching, but also noticeably prolonged the time prior to photobleaching, which made many of the following investigations possible in the first place.

For emitters used in displays, emission properties such as narrow-band luminescence and short fluorescence lifetimes are desired. These properties can be influenced not only by the emitter molecule itself, but also by the interaction with the chosen environment. Therefore, before focusing on the photophysics of individual small organic molecules, Section 4.2 highlighted the interaction of a perylene bisimide-based molecular species with its local environment in a disordered polymethyl methacrylate matrix. In a statistical approach, individual photophysical properties were measured for 32 single molecules and correlations in the variation of the properties were analyzed. This revealed how the local polarity of the molecules' environment influences their photophysics. In particular, it was shown how an increase in local polarity leads to a red-shifted emission, narrower emission lines, broader vibronic splitting between different emission lines in combination with a smaller Huang-Rhys parameter, and a longer fluorescence lifetime. In the future, these results may help to embed individual chromophores into larger macromolecules to provide the chromophore with the optimal local environment to exhibit the desired emission properties.

The next two sections focused on a novel and promising class of chromophores, namely linear coordinated copper complexes, synthesized in the group of Dr. Andreas Steffen at the Institute of Inorganic Chemistry at the University of Würzburg. In copper atoms, the d-orbitals are fully occupied, which prevents undesirable metal-centered d-d* states, which tend to lie low in energy and recombine non-radiatively. Simultaneously, the copper atom provides a flexible coordination geometry, while complexes in their linear form are expected to exhibit the least amount of excited state distortions. Depending on the chosen ligands, these copper complexes can exhibit phosphorescence as well as temperature activated delayed fluorescence. In Section 4.3, a phosphorescent copper complex with a chlorine atom and a 1-(2,6-diisopropylphenyl)-3,3,5,5-tetramethyl-2-pyrrolidine-ylidene-ligand was tested for its suitability as an optically active material in an OLED.

For this purpose, an OLED with a polyspirobifluorene-based copolymer matrix and the dopant at a concentration of 20 wt% was electrically excited. Deconvolution of the emission spectrum in contributions from the matrix and the dopant revealed that 60 % of the OLEDs emission was due to the copper complex. It was also shown that the shape of the emission spectrum of the copper complex remains unchanged upon incorporation into the OLED, but is red-shifted by about 233 meV.

In Section 4.4, a second copper complex exhibiting thermally activated delayed fluorescence was analyzed. This complex comprised a carbazolate as well as a 2-(2,6-diisopropyl)-phenyl-1,1-diphenyl-isoindol-2-ium-3-ide ligand and was examined in the solid state and at the single-molecule level, where single photon emission was recorded up to an intensity of 78'000 counts per second. The evaluation of the second-order autocorrelation function of the emitted light proved an efficient transition between singlet and triplet excited states on the picosecond time scale. In the solid state, the temperature-dependent fluorescence decay of the complex was analyzed after pulsed photoexcitation in the temperature range between 300 K and 5 K. From these measurements, a small singlet-triplet energy gap of only 65 meV and a triplet sublevel splitting of 3.0 meV were derived. The transition rates between molecular states could also be determined. Here, the fast singlet decay time of τ_{S1} = 9.8 ns proved the efficient thermally activated delayed fluorescence process, which was demonstrated for the first time for this new class of copper(I) complexes thus.

While the use of thermally activated delayed fluorescence is a potential way to harness otherwise long-living dark triplet states, radicals completely avoid dark triplet states. However, this usually comes with the huge drawback of the molecules being chemically unstable. Therefore, two chemically stable biradical species were synthesized in the framework of the DFG research training school GRK 2112 on *Molecular biradicals: structure, properties and reactivity*, by Yohei Hattori in the group of Prof. Dr. Christoph Lambert and Rodger Rausch in the group of Prof. Dr. Frank Würthner at the Institute of Organic Chemistry at the University of Würzburg, respectively. In Section 4.5, it was investigated how these molecules can be used in OLEDs.

In the first isoindigo based biradical (6,6'-bis(3,5-di-tert-butyl-4-phenoxyl)-1,1'-bis(2-ethylhexyl)-[3,3'-biindolinyl-idene]-2,2'-dione) two tert-butyl moieties kinetically block chemical reactions at the place of the lone electrons and an electron-withdrawing core shifts the electron density into the center of the chromophore. With these properties, it was possible to realize a poly(p-phenylene vinylene) copolymer based OLED doped with the biradical and to observe luminescence during optical as well as electrical excitation. Analyzing shapes of the photo- and electroluminescence spectra at different doping

concentrations, Förster resonance energy transfer was determined to be the dominant transition mechanism for excitons from the matrix to the biradical dopants.

Likewise, OLEDs could be realized with the second diphenylmethylpyridine based biradical (4-(5-(bis(2,4,6-trichlorophenyl)methyl)-4,6-dichloropyridin-2-yl)-N-(4-(5-(bis(2,4,6--trichlorophenyl)methyl)-4,6-dichloropyridin-2-yl)phenyl)-N-(4-methoxyphenyl)aniline) as dopant. In this biradical, chlorinated diphenylmethyl groups protect the two unpaired electrons. Photo- and electroluminescence spectra showed an emission in the near infrared spectral range between 750 nm and 1000 nm. Also, Förster resonance energy transfer was the dominant energy transfer mechanism with an transfer efficiency close to 100 % even at doping concentrations of only 5 wt%. In addition to demonstrating the working OLEDs based in biradicals, the detection of luminescence of the two biradical species in devices also constitutes an important step toward making use of experimental techniques such as optically detected electron spin resonance, which could provide information about the electronic states of the emitter and their spin manifold during OLED operation.

Another class of emitters studied are molecules in which several chromophores are covalently linked to form a macrocyclic system. The properties of these multichromophores were highlighted in Section 4.6. Here, it was analyzed how the photophysical behavior of the molecules is affected by the covalent linking, which determines the interaction between the chromophores. The first multichromophore, 2,2'-ditetracene, was synthesized by Lena Ross in the group of Prof. Dr. Anke Krüger at the Institute of Organic Chemistry at the University of Würzburg and was analyzed in this work both at the single-molecule level and in its aggregated crystalline form. While the single crystals were purified and grown in a vertical sublimation oven, the samples for the single molecule studies were prepared in matrices of amorphous polymethyl methacrylate and crystalline anthracene. Tetracene was analyzed concurrently to evaluate the effects of covalent linking. In samples where the distance between two molecules is sufficiently large, tetracene and 2,2'-ditracene show matching emission profiles with the only difference in the Franck-Condon factors and a decreased photoluminescence decay time constant from 14 ns for tetracene to 5 ns for 2,2'-ditracene, which can be attributed to the increased density of the vibrational modes in 2,2'-ditracene. Evaluation of the photon statistics of individual 2,2'-ditracene molecules however showed that the system does not behave as two individual chromophores but as a collective state, preserving the spectral properties of the two tetracene chromophores. Complementary calculations performed by Marian Deutsch in the group of Prof. Dr. Bernd Engels at the Institute of Physical and Theoretical Chemistry at the University of Würzburg helped to understand the processes in the materials and could show that the electronic and vibronic modes of 2,2'-ditracene are superpositions of the modes occurring in tetracene. In

contrast, single-crystalline 2,2'-ditetracene behaves significantly different than tetracene, namely exhibiting a red shift in photoluminescence of 150 meV, caused by an altered crystalline packing that lowers the S_1-state energy level. Temperature-dependent photoluminescence measurements revealed a rich emission pattern from 2,2'-ditetracene single crystals. The mechanisms behind this were unraveled using photoluminescence lifetime density analysis in different spectral regions of the emission spectrum and at different temperatures. An excimer state was identified that is located about 5 meV below the S_1-state, separated by a 1 meV barrier, and which can decay to the ground state with a time constant of 9 ns. Also, as the S_1-state energy level is lowered below the $E(S_1) \geq 2 \times E(T_1)$ threshold, singlet fission is suppressed in 2,2'-ditetracene in contrast to tetracene. Therefore, at low temperatures, photoluminescence is enhanced by a factor of 46, which could make 2,2'-ditetracene a useful material for future applications in devices such as OLEDs or lasers.

The second multichromophore species, para-xylylene bridged perylene bisimide macrocycles, were synthesized by Peter Spenst in the group of Prof. Dr. Frank Würthner at the Institute of Organic Chemistry at the University of Würzburg, by linking three and four perylene bisimides, respectively. To reveal the exciton dynamics in these macrocycles, highly diluted monomers as well as trimers and tetramers were doped into matrices of polymethyl methacrylate to create thin films in which individual macrocycles could be analyzed. The emission spectra of the macrocycles remained identical to those of the monomers, indicating weak coupling between the chromophores. Single photon emission could be verified for monomers as well as macrocycles, as exciton-exciton annihilation processes suppress the simultaneous emission of two photons from one macrocycle. Nevertheless, the proof of the occurrence of a doubly excited state was obtained by excitation power dependent photon statistics measurements. The formalism developed in the theory part of this thesis for calculating the photon statistics of multichromophore systems was used here to find a theoretical model that matches the experimental results. The main features of this model are a doubly excited state, fast singlet-singlet annihilation, and an efficient transition from the doubly excited state to a dark triplet state. The occurrence of triplet-triplet annihilation was demonstrated in a subsequent experiment in which the macrocycles were excited at a laser intensity well above the saturation intensity of the monomer species. In contrast to the monomers, the trimers and tetramers exhibited neither a complete dark state nor saturation of photoluminescence. Both processes, efficient singlet-singlet and triplet-triplet annihilation make perylene bisimide macrocycles exceptionally bright single photon emitters. These advantages were utilized to realize a room temperature electrically driven fluorescent single photon source. For this purpose, OLEDs were fabricated using polyvinylcarbazole and 2-tert-

butylphenyl-5-biphenyl-1,3,4-oxadiazol blends as a host material for perylene bisimide trimers. Photon antibunching could be observed in both optically and electrically driven devices, representing the first demonstration of electrically driven single photon sources using fluorescent emitters at room temperature. As expected from the previous optical experiments, the electroluminescence of the molecules was exceptionally bright, emitting about 10^5 photons per second, which could be seen even by eye under the microscope.

Finally, in the last section 4.7 of this thesis, two additional measurement schemes were proposed as an alternative to the measurement of the second-order correlation function $g^{(2)}(t)$ of single molecules, which only provides information about the first two factorial moments of the molecules' photon statistics. In the first scheme, the $g^{(3)}(t)$ function was measured with three photodiodes, which is a consequential extension of the Hanbury Brown and Twiss measurement with two photodiodes. It was demonstrated how measuring the $g^{(3)}(t)$ function is able to identify interfering emitters with non-Poisson statistics in the experiment.

The second setup was designed with an electro-optic modulator that repeatedly generates photoexcitation in the form of a step function. The recording of luminescence transients for different excitation intensities yields the same results as the corresponding $g^{(2)}$-functions measured on single emitters, both in their shape and in their dependence on excitation power. To demonstrate this concept, the TADF emitter TXO-TPA (2-[4-(diphenylamino)phenyl]-10,10-dioxide-9H-thioxanthen-9-one) was doped at a concentration of 10^{-4} wt% in a mCP (1,3-Bis(N-carbazolyl)benzene) matrix. This concentration was low enough that TXO-TPA molecules did not interact with each other, but an ensemble of molecules was still present in the detection volume. The intramolecular transition rates between singlet and triplet states of TXO-TPA could be derived with an error of at most 5 %. Other experimental techniques designed to obtain this information require either lengthy measurements on single molecules, where sample preparation is also often a challenge, or temperature-dependent fluorescence lifetime measurements, which require a cryostat, which in turn places constraints on the sample design used. In future, this approach could establish a powerful method to study external factors influencing molecular transition rates.

Overall, this thesis has introduced new molecular materials, revealed their photophysical properties, and demonstrated how they can be used to fabricate efficient and even novel light sources.

7 Zusammenfassung

Diese Dissertation befasst sich mit der Photophysik ausgewählter kleiner organischer Moleküle mit dem Ziel, diese für effiziente und sogar neuartige Lichtquellen zu nutzen. Die vorgestellten Studien konzentrierten sich insbesondere darauf, die zugrunde liegende Exzitonendynamiken offenzulegen und die Übergangsraten zwischen verschiedenen molekularen Zuständen zu bestimmen. Es wurde gezeigt, wie die spezifischen Eigenschaften und Mechanismen der Lichtemission in fluoreszierenden Molekülen, Molekülen mit Phosphoreszenz oder thermisch aktivierter verzögerter Fluoreszenz (TADF), Biradikalen und Multichromophoren genutzt werden können, um neuartige lichtemittierende Bauelemente herzustellen. Das wichtigste Instrument, das dabei zum Einsatz kam, war die Analyse der Photonenstatistik der Emitter, d. h. die Analyse der zeitlichen Verteilung der emittierten Photonen während der elektrischen oder optischen Anregung.

In der Einleitung dieser Arbeit wurde das Funktionsprinzip organischer Leuchtdioden (OLED) vorgestellt, während in Kapitel 2 der physikalische Hintergrund relevanter Eigenschaften organischer Moleküle, des Lichts und ihrer Wechselwirkung miteinander behandelt wurde. Insbesondere wurden das Auftreten von diskreten Energieniveaus in organischen Halbleitern und der Prozess der spontanen Lichtemission erörtert. Darüber hinaus wurde in diesem Kapitel ein mathematischer Formalismus ausgearbeitet, um herauszufinden, welche Informationen über das untersuchte Molekül durch die Analyse seiner Photonenstatistik gewonnen werden können. Es wurde mathematisch gezeigt, dass die Intensitätskorrelationsfunktion $g^{(2)}(t)$ Informationen über die ersten beiden faktoriellen Momente der Photonenstatistik enthält und faktorielle Momente höherer Ordnung keine zusätzlichen Informationen über das untersuchte System enthalten, wenn sich das System nach der Emission eines Photons immer im gleichen Zustand befindet. Zum Abschluss des Grundlagenteil dieser Arbeit wurden in Kapitel 3 die verwendeten Charakterisierungsmethoden vorgestellt, darunter die konfokale Mikroskopie einzelner Moleküle, die zeitkorrelierte Einzelphotonenzählung und temperaturabhängige Photolumineszenzmessungen.

Um den für das Verständnis der folgenden Ergebniskapitel notwendigen Hintergrund zu schaffen, wurde in Abschnitt 4.1 die Phänomene des Photoblinkens und des Photobleichens einzelner Moleküle näher betrachtet. Bei einem Squarain-basierten fluoreszie-

renden Emitter wurde während der Photoanregung ein schneller Wechsel zwischen einem hellen und einem dunklen Zustand beobachtet. Anhand von Übergangsraten zwischen den Molekülzuständen, die aus der Literatur bekannt sind, wurde ein konsistentes Modell vorgestellt, das die Verteilung der Verweilzeiten des Moleküls in den hellen und dunklen Zuständen erklären kann. Insbesondere wurde eine Exponential- und eine Potenzgesetz-Wahrscheinlichkeitsverteilung für die Zeit gemessen, die das Molekül im hellen bzw. dunklen Zustand verweilte. Dieses Verhalten sowie der Wechsel der Photolumineszenzintensität zwischen den beiden Zuständen wurde schlüssig durch diffundierenden Restsauerstoff in der Probe erklärt, die in einer mit Stickstoff gefüllten Glovebox hergestellt worden war. Auf die organischen Gast-Wirts-Filme der nachfolgenden Proben dieser Arbeit wurden dünne Streifen aus Aluminium aufgebracht, die als Sauerstoffgetter dienten. Dadurch wurde nicht nur der Effekt des Photobleichens unterdrückt, sondern auch die Zeit bis zu diesem deutlich verlängert, was viele der folgenden Untersuchungen überhaupt erst möglich machte.

Für Emitter, die in Displays verwendet werden, sind Emissionseigenschaften wie schmalbandige Lumineszenz und kurze Fluoreszenzlebensdauern wünschenswert. Diese Eigenschaften können nicht nur durch das Emittermolekül selbst, sondern auch durch die Wechselwirkung mit der Umgebung beeinflusst werden. Bevor der Fokus auf die Photophysik einzelner kleiner organischer Moleküle gelegt wurde, wurde daher in Abschnitt 4.2 die Wechselwirkung einer molekularen Spezies auf Perylenbisimid-Basis mit ihrer lokalen Umgebung in einer ungeordneten Polymethylmethacrylatmatrix untersucht. In einem statistischen Ansatz wurden individuelle photophysikalische Eigenschaften für 32 einzelne Moleküle gemessen und Korrelationen in der Variation dieser Merkmale analysiert. Dadurch wurde deutlich, wie die lokale Polarität der Umgebung der Moleküle deren Photophysik beeinflusst. Insbesondere wurde gezeigt, wie eine Erhöhung der lokalen Polarität zu einer rotverschobenen Emission, schmaleren Emissionslinien, einer breiteren vibronischen Aufspaltung zwischen verschiedenen Emissionslinien in Kombination mit einem kleineren Huang-Rhys-Parameter und einer längeren Fluoreszenzlebensdauer führt. In Zukunft könnten diese Ergebnisse dazu beitragen, einzelne Chromophore in größere Makromoleküle einzubetten, um dem Chromophor die optimale lokale Umgebung zu bieten, damit es die gewünschten Emissionseigenschaften aufweist.

Die nächsten beiden Abschnitte widmeten sich einer innovativen und vielversprechenden Klasse von Chromophoren, linear koordinierten Kupferkomplexen, die in der Gruppe von Dr. Andreas Steffen am Institut für Anorganische Chemie der Universität Würzburg synthetisiert wurden. Bei Kupferatomen sind die d-Orbitale vollständig besetzt,

was unerwünschte metallzentrierte d-d*-Zustände verhindert, die in der Regel eine niedrige Energie besitzen und nicht strahlend rekombinieren. Gleichzeitig bietet das Kupferatom eine flexible Koordinationsgeometrie, und es wird erwartet, dass Komplexe in ihrer linearen Form die geringsten Molekülverformung nach optischer Anregung erfahren. Je nach Wahl der Liganden können diese Kupferkomplexe sowohl Phosphoreszenz als auch temperaturaktivierte verzögerte Fluoreszenz zeigen. In Abschnitt 4.3 wurde ein phosphoreszierender Kupferkomplex mit einem Chloratom und einem 1-(2,6-Diisopropylphenyl)-3,3,5,5-Tetramethyl-2-pyrrolidin-yliden-Liganden auf seine Eignung als optisch aktives Material in einer OLED untersucht. Zu diesem Zweck wurde eine OLED mit einer auf Polyspirobisfluoren basierenden Copolymermatrix und dem Dotant in einer Konzentration von 20 wt% elektrisch angeregt. Die Entfaltung des Emissionsspektrums in Beiträge der Matrix und des Dotanten ergab, dass 60 % der OLED-Emission auf den Kupferkomplex zurückzuführen war. Außerdem wurde gezeigt, dass die Form des Emissionsspektrums des Kupferkomplexes beim Einbau in die OLED unverändert bleibt, aber um etwa 233 meV rot verschoben ist.

In Abschnitt 4.4 wurde ein zweiter Kupferkomplex analysiert, der eine thermisch aktivierte verzögerte Fluoreszenz (TAFD) aufweist. Dieser Komplex besteht aus einem Carbazolat sowie einem 2-(2,6-Diisopropyl)-phenyl-1,1-diphenyl-isoindol-2-ium-3-id-Liganden und wurde als Festkörper und auf Einzelmolekülebene untersucht, wobei eine Einzelphotonenemission bis zu einer Intensität von 78.000 Photonen pro Sekunde gemessen wurde. Die Auswertung der Autokorrelationsfunktion zweiter Ordnung des emittierten Lichts belegt einen effizienten Übergang zwischen den angeregten Singulett- und Triplett-Zuständen auf der Pikosekunden-Zeitskala. Im Festkörper wurde der temperaturabhängige Fluoreszenzabfall des Komplexes nach gepulster Photoanregung im Temperaturbereich zwischen 300 K und 5 K untersucht. Aus diesen Messungen wurde eine kleine Singulett-Triplett-Energielücke von nur 65 meV und eine Triplett-Subniveau-Aufspaltung von 3.0 meV ermittelt. Die Übergangsraten zwischen den entsprechenden molekularen Zuständen konnten ebenfalls bestimmt werden. Die schnelle Singulett-Zerfallszeit von τ_{S1} = 9.8 ns konnte den effizienten thermisch aktivierten verzögerten Fluoreszenzprozess zugeordnet werden, der somit erstmals für diese neue Klasse der Kupfer(I)-Komplexe nachgewiesen wurde.

Während die thermisch aktivierte verzögerte Fluoreszenz eine elegante Möglichkeit ist, ansonsten dunkle Triplettzustände für die strahlende Emission zu nutzen, vermeiden Radikale Molekülspezies dunkle Triplettzustände vollständig. Dies hat jedoch in der Regel den großen Nachteil, dass die Moleküle chemisch instabil sind. Daher wurden im Rahmen des DFG-Graduiertenkollegs GRK 2112 *Molecular biradicals: structure, properties*

and reactivity von Yohei Hattori aus der Arbeitsgruppe von Prof. Dr. Christoph Lambert und Rodger Rausch aus der Arbeitsgruppe von Prof. Dr. Frank Würthner am Institut für Organischen Chemie an der Universität Würzburg zwei chemisch stabile Radikal-Spezies synthetisiert. In Abschnitt 4.5 wurde untersucht, wie diese Moleküle in OLEDs verwendet werden können.

Im ersten Biradikal auf Isoindigo-Basis (6,6'-Bis(3,5-di-tert-butyl-4-phenoxyl)-1,1'-bis(2-ethylhexyl)-[3,3'-biindolinyl-iden]-2,2'-dion) blockieren zwei tert-Butyl-Einheiten sterisch chemische Reaktionen an der Stelle des ungepaarten Elektrons und ein elektronenziehender Kern verschiebt die Elektronendichte ins Zentrum des Chromophors. Mit diesen Eigenschaften war es möglich, eine mit dem Biradikal dotierte OLED auf Basis eines Poly(p-phenylenvinylen)-Copolymers zu realisieren und Lumineszenz sowohl unter optischer als auch unter elektrischer Anregung zu beobachten. Die Analyse der Formen der Photo- und Elektrolumineszenzspektren bei unterschiedlichen Dotierungskonzentrationen ergab, dass der Förster-Resonanz-Energietransfer der dominierende Übergangsmechanismus für Exzitonen von der Matrix auf die biradikalischen Dotierstoffe ist. Ebenso konnten OLEDs mit dem zweiten Biradikal auf Diphenylmethylpyridinbasis (4-(5-(Bis(2,4,6-trichlorphenyl)methyl)-4,6-dichlorpyridin-2-yl)-N-(4-(5-(Bis(2,4,6-trichlorphenyl)methyl)-4,6-dichlorpyridin-2-yl)phenyl)-N-(4-methoxyphenyl)anilin) als Dotierstoff realisiert werden. In diesem Biradikal schützen chlorierte Diphenylmethylgruppen die beiden ungepaarten Elektronen. Die Photo- und Elektrolumineszenzspektren zeigten eine Emission im nahen Infrarotbereich zwischen 750 nm und 1000 nm. Ebenso war der Försterresonanz-Energietransfer der dominierende Energietransfermechanismus mit einer Transfereffizienz von nahezu 100 %, selbst bei Dotierungskonzentrationen von etwa 5 wt%. Neben der Demonstration funktionierender OLEDs auf der Basis von Biradikalen stellt der Nachweis der Lumineszenz der beiden Biradikal-Spezies in den Bauteilen auch einen wichtigen Schritt zur Nutzung experimenteller Techniken wie der optisch detektierten Elektronenspinresonanz dar, die komplementäre Informationen über die elektronischen Zustände der Emitters und deren Spin-Verteilung während des OLED-Betriebs liefern können.

Eine weitere untersuchte Klasse von Emittern sind Moleküle, bei denen mehrere Chromophore kovalent zu einem molekularen System verbunden sind. Die Eigenschaften dieser Multichromophore wurden in Abschnitt 4.6 analysiert. Dabei wurde untersucht, wie das photophysikalische Verhalten der Moleküle durch die kovalente Bindung beeinflusst wird, welche maßgeblich die Wechselwirkung zwischen den Chromophoren bestimmt. Das erste Multichromophor, 2,2'-Ditetracen, wurde von Lena Ross in der Gruppe von Prof. Dr. Anke Krüger am Institut für Organischen Chemie an der Universität Würzburg syntheti-

siert und in dieser Arbeit sowohl auf Einzelmolekülebene als auch in seiner kristallinen Form analysiert. Während die Einkristalle in einem vertikalen Sublimationsofen aufgereinigt und gewachsen wurden, wurden die Proben für die Einzelmolekülstudien an Matrizen von Polymethylmethacrylat und kristallinem Anthracen präpariert. Simultan wurde Tetracen analysiert, um die Auswirkungen der kovalenten Bindung beurteilen zu können. In Proben, bei denen der Abstand zwischen zwei Gastmolekülen ausreichend groß ist, zeigen Tetracen und 2,2'-Ditracen übereinstimmende Emissionsprofile mit lediglich veränderten Franck-Condon-Faktoren und einer verringerten Photolumineszenz-Abklingzeitkonstante von 14 ns für Tetracen auf 5 ns für 2,2'-Ditracen, was auf die erhöhte Dichte der Schwingungsmoden in 2,2'-Ditracen zurückgeführt werden kann. Die Auswertung der Photonenstatistiken der einzelnen 2,2'-Ditracen-Moleküle zeigte, dass sich das System erwartungsgemäß nicht wie zwei einzelne Chromophore verhält, sondern wie ein kollektiver Zustand, der jedoch die spektralen Eigenschaften der beiden Tetracen-Chromophore beibehält. Ergänzende Berechnungen, die von Marian Deutsch in der Gruppe von Prof. Dr. Bernd Engels am Institut für Physikalische und Theoretische Chemie an der Universität Würzburg durchgeführt wurden, halfen, die Prozesse in den Materialien zu verstehen und konnten zeigen, dass die elektronischen und vibronischen Moden von 2,2'-Ditracen eine Superposition der Moden in Tetracen sind. Im Gegensatz dazu unterscheidet sich einkristallines 2,2'-Ditetracen von Tetracen. So weist es eine Rotverschiebung der Photolumineszenz von 150 meV auf, die durch eine veränderte kristalline Packung verursacht wird, die das Energieniveau des S_1-Zustands absenkt. Temperaturabhängige Photolumineszenzmessungen zeigten ein reichhaltiges Emissionsmuster von 2,2'-Ditetracen-Einkristallen. Die zugrunde liegenden Mechanismen wurden mithilfe der Analyse von Photolumineszenz-Lebensdauern in verschiedenen Spektralbereichen des Emissionsspektrums und bei unterschiedlichen Temperaturen ermittelt. Es wurde ein Excimer-Zustand identifiziert, der sich etwa 5 meV unterhalb des S_1-Zustands befindet, der durch eine 1 meV-Barriere von diesem getrennt ist und der mit einer Zeitkonstante von 9 ns in den Grundzustand zerfallen kann. Außerdem wird die Singulett-Aufspaltung in 2,2'-Ditetracen im Gegensatz zu Tetracen unterdrückt, da das Energieniveau des S_1-Zustands unter die Schwelle von $E(S_1) \geq 2 \times E(T_1)$ abgesenkt wird. Folglich wird die Photolumineszenz bei niedrigen Temperaturen um einen Faktor von bis zu 46 verstärkt, was 2,2'-Ditetracen zu einem nützlichen Material für zukünftige Anwendungen in Geräten wie OLEDs oder Lasern machen könnte.

Die zweite multichromophore Spezies, para-Xylylen-verbundene Perylenbisimid-Makrozyklen, wurden von Peter Spenst in der Gruppe von Prof. Dr. Frank Würthner am Institut der Organischen Chemie an der Universität Würzburg synthetisiert, indem drei bzw. vier Perylenbisimide miteinander verknüpft wurden. Um die Exzitonendynamik in diesen Ma-

krozyklen zu untersuchen, wurden stark verdünnte Monomere sowie Trimere und Tetramere in Matrizen aus Polymethylmethacrylat mit sehr niedriger Konzentration dotiert, um dünne Filme zu erzeugen, in denen individuelle Makrozyklen analysiert werden konnten. Die Emissionsspektren der Makrozyklen blieb identisch zu denen der Monomere, was auf eine schwache Kopplung zwischen den Chromophoren hindeutet. Die Emission einzelner Photonen konnte sowohl für Monomere als auch für Makrozyklen nachgewiesen werden, da Exziton-Exziton-Annihilationsprozesse die gleichzeitige Emission von zwei Photonen aus einem Makromolkül unterdrücken. Der Nachweis eines doppelt angeregten Zustands wurde durch Messungen der von der Anregungsleistung abhängigen Photonenstatistik erbracht. Der im theoretischen Teil dieser Arbeit entwickelte Formalismus zur Berechnung der Photonenstatistik von multichromophoren Systemen wurde hier verwendet, um ein theoretisches Modell zu finden, das mit den experimentellen Ergebnissen übereinstimmt. Die wichtigsten Merkmale dieses Modells sind ein doppelt angeregter Zustand, eine schnelle Singulett-Singulett-Annihilation und ein effizienter Übergang vom doppelt angeregten Zustand in einen dunklen Triplett-Zustand. Das Auftreten der Triplett-Triplett-Annihilation wurde in einem anschließenden Experiment nachgewiesen, bei dem die Makrozyklen mit einer Laserintensität angeregt wurden, die deutlich über der Sättigungsintensität der Monomerspezies lag. Im Gegensatz zu den Monomeren wiesen die Trimere und Tetramere weder einen vollständig dunklen Zustand noch eine Sättigung der Photolumineszenz auf. Beide Prozesse, Singulett-Singulett- und Triplett-Triplett-Annihilation, machen Perylenbisimid-Makrozyklen zu außergewöhnlich hellen Einzelphotonen-Emittern. Diese Vorteile wurden genutzt, um eine elektrisch betriebene Einzelphotonenquelle bei Raumtemperatur zu realisieren. Zu diesem Zweck wurden OLEDs unter Verwendung von Polyvinylcarbazol und 2-tert-Butylphenyl-5-biphenyl-1,3,4-oxadiazol als Wirtsmaterialien für Perylenbisimid-Trimere hergestellt. Photonen-Antibunching konnte sowohl in optisch als auch in elektrisch betriebenen OLEDs beobachtet werden, was die erste Demonstration von elektrisch betriebenen Einzelphotonenquellen mit fluoreszierenden Emittern bei Raumtemperatur darstellt. Wie aufgrund der vorangegangenen optischen Experimente zu erwarten war, war die Elektrolumineszenz der Moleküle außergewöhnlich hell und wies etwa 10^5 Photonen pro Sekunde auf, so dass die Einzelemitteremission sogar mit dem Auge unter dem Mikroskop gesehen werden konnten.

Im letzten Abschnitt 4.7 dieser Dissertation wurden schließlich zwei zusätzliche Messverfahren als Alternative zur Messung der Korrelationsfunktion zweiter Ordnung $g^{(2)}(t)$ einzelner Moleküle vorgeschlagen, da die $g^{(2)}(t)$-Funktion nur Informationen über die ersten beiden faktoriellen Momente der Photonenstatistik der Moleküle liefert. In einem ersten Ansatz wurde die $g^{(3)}(t)$-Funktion mit drei Photodioden gemessen, was eine

logische Erweiterung der Messung nach Hanbury Brown und Twiss mit zwei Photodioden darstellt. Hierbei wurde gezeigt, wie die Messung der $g^{(3)}(t)$-Funktion in der Lage ist, störende Emitter mit Nicht-Poisson-Statistik im Experiment zu identifizieren.

Das zweite Messverfahren ist mit einem elektro-optischen Modulator ausgestattet, der wiederholt Photoanregungen in Form einer Stufenfunktion ermöglicht. Die Aufzeichnung von Lumineszenz-Transienten für verschiedene Anregungsintensitäten erzeugt am molekularen Ensemble die gleichen Ergebnisse wie $g^{(2)}(t)$-Messungen, die an Einzelemittern durchgeführt wurden, sowohl in ihrer Form als auch in ihrer Abhängigkeit von der Anregungsleistung. Zur Demonstration dieses Konzepts wurde der TADF-Emitter TXO-TPA (2-[4-(Diphenylamino)phenyl]-10,10-dioxide-9H-thioxanthen-9-one) in einer Konzentration von 10^{-4} wt% mit einer mCP (1,3-Bis(N-carbazolyl)benzol)-Matrix gemischt. Diese Konzentration war gering genug, dass die TXO-TPA-Moleküle nicht miteinander wechselwirkten, aber dennoch ein Ensemble von Molekülen im Detektionsvolumen vorhanden war. Die intramolekularen Übergangsraten zwischen Singulett- und Triplett-Zuständen von TXO-TPA konnten mit einem Fehler von nur 5 % abgeleitet werden. Andere experimentelle Techniken, mit denen diese Informationen gewöhnlich gewonnen werden, erfordern entweder langwierige Messungen an einzelnen Molekülen, bei denen die Probenvorbereitung oft eine Herausforderung darstellt, oder temperaturabhängige Messungen der Fluoreszenzlebensdauer, für die ein Kryostat erforderlich ist, was wiederum Anforderungen an das verwendete Probendesign stellt. In Zukunft könnte dieser Ansatz eine nützliche Methode darstellen, um externer Faktoren, die die molekularen Übergangsraten beeinflussen, zu bestimmen und zu quantifizieren.

Insgesamt wurden in dieser Arbeit neue molekulare Materialien vorgestellt, ihre photophysikalischen Eigenschaften offengelegt und demonstriert, wie sie zur Herstellung effizienter und sogar neuartiger Lichtquellen verwendet werden können.

List of Figures

List of Tables

Bibliography

[1] K. Koch, J. McLean, R. Segev, M. A. Freed, M. J. Berry, V. Balasubramanian and P. Sterling. How much the eye tells the brain. *Current Biology*, **16**, 14, 1428 (2006). doi: 10.1016/j.cub.2006.05.056.

[2] E. Erb. Ct-100 the merrill (https://www.radiomuseum.org/r/rca_ct_100ct10_the_merrill_ch.html) (2018-04-18).

[3] H. Chen, J. Lee, B. Lin, S. Chen and S. Wu. Liquid crystal display and organic light-emitting diode display: Present status and future perspectives. *Light: Science & Applications*, **7**, 3, 17168 (2018). doi: 10.1038/lsa.2017.168.

[4] Steve D. Steve's vintage color tv page (http://www.wtv-zone.com/stevetek/) (2020-06-13).

[5] Sony. press release, xperia 1 ii (https://presscentre.sony.de/pressreleases/sony-stellt-neue-smartphones-vor-2975293) (2020-02-24).

[6] H. Yersin. *Highly Efficient OLEDs with Phosphorescent Materials*. Wiley-VCH, Weinheim, 1., auflage edition (2008). ISBN 9783527621316.

[7] L. Duan, K. Xie and Y. Qiu. Review paper: progress on efficient cathodes for organic light-emitting diodes: Progress on efficient cathodes for organic light-emitting diodes. *Journal of the Society for Information Display*, **19**, 6, 453 (2011). doi: 10.1889/JSID19.6.453.

[8] Y. Sun and S. R. Forrest. Enhanced light out-coupling of organic light-emitting devices using embedded low-index grids. *Nature Photonics*, **2**, 8, 483 (2008). doi: 10.1038/nphoton.2008.132.

[9] T. Tsujimura. *OLED display fundamentals and applications*. Wiley series in display technology. John Wiley & Sons Inc, Hoboken, New Jersey, second edition edition (2017). ISBN 9781119187493.

[10] C. Mayr and W. Brütting. Control of molecular dye orientation in organic luminescent films by the glass transition temperature of the host material. *Chemistry of Materials*, **27**, 8, 2759 (2015). doi: 10.1021/acs.chemmater.5b00062.

[11] C. Murawski, K. Leo and M. C. Gather. Efficiency roll-off in organic light-emitting diodes. *Advanced Materials*, **25**, 47, 6801 (2013). doi: 10.1002/adma.201301603.

[12] S.-W. Wen, M.-T. Lee and C. H. Chen. Recent development of blue fluorescent oled materials and devices. *Journal of Display Technology*, **1**, 1, 90 (2005). doi: 10.1109/JDT.2005.852802.

[13] J. K. Bowmaker and H. J. A. Dartnall. Visual pigments of rods and cones in a human retina. *The Physiological Society*, **298**, 501 (1980). doi: 10.1113/jphysiol.1980.sp013097.

[14] K. Masaoka, Y. Nishida, M. Sugawara and E. Nakasu. Design of primaries for a wide-gamut television colorimetry. *IEEE Transactions on Broadcasting*, **56**, 4, 452 (2010). doi: 10.1109/TBC.2010.2074450.

[15] C. Adachi, M. A. Baldo, M. E. Thompson and S. R. Forrest. Nearly 100% internal phosphorescence efficiency in an organic light-emitting device. *Journal of Applied Physics*, **90**, 10, 5048 (2001). doi: 10.1063/1.1409582.

[16] J. Zhang, Y. Guan, J. Yang, W. Hua, S. Wang, Z. Ling, H. Lian, Y. Liao, W. Lan, B. Wei and W.-Y. Wong. Highly-efficient solution-processed green phosphorescent organic light-emitting diodes with reduced efficiency roll-off using ternary blend hosts. *Journal of Materials Chemistry C*, **7**, 36, 11109 (2019). doi: 10.1039/C9TC02701G.

[17] H. Haken and H. C. Wolf. *Molekülphysik und Quantenchemie*. Springer-Lehrbuch. Springer, Berlin (2006). ISBN 9783540303145.

[18] N. J. Turro, V. Ramamurthy and J. C. Scaiano. *Modern molecular photochemistry of organic molecules*. University Science Books, Sausalito, California (2010). ISBN 1891389254.

[19] M. A. Baldo, D. F. O'Brien, Y. You, A. Shoustikov, S. Sibley, M. E. Thompson and S. R. Forrest. Highly efficient phosphorescent emission from organic electroluminescent devices. *Nature*, **395**, 6698, 151 (1998). doi: 10.1038/25954.

[20] A. Einstein. Über einen die Erzeugung und Verwandlung des Lichtes betreffenden heuristischen Gesichtspunkt [adp 17, 132 (1905)]. *Annalen der Physik*, **14**, 1, 164 (2005). doi: 10.1002/andp.200590004.

[21] J. F. Clauser. Experimental distinction between the quantum and classical field-theoretic predictions for the photoelectric effect. *Physical Review D*, 853–860 (1974). doi: 10.1103/PhysRevD.9.853.

[22] R. Hanbury Brown and R. Q. Twiss. A test of a new type of stellar interferometer on sirius. *Nature*, **178**, 4541, 1046 (1956). doi: 10.1038/1781046a0.

[23] P. A. M. Dirac. The quantum theory of the emission and absorption of radiation. *Proceedings of the royal society A*, **114**, 1, 243 (1927). doi: 10.1098/rspa.1927.0039.

[24] D. Y. Kondakov, T. D. Pawlik, T. K. Hatwar and J. P. Spindler. Triplet annihilation exceeding spin statistical limit in highly efficient fluorescent organic light-emitting diodes. *Journal of Applied Physics*, **106**, 12, 124510 (2009). doi: 10.1063/1.3273407.

[25] X. Qiao, P. Yuan, D. Ma, T. Ahamad and S. M. Alshehri. Electrical pumped energy up-conversion: A non-linear electroluminescence process mediated by triplet-triplet annihilation. *Organic Electronics*, **46**, 1 (2017). doi: 10.1016/j.orgel.2017.03.020.

[26] V. Abraham and N. J. Mayhall. Simple rule to predict boundedness of multiexciton states in covalently linked singlet-fission dimers. *The Journal of Physical Chemistry Letters*, **8**, 22, 5472 (2017). doi: 10.1021/acs.jpclett.7b02476.

[27] S. Toyota, R. Miyaji, Y. Yamamoto, M. Inoue, K. Wakamatsu and T. Iwanaga. An enantiopure 5,5'-bitetracene. *European Journal of Organic Chemistry*, **2015**, 35, 7648 (2015). doi: 10.1002/ejoc.201501135.

[28] M. Roth, M. Ahles, C. Gawrisch, T. Schwalm, R. Schmechel, C. Melzer, H. von Seggern and M. Rehahn. Rodlike tetracene derivatives. *Chemistry (Weinheim an der Bergstrasse, Germany)*, **23**, 54, 13445 (2017). doi: 10.1002/chem.201702382.

[29] S. Masuo, T. Vosch, M. Cotlet, P. Tinnefeld, S. Habuchi, Bell, Toby D. M., I. Oesterling, D. Beljonne, B. Champagne, K. Müllen, M. Sauer, J. Hofkens and F. C. De Schryver. Multichromophoric dendrimers as single-photon sources: A single-molecule study. *The Journal of Physical Chemistry B*, **108**, 43, 16686 (2004). doi: 10.1021/jp047804b.

[30] Y. Tao, K. Yuan, T. Chen, P. Xu, H. Li, R. Chen, C. Zheng, L. Zhang and W. Huang. Thermally activated delayed fluorescence materials towards the breakthrough of

organoelectronics. *Advanced materials (Deerfield Beach, Fla.)*, **26**, 47, 7931 (2014). doi: 10.1002/adma.201402532.

[31] C. Baleizão and M. N. Berberan-Santos. Recent developments in the thermally activated delayed fluorescence of fullerenes. *ECS Transactions*, **13**, 14, 3 (2008). doi: 10.1149/1.2998526.

[32] C. A. Parker and C. G. Hatchard. Triplet-singlet emission in fluid solutions. phosphorescence of eosin. *Transactions of the Faraday Society*, **57**, 1894 (1961). doi: 10.1039/tf9615701894.

[33] A. Endo, M. Ogasawara, A. Takahashi, D. Yokoyama, Y. Kato and C. Adachi. Thermally activated delayed fluorescence from sn(4+)-porphyrin complexes and their application to organic light emitting diodes–a novel mechanism for electroluminescence. *Advanced materials (Deerfield Beach, Fla.)*, **21**, 47, 4802 (2009). doi: 10.1002/adma.200900983.

[34] X.-K. Chen, B. W. Bakr, M. Auffray, Y. Tsuchiya, C. D. Sherrill, C. Adachi and J.-L. Bredas. Intramolecular noncovalent interactions facilitate thermally activated delayed fluorescence (tadf). *The journal of physical chemistry letters*, **10**, 12, 3260 (2019). doi: 10.1021/acs.jpclett.9b01220.

[35] D. Beljonne, Z. Shuai, G. Pourtois and J. L. Bredas. Spin−orbit coupling and intersystem crossing in conjugated polymers: A configuration interaction description. *The Journal of Physical Chemistry A*, **105**, 15, 3899 (2001). doi: 10.1021/jp010187w.

[36] M. A. Baldo, S. Lamansky, P. E. Burrows, M. E. Thompson and S. R. Forrest. Very high-efficiency green organic light-emitting devices based on electrophosphorescence. *Applied Physics Letters*, **75**, 1, 4 (1999). doi: 10.1063/1.124258.

[37] A. J. Lees and F. N. Castellano, editors. *Photophysics of Organometallics*, volume 29 of *Topics in Organometallic Chemistry*. Springer-Verlag Berlin Heidelberg, Berlin, Heidelberg (2010). ISBN 978-3-642-04729-9.

[38] K. Tang, K. Liu and I. Chen. Rapid intersystem crossing in highly phosphorescent iridium complexes. *Chemical Physics Letters*, **386**, 4-6, 437 (2004). doi: 10.1016/j.cplett.2004.01.098.

[39] Y. V. Romanovskii, A. Gerhard, B. Schweitzer, U. Scherf, R. I. Personov and H. Bässler. Phosphorescence of π-conjugated oligomers and polymers. *Physical Review Letters*, **84**, 5, 1027 (2000). doi: 10.1103/PhysRevLett.84.1027.

[40] Z. Sun, Q. Ye, C. Chi and J. Wu. Low band gap polycyclic hydrocarbons: From closed-shell near infrared dyes and semiconductors to open-shell radicals. *Chemical Society Reviews*, **41**, 23, 7857 (2012). doi: 10.1039/c2cs35211g.

[41] E. Barkai. *Theory and evaluation of single-molecule signals*. World Scientific, Singapore and Hackensack, NJ (2008). ISBN 9789812793485.

[42] D. Meltzer and L. Mandel. Determination of intensity correlation functions from photoelectric counting distributions. *IEEE Journal of Quantum Electronics*, **6**, 11, 661 (1970). doi: 10.1109/JQE.1970.1076341.

[43] M. Frank. Aufbau und Optimierung eines Messplatzes zur zeitaufgelösten Fluoreszenzspektroskopie an Tetracen und Ditetracen. Masterarbeit, Julius-Maximilians-Universität Würzburg, Würzburg (2018).

[44] P. Török. Propagation of electromagnetic dipole waves through dielectric interfaces. *Optics Letters*, **25**, 19, 1463 (2000). doi: 10.1364/OL.25.001463.

[45] K. G. Lee, X. W. Chen, H. Eghlidi, P. Kukura, R. Lettow, A. Renn, V. Sandoghdar and S. Götzinger. A planar dielectric antenna for directional single-photon emission and near-unity collection efficiency. *Nature Photonics*, **5**, 3, 166 (2011). doi: 10.1038/NPHOTON.2010.312.

[46] M. Lippitz, F. Kulzer and M. Orrit. Statistical evaluation of single nano-object fluorescence. *ChemPhysChem*, **6**, 5, 770 (2005). doi: 10.1002/cphc.200400560.

[47] W. E. Moerner. Those blinking single molecules. *Science*, **277**, 5329, 1059 (1997). doi: 10.1126/science.277.5329.1059.

[48] C. Bradac, T. Gaebel, N. Naidoo, M. J. Sellars, J. Twamley, L. J. Brown, A. S. Barnard, T. Plakhotnik, A. V. Zvyagin and J. R. Rabeau. Observation and control of blinking nitrogen-vacancy centres in discrete nanodiamonds. *Nature nanotechnology*, **5**, 5, 345 (2010). doi: 10.1038/NNANO.2010.56.

[49] J. P. Hoogenboom, J. Hernando, E. M. H. P. van Dijk, N. F. van Hulst and M. F. García-Parajó. Power-law blinking in the fluorescence of single organic molecules. *ChemPhysChem*, **8**, 6, 823 (2007). doi: 10.1002/cphc.200600783.

[50] M. Sliwa, C. Flors, I. Oesterling, J. Hotta, K. Müllen, De Schryver, F. C. and J. Hofkens. Single perylene diimide dendrimers as single-photon sources. *Journal of Physics: Condensed Matter*, **19**, 44, 445004 (2007). doi: 10.1088/0953-8984/19/44/445004.

[51] H. Lin, R. Camacho, Y. Tian, T. E. Kaiser, F. Würthner and I. G. Scheblykin. Collective fluorescence blinking in linear j-aggregates assisted by long-distance exciton migration. *Nano letters*, **10**, 2, 620 (2010). doi: 10.1021/nl9036559.

[52] M. Kuno, D. P. Fromm, H. F. Hamann, A. Gallagher and D. J. Nesbitt. "on"/"off" fluorescence intermittency of single semiconductor quantum dots. *The Journal of Chemical Physics*, **115**, 2, 1028 (2001). doi: 10.1063/1.1377883.

[53] H. Peter Lu and X. Sunney Xie. Single-molecule spectral fluctuations at room temperature. *Nature*, **385**, 6612, 143 (1997). doi: 10.1038/385143a0.

[54] S. F. Völker and C. Lambert. Exciton coupling effects in polymeric cis -indolenine squaraine dyes. *Chemistry of Materials*, **24**, 13, 2541 (2012). doi: 10.1021/cm301109u.

[55] B. Stender, S. F. Völker, C. Lambert and J. Pflaum. Optoelectronic processes in squaraine dye–doped oleds for emission in the near–infrared. *Advanced Materials*, **25**, 21, 2943 (2013). doi: 10.1002/adma.201204938.

[56] H. M. Zidan and M. Abu-Elnader. Structural and optical properties of pure pmma and metal chloride-doped pmma films. *Physica B: Condensed Matter*, **355**, 1-4, 308 (2005). doi: 10.1016/j.physb.2004.11.023.

[57] F. Urbach. The long-wavelength edge of photographic sensitivity and of the electronic absorption of solids. *Physical Review*, **92**, 5, 1324 (1953). doi: 10.1103/PhysRev.92.1324.

[58] W. P. Ambrose, T. Basché and W. E. Moerner. Detection and spectroscopy of single pentacene molecules in a p–terphenyl crystal by means of fluorescence excitation. *The Journal of Chemical Physics*, **95**, 10, 7150 (1991). doi: 10.1063/1.461392.

[59] R. Zondervan, F. Kulzer, S. B. Orlinskii and M. Orrit. Photoblinking of rhodamine 6g in poly(vinyl alcohol): Radical dark state formed through the triplet. *The journal of physical chemistry. A*, **107**, 35, 6770 (2003). doi: 10.1021/jp034723r.

[60] P. Tinnefeld, J. Hofkens, D.-P. Herten, S. Masuo, T. Vosch, M. Cotlet, S. Habuchi, K. Müllen, F. C. de Schryver and M. Sauer. Higher-excited-state photophysical

pathways in multichromophoric systems revealed by single-molecule fluorescence spectroscopy. *ChemPhysChem*, **5**, 11, 1786 (2004). doi: 10.1002/cphc.200400325.

[61] O. Panzer, W. Göhde, U. C. Fischer, H. Fuchs and K. Müllen. Influence of oxygen on single molecule blinking. *Advanced Materials*, **10**, 17, 1469 (1998). doi: 10.1002/(SICI)1521-4095(199812)10:17<1469::AID-ADMA1469>3.0.CO;2-O.

[62] K. Itô and H. P. McKean. *Diffusion Processes and their Sample Paths: Reprint of the 1974 Edition*, volume 125 of *Classics in Mathematics*. Springer, Berlin and Heidelberg (1965). ISBN 9783540606291.

[63] C. G. Hübner, A. Renn, I. Renge and U. P. Wild. Direct observation of the triplet lifetime quenching of single dye molecules by molecular oxygen. *The Journal of Chemical Physics*, **115**, 21, 9619 (2001). doi: 10.1063/1.1421382.

[64] E. Mei, S. Vinogradov and R. M. Hochstrasser. Direct observation of triplet state emission of single molecules: Single molecule phosphorescence quenching of metalloporphyrin and organometallic complexes by molecular oxygen and their quenching rate distributions. *Journal of the American Chemical Society*, **125**, 43, 13198 (2003). doi: 10.1021/ja030271k.

[65] B. Stender. Einzelmolekülspektroskopie an organischen molekülen. Dissertation, Julius-Maximilians-Universität Würzburg, Würzburg (2014).

[66] A. E. Clark, C. Qin and A. D. Q. Li. Beyond exciton theory: A time-dependent dft and franck−condon study of perylene diimide and its chromophoric dimer. *Journal of the American Chemical Society*, **129**, 24, 7586 (2007). doi: 10.1021/ja0687724.

[67] C.-H. Chin and S. H. Lin. Theoretical investigations of absorption and fluorescence spectra of protonated pyrene. *Physical Chemistry Chemical Physics*, **18**, 21, 14569 (2016). doi: 10.1039/C6CP00327C.

[68] G. Angulo, G. Grampp and A. Rosspeintner. Recalling the appropriate representation of electronic spectra. *Spectrochimica acta. Part A, Molecular and biomolecular spectroscopy*, **65**, 3-4, 727 (2006). doi: 10.1016/j.saa.2006.01.007.

[69] T. Fließbach. *Lehrbuch zur theoretischen Physik: Quantenmechanik*. Springer Spektrum (2018). ISBN 3662580306.

[70] C. M. Hansen. *Hansen solubility parameters: A user's handbook*. CRC Press (2007). ISBN 1420006835.

[71] B. Shivraj, B. Siddlingeshwar, A. Thomas, E. M. Kirilova, D. D. Divakar and A. A. Alkheraif. Experimental and theoretical insights on the effect of solvent polarity on the photophysical properties of a benzanthrone dye. *Spectrochimica acta. Part A, Molecular and biomolecular spectroscopy*, **218**, 221 (2019). doi: 10.1016/j.saa.2019.04.001.

[72] A. Hattori, H. Sato and M. Vacha. Microscale polarity in polymer films probed by fluorescence of a benzanthrone derivative on ensemble and single-molecule level. *Chemical Physics Letters*, **435**, 4, 311 (2007). doi: 10.1016/j.cplett.2006.12.093.

[73] A. Yadigarli, Q. Song, S. I. Druzhinin and H. Schönherr. Probing of local polarity in poly(methyl methacrylate) with the charge transfer transition in nile red. *Beilstein Journal of Organic Chemistry*, **15**, 2552 (2019). doi: 10.3762/bjoc.15.248.

[74] A. Amirav, U. Even and J. Jortner. Microscopic solvation effects on excited–state energetics and dynamics of aromatic molecules in large van der waals complexes. *The Journal of Chemical Physics*, **75**, 6, 2489 (1981). doi: 10.1063/1.442426.

[75] P. Kapusta, O. Machalický, R. Hrdina, M. Nepraš, M. B. Zimmt and V. Fidler. Photophysics of 3-substituted benzanthrones: Substituent and solvent control of intersystem crossing. *The journal of physical chemistry. A*, **107**, 46, 9740 (2003). doi: 10.1021/jp035610a.

[76] A. D. Quartarolo, S. G. Chiodo and N. Russo. A tddft investigation of bay substituted perylenediimides: Absorption and intersystem crossing. *Journal of Computational Chemistry*, **33**, 11, 1091 (2012). doi: 10.1002/jcc.22914.

[77] W. Yang, J. Zhao, C. Sonn, D. Escudero, A. Karatay, H. G. Yaglioglu, B. Küçüköz, M. Hayvali, C. Li and D. Jacquemin. Efficient intersystem crossing in heavy-atom-free perylenebisimide derivatives. *The Journal of Physical Chemistry C*, **120**, 19, 10162 (2016). doi: 10.1021/acs.jpcc.6b01584.

[78] E. Lang, R. Hildner, H. Engelke, P. Osswald, F. Würthner and J. Köhler. Comparison of the photophysical parameters for three perylene bisimide derivatives by single-molecule spectroscopy. *ChemPhysChem*, **8**, 10, 1487 (2007). doi: 10.1002/cphc.200700186.

[79] P. Spenst, R. M. Young, M. R. Wasielewski and F. Würthner. Guest and solvent modulated photo-driven charge separation and triplet generation in a perylene bisimide cyclophane. *Chemical science*, **7**, 8, 5428 (2016). doi: 10.1039/c6sc01574c.

[80] Y. J. Zhang, T. Oka, R. Suzuki, J. T. Ye and Y. Iwasa. Electrically switchable chiral light-emitting transistor. *Science (New York, N.Y.)*, **344**, 6185, 725 (2014). doi: 10.1126/science.1251329.

[81] David R. Lide. *CRC Handbook of Chemistry and Physics: Internet Version 2005, <http://www.hbcpnetbase.com>*. CRC Press (2005).

[82] N. Armaroli and H. J. Bolink, editors. *Photoluminescent materials and electroluminescent devices*. Topics in current chemistry collections. Springer, Cham (2017). ISBN 9783319593043.

[83] M. Gernert, U. Müller, M. Haehnel, J. Pflaum and A. Steffen. A cyclic alkyl(amino)carbene as two-atom pi-chromophore leading to the first phosphorescent linear cui complexes. *Chemistry (Weinheim an der Bergstrasse, Germany)*, **23**, 9, 2206 (2017). doi: 10.1002/chem.201605412.

[84] P.-T. Chou, Y. Chi, M.-W. Chung and C.-C. Lin. Harvesting luminescence via harnessing the photophysical properties of transition metal complexes. *Coordination Chemistry Reviews*, **255**, 21-22, 2653 (2011). doi: 10.1016/j.ccr.2010.12.013.

[85] K. C. Mondal, S. Roy, B. Maity, D. Koley and H. W. Roesky. Estimation of σ-donation and π-backdonation of cyclic alkyl(amino) carbene-containing compounds. *Inorganic chemistry*, **55**, 1, 163 (2016). doi: 10.1021/acs.inorgchem.5b02055.

[86] J. R. Bellingham, W. A. Phillips and C. J. Adkins. Intrinsic performance limits in transparent conducting oxides. *Journal of Materials Science Letters*, **11**, 5, 263 (1992). doi: 10.1007/BF00729407.

[87] R. Schlaf, H. Murata and Z. Kafafi. Work function measurements on indium tin oxide films. *Journal of Electron Spectroscopy and Related Phenomena*, **120**, 1-3, 149 (2001). doi: 10.1016/S0368-2048(01)00310-3.

[88] F. Jonas and W. Krafft. Neue Polythiophen-Dispersionen, ihre Herstellung und ihre Verwendung - European Patent Office - EP 0440957 A2 (1991).

[89] G. Greczynski, T. Kugler, M. Keil, W. Osikowicz, M. Fahlman and W. Salaneck. Photoelectron spectroscopy of thin films of pedot–pss conjugated polymer blend: A mini-review and some new results. *Journal of Electron Spectroscopy and Related Phenomena*, **121**, 1, 1 (2001). doi: 10.1016/S0368-2048(01)00323-1.

[90] A. Elschner, F. Bruder, H.-W. Heuer, F. Jonas, A. Karbach, S. Kirchmeyer, S. Thurm and R. Wehrmann. Pedt/pss for efficient hole-injection in hybrid organic light-emitting diodes. *Synthetic Metals*, **111-112**, 139 (2000). doi: 10.1016/S0379-6779(99)00328-8.

[91] A. Berntsen, Y. Croonen, C. Liedenbaum, H. Schoo, R.-J. Visser, J. Vleggaar and P. van de Weijer. Stability of polymer leds. *Optical Materials*, **9**, 1-4, 125 (1998). doi: 10.1016/S0925-3467(97)00082-7.

[92] S. A. Carter, M. Angelopoulos, S. Karg, P. J. Brock and J. C. Scott. Polymeric anodes for improved polymer light-emitting diode performance. *Applied Physics Letters*, **70**, 16, 2067 (1997). doi: 10.1063/1.118953.

[93] S. Tang, A. Sandström, J. Fang and L. Edman. A solution-processed trilayer electrochemical device: Localizing the light emission for optimized performance. *Journal of the American Chemical Society*, **134**, 34, 14050 (2012). doi: 10.1021/ja3041916.

[94] F. Laquai, G. Wegner, C. Im, H. Bässler and S. Heun. Comparative study of hole transport in polyspirobifluorene polymers measured by the charge-generation layer time-of-flight technique. *Journal of Applied Physics*, **99**, 2, 023712 (2006). doi: 10.1063/1.2165413.

[95] M. A. Parshin, J. Ollevier, M. Van der Auweraer, M. M. de Kok, H. T. Nicolai, A. J. Hof and P. W. M. Blom. Hole transport in blue and white emitting polymers. *Journal of Applied Physics*, **103**, 11, 113711 (2008). doi: 10.1063/1.2938057.

[96] B. Park, I.-G. Bae, S. Y. Na, Y. Aggarwal and Y. H. Huh. High brightness and efficiency of polymer-blend based light-emitting layers without the assistance of the charge-trapping effect. *Optics Express*, **27**, 12, A693 (2019). doi: 10.1364/OE.27.00A693.

[97] S. L. Lai, M. Y. Chan, C. S. Lee and S. T. Lee. Investigation of calcium as high performance cathode in small-molecule based organic light-emitting devices. *Journal of Applied Physics*, **94**, 11, 7297 (2003). doi: 10.1063/1.1623326.

[98] D. Foreman-Mackey, D. W. Hogg, D. Lang and J. Goodman. emcee: The mcmc hammer. doi: 10.1086/670067.

[99] R. Rausch, D. Schmidt, D. Bialas, I. Krummenacher, H. Braunschweig and F. Würthner. Stable organic (bi)radicals by delocalization of spin density into the electron-poor chromophore core of isoindigo. *Chemistry (Weinheim an der Bergstrasse, Germany)*, **24**, 14, 3420 (2018). doi: 10.1002/chem.201706002.

[100] Y. Hattori, E. Michail, A. Schmiedel, M. Moos, M. Holzapfel, I. Krummenacher, H. Braunschweig, U. Müller, J. Pflaum and C. Lambert. Luminescent mono-, di-, and triradicals: Bridging polychlorinated triarylmethyl radicals by triarylamines and triarylboranes. *Chemistry (Weinheim an der Bergstrasse, Germany)*, **25**, 68, 15463 (2019). doi: 10.1002/chem.201903007.

[101] I. N. Hulea, R. F. J. van der Scheer, H. B. Brom, B. M. W. Langeveld-Voss, A. van Dijken and K. Brunner. Effect of dye doping on the charge carrier balance in ppv light emitting diodes as measured by admittance spectroscopy. *Applied Physics Letters*, **83**, 6, 1246 (2003). doi: 10.1063/1.1600850.

[102] P. W. M. Blom, M. J. M. de Jong and J. J. M. Vleggaar. Electron and hole transport in poly(p –phenylene vinylene) devices. *Applied Physics Letters*, **68**, 23, 3308 (1996). doi: 10.1063/1.116583.

[103] M. Bajpai, K. Kumari, R. Srivastava, M. N. Kamalasanan, R. S. Tiwari and S. Chand. Electric field and temperature dependence of hole mobility in electroluminescent pdy 132 polymer thin films. *Solid State Communications*, **150**, 13-14, 581 (2010). doi: 10.1016/j.ssc.2010.01.001.

[104] V. Lejeune, A. Despres and E. Migirdicyan. Zero-field splitting of the first excited triplet state in biradicals estimated from magnetic effects on the fluorescence decays. *Journal of Physical Chemistry*, **94**, 26, 8861 (1990).

[105] X. Ai, E. W. Evans, S. Dong, A. J. Gillett, H. Guo, Y. Chen, T. J. H. Hele, R. H. Friend and F. Li. Efficient radical-based light-emitting diodes with doublet emission. *Nature*, **563**, 7732, 536 (2018). doi: 10.1038/s41586-018-0695-9.

[106] U. Müller, L. Roos, M. Frank, M. Deutsch, S. Hammer, M. Krumrein, A. Friedrich, T. B. Marder, B. Engels, A. Krueger and J. Pflaum. Role of intermolecular interactions in the excited-state photophysics of tetracene and 2,2'-ditetracene. *The Journal of Physical Chemistry C* (2020). doi: 10.1021/acs.jpcc.0c04066.

[107] E. Sackmann and D. Rehm. Fluorescence polarization measurements on molecules oriented in liquid crystals. *Chemical Physics Letters*, **4**, 9, 537 (1970). doi: 10.1016/0009-2614(70)87055-5.

[108] S. Tavazzi, L. Raimondo, L. Silvestri, P. Spearman, A. Camposeo, M. Polo and D. Pisignano. Dielectric tensor of tetracene single crystals: The effect of anisotropy

on polarized absorption and emission spectra. *The Journal of chemical physics*, **128**, 15, 154709 (2008). doi: 10.1063/1.2897436.

[109] K. Danel, T.-H. Huang, J. T. Lin, Y.-T. Tao and C.-H. Chuen. Blue-emitting anthracenes with end-capping diarylamines. *Chemistry of Materials*, **14**, 9, 3860 (2002). doi: 10.1021/cm020250+.

[110] S. A. Odom, S. R. Parkin and J. E. Anthony. Tetracene derivatives as potential red emitters for organic leds. *Organic letters*, **5**, 23, 4245 (2003). doi: 10.1021/ol035415e.

[111] L. C. Picciolo, H. Murata and Z. H. Kafafi. Organic light-emitting devices with saturated red emission using 6,13-diphenylpentacene. *Applied Physics Letters*, **78**, 16, 2378 (2001). doi: 10.1063/1.1362259.

[112] J. Niemax. Tetracen – kristallzucht und elektronischer transport. Dissertation, Universität Stuttgart, Stuttgart (2005).

[113] L. Yarmus, J. Rosenthal and M. Chopp. Epr of triplet excitions in tetracene crystals: spin polarization and the role of singlet exciton fission. *Chemical Physics Letters*, **16**, 3, 477 (1972). doi: 10.1016/0009-2614(72)80404-4.

[114] M. B. Smith and J. Michl. Singlet fission. *Chemical reviews*, **110**, 11, 6891 (2010). doi: 10.1021/cr1002613.

[115] Z. Birech, M. Schwoerer, T. Schmeiler, J. Pflaum and H. Schwoerer. Ultrafast dynamics of excitons in tetracene single crystals. *The Journal of chemical physics*, **140**, 11, 114501 (2014). doi: 10.1063/1.4867696.

[116] M. J. Y. Tayebjee, R. G. C. R. Clady and T. W. Schmidt. The exciton dynamics in tetracene thin films. *Physical Chemistry Chemical Physics*, **15**, 35, 14797 (2013). doi: 10.1039/c3cp52609g.

[117] U. Sondermann, A. Kutoglu and and H. Bassler. X-ray diffraction study of the phase transition in crystalline tetracene. *The Journal of Physical Chemistry* (1984).

[118] J. D. Cook. Informing singlet fission chromophore design via photophysical exploration of tetracene and tetracene-inspired covalent dimers. Dissertation, University of Colorado, Boulder, Colorado (2017).

[119] T. Sun, L. Shen, H. Liu, X. Sun and X. Li. Synthesis and photophysical properties of a single bond linked tetracene dimer. *Journal of Molecular Structure*, **1116**, 200 (2016). doi: 10.1016/j.molstruc.2016.03.048.

[120] A. M. Müller, Y. S. Avlasevich, K. Müllen and C. J. Bardeen. Evidence for exciton fission and fusion in a covalently linked tetracene dimer. *Chemical Physics Letters*, **421**, 4-6, 518 (2006). doi: 10.1016/j.cplett.2006.01.117.

[121] F. R. Lipsett. On the production of single crystals of naphthalene and anthracene. *Canadian Journal of Physics*, **35**, 3, 284 (1957). doi: 10.1139/p57-033.

[122] R. Jankowiak and H. Bässler. Temperature dependence of non-photochemical holes in a tetracene-doped anthracene glass. *Chemical Physics Letters*, **95**, 4, 310 (1983). doi: 10.1016/0009-2614(83)80564-8.

[123] A. A. L. Nicolet, M. A. Kol'chenko, B. Kozankiewicz and M. Orrit. Intermolecular intersystem crossing in single-molecule spectroscopy: Terrylene in anthracene crystal. *The Journal of chemical physics*, **124**, 16, 164711 (2006). doi: 10.1063/1.2184311.

[124] A. A. L. Nicolet, C. Hofmann, M. A. Kol'chenko, B. Kozankiewicz and M. Orrit. Single dibenzoterrylene molecules in an anthracene crystal: Spectroscopy and photophysics. *ChemPhysChem*, **8**, 8, 1215 (2007). doi: 10.1002/cphc.200700091.

[125] I. Zschokke-Gränacher, H. Schwob and E. Baldinger. Recombination radiation in anthracene doped with tetracene. *Solid State Communications*, **5**, 10, 825 (1967). doi: 10.1016/0038-1098(67)90718-1.

[126] K. H. Probst and N. Karl. Energy levels of electron and hole traps in the band gap of doped anthracene crystals. *physica status solidi (a)*, **27**, 2, 499 (1975). doi: 10.1002/pssa.2210270219.

[127] H. J. Queisser. *Festkörperprobleme 14: Plenary Lectures of the Divisions "Semiconductor Physics", "Low Temperature Physics", "Metal Physics" of the German Physical Society, Freudenstadt, April 1-5, 1974*, volume 14 of *Advances in Solid State Physics*. Springer, Berlin and Heidelberg (1974). ISBN 9783528080204.

[128] S. Lukman, A. J. Musser, K. Chen, S. Athanasopoulos, C. K. Yong, Z. Zeng, Q. Ye, C. Chi, J. M. Hodgkiss, J. Wu, R. H. Friend and N. C. Greenham. Tuneable singlet exciton fission and triplet-triplet annihilation in an orthogonal pentacene dimer. *Advanced Functional Materials*, **25**, 34, 5452 (2015). doi: 10.1002/adfm.201501537.

[129] S. N. Sanders, E. Kumarasamy, A. B. Pun, M. L. Steigerwald, M. Y. Sfeir and L. M. Campos. Intramolecular singlet fission in oligoacene heterodimers. *Angewandte Chemie*, **128**, 10 (2016). doi: 10.1002/ange.201510632.

[130] C. Kloc, T. Siegrist and J. Pflaum. Growth of single-crystal organic semiconductors. In G. Dhanaraj, editor, *Springer handbook of crystal growth*. Springer, Heidelberg and New York (2010). ISBN 978-3-540-74182-4.

[131] D. Holmes, S. Kumaraswamy, A. J. Matzger and K. P. C. Vollhardt. On the nature of nonplanarity in the [n]phenylenes. *Chemistry - A European Journal*, **5**, 11, 3399 (1999). doi: 10.1002/(SICI)1521-3765(19991105)5:11<3399::AID-CHEM3399>3.0.CO;2-V.

[132] K. S. Novoselov, A. K. Geim, S. V. Morozov, D. Jiang, Y. Zhang, S. V. Dubonos, I. V. Grigorieva and A. A. Firsov. Electric field effect in atomically thin carbon films. *Science (New York, N.Y.)*, **306**, 5696, 666 (2004). doi: 10.1126/science.1102896.

[133] H. Müller and H. Bässler. Fluorescence of crystalline tetracene between 4.2 and 300 k. *Journal of Luminescence*, **12-13**, 259 (1976). doi: 10.1016/0022-2313(76)90090-9.

[134] G. Landl, T. Langthaler, H. W. Englt and H. F. Kauffmann. Distribution of event times in time-resolved fluorescence: The exponential series approach—algorithm, regularization, analysis. *Journal of computational Physics*, **95**, 1, 1 (1991). doi: 10.1016/0021-9991(91)90250-O.

[135] P. M. Zimmerman, C. B. Musgrave and M. Head-Gordon. A correlated electron view of singlet fission. *Accounts of chemical research*, **46**, 6, 1339 (2013). doi: 10.1021/ar3001734.

[136] W.-L. Chan, M. Ligges and X.-Y. Zhu. The energy barrier in singlet fission can be overcome through coherent coupling and entropic gain. *Nature chemistry*, **4**, 10, 840 (2012). doi: 10.1038/nchem.1436.

[137] U. Müller, P. Spenst, P. Kagerer, M. Stolte, F. Würthner and J. Pflaum. Photon–correlation studies on multichromophore macrocycles of perylene dyes. *Advanced Optical Materials*, 2200234 (2022). doi: 10.1002/adom.202200234.

[138] F. Würthner. Perylene bisimide dyes as versatile building blocks for functional supramolecular architectures. *Chemical communications (Cambridge, England)*, , 14, 1564 (2004). doi: 10.1039/b401630k.

[139] W. Herbst and K. Hunger. *Industrial Organic Pigments*. Wiley-VCH, Hoboken (2006). ISBN 9783527305766.

[140] F. Schlosser, J. Sung, P. Kim, D. Kim and F. Würthner. Excitation energy migration in covalently linked perylene bisimide macrocycles. *Chemical Science*, **3**, 9, 2778 (2012). doi: 10.1039/c2sc20589k.

[141] P. Tinnefeld, K. D. Weston, T. Vosch, M. Cotlet, T. Weil, J. Hofkens, K. Müllen, De Schryver, Frans C. and M. Sauer. Antibunching in the emission of a single tetrachromophoric dendritic system. *Journal of the American Chemical Society*, **124**, 48, 14310 (2002). doi: 10.1021/ja027343c.

[142] C. Hettich, C. Schmitt, J. Zitzmann, S. Kühn, I. Gerhardt and V. Sandoghdar. Nanometer resolution and coherent optical dipole coupling of two individual molecules. *Science (New York, N.Y.)*, **298**, 5592, 385 (2002). doi: 10.1126/science.1075606.

[143] M. Nothaft, S. Höhla, F. Jelezko, N. Frühauf, J. Pflaum and J. Wrachtrup. Electrically driven photon antibunching from a single molecule at room temperature. *Nature communications*, **3**, 628 (2012). doi: 10.1038/ncomms1637.

[144] C. C. Yap, M. Yahaya and M. M. Salleh. The effect of driving voltage on the electroluminescent property of a blend of poly(9-vinylcarbazole) and 2-(4-biphenylyl)-5-phenyl-1,3,4-oxadiazole. *Current Applied Physics*, **9**, 5, 1038 (2009). doi: 10.1016/j.cap.2008.11.004.

[145] X. Gong, S.-H. Lim, J. C. Ostrowski, D. Moses, C. J. Bardeen and G. C. Bazan. Phosphorescence from iridium complexes doped into polymer blends. *Journal of Applied Physics*, **95**, 3, 948 (2004). doi: 10.1063/1.1635976.

[146] J. Y. Park and R. C. Advincula. Tunable electroluminescence properties in cdse/pvk guest-host based light-emitting devices. *Physical Chemistry Chemical Physics*, **16**, 18, 8589 (2014). doi: 10.1039/c4cp00066h.

[147] D. Tanaka, T. Takeda, T. Chiba, S. Watanabe and J. Kido. Novel electron-transport material containing boron atom with a high triplet excited energy level. *Chemistry Letters*, **36**, 2, 262 (2007). doi: 10.1246/cl.2007.262.

[148] N. Bunzmann, S. Weissenseel, L. Kudriashova, J. Gruene, B. Krugmann, J. V. Grazulevicius, A. Sperlich and V. Dyakonov. Optically and electrically excited intermediate electronic states in donor:acceptor based oleds. *Materials Horizons*, **7**, 4, 1126 (2020). doi: 10.1039/C9MH01475F.

[149] L. Novotny and B. Hecht. *Principles of nano-optics*. Cambridge University Press, Cambridge, second edition edition (2012). ISBN 9781107005464.

[150] S. C. Kitson, P. Jonsson, J. G. Rarity and P. R. Tapster. Intensity fluctuation spectroscopy of small numbers of dye molecules in a microcavity. *Physical Review A*, **58**, 1, 620 (1998). doi: 10.1103/PhysRevA.58.620.

[151] S. Kako, M. Holmes, S. Sergent, M. Bürger, D. J. As and Y. Arakawa. Single-photon emission from cubic gan quantum dots. *Applied Physics Letters*, **104**, 1, 011101 (2014). doi: 10.1063/1.4858966.

[152] A. J. Gesquiere, Y. J. Lee, J. Yu and P. F. Barbara. Single molecule modulation spectroscopy of conjugated polymers. *The journal of physical chemistry. B*, **109**, 25, 12366 (2005). doi: 10.1021/jp0507851.

Publications

Within the framework of this thesis, the following scientific publications have been produced. During the writing of this thesis the surname of the author changed from Müller to Genheimer.

Publications in peer-reviewed journals

1. U. Müller, P. Spenst, P. Kagerer, M. Stolte, F. Würthner and J. Pflaum. Photon-Correlation Studies on Multichromophore Macrocycles of Perylene Dyes. *Advanced Optical Materials*, (2022). doi: 10.1002/adom.202200234.

2. U. Müller, L. Roos, M. Frank, M. Deutsch, S. Hammer, M. Krumrein, A. Friedrich, T. B. Marder, B. Engels, A. Kreuger and J. Pflaum. Role of Intermolecular Interactions in the Excited-State Photophysics of Tetracene and 2,2'-Ditetracene. *The Journal of Physical Chemistry C*, **124**, 36, (2020). doi: 10.1021/acs.jpcc.0c04066.

3. M. Gernert, L. Balles-Wolf, F. Kerner, U. Müller, A. Schmiedel, M. Holzapfel, C. M. Marian, J. Pflaum, C. Lambert and A. Steffen. Cyclic (amino)(aryl)carbenes (CAArCs) enter the field of chromophore ligands - Expanded π system leads to unusually deep red emitting Cu I compounds. *Journal of the American Chemical Society*, **19**, 8897 (2020). doi: 10.1021/jacs.0c02234.

4. Y. Hattori, E. Michail, A. Schmiedel, M. Moos, M. Holzapfel, I. Krummenacher, H. Braunschweig, U. Müller, J. Pflaum and C. Lambert. Luminescent Mono-, Di-, and Triradicals. Bridging Polychlorinated Triarylmethyl Radicals by Triarylamines and Triarylboranes. *Chemistry*, **25**, 68, (2019). doi: 10.1002/chem.201903007.

5. M. Gernert, U. Müller, M. Haehnel, J. Pflaum and A. Steffen. A Cyclic Alkyl(amino)-carbene as Two-Atom π-Chromophore Leading to the First Phosphorescent Linear CuI Complexes; *Chemistry*, **23**, 2206 (2017). doi: 10.1002/chem.201605412.

Acknowledgments

Ich möchte mich bei allen bedanken, die mich direkt oder indirekt bei meiner wissenschaftlichen Arbeit unterstützt haben.

- Mein Dank gilt an erster Stelle meinem Doktorvater **Prof. Dr. Jens Pflaum**. Vielen Dank für die großartige Zeit in deiner Arbeitsgruppe. Eine herausfordernde Aufgabenstellung, viel Gestaltungsfreiraum und dein Vertrauen machten die Arbeit im Labor zu einer wertvollen und lehrreichen Zeit. Durch die zahlreichen wissenschaftlichen Diskussionen konnte ich mich schnell in einem neuen Fachbereich zurechtfinden und sehr viel lernen. Deine offene Art war maßgeblich für die familiäre und kooperative Atmosphäre in der Arbeitsgruppe verantwortlich.

- Außerdem gilt mein Dank allen, die dazu beigetragen haben, dass das Arbeiten im Labor mit minimalen Reibungsverlusten möglich war. Ich bedanke mich bei **Prof. Dr. Vladimir Dyakonov** für die Bereitstellung vieler Geräte, die ich mitverwenden durfte, bei **André Thiem-Riebe** für die Instanthaltungsarbeiten und die Unterstützung bei allen technischen Problemen im Labor und auch bei all denjenigen, die ihren **Labordienst** ordnungsgemäß durchgeführt haben. Außerdem möchte ich an dieser Stelle den technischen Mitarbeitern aus der **Wissenschaftliche Werkstatt** und der **Abteilung Tieftemperaturtechnik** für ihre engagierte Unterstützung bei der Umsetzung zahlreicher Projekte danken.

- Viel Unterstützung habe ich auch durch die wissenschaftlichen Diskussionen mit **Prof. Dr. Anke Krueger**, **Prof. Dr. Bernd Engels**, **Prof. Dr. Andreas Steffen** und **Dr. habil. Andreas Sperlich** bekommen, die mit reichlich Geduld meinen Fragen beantwortet haben. Außerdem möchte ich **Prof. Dr. Heinrich Schwoerer** für die Einladung zum PhD-Symposium 2016 an die Universität Stellenbosch in Südafrika bedanken.

- Als nächstes möchte ich **Diep Phan** danken, die mich bei allen formellen Angelegenheiten unterstützt hat und so dafür gesorgt hat, ein Maximum an Zeit für die Arbeit im Labor zur Verfügung stand.

- Innerhalb unserer Arbeitsgruppe möchte ich besonders **Thomas Ferschke** danken, der unser IT-System vorbildlich verwaltet hat und mir außerdem als Experte für alle chemischen Fragen zur Seite stand. Mein Dank gilt außerdem **Sebastian Hammer**, der sich immer viel Zeit genommen hat mit mir theoretische und experimentelle Probleme bis ins letzte Detail zu diskutieren. Durch diese Diskussionen konnten wir einige Fehler in den gängigen Arbeitsabläufen ausfindig machen und beheben. Ich danke **Benedikt Stender** für die Einarbeitung am Confo-Setup und **Michael Brendl** für die vielen Tipps zu Beginn meiner Promotionszeit.

- Viele Ideen, die in dieser Arbeit umgesetzt wurden, konnten nur durch die engagierte Arbeit von zahlreichen Bacheloranten und Masteranten verwirklicht werden. Ich danke **Marcel Krumrein**, **Philipp Kagerer**, **Oliver Schneider**, **Maximilian Frank**, **Jonas Bellmann** und **Jonas Gehrig** für ihre Arbeit bei uns in der Arbeitsgruppe und wünsche ihnen viel Erfolg bei ihren zukünftigen wissenschaftlichen Tätigkeiten.

- Außerdem möchte ich den Doktoranten **Nikolai Bunzmann**, **Jeannine Grüne**, **Sebastian Weißenseel** und **Liudmila Kudriashova** und **Dr. Maria Kotova** aus der **Dyakonov-Gruppe** sowie **Daniel Friedrich** aus der Gruppe von Prof. Dr. Bert Hecht für den guten wissenschaftlichen Austausch und ihre Unterstützung danken.

- Abschließend möchte ich den Menschen danken, die mir abseits der Arbeiten am Hubland den Rücken freigehalten haben: Meinen Eltern **Berta und Klaus Müller**, nicht weniger meinen Schwiegereltern **Petra und Ulrich Genheimer**, und natürlich der wichtigsten Person in meinem Leben. **Hannah**, vielen Dank für deine grenzenlose Unterstützung!

Funding

This work was supported by the *Deutsche Forschungsgemeinschaft* (GRK2112 and PF385/11) and the *Bavarian State Ministry for Science and the Arts* (SolTech).